REVIEWS OF MODERN PHYSICS, VOLUME 93, APRIL–JUNE 2021

# Experimental perspective on three-dimensional topological semimetals

B. Q. Lv

*Beijing National Laboratory for Condensed Matter Physics and Institute of Physics,*
*Chinese Academy of Sciences, Beijing 100190, China*
*and Department of Physics, Massachusetts Institute of Technology,*
*Cambridge, Massachusetts 02139, USA*

T. Qian and H. Ding

*Beijing National Laboratory for Condensed Matter Physics and Institute of Physics,*
*Chinese Academy of Sciences, Beijing 100190, China*

(published 26 April 2021)

Topological semimetals (TSMs) are characterized by bulk band crossings in their electronic structures, which are expected to give rise to gapless electronic excitations and topological features that underlie exotic physical properties. The most famous examples are Dirac and Weyl semimetals, in which the corresponding low-energy fermionic excitations, i.e., the Dirac and Weyl fermions, are direct analogs of elementary particles in quantum field theory. The last decade has witnessed an explosion of research activities in the field of TSMs thanks to precise theoretical predictions, well-controlled material synthesis, and advanced characterization techniques including angle-resolved photoemission spectroscopy, scanning tunneling microscopy, magnetotransport measurements, optical spectroscopy, etc. Here recent progress in three-dimensional TSMs is reviewed with an emphasis on their characteristic bulk electronic structures, including dimensionality (such as zero-dimensional nodal points, one-dimensional nodal lines, and two-dimensional nodal surfaces), degeneracy (twofold, threefold, fourfold, sixfold, or eightfold) of the band crossing, the slope (type I and type II) and order (linear, quadratic, or cubic) of the band dispersion near the crossing, the characteristic topological invariants (such as monopole charges), and the crystallographic symmetries that stabilize the band crossings. The distinct signatures of the various topological semimetal phases, such as the nontrivial surface states (including Fermi arcs of Dirac and Weyl semimetals) and the unique transport and optical responses (such as chiral anomaly-induced negative magnetoresistance in Dirac and Weyl semimetals), are also reviewed.

DOI: 10.1103/RevModPhys.93.025002

## CONTENTS

## I. INTRODUCTION

One of the major themes of condensed-matter physics has been the discovery, classification, and characterization of miscellaneous phases of matter, especially for solids. Historically, i.e., before the 1980s, it was believed that Landau-Ginzburg theory (Landau and Lifshitz, 1980), which characterizes states through the principle of spontaneous symmetry breaking and local order parameters, can give a universal description of all kinds of states as well as the phase transitions among them. In the 1980s, the discovery of quantum integer and fractional Hall states (Klitzing, Dorda, and Pepper, 1980; Laughlin, 1981; Tsui, Stormer, and Gossard, 1982; Laughlin, 1983), which occur in high-mobility 2D electron gasses under an intense magnetic field, evaded the traditional Landau-Ginzburg-Wilson paradigm, as no symmetry is spontaneously broken. Instead, the quantum Hall states are described by a topological invariant, the Thouless-Kohmoto-Nightingale-Nijs number, or the Chern number (Thouless *et al.*, 1982; Simon, 1983), which is a global parameter determined by the topological structure of the enclosing manifold. The topological understanding of the quantum Hall effect is a landmark, opening up a new era of condensed-matter physics: topological quantum states of matter.

In the last 40 years, we have witnessed the emergence of many types of topological states and topological phase transitions, including quantum integer and fractional Hall states (Klitzing, Dorda, and Pepper, 1980; Laughlin, 1981; Tsui, Stormer, and Gossard, 1982; Laughlin, 1983), quantum spin Hall states (Kane and Mele, 2005a, 2005b; Bernevig, Hughes, and Zhang, 2006; Fu and Kane, 2006; König *et al.*, 2007), quantum anomalous Hall states (Haldane, 1988; Yu *et al.*, 2010; Chang *et al.*, 2013), topological insulators (TIs) (Fu and Kane, 2007; Fu, Kane, and Mele, 2007; Moore and Balents, 2007; Hsieh *et al.*, 2008; Qi, Hughes, and Zhang, 2008; Chen *et al.*, 2009; Hsieh *et al.*, 2009; Roy, 2009; Y. Xia *et al.*, 2009; Zhang *et al.*, 2009; Hasan and Kane, 2010; Qi and Zhang, 2011), topological crystalline insulators (Fu, 2011; Dziawa *et al.*, 2012; Hsieh *et al.*, 2012; Tanaka *et al.*, 2012; Ando and Fu, 2015; Wang, Alexandradinata *et al.*, 2016; J. Ma *et al.*, 2017), topological Kondo insulators (Dzero *et al.*, 2010; Jiang *et al.*, 2013; Lu *et al.*, 2013; Neupane *et al.*, 2013; Xu *et al.*, 2013), topological semimetals (TSMs) (Wan *et al.*, 2011; G. Xu *et al.*, 2011; Wang *et al.*, 2012; Young *et al.*, 2012; Armitage, Mele, and Vishwanath, 2018) (see Fig. 1), and high-order topological insulators and semimetals (Benalcazar, Bernevig, and Hughes, 2017; Langbehn *et al.*, 2017; Song, Fang, and Fang, 2017; Imhof *et al.*, 2018; Peterson *et al.*, 2018; Schindler *et al.*, 2018; Schindler, Cook *et al.*, 2018; Serra-Garcia *et al.*, 2018), as well as topological insulator (Sato *et al.*, 2011; S.-Y. Xu *et al.*, 2011; Xu *et al.*, 2012; Wu *et al.*, 2013) and semimetal transitions (Burkov and Balents, 2011; Young *et al.*, 2011; Singh *et al.*, 2012; Wang *et al.*, 2012; Liu and Vanderbilt, 2014; Cheng *et al.*, 2016; Collins *et al.*, 2018; Xu, Zhao *et al.*, 2018). Particularly significant effort has been devoted to searching and characterizing topological semimetal phases in the past ten years.

It is well known that semimetals possess a small or vanishing density of states near the Fermi energy ($E_F$). Among them, there exists a specific class of materials in which the finite density of states is caused by crossings or touching of conduction and valence bands in the three-dimensional (3D) Brillouin zone (BZ). Such band touchings usually would result in a topological phase transition and can be associated with a topological invariant (Wang *et al.*, 2012). In other words, semimetals with band touchings are generally topologically distinct from others; therefore, they are referred to as TSMs (Fang, Weng *et al.*, 2016; Weng, Dai, and Fang, 2016; Hasan *et al.*, 2017; Yan and Felser, 2017; Armitage, Mele, and Vishwanath, 2018). In the past few years, TSMs have stimulated intensive research interest, and many TSMs with different types of fermionic excitations, known as topological fermions, have been discovered (an incomplete table list of experimentally confirmed TSMs can be found in Appendix A). These TSMs can be simply divided into three groups according to the dimensionality of the band crossings. The first group has zero-dimensional (0D) band crossings, generally known as nodes or nodal points. The most famous examples include Dirac semimetals (DSMs) and Weyl semimetals (WSMs), in which two doubly or singly degenerate bands cross each other at discrete points near $E_F$, forming the fourfold Dirac points or twofold Weyl points. The corresponding low-energy excitations behave as Dirac and Weyl fermions, respectively, in high-energy physics. The solid-state realizations of Dirac and Weyl fermions gave not only new insights into long-sought-after particles in high-energy physics but also provided platforms to examine their unique topological features, including the Fermi-arc surface states

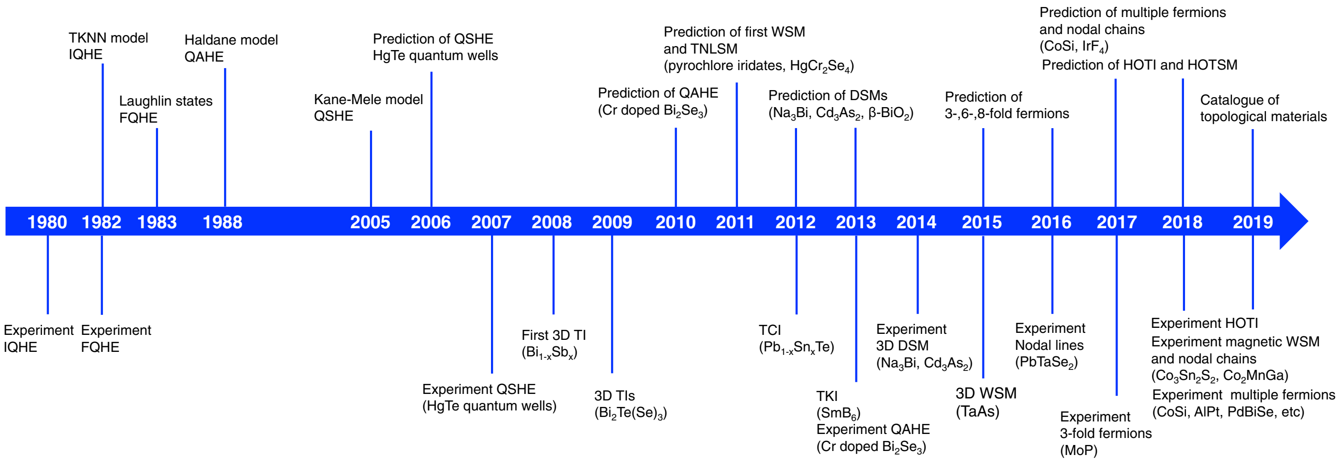

FIG. 1. Timeline of developments of topological quantum phases in condensed-matter systems. IQHE, integer quantum Hall effect; FQHE, fractional Hall effect; QAHE, quantum anomalous Hall effect; QSHE, quantum spin Hall effect; TI, topological insulator; TCI, topological crystalline insulator; TKI, topological Kondo insulator; DSM, Dirac semimetal; WSM, Weyl semimetal; TNLSM, topological nodal-line semimetal; HOTI, high-order topological insulator; HOTSM, high-order topological semimetal.

(Wan *et al.*, 2011) and the chiral anomaly effect (Nielsen and Ninomiya, 1983; Hosur, Parameswaran, and Vishwanath, 2012; Kim *et al.*, 2013; Parameswaran *et al.*, 2014). Moreover, researchers also predicted many other types of nodal points in which the fermionic excitations have no analogs in high-energy physics, such as type-II nodal points (Soluyanov *et al.*, 2015), threefold, sixfold, and eightfold degenerate nodal points (Heikkilä and Volovik, 2015; Bradlyn *et al.*, 2016; Hyart and Heikkilä, 2016; Weng *et al.*, 2016a, 2016b; Wieder *et al.*, 2016; G. Chang *et al.*, 2017b), with several of them experimentally confirmed recently (B. Q. Lv *et al.*, 2017; Ma *et al.*, 2018; Lv *et al.*, 2019; Rao *et al.*, 2019; Sanchez *et al.*, 2019; Schröter *et al.*, 2019; Takane *et al.*, 2019).

The second group has fourfold or twofold band crossings along one-dimensional (1D) lines in the momentum space. Materials with such nodal lines are generally called topological nodal-line semimetals (TNLSMs) (Burkov, Hook, and Balents, 2011; Heikkilä and Volovik, 2011; Chiu and Schnyder, 2014; Fang *et al.*, 2015). Compared to the 0D nodal points, the 1D nodal lines form a much larger variety of topological configurations, which may either take the form of an extended line running across the BZ (Chen, Xie *et al.*, 2015) or wind into a closed-loop inside the BZ (G. Xu *et al.*, 2011; Bian *et al.*, 2016), or even form chains (Bzdušek *et al.*, 2016; Yu, Wu *et al.*, 2017; Zhang, Yu *et al.*, 2017; Feng *et al.*, 2018), links as well as knots (Bi *et al.*, 2017; Chang and Yee, 2017; Chen, Lu, and Hou, 2017; Ezawa, 2017b; Z. Yan *et al.*, 2017). Like WSMs, TNLSMs are also accompanied by distinct surface states, the so-called drumhead surface states (Weng, Liang *et al.*, 2015), which are characterized by flat surface bands that are embedded inside the surface projection of the bulk nodal lines. Conversely, the drumhead surface states are not topologically protected, and a small perturbation to the surface can destroy the flatness of the surface bands (Fang, Weng *et al.*, 2016). In addition to the 0D nodal points and 1D nodal lines, recent advances in band theory have further expanded the scope of TSMs by proposing another type of band crossing that is preserved in a 2D surface in the 3D BZ; materials with such band crossings are called topological nodal-surface semimetals (Liang *et al.*, 2016; Zhong *et al.*, 2016). Compared to Dirac, Weyl, and nodal-line semimetals, nodal-surface semimetals have not been extensively explored. To date only a few nodal-surface semimetals have been predicted, and the nodal surface has been observed in the ZrSiS family of materials recently (Fu *et al.*, 2019b).

TSMs are well known for characteristic bulk band crossings, distinct surface states, and other physical consequences, such as the Weyl-fermion-related chiral anomaly effect. Theoretically, first-principles calculations have demonstrated the unprecedented capability for predicting and engineering a variety of topological phases in solids. Experimentally, angle-resolved photoemission spectroscopy (ARPES), due to its unique capability to directly probe the 3D band structure even with its spin polarization, can play a leading role in pinning down the existence of topological phases in single-crystal materials (Hasan *et al.*, 2017; Yang, Liang *et al.*, 2018; Lv, Qian, and Ding, 2019). Meanwhile, other experimental techniques, including scanning tunneling microscopy (STM), scanning tunneling spectroscopy (STS), transport, and optical measurements, have also had success in achieving a comprehensive understanding of the distinct consequences of these TSMs. To name a few, one of the transport signatures of Dirac and Weyl fermions, the chiral anomaly effect, is evident by observing negative magnetoresistance (X. Huang *et al.*, 2015; Xiong *et al.*, 2015; Hirschberger *et al.*, 2016; Li, He *et al.*, 2016; Zhang *et al.*, 2016) and/or the planar Hall effect (PHE) (Guo *et al.*, 2016; Li, Wang *et al.*, 2018; Wu *et al.*, 2018). The nontrivial $\pi$ Berry phase of Dirac and Weyl fermions can be deduced by Shubnikov–de Haas (SdH) oscillations (He *et al.*, 2014; Cao *et al.*, 2015; Xiang *et al.*, 2015; Zhao *et al.*, 2015b). In addition to ARPES, the nontrivial surface states can be also visualized by STS measurements (Batabyal *et al.*, 2016; Inoue *et al.*, 2016; Zheng *et al.*, 2016a, 2016b; Sessi *et al.*, 2017; H. Zheng *et al.*, 2017). The optical manifestations of 3D Dirac and Weyl and nodal-line fermions, i.e., the $\omega$-linear and $\omega$-independent optical conductivity $\sigma_1(\omega)$, respectively, can be proved by optical

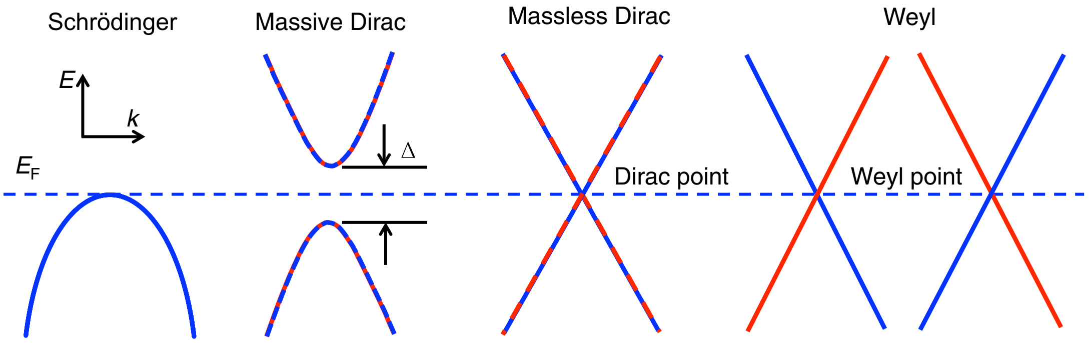

FIG. 2. Schematic plots of the band structures of Schrödinger, massive Dirac, massless Dirac, and Weyl fermions. The curves with mixed and uniform colors represent doubly degenerate and nondegenerate bands, respectively.

spectroscopy (Chen, Zhang *et al.*, 2015; Neubauer *et al.*, 2016; B. Xu *et al.*, 2016; Schilling *et al.*, 2017; Shao *et al.*, 2019).

This review, written from an experimental perspective, makes the growing field of TSMs accessible to a broad community of researchers by capturing the major developments of various types of TSMs. The review is organized as follows. We begin in Sec. I with a brief introduction to the developments of TSMs. Then in Sec. II we systematically discuss the basics, topological features, and classifications of TSMs. In Secs. III and IV, we review recent theoretical proposals, ARPES and STM confirmations, and characteristic transport and optical properties of topological nodal point semimetals, topological nodal-line and nodal-surface semimetals, respectively. Finally, in Sec. V the remaining issues, challenges, and an outlook regarding the TSMs are provided.

In this review, we include the major developments of TSMs at this stage. Given the tremendous amount of work on TSMs that has been published, this review cannot provide complete coverage of the subject, so the examples highlighted and the literature cited in this review should not be considered exhaustive. Some aspects of this subject have been described in other reviews. For example, Dirac and WSMs were recently reviewed by Burkov (2016, 2018), Jia, Xu, and Hasan (2016), Hasan *et al.* (2017), Armitage, Mele, and Vishwanath (2018), Crassee, Sankar *et al.* (2018), Manna *et al.* (2018), and Zheng and Zahid Hasan (2018); many theorists have reviewed the *ab initio* approach to the discovery and characterization of TSMs (Weng, Dai, and Fang, 2014; Bansil, Lin, and Das, 2016; Fang, Weng *et al.*, 2016; Weng, Dai, and Fang, 2016; Yu, Fang *et al.*, 2017; Bernevig *et al.*, 2018; Hirayama, Okugawa, and Murakami, 2018; Yang, Yang *et al.*, 2018); transport or optical properties of TSMs were reviewed by Hosur and Qi (2013), Burkov (2015a), He and Li (2016), Xu and Jia (2016), Li, Wang *et al.* (2017), Lu and Shen (2017), Song *et al.* (2017), Wang, Lin *et al.* (2017), Gooth *et al.* (2018), X.-C. Pan *et al.* (2018), Schoop, Pielnhofer, and Lotsch (2018), Wang and Wang (2018), and Pronin and Dressel (2021). Furthermore, there are also many reviews on other related topological phases in condensed-matter systems, such as topological insulators and/or topological superconductors (Hasan and Kane, 2010; Qi and Zhang, 2011; Cayssol, 2013; Vafek and Vishwanath, 2014; Wehling, Black-Schaffer, and Balatsky, 2014; Hasan, Xu, and Bian, 2015; Schnyder and Brydon, 2015; Sato and Ando, 2017).

## II. TSMS IN THREE DIMENSIONS

### A. Background

In solids, the nearly free quasiparticles are usually described by the well-known Schrödinger equation with the Hamiltonian $H_s = \boldsymbol{p}^2/2m^*$, where $\boldsymbol{p}$ is the momentum, $m^*$ is the so-called effective mass, which is a quantity used to simplify and describe the low-energy excitations. These low-energy excitations are often simply referred to as "Schrödinger fermions."

The Schrödinger equation provides a successful description of nearly free quasiparticles; however, there are many other types of low-energy excitations that do not obey the Schrödinger Hamiltonian, such as graphene (Novoselov *et al.*, 2005; Castro Neto *et al.*, 2009) and high-temperature $d$-wave superconductors (Bednorz and Müller, 1986; Damascelli, Hussain, and Shen, 2003). To describe these quasiparticles, new equations have been utilized, i.e., realistic Dirac and Weyl equations (Herring, 1937). In solids, the Dirac Hamiltonian has the following form:

$$H_D = \nu_F \alpha \cdot \boldsymbol{k} + \beta m {\nu_F}^2 = \begin{pmatrix} \nu_F \boldsymbol{\sigma} \cdot \boldsymbol{k} & m\nu_F^2 \\ m\nu_F^2 & -\nu_F \boldsymbol{\sigma} \cdot \boldsymbol{k} \end{pmatrix}. \quad (1)$$

Here $\boldsymbol{k} = (k_x, k_y, k_z)$ represents the momentum, $\nu_F$ is the Fermi velocity (a quantity tied to the dispersions of the bands), and $m$ is the effective mass. Equation (1) has the same form as the Dirac Hamiltonian in high-energy physics, with the effective speed of light $c$ given by the Fermi velocity, and is therefore called the Dirac Hamiltonian of condensed-matter systems. The Dirac fermions in condensed-matter systems obey a similar relativistic energy-momentum relation, i.e., $E_\pm = \pm\sqrt{m^2\nu_F^4 + k^2\nu_F^2}$, which naturally leads to spectral gap $\Delta = 2m\nu_F^2$ at $k = 0$, as shown in Fig. 2. Thus, the effective mass is directly related to the spectral gap.

In the special case of vanishing effective mass ($m \to 0$), the Dirac Hamiltonian becomes Block diagonal, that is,

$$H_D^{m=0} = \begin{pmatrix} \nu_F \boldsymbol{\sigma} \cdot \boldsymbol{k} & 0 \\ 0 & -\nu_F \boldsymbol{\sigma} \cdot \boldsymbol{k} \end{pmatrix}. \quad (2)$$

As a result, the spectrum of this massless Dirac Hamiltonian is gapless at $k = 0$, giving rise to a fourfold-degenerate node with linear dispersion in all the $k_x$, $k_y$, and $k_z$ directions, known as the Dirac point (Fig. 2). The corresponding low-energy excitations at the Dirac point are massless Dirac fermions, and materials with such 3D Dirac band crossings near $E_F$ are called DSMs.

When $m = 0$, the upper two components ($\psi_+$) and the lower two components ($\psi_-$) of $\psi$ are no longer coupled. Thus, the Bloch diagonal $H_D$ can be written in a simpler $2 \times 2$ form

$$H_\pm = \pm \nu_F \boldsymbol{\sigma} \cdot \boldsymbol{k}. \tag{3}$$

This is the Weyl Hamiltonian of condensed-matter systems, and ± corresponds to different chirality of the massless Weyl fermion: right handed ($+1$) or left handed ($-1$). Either $H_+$ or $H_-$ has two eigenvalues, i.e., $E = \pm \nu_F |k|$, which implies that the spectrum of Weyl Hamiltonian is also gapless, and two linearly dispersed and nondegenerate bands cross each other at $k = 0$ and form a two-fold-degenerate point, called the Weyl point. A fourfold-degenerate Dirac point can therefore be considered the composite of two Weyl points of opposite chirality. As expected, quasiparticles near the Weyl point act like massless relativistic Weyl fermions, and materials with such Weyl points in the 3D BZ can be termed topological WSMs.

## B. Topological aspects

### 1. Magnetic monopoles

The previously discussed nontrivial electronic structure of WSMs can be further characterized by a topological invariant, i.e., the Fermi surface (FS) Chern number ($C_{\mathrm{FS}}$) or the monopole charge (Wan *et al.*, 2011), which can be expressed as the following integration of Berry curvature over a closed Fermi surface:

$$C_{\mathrm{FS}} = \frac{1}{2\pi} \oint\!\!\!\oint_{\mathrm{FS}} \Omega(\boldsymbol{k}) \cdot d\boldsymbol{S}. \tag{4}$$

Consider the 3D Weyl nodes described by Eq. (3), the corresponding Berry curvature and Chern number are found to be

$$\begin{aligned} \boldsymbol{\Omega}_\pm(\boldsymbol{k}) &= \nabla_{\boldsymbol{k}} \times \boldsymbol{A}_\pm(\boldsymbol{k}) = \pm \frac{\hat{e}_k}{2k^2}, \\ C_{\mathrm{FS}}^\pm &= \frac{1}{2\pi} \oint\!\!\!\oint_{\mathrm{FS}} \boldsymbol{\Omega}_\pm(\boldsymbol{k}) \cdot d\boldsymbol{S} = \pm 1. \end{aligned} \tag{5}$$

Equations (5) reveal several special features of Weyl points. First, a Weyl point is a singularity (source or drain) of the Berry curvature, which is a close analog of the magnetic field but is defined in $k$ rather than real space. Therefore, Weyl points of opposite chirality can be regarded as the magnetic monopole and antimonopole in $k$ space (Fang, 2003; Balents, 2011; Wan *et al.*, 2011; G. Xu *et al.*, 2011). Second, to satisfy the periodic BZ boundary condition, the Berry curvature must begin and end somewhere within the BZ, if there is one. This leads to an important conclusion, the so-called no-go theorem (Nielsen and Ninomiya, 1981a, 1981b), indicating that the Weyl points should always come in pairs of opposite chirality so that the total monopole charge integrated over the first BZ is zero. Consequently, the only way to eliminate the Weyl points without breaking charge conservation is to annihilate them pairwise, which happens only if one can move them to the same $k$ point (Burkov and Balents, 2011; Wan *et al.*, 2011; Zyuzin, Wu, and Burkov, 2012). Thus, the Weyl points are topologically stable as long as they remain separated in $k$ space. Finally, we note the difference between the $\mathcal{T}$-breaking WSMs and $\mathcal{P}$-breaking WSMs. In a $\mathcal{P}$-breaking Weyl system, for a Weyl point at $\boldsymbol{k}$ there must be another Weyl point with the same chirality $-\boldsymbol{k}$, since the $\mathcal{T}$ invariance imposes the condition that the Berry curvatures at the $\boldsymbol{k}$ and $-\boldsymbol{k}$ points are negatives of each other, i.e., $\boldsymbol{\Omega}(\boldsymbol{k}) = -\boldsymbol{\Omega}(-\boldsymbol{k})$. However, for a $\mathcal{T}$-breaking system, the presence of $\mathcal{P}$ symmetry requires $\boldsymbol{\Omega}(\boldsymbol{k}) = \boldsymbol{\Omega}(-\boldsymbol{k})$, which implies that Weyl points at $\boldsymbol{k}$ and $-\boldsymbol{k}$ should have opposing monopole charges. Combined with the no-go theorem, one can hence conclude that an $\mathcal{P}$-breaking Weyl semimetal possesses at least two pairs of Weyl points in the BZ, whereas a $\mathcal{T}$-breaking Weyl semimetal can have a minimum of one pair of Weyl points at $\boldsymbol{k}$ and $-\boldsymbol{k}$ of opposite chirality in the BZ.

### 2. Fermi-arc surface states

One of the most striking consequences of the fact that the Weyl nodes behave as monopoles of the Berry curvature field is the appearance of unique surface states, i.e., the Fermi arcs (Balents, 2011; Wan *et al.*, 2011; G. Xu *et al.*, 2011). The reason for this can be interpreted intuitively as follows. Consider the simplest example of a hypothetical "hydrogen atom" of a WSM containing only one pair of Weyl nodes near $E_F$ in which the $\mathcal{T}$ symmetry is naturally broken. As shown in Fig. 3(a), the two Weyl nodes sit at $(0, 0, k_0)$ and one can rewrite the two Weyl Hamiltonians as $H_\pm = \pm \nu_F [k_x \sigma_x + k_y \sigma_y + m(k_z) \sigma_z]$, where $m(k_z) = k_z \pm k_0$. This rewriting is suggestive, as for every $m(k_z) \neq 0$, i.e., $k_z \neq \pm k_0$, there is precisely a massive or gapped 2D $k_x$-$k_y$-plane Dirac Hamiltonian. Assuming that all trivial states are far away from $E_F$, this implies that band structures within the $k_x$-$k_y$ plane should be fully gapped unless the slice cuts through a Weyl point ($k_z = \pm k_0$ plane). Since the Weyl nodes are sources or sinks of Berry curvature, there must be a Berry flux penetrating all the 2D layers between the two Weyl nodes of opposite monopole charge. Hence, all these 2D $k$ planes between the two Weyl nodes have a nonzero Chern number, indicating the existence of a topological edge state in this region ($-k_0 < k_z < k_0$), whereas the net Berry flux is zero in other planes ($-k_0 > k_z$ or $k_z > k_0$), resulting in a Chern number of zero. In other words, each 2D BZ that lies between the pair of Weyl nodes can be viewed as a Chern insulator state, which is associated with a chiral edge state that is guaranteed to cross $E_F$. Note that one can also consider a 2D cylinder that encloses a single Weyl point. Similarly, this 2D cylinder can be viewed as a Chern insulator, and one would expect a chiral edge state on the 1D curve that encircles the projection of the bulk Weyl point, as shown in Figs. 3(b) and 3(c). By stringing the topological edge states of all possible 2D Chern insulator planes together, one arrives at a Fermi-arc surface state. Specifically, the locus of all these edge state crossings

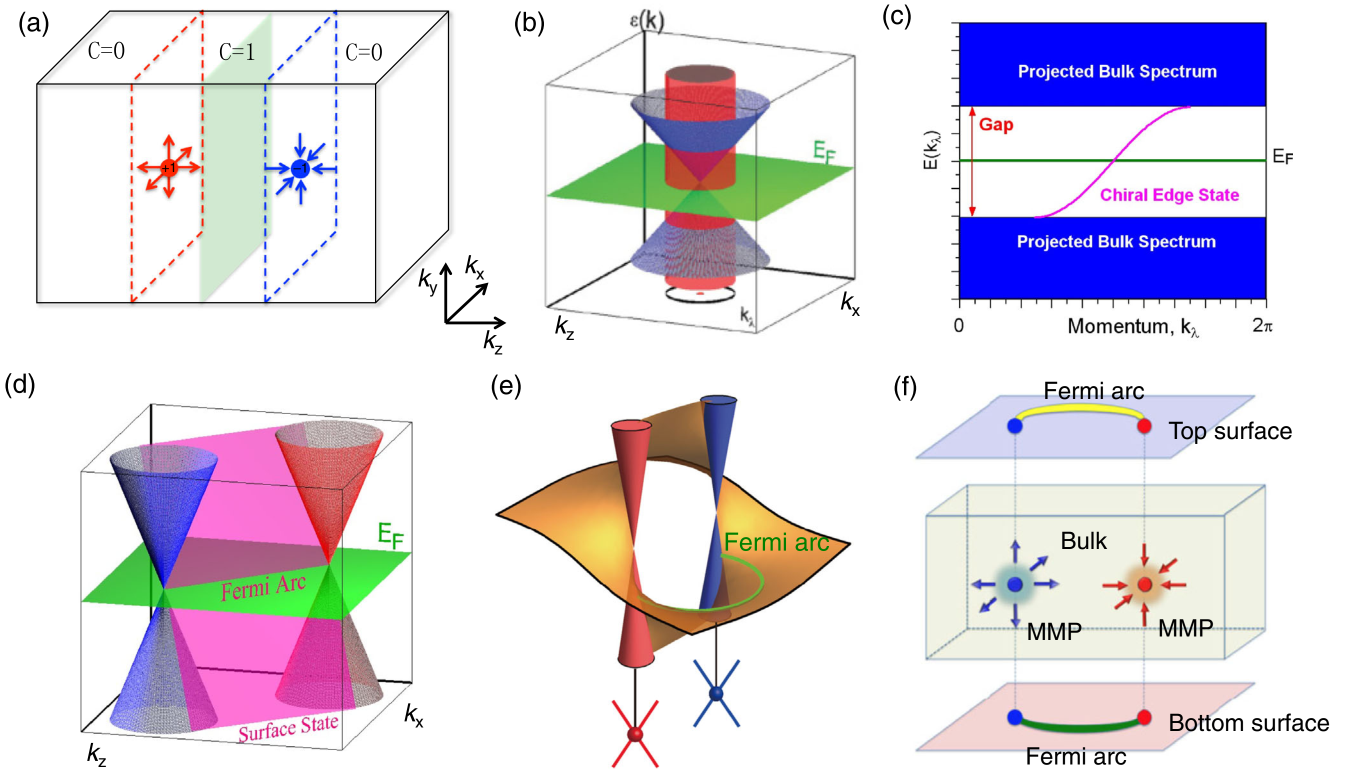

FIG. 3. (a) Schematic drawing of one pair of Weyl nodes of opposite chirality in 3D momentum space. (b),(c) Consider a 2D cylinder enclosing a Weyl node; a chiral edge state appears due to the nonzero Chern number. (d)–(f) Connection of surface states to bulk Weyl nodes. A Weyl node behaves as a magnetic monopole (MMP) in momentum space, and the helicoid edge states appear as a Fermi arc on the surface connecting projections of two Weyl nodes of opposite chirality. Adapted from Wan *et al.*, 2011, Lv *et al.*, 2015b, and Fang, Lu *et al.*, 2016.

forms an unclosed contour shape that starts from the projection of one Weyl point and ends at the other with the opposite monopole charge and is thus accordingly called a Fermi arc. This unique surface state is illustrated in Figs. 3(d)–3(f). A more detailed investigation tells us that the $E-k$ dispersions of the chiral surface states can be mapped to a helicoidal structure [Fig. 3(e)] (Fang, Lu *et al.*, 2016), and the top and bottom surface states have opposing Fermi velocities.

Generally speaking, one would expect the Fermi surface to form closed loops, such as the Fermi surface of a normal metal, but the existence of Fermi arcs in WSMs is apparently an exception. Therefore, this unusual type of surface state is viewed as a hallmark of WSMs.

### 3. Chiral anomaly

The fact that each Weyl node is a chiral magnetic monopole leads to another extraordinary phenomenon: the condensed-matter manifestation of the Adler-Bell-Jackiw anomaly (Adler, 1969; Bell and Jackiw, 1969) or the chiral anomaly (Nielsen and Ninomiya, 1983; Hosur, Parameswaran, and Vishwanath, 2012; Kim *et al.*, 2013; Parameswaran *et al.*, 2014). The simplest way to understand the chiral anomaly is by introducing the quantum limit and Landau levels. To start we consider the simplest Weyl semimetal with only one pair of Weyl nodes of opposite chirality located at $E_F$. As shown in Fig. 4, in the absence of electromagnetic field $\boldsymbol{E}$ and $\boldsymbol{B}$ the left-handed and right-handed Weyl fermions have equal chemical potentials, which implies that more electrons of one chirality than of the other cannot exist, the chirality of Weyl fermions is thus conserved.

When a magnetic field is applied, the Weyl bands formulates Landau levels, which can be expressed as

$$\varepsilon_n = \nu_F \mathrm{sgn}(n)\sqrt{2\hbar|n|eB + (\hbar\boldsymbol{k}\cdot\hat{\boldsymbol{B}})^2}, \qquad n = \pm1, \pm2, \ldots,$$
$$\varepsilon_0 = -\chi\hbar\nu_F\boldsymbol{k}\cdot\hat{\boldsymbol{B}}, \qquad (6)$$

where $n$ is the index of the Landau level, $\nu_F$ is the Fermi velocity of the Weyl bands, and $\chi$ is the chirality of the Weyl nodes, i.e., $\chi = \pm1$. Comparing this with the chiral Weyl bands, one immediately realizes that the zeroth Landau level is also linearly dispersed and chiral, as shown in Fig. 4(b). Only the zeroth Landau band crosses $E_F$, and the energy gap of the first Landau level is $\nu_F\sqrt{2\hbar eB}$. At low temperatures, suppose that the temperature-induced electron excitations is much smaller than the energy gap. Then only the zeroth Landau band is relevant for the low-energy physics and we are in the so-called quantum limit (Nielsen and Ninomiya, 1983). Now if also we apply an external electric field $\boldsymbol{E}$, the $\boldsymbol{E}$ component parallel to $\boldsymbol{B}$ would generate a coherent motion of electrons. For simplicity, imagine $\boldsymbol{E}\|\boldsymbol{B}$. The electrons are then accelerated at a rate of $eE$ in the $-\boldsymbol{E}$ direction. This motion would cause electron pumping between right-moving and

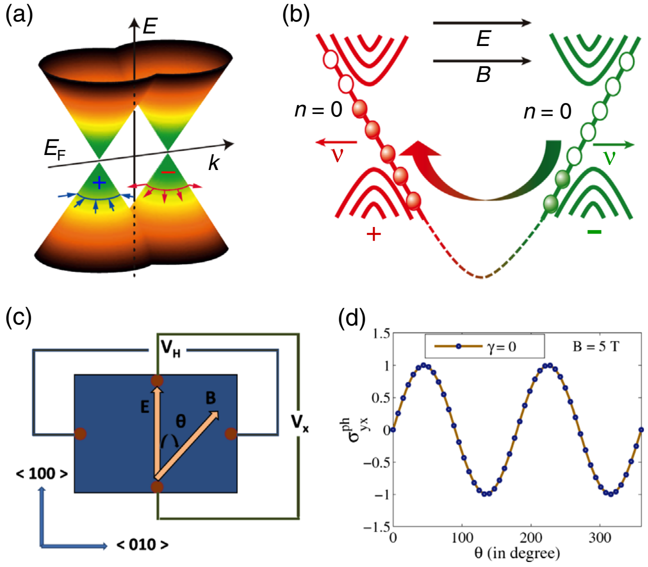

FIG. 4. (a) Schematic band dispersions of one pair of Weyl nodes of opposite chirality. (b) Illustration of the chiral anomaly based on a Landau-level spectrum of Weyl fermions in parallel electric and magnetic fields in the quantum limit. Filled (empty) circles denote occupied (unoccupied) states, while red and green areas indicate the right-handed (+) electrons and left-handed (−) electrons, respectively. (c) Schematic diagram for the planar Hall effect measurement geometry ($V_H$ is the Hall voltage). (d) Angular dependence of planar Hall conductivity for $B = 5$ T and $\gamma = 0$ ($\gamma$ is the tilt parameter). Adapted from Lv *et al.*, 2015c, Nandy *et al.*, 2017, and Yan and Felser, 2017.

left-moving zeroth Landau bands, and results in the following modified charge continuity equation for each Weyl node of opposite chirality:

$$\frac{\partial \rho_\chi}{\partial t} = -\chi \frac{e^3}{4\pi^2\hbar^2}\boldsymbol{E}\cdot\boldsymbol{B}, \tag{7}$$

where $\rho_\chi$ is the charge density of $\chi$ chirality Weyl fermions. One immediately finds that there is charge flow around an individual Weyl point, and the chiral charge of each Weyl node is thus not conserved. Note that if consider all the chiral charge in the BZ, one finds that the total charges are conserved as $(\partial/\partial t)(\rho_+ + \rho_-) = 0$. In short, the presence of parallel $\boldsymbol{E}$ and $\boldsymbol{B}$ fields induces a charge pumping from one Weyl node to the other, leading to an imbalance of chiral charge within an individual Weyl point known as the chiral anomaly. (Son and Spivak, 2013; Burkov, 2014, 2015b).

One direct consequence of the chiral anomaly is negative longitudinal magnetoresistance (NLMR) (Nielsen and Ninomiya, 1983), as explained later. Since the Weyl nodes are separated in momentum space, the previously discussed charge pumping can be relaxed only by the inter-Weyl impurity scattering, and the final chiral imbalance can thus be expressed as

$$\frac{\partial}{\partial t}(\rho_+ - \rho_-) = -\frac{e^3}{2\pi^2\hbar^2}\boldsymbol{E}\cdot\boldsymbol{B}\cdot\tau_{\mathrm{int}}, \tag{8}$$

where $\tau_{\mathrm{int}}$ is the intervalley relaxation time. Equation (8) defines an extra electric current along the magnetic field. In a sufficiently clean system, the backscattering of electrons of opposite chirality is suppressed, resulting in a large $\tau_{\mathrm{int}}$ that is nearly independent of the magnetic field in a certain range. Consequently, the longitudinal conductivity along the applied magnetic field is large and proportional to the magnitude of $\boldsymbol{B}$. In other words, the resistivity decreases with increasing magnetic field, leading to NLMR.

Note that the NLMR is a simple but not universal behavior of chiral anomaly. For example, if $\boldsymbol{B}\perp\boldsymbol{E}$, the system will have a positive magnetoresistance due to the Lorentz force. In addition, the quantum limit condition requires that no other states (such as trivial bands) cross $E_F$, otherwise, the zeroth Landau-level contribution and the NLMR would be smeared out. What is more, in a strong magnetic field the relaxation time can be proportional to $|B|^{-1}$, which cancels out the dependence on the magnitude of the magnetic field in Eq. (8). Finally, in the semiclassical limit or weak magnetic field case, researchers found that the magnetoresistance is always negative and proportional to $B^2$ (Kim *et al.*, 2013; X. Huang *et al.*, 2015; Xiong *et al.*, 2015; Li, He *et al.*, 2016; Li, Kharzeev *et al.*, 2016).

Recent advances besides NLMR reveal that the chiral anomaly and the nonzero Berry curvature in WSMs can lead to another key effect, the PHE (Burkov, 2017; Nandy *et al.*, 2017), which refers to the appearance of a large in-plane transverse voltage when the coplanar electric and magnetic fields are not perfectly aligned. Theoretically, the chiral-anomaly-induced PHE resistivity ($\rho_{xy}^{\mathrm{PHE}}$) and related longitudinal anisotropic magnetoresistance ($\rho_{xx}^{\mathrm{planar}}$) in pure WSMs can be described as

$$\begin{aligned} \rho_{xy}^{\mathrm{PHE}} &= -\Delta\rho_{\mathrm{chiral}}\sin\theta\cos\theta, \\ \rho_{xx}^{\mathrm{planar}} &= \rho_\perp - \Delta\rho_{\mathrm{chiral}}\cos^2\theta, \end{aligned} \tag{9}$$

where $\Delta\rho_{\mathrm{chiral}} = \rho_\perp - \rho_\parallel$ is the anisotropic resistivity and $\rho_\perp$ and $\rho_\parallel$ represent the resistivity with the planar magnetic field perpendicular or parallel to the current, respectively. $\theta$ is illustrated in Fig. 4(c). Experimentally, observation of both the NLMR and the PHE with a specific angular dependence given by Eq. (9) is believed to give strong evidence for the chiral anomaly.

Note that in addition to engendering the NLMR and PHE, the chiral anomaly can also lead to a large thermopower and a strong magnetic field dependence of the thermoelectric transport coefficients called the axial gravitational anomaly (Landsteiner, Megías, and Pena-Benitez, 2011; Lundgren, Laurell, and Fiete, 2014; Lucas, Davison, and Sachdev, 2016; Gooth *et al.*, 2017).

### 4. Other phenomena

Beyond the previously discussed consequences, the nontrivial electronic structure of Dirac and Weyl semimetals can generate many other interesting effects.

(i) One important transport feature expected for the case of magnetic WSMs (Fang, 2003; G. Xu *et al.*, 2011; Yang, Lu, and Ran, 2011) is the intrinsic anomalous Hall effect. Consider again a $\mathcal{T}$-breaking magnetic Weyl semimetal with a pair of Weyl nodes along the $k_z$ direction, which is shown in Fig. 3. As discussed in Sec. II.B.1, the region between the two Weyl points of opposite monopole charge can be seen as a collection of 2D Chern insulators. Owing to the nonzero Chern number, these 2D planes would naturally exhibit chiral edge states and quantized Hall conductance. Finally, the total Hall conductivity of the system should be directly given by the integral of $dk_z$ as

$$\sigma_{xy}^{\text{total}} = \frac{1}{2\pi}\int_{-\pi}^{\pi}\sigma_{xy}(k_z)dk_z = \frac{e^2}{2\pi h}(k_+^w - k_-^w), \qquad (10)$$

where $k_+^w$ and $k_-^w$ are the momentum locations of the two Weyl points. The total Hall conductance can be considered a "quantized" Hall response of a Weyl semimetal in the sense that the ratio of $\sigma_{xy}^{\text{total}}$ and $k_+^w - k_-^w$ is quantized as $e^2/2\pi h$. Note that the anomalous Hall effect principally diminishes in a $\mathcal{P}$-breaking Weyl semimetal; this is because a $\mathcal{P}$-breaking WSM possess at least two pairs of Weyl points in the BZ, and the total Berry phase contributed by the two Weyl pairs cancel each other. Instead, a spin Hall effect arises in a $\mathcal{P}$-breaking WSM (Sun *et al.*, 2016) and, similarly, this can be understood in the framework of 2D topological insulators with the spin-dependent Berry phase.

(ii) Generally, for Dirac systems with linear band dispersion, such as graphene, TIs, DSMs, and WSMs, a nontrivial $\pi$ Berry phase could be induced as the electron orbits enclose a single Dirac or Weyl point. This nontrivial Berry phase, another distinguishing feature of Dirac and Weyl fermions, has been identified using SdH oscillations (He *et al.*, 2014; Cao *et al.*, 2015; Xiang *et al.*, 2015; Zhao *et al.*, 2015b; Pan *et al.*, 2016).

(iii) Dirac and Weyl semimetals also manifest themselves in specific optical responses. One such manifestation is the real part of their optical conductivity $\sigma_1(\omega)$. Specifically, the interband optical transition in the vicinity of 3D Dirac or Weyl nodes is expected to give rise to a $\omega$-linear $\sigma_1(\omega)$ (Hosur, Parameswaran, and Vishwanath, 2012; Ashby and Carbotte, 2013, 2014; Bácsi and Virosztek, 2013; Timusk *et al.*, 2013; Tabert and Carbotte, 2016; Tabert, Carbotte, and Nicol, 2016). For WSMs with Weyl nodes located at different energies there would be a chiral chemical potential between the Weyl nodes, and this can give rise to unique nonlinear optical properties, such as the quantized circular photogalvanic effect (CPGE) (Chan, Lindner *et al.*, 2017; de Juan *et al.*, 2017; Q. Ma *et al.*, 2017; Osterhoudt *et al.*, 2019).

(iv) Other effects such as nonlocal transport (Parameswaran *et al.*, 2014), the chiral gauge anomaly (Liu, Ye, and Qi, 2013), unusual plasmon modes (Liu, Ye, and Qi, 2013; Panfilov, Burkov, and Pesin, 2014; Zhou, Chang, and Xiao, 2015; Araki and Nomura, 2016), and topological superconductivity (TSC) (Meng and Balents, 2012; Hosur *et al.*, 2014; Bednik, Zyuzin, and Burkov, 2015; Kobayashi and Sato, 2015) have also been studied.

### C. Topological classifications

As discussed, only three types of fermions are allowed in high-energy physics, while the zoology of quasiparticles in TSMs is much more abundant; this is because low-energy excitations in TSMs are constrained by the space-group symmetries of the crystal, which are much lower than the Poincaré symmetry imposed in high-energy physics. Indeed, condensed-matter physics is witnessing a rapid expansion of TSMs with various types of band crossings in the BZ, with examples including 1D topological nodal lines, type-II band crossings, symmetry-enforced twofold, threefold, fourfold, sixfold, and eightfold band crossings, and quadratic and cubic band crossings. In the following, we classify and discuss these uncovered band crossings in condensed-matter systems.

#### 1. Accidental and essential band crossings

Depending on the formation mechanism, the band crossings in TSMs can be broadly divided into two major categories: accidental and essential band crossings (Wang *et al.*, 2012; Young *et al.*, 2012; Yang and Nagaosa, 2014). The first type of band crossings is formed by band inversions in certain regions of the BZ, and the band crossings can be removed without changing the symmetry of the system; therefore, they are referred to as accidental band crossings. The second category consists of the so-called essential or symmetry-enforced band crossings. Unlike the accidental crossings, these essential band crossings are enforced by specific space-group symmetries, such as $\mathcal{T}$ symmetry and nonsymmorphic group symmetry, and cannot be removed as long as the symmetry is maintained.

##### *a. Accidental band crossings*

Band inversion is arguably the most intuitive picture and most practically useful guideline for the initial screening of possible accidental band crossings. Strictly speaking, band inversion involves the energy order switching of two electronic states around a certain time-reversal-invariant momenta (TRIM) in the BZ when compared with the conventional discrete energy level in the atomic limit. Generally, band inversion may happen when atoms form a periodical lattice and acquire sufficient band dispersion, such as a HgTe/CdTe quantum well (Bernevig, Hughes, and Zhang, 2006). In particular, when the two inverted electronic bands are located near $E_F$, the band inversion usually leads to nontrivial topological states, including 2D and 3D TIs, DSMs, WSMs, and TNLSMs.

To be explicit, we consider two electronic bands close to $E_F$ around the high-symmetric point, that is, the $\Gamma$ point. As illustrated in Fig. 5, far from this point, the red band is occupied and energetically lower than the unoccupied blue state. However, close to this high-symmetric point the two states would have inverted energy ordering with the blue state lower and occupied. Assuming that the two inverted bands are not coupled in the absence of spin-orbit coupling (SOC), they must cross at certain $k$ points, and together these band crossings form a 1D spinless nodal line in the BZ. However, this accidental nodal line is typically vulnerable to SOC. When SOC is taken into account, this nodal line will transfer into the following topological states, depending on the crystal symmetries, SOC strength, and orbital character.

(i) If the system has $\mathcal{P}$ and $\mathcal{T}$ symmetry, the inclusion of SOC will, in general, hybridize the two inverted electronic states and open up an energy gap at the band crossings, turning the system into a bulk insulator if the $E_F$ is located within the energy gap. This gapped state may be topologically nontrivial and may host conducting surface states depending on the coupling terms. Examples include the 3D TI $Bi_2Se_3$ (Zhang *et al.*, 2009), the topological crystalline insulator PbTe family (Hsieh *et al.*, 2012), the Mackay-Terrones crystal (Weng, Liang *et al.*, 2015), etc. However, if the system has additional symmorphic symmetry (i.e., point group rotations coupled with Bravais lattice translations), such as $n$-fold uniaxial rotation symmetry ($n = 3, 4, 6$), the band crossings along the rotation axis are stabilized after including SOC since the two inverted bands belong to different irreducible representations, or rotation eigenvalues. Each of the two inverted bands is doubly degenerate protected by $\mathcal{PT}$ symmetry; therefore, pairs of fourfold-degenerate Dirac points would appear along the rotation axis, turning the system into a 3D DSM in the presence of SOC. This mechanism leads to the successful prediction of two well-known DSM materials $Na_3Bi$ and $Cd_3As_2$ (Wang *et al.*, 2012, 2013).

(ii) On the contrary, if the system has no $\mathcal{P}$ or $\mathcal{T}$ symmetry, taking into account SOC the spinless nodal line can be transformed into the following topological states:

(a) If the system has no other symmetries that protect the band crossings, the inclusion of SOC can turn the system into a fully gapped TI such as CaAgAs (Yamakage *et al.*, 2016).

(b) Specifically, under a proper strength of SOC, the two electronic states with the orthogonal orbital component can touch at a discrete $k$ point, and at the same time everywhere else is gapped, transferring the system into a WSM state. Examples include the first experimentally confirmed WSM TaAs family (S.-M. Huang *et al.*, 2015; Weng, Fang *et al.*, 2015).

(c) When the system respects the combined $\mathcal{PT}$ symmetry, the bands remain spin degenerate after the inclusion of SOC. Therefore, a DSM state can be realized if there is additional crystal symmetry, such as screw rotational symmetry, to protect the Dirac point. An example is the antiferromagnetic CuMnAs (Tang *et al.*, 2016), in which the Dirac points are protected by the twofold screw rotation ($S_{2z}$) symmetry.

(d) If the system has a reflection mirror symmetry, this protects the nodal line on the mirror-invariant plane in the absence of SOC. In the $\mathcal{PT}$-asymmetric case, the mirror-protected nodal line can split into two twofold-degenerate Weyl nodal lines within the mirror plane after the inclusion of SOC. For example, the $PbTaSe_2$ family of materials lacks inversion symmetry, and two spinful Weyl nodal rings appear within the mirror plane when SOC is included (Bian *et al.*, 2016).

(e) Recently researchers also predicted and experimentally confirmed the existence of another type of band crossings in a class of noncentrosymmetric (without $\mathcal{P}$ symmetry) and nonmagnetic (with $\mathcal{T}$ symmetry) materials, that is, the triply degenerate points (Weng *et al.*, 2016a, 2016b; Zhu *et al.*, 2016; B. Q. Lv *et al.*, 2017). These triply degenerate points are protected by the $C_3$ rotation symmetry and can be viewed as the "intermediate species" between the fourfold Dirac and twofold Weyl points. The low-energy excitations near the triply degenerate point, i.e., class-I three-component fermions, have no high-energy counterparts; thus, they are called unconventional fermions, or new fermions.

### *b. Essential band crossings*

(i) Kramers-Weyl fermions. As discussed, to realize accidental Weyl points in the BZ several conditions should be satisfied simultaneously, including band inversion, proper strength of SOC, breaking $\mathcal{T}$ or $\mathcal{P}$ symmetry, and irreducible representation of electronic states that protect the band crossings from hybridization. There is a relatively easy way to create Weyl points in crystals, i.e., Kramers-Weyl points. To be explicit, start from one band protected by the $\mathcal{P}$ and $\mathcal{T}$ symmetries and the combination of these two symmetries will always force the band to be doubly degenerate everywhere. If inversion symmetry is broken, this degeneracy can be lifted with the help of SOC. However, at some specific high-symmetry points in the BZ (only the ones where $k_x$, $k_y$, and $k_z$ are all either 0 or $\pi$), i.e., TRIM, $\mathcal{T}$ symmetry still enforces twofold degeneracy and the band splits everywhere else, giving rise to Weyl points at all TRIMs, as illustrated in Fig. 6. Unlike the usual Weyl points, these Weyl points are protected by SOC and the Kramers theorem, and thus are also attributed to Kramers-Weyl points (Chang *et al.*, 2018). To realize Kramers-Weyl points, two criteria should be met: one breaks $\mathcal{P}$ but respects $\mathcal{T}$ symmetry, whereas the other is the removal of double degeneracy at non-TRIMs. In particular, the second criterion forbids symmetries that can cause additional band degeneration, such as mirror or glide-mirror symmetry. Therefore, a chiral lattice, which contains only $\mathcal{T}$, rotation, and screw symmetries and has a well-defined handedness due to the lack of inversion, mirror, or other rotoinversion symmetries, is essential for realizing Kramers-Weyl fermions.

(ii) Nonsymmorphic symmetry-enforced band degeneracy

The Kramers theorem enforces the lowest band degeneracy, i.e., twofold degeneracy. At the same time, if additional

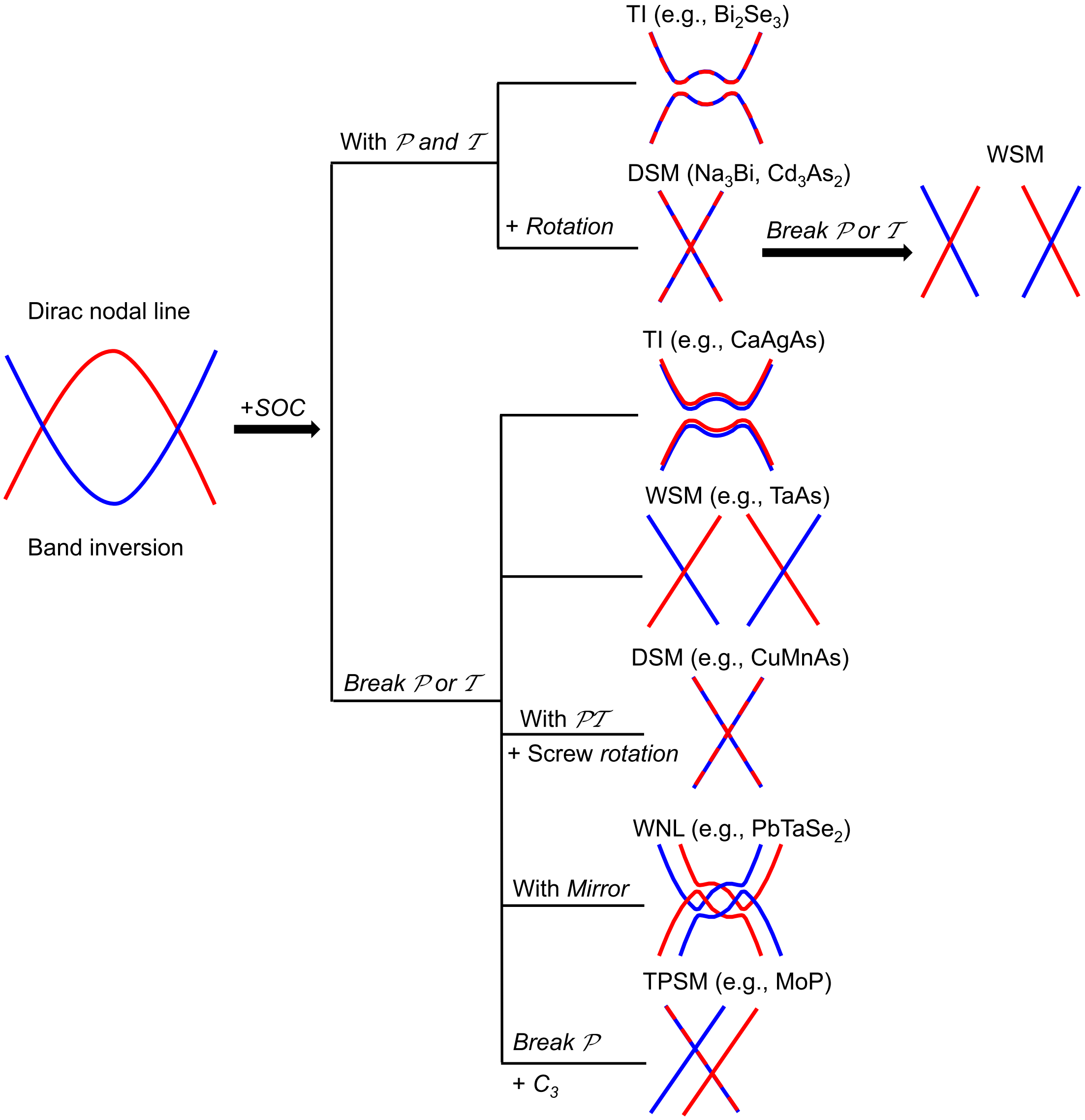

FIG. 5. Schematic illustration of possible band-inversion-induced topological states. The curves with mixed and uniform colors represent doubly degenerate bands and nondegenerate bands, respectively. WNL, Weyl nodal line; TPSM, triple point semimetal.

nonsymmorphic symmetries are introduced, the following higher-order band degeneracies can be imposed at the BZ boundary, depending on the nonsymmorphic space group of the crystal.

*Fourfold band degeneracy.*—Young *et al.* (2012) proposed the first class of nonsymmorphic symmetry-enforced TSMs, i.e., the Dirac semimetal with fourfold band degeneracy. They systematically examined the conditions under which the

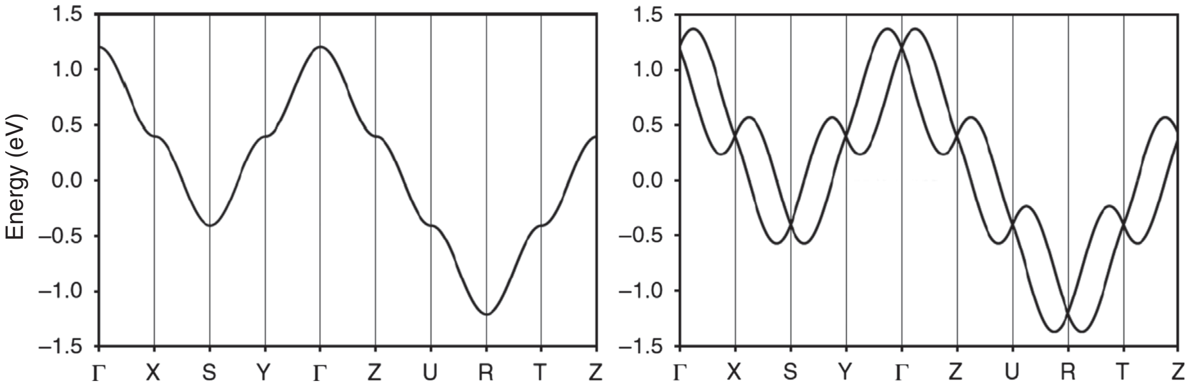

FIG. 6. Schematic plot of the band structure for space group 16 with and without SOC. From Chang *et al.*, 2018.

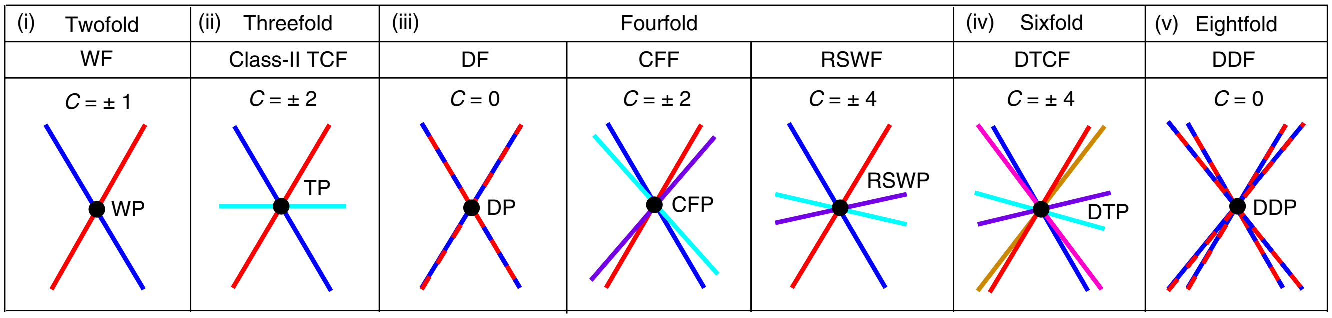

FIG. 7. Schematic plot of the band structure of various symmetry-enforced band degeneracies in condensed-matter systems. WF, Weyl fermion; WP, Weyl point; TCF, three-component fermion; TP, triple point; DF, Dirac fermion; DP, Dirac point; CFF, charge-2 fourfold fermion; CFP, charge-2 fourfold point; RSWF, Rarita-Schwinger-Weyl fermion; RSWP, Rarita-Schwinger-Weyl point; DTCF, double class-II three-component fermion; DTP, double triple point; DDF, double Dirac fermion; DDP, double Dirac point. Adapted from Lv *et al.*, 2019.

symmetries of the crystal allow fourfold degeneracy with linear dispersion and revealed that such an essential Dirac point could occur only in the case of nonsymmorphic space groups. Concretely, when the double point group of a crystal, i.e., the group that represents the symmetries of the lattice doubled by the spin degree of freedom, possesses a four-dimensional irreducible representation, a Dirac point can appear at high-symmetry momenta on the BZ boundary. The main challenge of this proposal is the requirement of a near-$E_F$ degeneracy point, as well as linearly dispersed and spin-degenerate bands around the degeneracy point. Recently it was pointed out that in addition to the conventional Dirac point with zero topological charges, such fourfold irreducible representations can give rise to the other two types of symmetry-enforced fourfold band degeneracies with nonzero monopole charge (as shown in Fig. 7), and the corresponding low-energy excitations near these points are termed double Weyl or charge-2 fourfold fermions ($C = \pm 2$) and spin-$3/2$ Weyl fermions ($C = \pm 4$), respectively (Tang, Zhou, and Zhang, 2017), which violate the Poincaré symmetry of high-energy physics and can exist only in condensed-matter physics.

*Threefold, sixfold, and eightfold band degeneracy.*—Besides the four-dimensional irreducible representation, nonsymmorphic space groups may also host other-dimensional irreducible representations, and the dimension determines the number of bands that meet at the high-symmetric point in the BZ. Wieder *et al.* (2016) predicted the existence of eight-dimensional irreducible representations, or eightfold band degeneracy, at the BZ corner and showed that 7 of the 157 nonsymmorphic space groups could exhibit such a nodal point, called the double Dirac point, as illustrated in Fig. 7. Soon thereafter, Bradlyn *et al.* (2016) systematically examined all possible irreducible representations in nonsymmorphic space groups and revealed two other types of symmetry-enforced band degeneracy: threefold- and sixfold-degenerate points. They provided a full list of nonsymmorphic space groups that admit the previously mentioned threefold, sixfold, and eightfold band degeneracies. The corresponding low-energy excitations around these band degeneracies, i.e., class-II three-component, six-component, and eight-component or double Dirac fermions, are also termed unconventional fermions, in the sense that they are beyond the conventional Dirac-Weyl-Majorana classification.

*Nodal lines and others.*—Nonsymmorphic space groups can not only enforce the previously mentioned zero-dimensional threefold,fourfold, sixfold, and eightfold nodal points at high-symmetric points but also protect 1D nodal lines or 2D nodal surfaces at the BZ boundaries. The combination of $\mathcal{PT}$ and nonsymmorphic symmetries retains the fourfold-degenerate Dirac nodal lines in the ZrSiS (Chen *et al.*, 2017) and AIrO$_3$ (Chen, Lu, and Kee, 2015; Kim, Chen, and Kee, 2015) families of materials. On the other hand, in $\mathcal{PT}$-asymmetric systems, such as $\mathrm{Ta_3TeI_7}$ (Wu, Liu *et al.*, 2018), the nonsymmorphic symmetry can guarantee the Weyl nodal surfaces at the BZ boundaries. What is interesting about these nodal lines or nodal surfaces is that they are guaranteed to appear at a specific 2D surface of the BZ boundary, and they cannot be gapped by SOC. Recently it was also demonstrated that nonsymmorphic symmetries might give rise to other unidentified types of band crossings, such as hourglass band dispersions along high-symmetry lines of the BZ (Wang, Jian, and Yao, 2017), and nodal chains that are formed by two or more nodal lines (Bzdušek *et al.*, 2016).

### 2. Cataloging the key attributes of the band crossings

#### *a. Dimensionality, degeneracy, and monopole charges*

TSMs come in different varieties, which can be distinguished based on the origin of the band crossings, that is, whether they are symmetry enforced or they arise as a result of a band inversion. A more intuitive distinction can be made according to the key attributes of the band crossings, and the band degeneracy can be characterized in at least the following four aspects. The first is the dimensionality of the band crossings, based on which types of band crossings may be broadly classified into three categories: 0D nodal points, 1D nodal lines, and 2D nodal surfaces.

The second is the degeneracy of the band crossings. Explicitly speaking, 0D band crossings can be further classified into twofold, threefold, fourfold, sixfold, and eightfold-degenerate nodal points. One-dimensional nodal lines, on the other hand, can be divided into two subsets, Dirac nodal lines with fourfold degeneracy and Weyl nodal lines with twofold degeneracy, respectively.

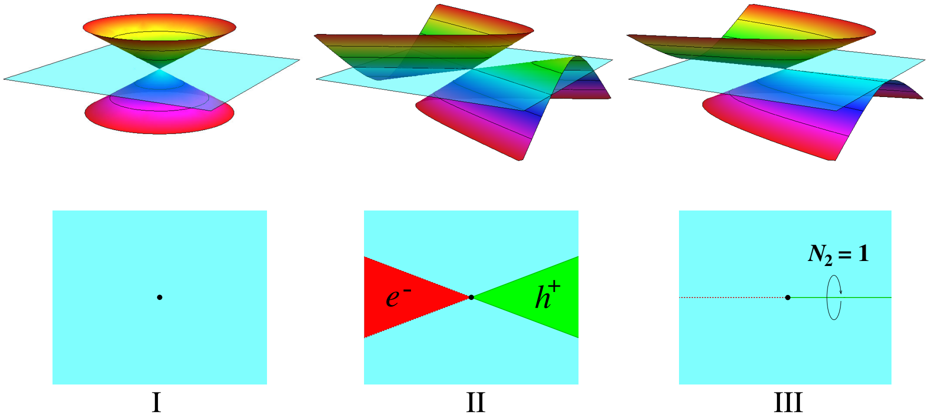

FIG. 8. Schematic plot of the band dispersion and Fermi surfaces of type-I, type-II, and type-III Dirac and Weyl points. From Huang, Jin, and Liu, 2018.

The third aspect is regarding the topological property of the band crossings. Nodal points can be characterized by the monopole charge that they host. In particular, a twofold Weyl point can exhibit three different monopole charges, i.e., $C = \pm 1, \pm 2, \pm 3$ (Liu and Zunger, 2017) (a derivation can be found in Appendix B.1), depending on the order of band dispersion, which we discuss later. Whereas a threefold nodal point can have no monopole charge (Weng *et al.*, 2016b) or a monopole charge of $\pm 2$ (Bradlyn *et al.*, 2016) (a derivation can be found in Appendix B.2), depending on the crystal symmetry that protects it. Moving on to fourfold band degeneracy, we note two types of band crossings differentiated by the topological charges and band dispersions besides the well-known Dirac points with zero charge: charge-2 fourfold points with $C = \pm 2$ and Rarita-Schwinger-Weyl points with $C = \pm 4$ (Tang, Zhou, and Zhang, 2017) (a derivation can be found in Appendix B.3). For even higher band degeneracies, shown in Figs. 7(iv) and 7(v), theory predicted a sixfold-degenerate point with $C = \pm 4$ and an eightfold-degenerate point with $C = 0$ (Bradlyn *et al.*, 2016), which can be viewed as a nontrivial doubling of threefold points with $C = \pm 2$ and Dirac points with $C = 0$, respectively.

The fourth aspect, which usually couples with the monopole charge, is the band dispersion around the degeneracy point. Next we discuss two classes of band crossings with distinct band dispersions.

#### *b. Type-I, type-II, and type-III band crossings*

Strictly speaking, in condensed-matter systems the high-energy counterparts of realistic Dirac fermions and Weyl fermions should respect Lorentz invariance and obey the Dirac and Weyl equations [Eqs. (2) and (3)], which give rise to an isotropic Dirac or Weyl cone with linear band dispersion in all momentum directions. However, band crossings in crystals are constrained by the symmetries of the 230 space groups rather than by Lorentz invariance, giving rise to the possibility of finding other types of band crossings. Soluyanov *et al.* (2015) predicted a distinct type of twofold band crossing with a highly tilted Weyl cone along a certain $k$ direction, as shown in Fig. 8. The quasiparticle excitations near the tilted Weyl cone violate Lorentz invariance and are thus called type-II Weyl fermions.

The essential physics of type-II Weyl points can be captured by adding a tilting term to the simplest $2 \times 2$ Weyl Hamiltonian

$$H = \pm \nu_0 \boldsymbol{\sigma} \cdot \boldsymbol{k} + \boldsymbol{t} \cdot \boldsymbol{k} I_2, \tag{11}$$

where $\nu_0$ is the Fermi velocity, $\boldsymbol{k} = (k_x, k_y, k_z)$ is the momentum vector, $\boldsymbol{\sigma} = (\sigma_x, \sigma_y, \sigma_z)$ is the vector of $2 \times 2$ Pauli matrices, $I_2$ is the $2 \times 2$ identity matrix, and $\boldsymbol{t}$ is the tilt vector. To be explicit, consider the right-handed fermion and assume that the vector $\boldsymbol{t}$ is along the $k_z$ direction. The Hamiltonian can then be further written as

$$H = \nu_0 \begin{pmatrix} k_z(1 + t/\nu_0) & k_x - ik_y \\ k_x + ik_y & -k_z(1 - t/\nu_0) \end{pmatrix}. \tag{12}$$

Equation (12) leads to the following two branches of the energy spectrum:

$$\varepsilon_{\pm}(k) = \pm \nu_0 (k_x + k_y) \pm \nu_0 \left(1 \pm \frac{t}{\nu_0}\right) k_z. \tag{13}$$

Here $\nu_0 k$ and $t k_z$ can be viewed as the kinetic and potential parts of the energy spectrum. These two energy branches cross each other and form a Weyl node at $k = 0$, and the potential energy $t k_z$ introduces an overall tilt of the Weyl cone, which consequently breaks the Lorentz invariance of Weyl fermions in quantum field theory. Depending on the ratio between $\nu_0 k_z$ and $t k_z$, the Weyl points can be divided into one of two types. In a type-I Weyl point, $t k_z$ always less than $\nu_0 k_z$ $(t/\nu_0 < 1)$, it is implied that the two linearly dispersed Weyl bands always have opposite velocities along any $k$ direction, and $\varepsilon(k) = 0$ occurs only at the $k = 0$ point. All these physical properties are similar to the standard Weyl cones that obey Eq. (3); hence they are classified as type-I Weyl points. However, if the potential energy exceeds the kinetic energy, i.e., $t/\nu_0 > 1$, the two energy branches have the same sign of Fermi velocity along the $k_z$ direction; in other words, the Weyl cone is tipped over along the $k_z$ direction. At a particular region in BZ, the equation of $\varepsilon(k) = 0$ has solutions not only at $k = 0$ but also at certain other nonzero $k_z$ points. Therefore, instead of a closed and pointlike Fermi surface for a type-I Weyl cone, this leads to a qualitatively different Fermi surface structure, i.e., the Fermi surface becomes open electron and hole pockets, which touch at the Weyl point as shown in Fig. 8. This kind of Weyl point is the so-called type-II Weyl point.

At the boundary or interface, i.e., $t/v_0 = 1$, instead of a nonzero Fermi velocity one of the Weyl bands would have a zero velocity along the $k_z$ direction. Consequently, this gives rise to another distinct type of Fermi surface, i.e., the Weyl-line Fermi surface, and this kind of transition state is thus called the type-III Weyl fermion state (Volovik, 2016, 2018; Volovik and Zhang, 2017; Huang, Jin, and Liu, 2018).

We previously discussed the characteristic electronic structures of type-I, type-II, and type-III Weyl points from a simple Weyl equation. Such distinctive type-II and type-III Weyl states can give rise to peculiar transport and optical features. To name a few, the magnetic-field-induced tunneling between the electron and hole pockets of a type-II WSM can lead to a magnetic breakdown when the Fermi energy approaches the Weyl point (O'Brien, Diez, and Beenakker, 2016). This magnetic breakdown, a momentum space counterpart of Klein tunneling, can be characterized by an additional quantum oscillation frequency in the de Haas–van Alphen effect measurements. In addition to the magnetic breakdown, the dumbbell-like Fermi pockets of a type-II WSM can also manifest as a strong anisotropy in the cyclotron resonance (Koshino, 2016), which can be detected by polarization-dependent optical conductivity measurements. Other important transport and optical signatures of type-II Weyl points include the Landau-level collapse effect (regardless of the magnetic field strength) (Yu, Yao, and Yang, 2016), the anisotropic chiral anomaly depending on the current direction (Tchoumakov, Civelli, and Goerbig, 2016; Udagawa and Bergholtz, 2016), the intrinsic anomalous Hall effect (Zyuzin and Tiwari, 2016), the absence of optical absorption tails, and new types of optical transitions (Tchoumakov, Civelli, and Goerbig, 2016; Yu, Yao, and Yang, 2016). For the transitional type-III Weyl state, in which the Weyl point is composed of a flatband and a dispersive band, unique characteristics such as the solid-state analog of the black hole horizon (Volovik, 2016, 2018; Volovik and Zhang, 2017), the critical chiral anomaly effect, can be pursued (Huang, Jin, and Liu, 2018).

Recently the concept of type-II and type-III Weyl points was extended to the Dirac points and nodal lines, leading to the discovery of type-II and type-III Dirac points (Huang, Zhou, and Duan, 2016; T.-R. Chang *et al.*, 2017; Huang, Jin, and Liu, 2018) and nodal lines (Li, Yu *et al.*, 2017; Zhang, Jin *et al.*, 2017; Liu, Jin *et al.*, 2018) in condensed-matter systems. In fact, the Lorenz invariance breaking type-II topological phases are not rare. Many materials exhibit touching electron and hole pockets near $E_F$, forming type-II Weyl points such as $\mathrm{Mo(W)Te_2}$ (Soluyanov *et al.*, 2015; Sun *et al.*, 2015; T.-R. Chang *et al.*, 2016; Wang, Gresch *et al.*, 2016), type-II Dirac points such as $\mathrm{VAl_3}$ (T.-R. Chang *et al.*, 2017), and type-II nodal lines such as $\mathrm{Mg_3Bi_2}$ (Zhang, Jin *et al.*, 2017). For type-III band crossings, this review stays mostly at the theoretical model and concept stage. Regarding material candidates, to our best knowledge the type-III Weyl fermion state has not been found; the type-III Dirac point and nodal line have been proposed to exist only in $\mathrm{Zn_2In_2S_5}$ (Huang, Jin, and Liu, 2018) and CaPd (Liu, Jin *et al.*, 2018) compounds, respectively. Furthermore, it was shown that type-I and type-II Weyl points could even coexist in a single material such as NbP, giving rise to a hybrid Weyl semimetal state and unique topological responses (Li, Luo *et al.*, 2016; Wu, Sun *et al.*, 2017).

### c. Quadratic and cubic band crossings

Thus far we have focused on band crossings with linearly dispersed bands; actually, band crossings in crystals can be accompanied by different dispersion powers in different $k$ directions. Generally speaking, in SOC systems respecting $\mathcal{T}$ symmetry (230 nonmagnetic space group), since the allowed rotation symmetries are $C_2$, $C_3$, $C_4$, $C_6$, it was pointed out that the degeneracy of multiband crossings in $k$ space could be 2, 3, 4, 6, and 8; the dispersion power at the crossing point could be linear, quadratic ($k^2$), or cubic ($k^3$), respectively (Liu and Zunger, 2017). The twofold, threefold, fourfold, sixfold, and eightfold band degeneracies have been discussed previously; here we focus on quadratic and cubic band dispersions.

In contrast to massless Weyl points with a monopole charge of $\pm 1$, Weyl points with quadratic and cubic dispersions along certain momentum directions would have monopole charges of $\pm 2$ and $\pm 3$, respectively, as illustrated in Fig. 9. Accordingly, the low-energy excitations are called double (or quadratic) and triple (or cubic) Weyl fermions (Fang *et al.*, 2012). A direct consequence of Weyl points with higher monopole charge is the equivalent increase of the number of Fermi arcs, as the number of chiral edge states is identical to $C_{\mathrm{FS}}$. Besides, the increase of monopole charge will also enhance a series of effects predicted or observed in WSMs with a single monopole charge, including the anomalous Hall effect, and the ones related to the chiral anomaly: negative magnetic resistance and others. Beyond this, the intrinsically anisotropic Weyl cone with quadratic or cubic dispersion will induce novel physics absent in a single Weyl fermion, such as unconventional correlation effects (Jian and Yao, 2015; Lai, 2015; Ahn, Hwang, and Min, 2016; Roy, Goswami, and Juričić, 2017) and unique quantum transports (Chen and Fiete, 2016; Dai *et al.*, 2016; Li, Roy, and Das Sarma, 2016; Huang, Zhou, and Shen, 2017; Park *et al.*, 2017). The double Weyl nodes are predicted to exist in the ferromagnetic phase of $\mathrm{HgCr_2Se_4}$, with one pair of double Weyl nodes along the $k_z$ direction (G. Xu *et al.*, 2011), as well as in $\mathrm{SrSi_2}$ (S.-M. Huang *et al.*, 2016), whereas cubic-Weyl nodes have not yet been found. Liu and Zunger (2017) systematically searched for and summarized possible material candidates with quadratic and cubic band crossings using density functional theory, suggesting the existence of cubic Dirac points in $A\mathrm{Mo}X_3$ ($A =$ Na, K, Rb, In, Tl; $X =$ S, Se, Te) materials.

In condensed-matter systems, the richness of space-group symmetries gives rise to a variety of TSMs. Here we catalog the known TSMs from two major aspects, i.e., the nature and the key attributes of band crossings. However, we point out that the full classification of TSMs has not yet been obtained since many new types of band crossings continual to be predicted or realized in solids. A general classification of degeneracies in 1651 magnetic groups was recently performed (Cano, Bradlyn, and Vergniory, 2019); however, a full list of candidate materials is still lacking due to the complexity of magnetic order. Given the diversity of space-group symmetries, it is expected that more and more TSMs with new types of band crossings will be identified in the near future.

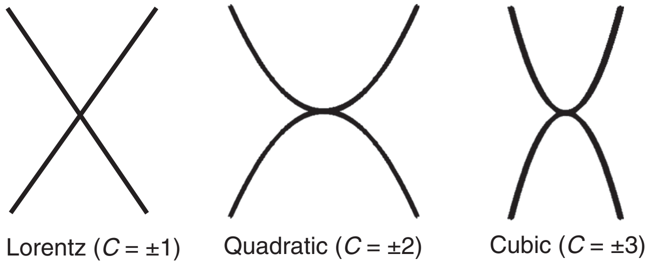

FIG. 9. Band crossings with linear, quadratic, and cubic dispersions.

## III. TOPOLOGICAL SEMIMETALS WITH 0D NODAL POINTS

### A. Dirac semimetals

DSMs are characterized by a fourfold Dirac point, which is usually formed by two spin-degenerated and linearly dispersed bands. In recent years, several DSMs have been identified, including the $Na_3Bi$, $Cd_3As_2$, and $PdTe_2$ families. We now highlight some DSMs and discuss their main features.

#### 1. Dirac semimetals $Na_3Bi$ and $Cd_3As_2$

*a. Theoretical prediction and ARPES*

As the first experimental confirmed 3D TSMs, $Na_3Bi$ and $Cd_3As_2$ have attracted extensive attention since their discovery. Wang *et al.* (2012, 2013) predicted that DSM might be realized in a hexagonal phase of alkali pnictides $A_3B$ ($A =$ alkali metal, $B =$ As, Sb, or Bi) represented by $Na_3Bi$ and a tetragonal structure of $Cd_3As_2$ material. Taking $Na_3Bi$ as a representative, we see that it crystallizes in the hexagonal space group $P6_3/mmc$ with $C_3$ rotation symmetry, which is crucial for the stabilization of Dirac points. The calculated electronic structure without SOC [Fig. 10(a)] shows a band inversion at the $\Gamma$ point. In the presence of SOC, most of the band crossings of the two inverted bands are gapped out, except for band crossings along the rotational axis, i.e., the $\Gamma$-$A$ axis because the two crossing bands belong to two

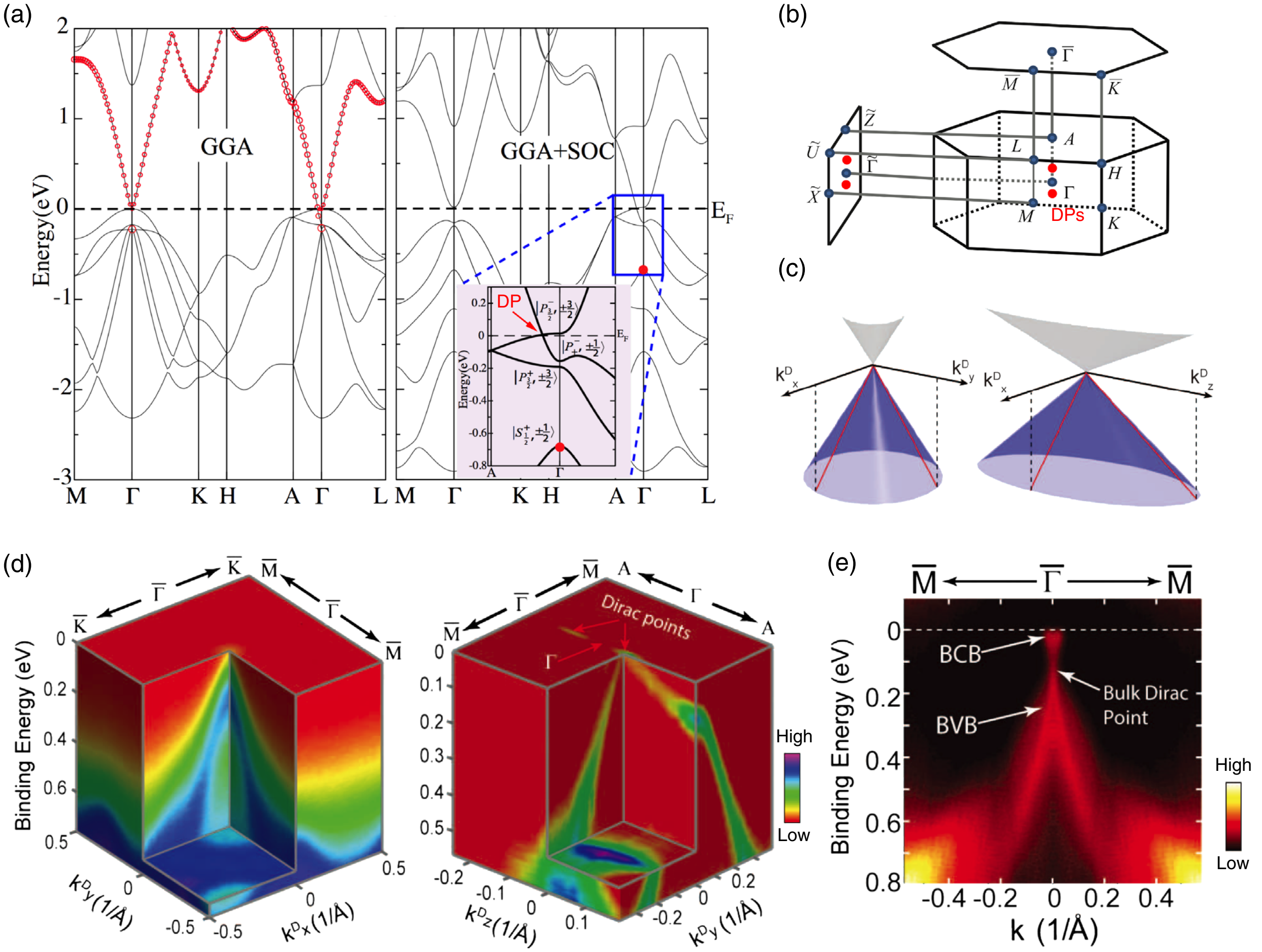

FIG. 10. (a) Calculated band structure of $Na_3Bi$ with and without including the SOC. (b) Bulk and projected (010) surface BZs of $Na_3Bi$.The red arrows indicate the momentum location of the Dirac points. (c) Schematic band dispersions near the Dirac points in the $k_x^D$-$k_y^D$ and $k_x^D$-$k_z^D$ planes, respectively. (d) 3D ARPES intensity plots, showing the band dispersion of the bulk Dirac cone along the in-plane ($k_x^D$-$k_y^D$-plane) and out-of-plane ($k_y^D$-$k_z^D$-plane) directions, respectively. (e) ARPES intensity plot shows the band dispersion of the upper Dirac cone along the $\bar{\Gamma}$-$\bar{M}$ direction after the *in situK* doping. Adapted from Wang *et al.*, 2012, and Liu *et al.*, 2014b.

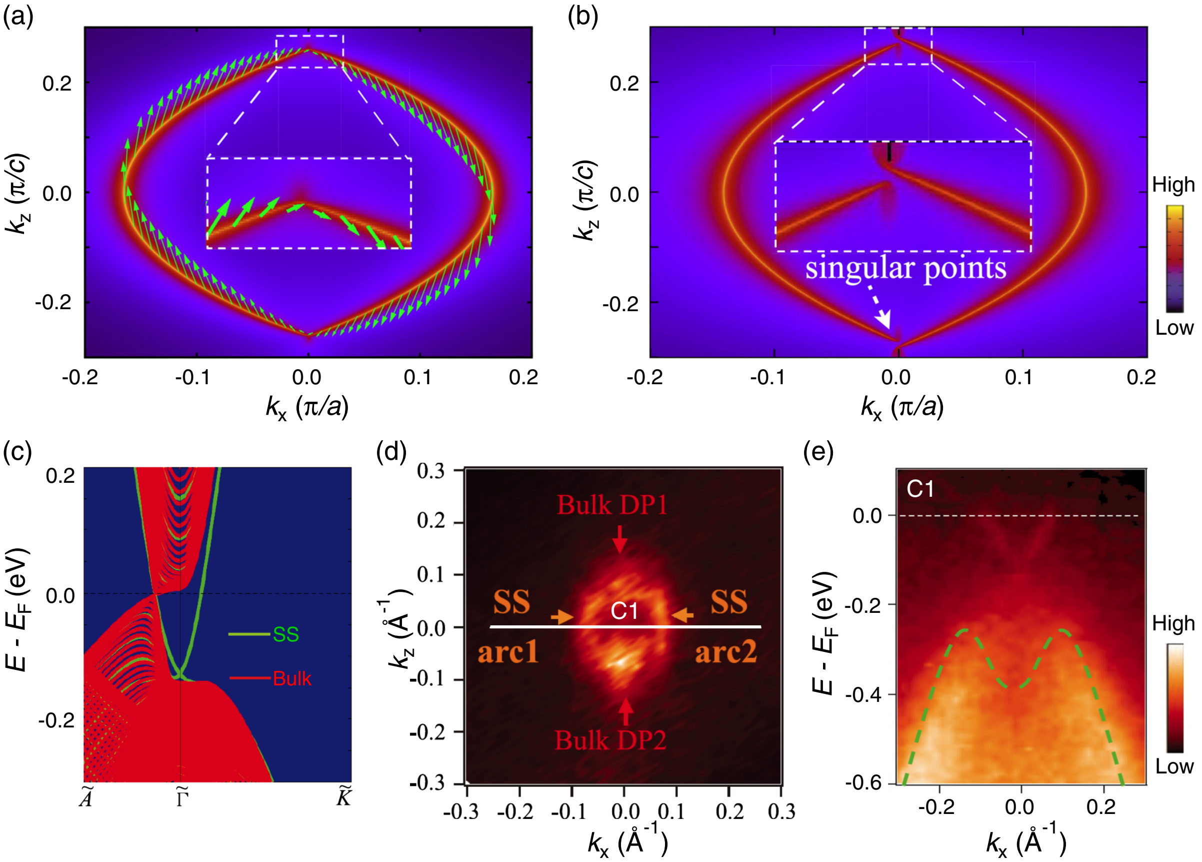

FIG. 11. (a) Calculated Fermi-arc surface states and their spin textures (in-plane components) for the (010) surface of $Na_3Bi$. (b) Similar to (a), but obtained from the fitted effective Hamiltonian with additional exchange field $h_1 = 6$ meV. (c) Calculated band structure of $Na_3Bi$ for the (100) surface. (d) ARPES intensity plot at $E_F$ in the (100) surface of $Na_3Bi$ recorded at $h\upsilon = 55$ eV. SS, surface states. (e) ARPES intensity plot for 2D $k$ slices shown in (d). Adapted from Wang *et al.*, 2012, and S.-Y. Xu *et al.*, 2015d.

different irreducible representations under $C_3$ rotational symmetry. Since both the $\mathcal{T}$ and $\mathcal{P}$ symmetries are present in this system, each band is spin degenerate; therefore, the band inversion results in two isolated Dirac points along the $\Gamma$-$A$ line, as illustrated in Fig. 10(b). In the vicinity of each Dirac point, the Dirac bands disperse linearly along all the $k_x$, $k_y$, and $k_z$ directions, but with different Fermi velocities. The energy-momentum relation near the Dirac point can thereby be written as $E_D = \nu_x k_x^D + \nu_y k_y^D + \nu_z k_z^D$, where $\nu_x$, $\nu_y$, and $\nu_z$ are the Fermi velocities along the $x$, $y$, and $z$ directions, respectively, and $k_x^D$, $k_x^D$, and $k_x^D$ represent the momentum measured from the Dirac point. Specifically, in $Na_3Bi$, $\nu_x \sim \nu_y$, and $\nu_x \sim 13\nu_z$ this gives rise to a nearly isotropic 2D Dirac cone on the $k_x$-$k_y$ plane, and a highly anisotropic 2D Dirac cone on the $k_x$-$k_z$ or $k_y$-$k_z$ plane, as shown in Fig. 10(c).

With the unique capability to directly visualize the electronic structure of a single crystal, ARPES has played an important role in the verification of TSMs. The first TSM to be experimentally verified by ARPES is the DSM $Na_3Bi$ (Liu *et al.*, 2014b). Figure 10(d) summarizes the ARPES measurements of two projections of 3D Dirac cones in the $k_x - k_y - E$ and $k_y - k_z - E$ subspaces, showing a nearly isotropic 2D Dirac cone and a highly anisotropic 2D Dirac cone, respectively. These results, which are consistent with the prediction made by Wang *et al.* (2012), directly demonstrate a pair of 3D anisotropic Dirac cones with linear dispersions in $Na_3Bi$. Furthermore, the upper branch of the Dirac cone was also accessed by *in situ* K-atom surface doping, as shown in Fig. 10(e), providing direct evidence for the existence of nongap bulk band crossings, i.e., the Dirac point, in $Na_3Bi$.

As discussed, each Dirac point can be regarded as two Weyl points of opposite monopole charge overlapping with each other as long as the crystalline symmetry protecting the band crossings stands. This fact leads to the coexistence of both bulk 3D Dirac cones and Fermi-arc surface states on certain surfaces. Like WSMs, the Fermi arcs in DSMs connect the projection of two Dirac points. Distinctively, there should be one pair of Fermi arcs that start or end at the projection of one Dirac point since each Dirac point consists of two Weyl points of opposite chirality. We now return to $Na_3Bi$, shown in Fig. 10(b). On the (001) surface, the two Dirac points project onto the same $\bar{\Gamma}$ point and the projection of the bulk 3D Dirac cone overlaps with the surface states, so the Fermi-arc surface states are invisible. In contrast, for the side (010) and (100) surfaces, on which two Dirac cones are projected at two different points, the two surface Fermi arcs that connect the projection of two Dirac points can be resolved, as shown in Figs. 11(a) and 11(b). The two surface bands cross each other at the TRIM $\bar{\Gamma}$ point and form a Dirac cone that is well separated from the bulk states and therefore ARPES detectable. Indeed, both the Fermi arcs and the accompanying surface Dirac cones have been confirmed by subsequent ARPES measurements on the (100) surface of $Na_3Bi$, as summarized in Figs. 11(d) and 11(e) (S.-Y. Xu *et al.*, 2015d).

These results demonstrate that $Na_3Bi$ is a topological DSM that features a pair of Fermi-arc surface states connecting the projection of two Dirac points on the side surface. It seems that the two Fermi arcs form a closed Fermi surface at $E_F$ that is similar to the Dirac cone surface states of topological insulators. Intrinsically, the Dirac cone surface states are different from those of TIs in the following two aspects. First, as shown in Figs. 11(a) the seemingly closed surface is formed by two Fermi arcs that eventually merge into the bulk states at the Dirac points; hence, the Fermi velocity of surface Dirac bands is ill defined at the two singular points corresponding to the projection of bulk Dirac points. The arc nature of the surface states is further illustrated in Fig. 11(b), where under an exchange field that breaks $\mathcal{T}$ symmetry each Dirac point splits into two separate Weyl points in momentum space. Consequently, the seemingly closed Fermi surface also splits into two open segments, which are precisely Fermi arcs that connecting the projection of two Weyl point of opposite chirality. Second, the spin texture of surface states has a helical structure, similar to that of TIs, while it does not always obey the "spin-momentum locking" feature. The magnitude of the spin vector vanishes at the singular points.

Theoretically, $Na_3Bi$ is an ideal DSM with a single pair of Dirac points located exactly at $E_F$. In practice, $Na_3Bi$ was found to be unstable in air, making it challenging for experimental verification and future applications. On the other hand, the low-temperature phase (space group $I4_1cd$) of $Cd_3As_2$ was also predicted to exhibit a single pair of Dirac points near $E_F$ along the $\Gamma$-$A$ axis resulting from the band inversion at the $\Gamma$ point, and the Dirac points are protected by the $C_4$ rotational symmetry instead of the $C_3$ rotational symmetry (Wang *et al.*, 2013). We point out that $Cd_3As_2$ has relatively complex crystal structures as a function of temperature (Steigmann and Goodyear, 1968; Pietraszko and Åukaszewicz, 1973; Ali, Gibson *et al.*, 2014). Nevertheless, the Dirac points in $Cd_3As_2$ have also been confirmed by ARPES (Borisenko *et al.*, 2014; Liu *et al.*, 2014a; Neupane *et al.*, 2014). Liu *et al.* (2014a) concluded the presence of a pair of 3D Dirac nodes along the [112] axis (or alternatively, along the [111] axis when an approximately cubic unit cell is considered), while Borisenko *et al.* (2014) and Neupane *et al.* (2014) reported the observation of a pair of 3D Dirac cones at the $C_4$ rotational axis, i.e., the [001] axis, which is consistent with the expectations based on symmetry arguments, as discussed. Moreover, a more recent vacuum ultraviolet (VUV) ARPES experiment (Roth *et al.*, 2018) performed on the (112) natural cleavage surface of $Cd_3As_2$ also revealed a sharp Dirac cone that closely resembles the one previously reported on by Liu *et al.* (2014a)-. However, they concluded that the observed Dirac cone does not come from the bulk but instead originates from the surface states based on systematic photon-energy-dependent ARPES measurements.

In addition to the disagreements in ARPES measurements, there are considerable discrepancies in $Cd_3As_2$ among ARPES, STM (Jeon *et al.*, 2014), magnetotransport (Zhao *et al.*, 2015b), and magneto-optical measurements (Akrap *et al.*, 2016; Hakl *et al.*, 2018). One primary difference is the energy scale of the Dirac cones $E_D$, i.e., the energy distance between the upper and lower saddle points of one pair of Dirac cones. Specifically, while ARPES measurements imply that $E_D$ extends over a few hundred meV, the magneto-optical and STM measurements demonstrate a much lower energy scale (several tens of meV), which we discuss later. Other discrepancies, such as the momentum location and the shape of the Dirac cone, were systematically summarized in a recent review on $Cd_3As_2$ (Crassee, Sankar *et al.*, 2018). Overall, there is still some controversy on the structure of the Dirac cones, and further bulk-sensitive soft x-ray ARPES measurements might be better able visualize the bulk Dirac cones in the low-temperature polymorph of $Cd_3As_2$.

#### *b. STM and STS*

Like ARPES, the real-space surface measurement techniques STM and STS played an important role in the studies of TSMs. As with ARPES, STM measurements have been performed on both $Cd_3As_2$ (Ali, Gibson *et al.*, 2014; Jeon *et al.*, 2014) and $Na_3Bi$ (Kushwaha *et al.*, 2015), showing the existence of Dirac points with linear band dispersions. Figure 12 summarizes the main STM results from the (112) natural cleaved surface of $Cd_3As_2$. The Fourier-transform scanning tunneling spectroscopy (FT-STS) measurements at different energies show an isotropic set of scattering wave vectors [Fig. 12(a)]. Specifically, Jeon *et al.* (2014) found that the outermost scattering vectors [the red dots in Fig. 12(a)] exhibit an approximately linear energy evolution, demonstrating the existence of Dirac bands, though the band dispersions close to the Dirac point were not resolved.

In addition to the FT-STS technique, scanning the energy structure of Landau levels formed in strong magnetic fields can provide another way to characterize the bulk electronic structure. As mentioned, in 3D materials applying a magnetic field leads to the formation of Landau levels dispersing along the momenta parallel to the field. The van Hove singularities of these Landau levels generate peaks in the density of states, which can be measured by STM. For 3D Dirac materials, the corresponding Landau-level energies for a linearly dispersing band are expected to scale as $E_N = E_{\mathrm{DP}} \pm \nu_F\sqrt{2\hbar eB|N|}$, where $E_{\mathrm{DP}}$ is the Dirac point energy, $e$ is the electron charge, $B$ is the magnetic field, $N$ is the orbital index ($N = 0, \pm1, \pm2, \pm3$), and $\nu_F$ is an effective Fermi velocity averaged over the directions perpendicular to the magnetic field. Hence, the van Hove singularities are expected to occur for all Landau levels with nonzero orbital index $N$, and the square-root dependence of these singularities in the energy spectrum indicates the linear dispersion of Dirac bands with the slope corresponding to the effective Fermi velocity. Indeed, Jeon *et al.* (2014) utilized this technique to quantify the bulk 3D dispersion of $Cd_3As_2$ by applying a magnetic field perpendicular to the cleaved (112) surface of the sample. Figures 12(b) and 12(c) summarize their main Landau-level STS measurements. The measured $dI/dV$ spectra exhibit intensity oscillations with pronounced peaks dispersing toward positive energies with increasing magnetic field, indicating the formation of electronlike Landau levels in $Cd_3As_2$. The energy position of

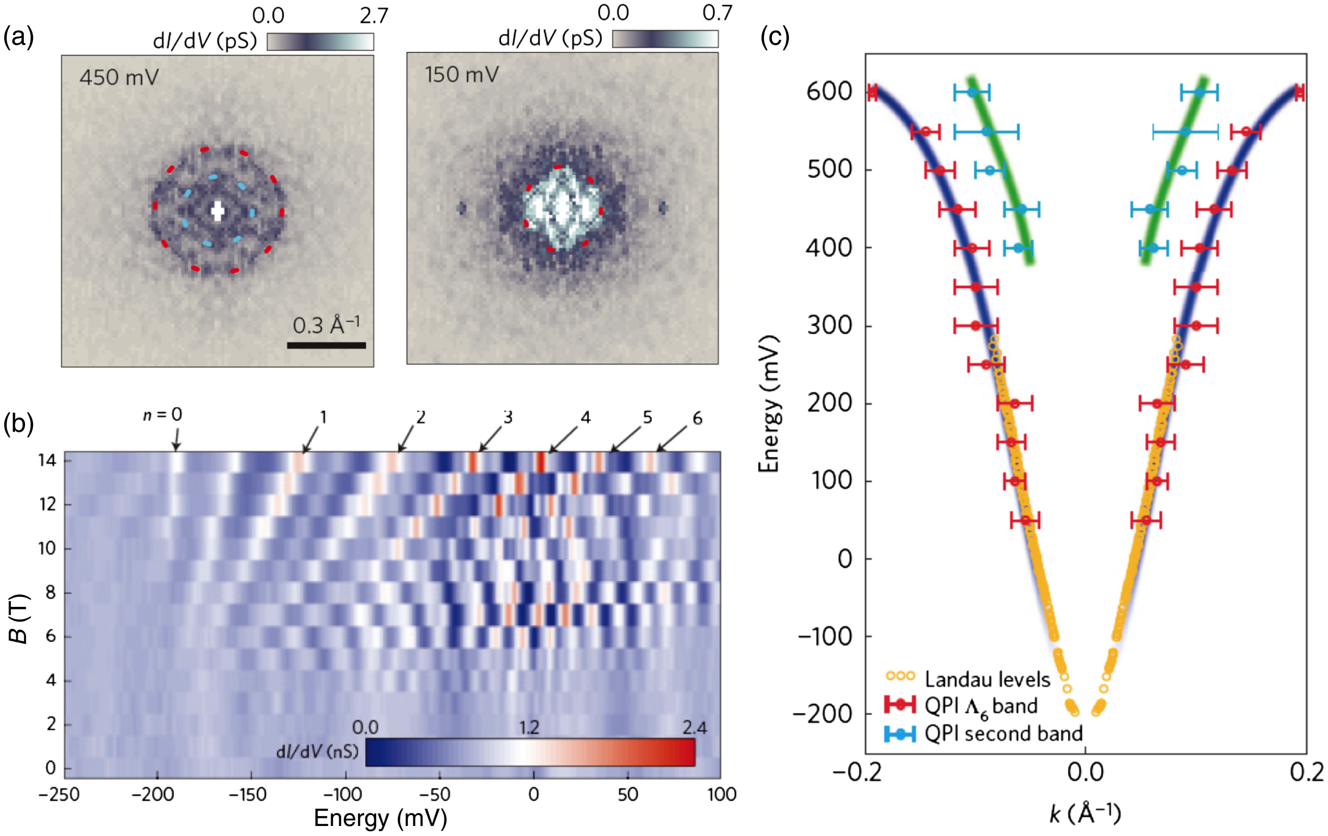

FIG. 12. STM measurements of $Cd_3As_2$. (a) Fourier transforms of $dI/dV$ conductance maps of $Cd_3As_2$ at different energies. The red and cyan dots show the scattering of the bulk conduction band and a second electronlike band, respectively. (b) Landau-level point spectra measured at 400 mK ($I = 400$ pA, $V = -250$ mV, $V_{\mathrm{osc}} = 0.8$ mV). Indices correspond to the Landau-level assignment. (c) Summary of the Dirac conduction band deduced from the quasiparticle interference pattern (indicated by red dots) and the Landau-level spectra (indicated by yellow circles). Blue and green curves are guides for the eye. Adapted from Jeon *et al.*, 2014.

these Landau-level peaks exhibits a scaling $E_N \propto \sqrt{NB}$, providing evidence of the linear dispersion of the bands. In addition, the measured slope or effective $v_F$ of the Dirac band, i.e., $9.4 \times 10^5$ m/s, is consistent with that of the quasiparticle interference (QPI) results [Fig. 12(c)], confirming the observation of Dirac bands with both techniques. Note that Jeon *et al.* (2014) performed Landau-level simulations and concluded that there is a much smaller energy scale (~20 meV) of massless Dirac fermions in $Cd_3As_2$, in contrast to the ARPES results.

### c. Quantum transport

Quantum transport measurement is another important tool for characterizing 3D topological materials. In recent years, DSMs, especially $Na_3Bi$ and $Cd_3As_2$, have been studied extensively using quantum transport measurements. Many transport phenomena have been revealed, including high carrier mobilities and large linear magnetoresistivity (Liang *et al.*, 2015), strong SdH oscillations and a nontrivial $\pi$ Berry phase (He *et al.*, 2014), chiral-anomaly-induced NLMR (Xiong *et al.*, 2015) and PHE effect (Guo *et al.*, 2016; Li, Wang *et al.*, 2018; Liang, Lin *et al.*, 2018; Wu *et al.*, 2018), thermal power suppression (Jia *et al.*, 2016), Fermi-arc-induced anomalous quantum oscillation, the Aharonov-Bohm effect (Moll, Nair *et al.*, 2016; Wang, Li *et al.*, 2016), and the 3D quantum Hall effect (QHE) (C. Zhang *et al.*, 2019b), and the anomalous Hall and Nernst effect (Liang *et al.*, 2017; Liang *et al.*, 2018), as well as point-contact-induced superconductivity (Wang, Wang *et al.*, 2016). In the following, we focus on three of these features: SdH oscillations, chiral-anomaly-induced NLMR and PHE, and Fermi-arc transport. For more information about the transport properties of DSMs, see He and Li (2016), Lu and Shen (2017), Song *et al.* (2017), Armitage, Mele, and Vishwanath (2018), Gooth *et al.* (2018), Schoop, Pielnhofer, and Lotsch (2018), and Wang and Wang (2018).

*SdH oscillations and nontrivial $\pi$ Berry phase.*—Quantum oscillations stem from the Landau quantization of electronic states under a high magnetic field. As the applied magnetic field is increased, $E_F$ crosses over the quantized Landau levels one after another, leading to an oscillation of the density of states as well as the associated physical parameters, such as magnetoresistance. The oscillation of the density of states can be detected by Landau-level STS, as shown in Fig. 12(b). On the other hand, the oscillation of magnetoresistance, better known as SdH oscillations, can be directly measured by transport measurements. Semiclassically, the SdH oscillation for a 3D Dirac system can be described by the Lifshitz-Kosevich (LK) theory (Lifshitz and Kosevich, 1956; Murakawa *et al.*, 2013; He *et al.*, 2014):

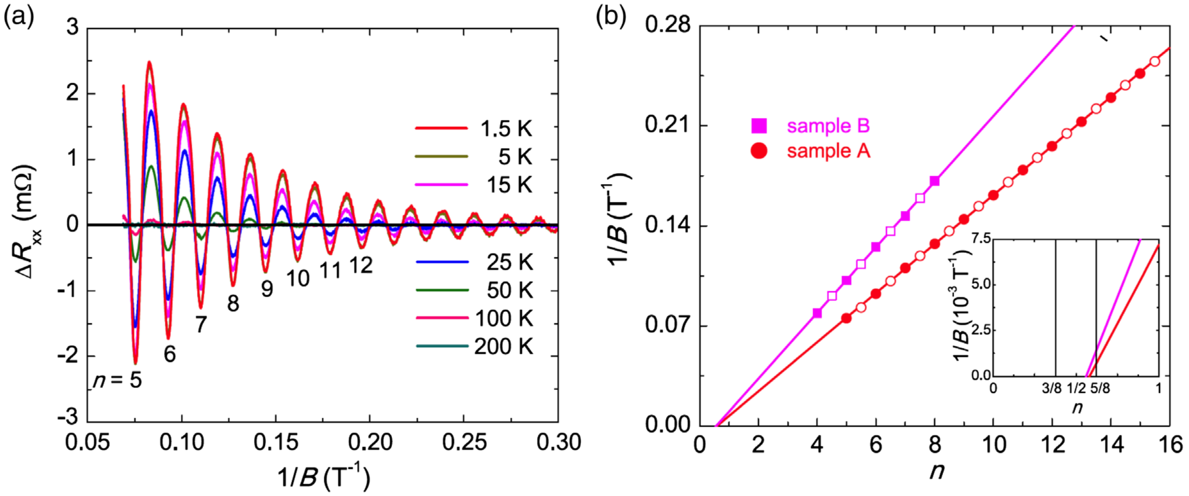

FIG. 13. SdH oscillations of $Cd_3As_2$. (a) SdH oscillatory component $\Delta R_{xx}$ as a function of $1/B$ at various temperatures. The current is in the (112) plane, and the magnetic field is perpendicular to the (112) plane. (b) Landau index plot $n$ vs $1/B$ for two $Cd_3As_2$ samples. The filled circles denote the integer index (valley), and the empty circles indicate the half-integer index (peak). From He *et al.*, 2014.

$$\Delta\sigma_{xx} \propto \cos\left[2\pi\left(\frac{F}{B}+\frac{1}{2}+\beta\right)\right], \tag{14}$$

where $\Delta\sigma_{xx}$ is the oscillatory amplitude of longitudinal conductivity $\sigma_{xx}$, $F$ is the SdH frequency of the oscillations, and $2\pi\beta$ is the Berry phase. For the parabolic band dispersion as in the case of conventional metals, $\beta$ should be zero; for Dirac systems with linear dispersion, there should be a nontrivial $\pi$ Berry phase as the electron orbits enclose a single Dirac point.

The SdH measurement is powerful: in principle, various physical parameters, such as carrier density and electron mobility, the geometry of the 3D Fermi surface, the cyclotron effective mass, and the scattering mechanism, can be extracted from the shape, period, and phase of the quantum oscillations. Therefore, this technique has been widely applied to investigate the electronic structure of DSMs, including $Na_3Bi$ (Xiong *et al.*, 2015) and $Cd_3As_2$ (He *et al.*, 2014; Cao *et al.*, 2015; Feng *et al.*, 2015; Liang *et al.*, 2015; Narayanan *et al.*, 2015; Pariari, Dutta, and Mandal, 2015; Zhang, Liu *et al.*, 2015; Pan *et al.*, 2016). Figure 13 shows an example of SdH oscillation measurements on the $Cd_3As_2$ single crystal. Oscillations of magnetoresistance as a function of $1/B$ can be resolved in Fig. 13(a). By employing the fast Fourier transform method, He *et al.* (2014) identified a single oscillation frequency of $F = 58.3$ T. Therefore, one can directly obtain the cross-sectional area of the Fermi surface normal to the applied field ($A_F$) via the Onsager relation $F = (\Phi_0/2\pi^2)A_F$, where $\Phi_0 = h/2e$ is the flux quantum. Then the corresponding Fermi momentum ($k_F$) can also be extracted by assuming a circular Fermi surface cross section, i.e., $A_F = \pi k_F^2$. $A_F^{(112)}$ and $k_F^{(112)}$ were determined as $\sim 5.6\times 10^{-3-2}$ and $\sim 0.042^{-1}$, respectively, which is in agreement with the ARPES measurements.

The nontrivial $\pi$ Berry phase, a distinct feature of Dirac fermions, can also be identified by SdH oscillations. Generally, any closed cyclotron orbit that is quantized under an external magnetic field can be described by the Lifshitz-Onsager quantization rule (Lifshitz and Kosevich, 1956)

$$A_F\frac{\hbar}{eB} = 2\pi\left(n+\frac{1}{2}+\beta+\delta\right), \tag{15}$$

where $n$ is the Landau-level index, $2\pi\beta$ is the Berry phase, and $2\pi\delta$ is the additional phase shift that results from the curvature of the Fermi surface in the $k_z$ direction, taking the value $\delta = 0$ for a quasi-two-dimensional cylindrical Fermi surface and $\delta = \pm 1/8$ (+ for holes and − for electrons) for a corrugated 3D Fermi surface. Therefore, the Berry phase can be experimentally accessed by plotting the Landau index ($n$) versus the inverse magnetic field ($1/B$) and tracking the intercept in the limit $B \to \infty$. Indeed, the nontrivial $\pi$ Berry phase has been detected in $Cd_3As_2$. As an example, Fig. 13(b) presents the Landau index plots of two $Cd_3As_2$ single crystals from He *et al.* (2014). As expected from the Lifshitz-Onsager quantization rule, the data points from the two samples fall into two straight lines, and the linear extrapolation gives the intercepts of $0.58 \pm 0.01$ and $0.56 \pm 0.03$, respectively. Before coming to a conclusion, we note that one should always keep in mind whether oscillation peaks or valleys are used to identify the Landau indices since the two different treatments can introduce an artificial phase difference of $\pi$. This difference might be confusing, as a trivial state with $n$ identified from oscillation peaks could have the same intercept value with a nontrivial Dirac state with $n$ identified from oscillation valleys. Returning to Fig. 13(b), He *et al.*, 2014 assigned integer Landau indices to the valley positions. Thus, according to the Lifshitz-Onsager quantization rule the obtained intercepts are identical to $\beta + \delta$, i.e., 0.58 and 0.56. This value was claimed as strong evidence for the existence of a nontrivial $\pi$ Berry phase ($\beta = -1/2$) in $Cd_3As_2$.

One should remember that the applied magnetic field in Fig. 13 is fixed along the (112) direction rather than the rotational axis, i.e., the (001) direction, and this breaks the $C_4$ rotational symmetry in $Cd_3As_2$, leading to a gap opening at the Dirac point. Consequently, the Berry phase is no longer $\pi$

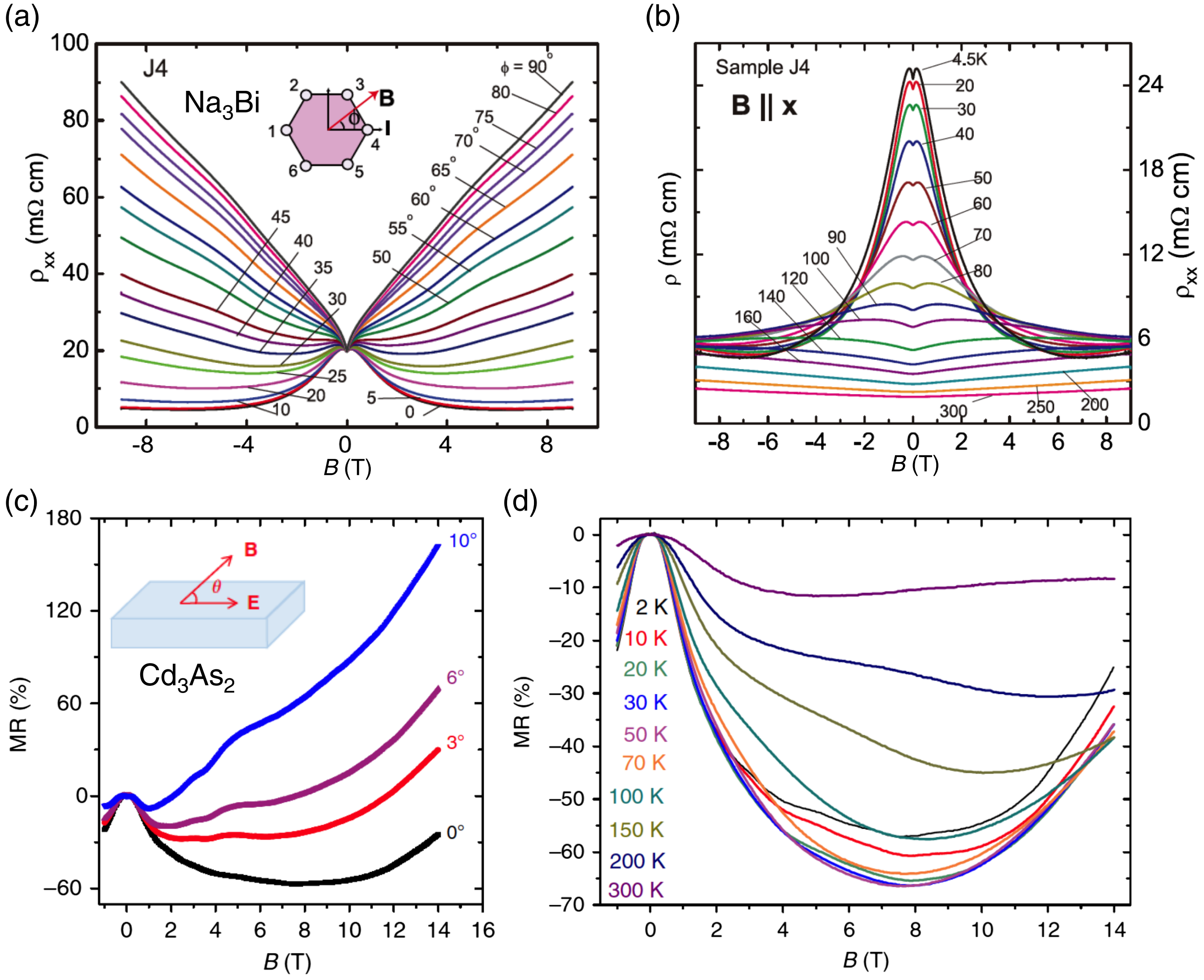

FIG. 14. (a) Resistance measured at 4.5 K with the applied magnetic field direction changing from perpendicular ($\phi = 90°$) to parallel ($\phi = 0°$) to the electric-field direction in the $x$-$y$ plane ([001] surface) of Na$_3$Bi (inset). (b) Longitudinal magnetoresistance of Na$_3$Bi measured at temperatures ranging from 4.5 to 300 K, with $B \| I \| x$. (c) Angle-dependent magnetoresistance of the Cd$_3$As$_2$ microribbon measured at 2 K. Here the applied constant current is along the [110] growth direction. (d) Corresponding temperature-dependent longitudinal magnetoresistance of the Cd$_3$As$_2$ microribbon. Adapted from Xiong *et al.*, 2015, and Li, He *et al.*, 2016.

and will change as a function of magnetic fields or the induced mass term. If the gap is large enough, the Berry phase will reduce to zero. In the case of Fig. 13, the field-induced Dirac gap is small (~8 meV at 14.5 T), which might explain the observation of the nontrivial Berry phase. Actually, several research groups (Cao *et al.*, 2015; Xiang *et al.*, 2015; Zhao *et al.*, 2015b) reported that the value of the Berry phase depends on the magnitude, orientation, and angle of the magnetic field by systematic SdH measurements, which might suggest possible topological phase transitions induced by the magnetic field.

*Negative longitudinal magnetoresistance and planar Hall effect*.—In a 3D DSM, the Dirac point described by a four-component massless Dirac equation is composed of two overlapped Weyl nodes with opposing monopole charges. Theoretically, applying a magnetic field breaks the $\mathcal{T}$ symmetry, and the two overlapping Weyl points in the DSMs would be split into two separate Weyl points along the direction of the external magnetic field, resulting in a transition from the DSM to the WSM phase (Gorbar, Miransky, and Shovkovy, 2013). Indeed, negative magnetoresistance, a simple signature of the Weyl fermion-induced chiral anomaly, has been observed in both Na$_3$Bi and Cd$_3$As$_2$ single crystals (Li *et al.*, 2015; Xiong *et al.*, 2015; Li, He *et al.*, 2016; C. Zhang *et al.*, 2017b), thus demonstrating the emergence of chiral Weyl fermions under the magnetic field.

Before showing the data, we note that many conditions need to be met to observe the chiral-anomaly-induced NLMR in DSMs or WSMs, including clean single crystals with negligible internode scattering and the quantum limit condition with only nontrivial Dirac or Weyl cones located at $E_F$. The quantum limit condition explains why the chiral-anomaly-induced NLMR is observed in Na$_3$Bi bulk materials and Cd$_3$As$_2$ nanostructures with near-$E_F$ Dirac points and low carrier density [Fig. 14(c)], while in $n$-type Cd$_3$As$_2$ bulk materials with ~200 meV below $E_F$ Dirac points and high

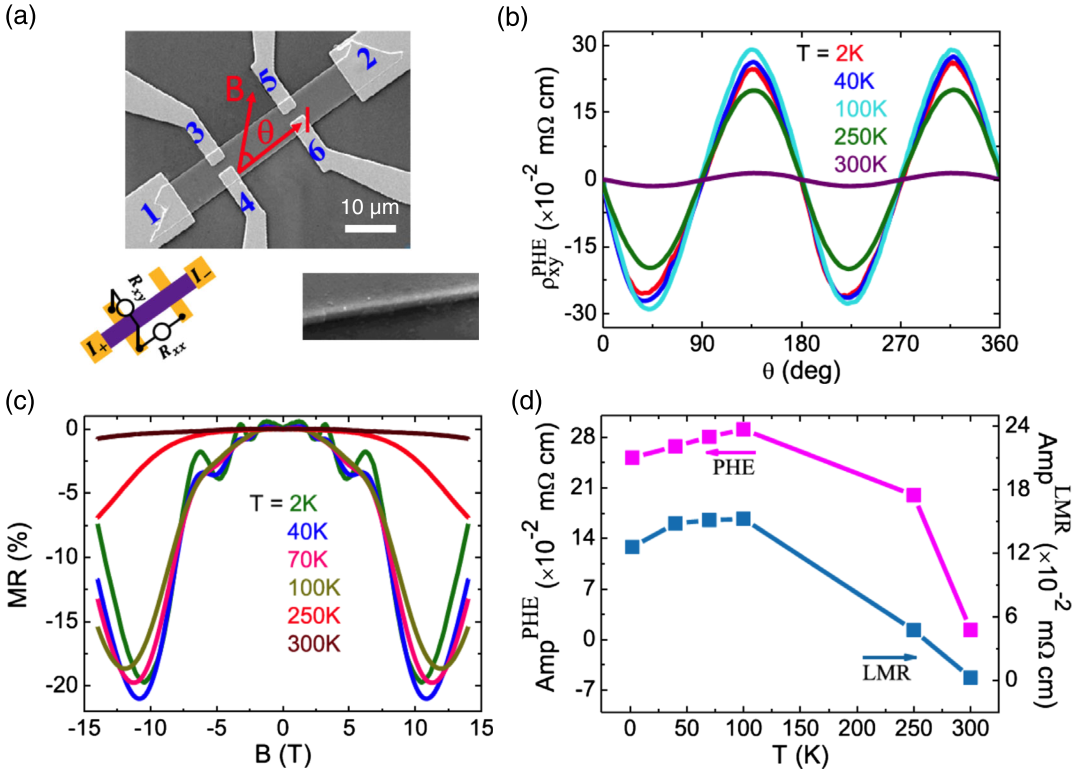

FIG. 15. PHE of $Cd_3As_2$ nanoplates. (a) Scanning electron microscope (SEM) image of a $Cd_3As_2$ nanoplate device. Lower left inset: schematic of the measurement configuration. Lower right inset: the thickness of the nanoplates determined by SEM is ∼90 nm. (b),(c) Measured planar Hall resistivity and negative longitudinal magnetoresistivity at different temperatures. (d) Corresponding temperature-dependent amplitudes of both the planar Hall resistivity and the negative longitudinal magnetoresistivity. Adapted from Wu *et al.*, 2018.

carrier density a large positive linear magnetoresistance was observed (Liang *et al.*, 2015). Figure 14 summarizes the measured NLMR from $Na_3Bi$ bulk materials and $Cd_3As_2$ nanostructures. In both materials, the observed negative magnetoresistance shows the following features: (i) sensitivity to the angle between magnetic and electrical fields, and (ii) robustness against temperature, with the observed negative magnetoresistance persisting up to 100 K in $Na_3Bi$ [Fig. 14(b)] and 300 K in $Cd_3As_2$ [Fig. 14(d)]. This sample and electric-field geometry-independent, carrier density, and angle-dependent NLMR was attributed to the chiral anomaly effect.

It is well known that the NLMR may have other physical origins, which requires consideration before ascribing the NLMR to the chiral anomaly. One origin is the quantum-interference-induced weak localization effect (Kim *et al.*, 2013; Lu and Shen, 2015), which usually appears at low temperatures since the phase coherence length decreases rapidly with increasing temperature. Because the observed NLMR is robust against temperature in both $Na_3Bi$ and $Cd_3As_2$, it cannot be fully attributed to the weak localization effect. In addition, the observed NLMR cannot be ascribed to the crystal anisotropy effect, as it is a sample and is electric field geometry independent. Last, the NLMR may arise from the inhomogeneous current distribution inside the sample, the so-called current jetting effect (Yoshida, 1976; Hu, Rosenbaum, and Betts, 2005). To study the influence of this effect, C. Zhang *et al.* (2017b) performed a nonlocal transport experiment in the $Cd_3As_2$ nanodevice and distinguished the chiral-anomaly-induced NLMR from the conventional magnetoresistance anisotropy through valley diffusion.

In addition to the NLMR, the PHE, a recently arising phenomenon closely related to the chiral anomaly and the nonzero Berry curvature, has also been observed in $Cd_3As_2$ microstructures or nanostructures (Guo *et al.*, 2016; Li, Wang *et al.*, 2018; Wu *et al.*, 2018). Figure 15 summarizes the main result from $Cd_3As_2$ nanoplates. Wu *et al.* (2018) concluded that the observed PHE originated from the chiral anomaly based on the following evidence: (1) The observed planar Hall resistivity shows a strict sin $2\theta$ angular dependence and can be well fitted by Eq. (9). (2) Accompanied by the large planar Hall resistivity, a negative longitudinal magnetoresistivity is observed, both of them can be suppressed synchronously by increasing the temperature, indicating that the two effects are engendered by the same origin. (3) In contrast to the conventional Hall effect, which originates from the Lorentz force, the observed planar Hall resistivity does not obey the antisymmetry principle, i.e., $\rho_{xy} \neq -\rho_{yx}$. This behavior further signifies that they are induced by the chiral anomaly. (4) The extrinsic current jetting effect is minimized by using nanoplates with a large aspect ratio and well-separated Hall-bar contacts.

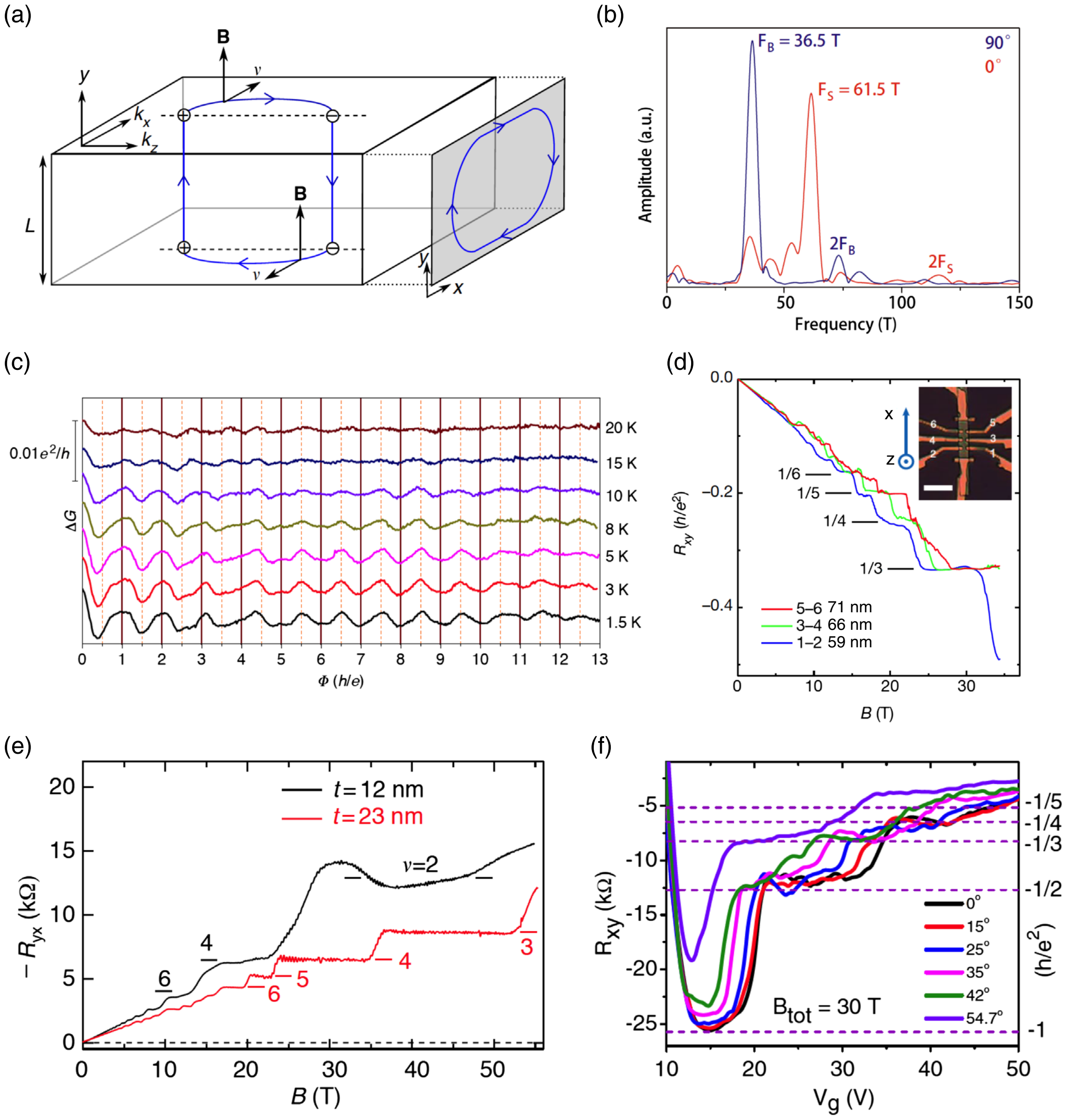

FIG. 16. (a) Weyl orbits in a slab of WSM of a finite thickness ($L$) in the presence of a perpendicular magnetic field. (b) Fourier transform of magnetoresistance measured on the $Cd_3As_2$ microplates (150 nm) at 2 K, with magnetic fields parallel (90°, blue curve) and perpendicular (0°, red curve) to the (010) surface, respectively. (c) Aharonov-Bohm oscillations in conductance as a function of magnetic flux, measured at variable temperatures in a $Cd_3As_2$ nanowire with a diameter of ~115 nm. (d) Magnetic field dependence of Hall resistance $R_{xy}$ measured at the three pairs of Hall electrodes, in a wedge-shaped $Cd_3As_2$ nanostructure, as illustrated in the inset. Scale bar, 15 $\mu$m. (e) Magnetic field dependence of $R_{yx}$ measured in (112)-oriented $Cd_3As_2$ thin films with thicknesses of 12 and 23 nm. The corresponding filling factors are labeled, with determined degeneracy factors of 2 and 1 for 12 and 23 nm thick films, respectively. (f) Gate voltage ($V_G$) dependence of $R_{xy}$ under a rotating magnetic field from 0° (along the [112] crystal direction) to 54.7° (along the [001] crystal direction). Adapted from Potter, Kimchi, and Vishwanath, 2014, Moll, Nair *et al.*, 2016, Wang, Li *et al.*, 2016, Uchida *et al.*, 2017, Lin *et al.*, 2019, and C. Zhang *et al.*, 2019b.

In addition to $Cd_3As_2$, the PHE has been observed in other TSMs, including $ZrTe_5$ (Li, Zhang *et al.*, 2018; Liang *et al.*, 2018), GdPtBi (Kumar *et al.*, 2018), W(Mo)$Te_2$ (Chen *et al.*, 2018; Wang, Gong *et al.*, 2018; Liang *et al.*, 2019), $VAl_3$ (Singha *et al.*, 2018), $Na_3Bi$ (Liang, Lin *et al.*, 2018), the TaAs family (J. Yang *et al.*, 2019; Q. R. Zhang *et al.*, 2019), the $PdTe_2$ family (Vashist *et al.*, 2018; Xu, Wang *et al.*, 2018; Li *et al.*, 2020; Meng *et al.*, 2020), $NiTe_2$ (Q. Liu *et al.*, 2019), ZrSiSe (Wei *et al.*, 2019), and $Co_3Sn_2S_2$ (Shama, Gopal, and Singh, 2020). We point out that the chiral anomaly is not the origin of the PHE in some of these materials. Actually, the PHE has a number of other origins in various systems, including the orbital magnetoresistance effect (Kumar *et al.*, 2018), interactions of magnetic order and spin-orbit coupling in ferromagnetic metals (Tang *et al.*, 2003; Nazmul *et al.*, 2008), and topological surface states in TIs (Taskin *et al.*, 2017). Beyond these, as with NLMR, the planar Hall resistivity measurements suffer from extrinsic effects such as the current jetting effect. In short, considering the various physical origins of NLMR and PHE and to provide reliable evidence for the chiral-anomaly-induced NLMR and PHE in DSMs and WSMs, it is important to obtain a comprehensive understanding of their band structures, such as the locations of Dirac and Weyl points, and to exclude other possible origins through systematic magnetotransport measurements.

*Fermi-arc transport*.—In contrast to the surface-sensitive ARPES and STM techniques, transport experiments are usually bulk sensitive. Indeed, the aforementioned transport phenomena in DSMs are all related to their bulk states, i.e., linearly dispersed Dirac cones. As we know, TSMs demonstrate their nontrivial topology not only from the bulk states but also from the topological surface states, such as the Fermi arcs of Dirac and Weyl fermions. Thus, one would ask whether it is possible to detect the Fermi arcs in topological Dirac or WSMs with transport measurements.

Potter, Kimchi, and Vishwanath (2014) gave a positive answer when considering a slab of WSM of finite thickness. As illustrated in Fig. 16(a), in the simplest case, assuming that the WSM has only one pair of Weyl points along the $k_z$ direction, the Fermi-arc surface states are thus expected on the top and bottom (010) surfaces, on which the projections of the two Weyl points are well separated in the $k$ space. In the presence of a static magnetic field perpendicular to the (010) surface, the surface electrons may propagate between the top and bottom surfaces via the bulk states without destroying the phase coherence if the propagation distance, i.e., the thickness of the slab, is smaller than the quantum mean free path of the electron. Under such conditions, the two Fermi arcs connecting the projection of Weyl nodes with opposite chirality from the top and bottom surfaces and the chiral bulk states couple and form a novel closed magnetic orbit, namely, the Weyl orbit. This Weyl orbit, which appears only in DSMs and WSMs with finite thickness under a perpendicular magnetic field, can be viewed as a sign of the Fermi arcs. Experimentally, such a Weyl orbit can be detected by transport measurements, as it will lead to additional quantum oscillation. Indeed, such Fermi-arc oscillation was observed in $Cd_3As_2$ microflakes and nanoflakes (Moll, Nair *et al.*, 2016; G. Zheng *et al.*, 2017). Figure 16(b) shows the main results from ~150 nm thickness $Cd_3As_2$ microflakes. While a single frequency ($F_B = 36.5$ T) arising from the bulk Fermi surface was observed when the magnetic field was applied parallel to the (010) surface (90°), an additional higher frequency ($F_S = 61.5$ T) appeared for the perpendicular magnetic field (0°). Systematic measurements and analysis found that the observed additional oscillation strongly depends on the sample thickness and the angle of the magnetic field, with the oscillating frequency close to the theoretical calculation of the Fermi-arc oscillation frequency. Therefore, the observation was ascribed to the manifestation of the Weyl orbits connecting the Fermi arcs from the opposing (010) surfaces of $Cd_3As_2$.

Along with the Fermi-arc oscillations, the Aharonov-Bohm (AB) effect (Bardarson, Brouwer, and Moore, 2010; Peng *et al.*, 2010; Zhang and Vishwanath, 2010) provides an effective method for proving the surface-state transport. Concretely, for a nanowire with perimeter comparable to the mean free path of carriers, due to the quantum confinement effect, the surface bands are enforced into discrete subbands. As it sweeps the magnetic field parallel to the nanowire direction, the Fermi energy crosses over the subbands one after another, leading to an oscillation of the carrier density of states, namely, AB oscillations. The corresponding oscillation period is described by $\Phi/\Phi_0$, where $\Phi$ is the total magnetic flux threading the nanowire cross section and $\Phi_0 = h/e$ is the flux quantum. Such AB oscillations have been observed in TIs (Peng *et al.*, 2010) and DSM nanowires (Wang, Li *et al.*, 2016). Figure 16(c) shows the main result from a $Cd_3As_2$ nanowire with a diameter ~115 nm that was reported by Wang, Li *et al.* (2016). Upon increasing the applied parallel magnetic field along the nanowire [112] direction, they observed periodic conductance oscillations, with the conductance oscillation peaks appearing at odd integers of $h/2e$ with a period of $h/e$, signifying that the Fermi-arc surface states were induced by the AB effect.

The third consequence of the Weyl orbits is the so-called 3D QHE predicted by Wang, Sun *et al.* (2017). Unlike the conventional QHE that originated from 2D electron gas, the 3D QHE in WSMs is supported by the bulk-state-connected top and bottom surface Fermi arcs. Therefore, it can be viewed as another transport signature of Fermi arcs. Experimentally, the QHE has been observed in both $Cd_3As_2$ thin films and $Cd_3As_2$ nanostructures (Uchida *et al.*, 2017; C. Zhang *et al.*, 2017a, 2019b; Nishihaya *et al.*, 2018; Schumann *et al.*, 2018; Lin *et al.*, 2019); however, the underlying mechanism has remained controversial. To be more specific, C. Zhang *et al.* (2019b) provided evidence of Weyl-orbit-based QHE in wedge-shaped $Cd_3As_2$ nanostructures by observing thickness-dependent (50–100 nm) and angle-dependent (direction of the magnetic field) quantum Hall resistance, as partly shown in Fig. 16(d). Uchida *et al.* (2017) also observed thickness-dependent quantum Hall resistance in (112)-oriented $Cd_3As_2$ thin films with thicknesses of up to 23 nm [Fig. 16(e)], and they attributed the observed QHE to the confined 2D bulk subbands. The third mechanism solely for DSMs consists of the surface states on a single surface. Concretely, the two surface Fermi arcs on a single surface of DSMs can form a closed Fermi loop, and thereby can support the conventional QHE without involving the Weyl orbits. Such a scenario was recently confirmed through observations of both the odd and even integer QHE in ~80 nm $Cd_3As_2$ nanoplates with a magnetic field along the [001] and [112] crystal directions, respectively, as shown in Fig. 16(f) (Lin *et al.*, 2019). In summary, the QHE in DSMs or WSMs can have different origins. Further investigations are required to distinguish the Weyl-orbit-induced QHE from other mechanisms. For example, high-quality WSM films can naturally exclude the surface-state scenario in DSMs. STM measurements should be able to probe the chiral edge states on one edge of the top and bottom surfaces.

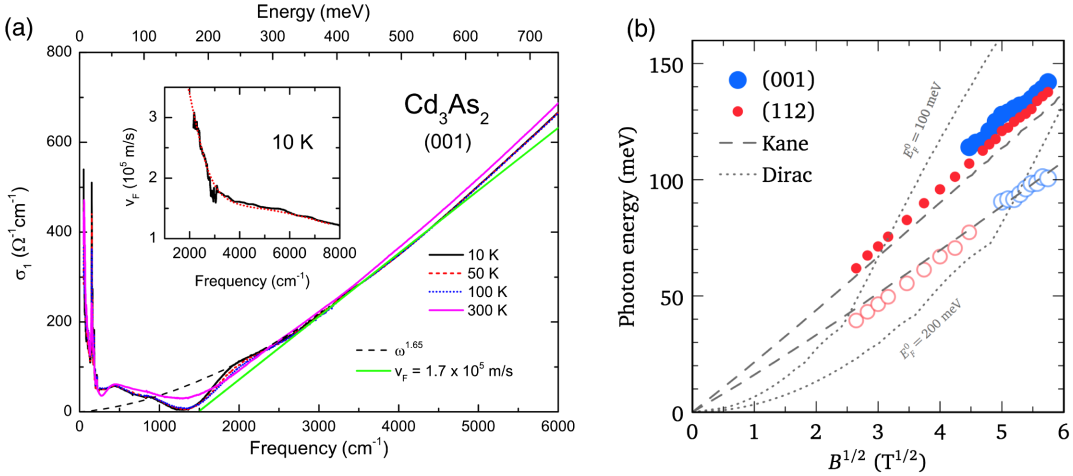

FIG. 17. (a) Real part of the optical conductivity of a [001]-oriented $Cd_3As_2$ sample measured at different temperatures. The black dashed line represents $\sigma_1(\omega) \propto \omega^{1.65}$, whereas the green line represents the linear fit. Inset: deduced Fermi velocity at 10 K. (b) $\sqrt{B}$ dependence of the Landau-level transition energy measured at 1.8 K, on (001)- and (112)-oriented $Cd_3As_2$ samples. The black dashed and dotted lines show the calculated curves based on the gapless Kane and Dirac models, respectively. Adapted from Akrap *et al.*, 2016, and Neubauer *et al.*, 2016.

### *d. Optical spectroscopy*

Optical spectroscopy is another powerful tool to evidence the 3D massless Dirac fermions. Consider a noninteracting electron system consisting of 3D isotropic Dirac or Weyl cones with the $E_F$ located near the nodes. The real part of optical conductivity that arises from interband transitions across the linear Dirac or Weyl cone is given by (Hosur, Parameswaran, and Vishwanath, 2012; Ashby and Carbotte, 2013; Bácsi and Virosztek, 2013; Timusk *et al.*, 2013; Neubauer *et al.*, 2016)

$$\sigma_1(\omega) = \frac{e^2 N}{12h} \frac{\omega}{\nu_F} \Theta\{\hbar\omega - 2E_F\}, \qquad (16)$$

where $N$ is the number of nondegenerate cones, $\nu_F$ is the Fermi velocity, $\omega$ is the photon frequency, and $\Theta\{x\}$ is the Heaviside step function.

The linear frequency dependence of $\sigma_1(\omega)$ has been observed in several 3D Dirac systems, including quasicrystals (Timusk *et al.*, 2013), $ZrTe_5$ (Chen, Zhang *et al.*, 2015), $Cd_3As_2$, and $Na_3Bi$ (Jenkins *et al.*, 2016; Neubauer *et al.*, 2016), and has been considered strong evidence for 3D massless Dirac fermions. Figure 17(a) shows the measured $\sigma_1(\omega)$ of the [001]-oriented $Cd_3As_2$ (Neubauer *et al.*, 2016), from which three features can be deduced. First is the observation of superlinear behavior of $\sigma_1(\omega)$ with a broad frequency (2000–8000 $cm^{-1}$) and temperature (10–300 K) range, and such behavior was interpreted as the manifestation of interband transitions between Dirac bands of sublinear dispersion. Second, the $\sigma_1(\omega)$ at low temperature almost vanishes at around 1300 $cm^{-1}$, signifying the position of the $E_F$. Last, from Eq. (16), Neubauer *et al.* (2016) further estimated the value of $\nu_F$. As shown in the inset of Fig. 17(a), the $\nu_F$ obtained is energy dependent and ranges from $1.2 \times 10^5$ to $3 \times 10^5$ m/s. Here it is important to mention that the $\nu_F$ determined from optical conductivity contains contributions from all momentum directions; therefore, it is not as accurate for $Cd_3As_2$, which hosts quite anisotropic Dirac cones.

Along with temperature and photon energy, the optical properties of $Cd_3As_2$ have been explored in other parameter spaces, such as magnetic field, carrier concentration, pressure, and crystal orientations. Akrap *et al.* (2016) performed magneto-optical measurements on both the (112)- and (001)-oriented $Cd_3As_2$ samples and observed a $\sqrt{B}$ dependence of the cyclotron resonance energy in both orientations, as shown in Fig. 17(b). The $\sqrt{B}$ Landau-level resonance persists up to the quantum limits and therefore is inconsistent with the 3D massless Dirac fermions, in which the characteristic $B$-independent zeroth Landau level dominates the interband transitions in the quantum limits. Instead, the observation was found to be consistent with the Kane-Bodnar model (Kane, 1957; Bodnar, 1977), indicating that the observed cyclotron resonance results from the so-called massless Kane fermions. Based on the Landau-level spectroscopy, Kane and Bodnar further estimated that the response of Dirac fermions appears at an energy scale (below 40 meV) (Hakl *et al.*, 2018) that is much smaller than the early surface-sensitive VUV ARPES studies (Borisenko *et al.*, 2014; Liu *et al.*, 2014a; Neupane *et al.*, 2014), in which the observed conical bands extend over a few hundred meV. Bulk-sensitive soft x-ray ARPES should be a good choice to visualize the bulk Dirac cones in $Cd_3As_2$. In addition to the Landau-level resonance, other interesting properties, such as the mass generation and topological phase transition (Yuan *et al.*, 2017), the nonuniform carrier density (Crassee *et al.*, 2018), the pressure-induced phase transitions (Uykur *et al.*, 2018), the efficient terahertz harmonic generation (Cheng, Kanda *et al.*, 2020), the relaxation of the chiral anomaly (Cheng, Schumann *et al.*, 2019), and the large effective phonon magnetic moment (Cheng, Schumann *et al.*, 2020), were also revealed by optical experiments.

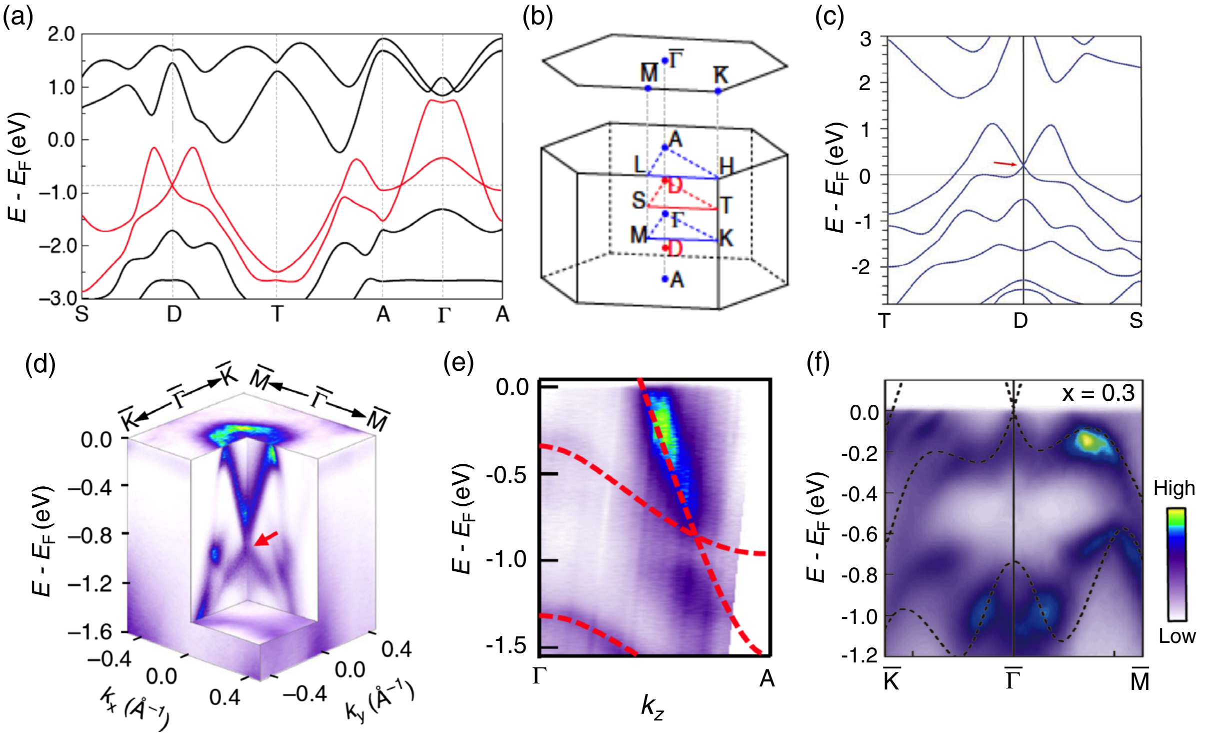

FIG. 18. Type-II Dirac semimetal in $PtTe_2$. (a) Calculated bulk band structures of $PtTe_2$ along the in-plane ($S$-$D$-$T$) and out-of-plane ($A$-$\Gamma$-$A$) directions through the Dirac point with SOC included. (b) Bulk BZ and the projected $(001)$ surface BZ, with high-symmetry points indicated. Red dots (labeled as $D$) mark the positions of type-II Dirac points. (c) Calculated bulk bands of $IrTe_2$ along the $S$-$D$-$T$ direction through the Dirac point with SOC included. (d),(e) ARPES intensity plots showing the band dispersion of the bulk Dirac cone along the (d) in-plane and (e) out-of-plane directions, respectively. (f) Second derivative intensity plot showing the Dirac point lying at $E_F$ for the $x = 0.1$ ($Ir_{1-x}Pt_xTe_2$) sample. Dashed lines are guides for the eye indicating the linear Dirac bands. Adapted from M. Yan *et al.*, 2017, and Fei *et al.*, 2018.

### 2. Type-II Dirac semimetals

#### *a. Theoretical prediction and ARPES*

$Na_3Bi$ and $Cd_3As_2$, which possess a pair of linearly dispersed Dirac cones along the $\Gamma$-$A$ direction, belong to type-I DSMs. In addition to the Lorentz-preserving type-I Dirac points, condensed-matter systems in 230 space groups are also allowed to host Lorentz-violating type-II Dirac points, which are manifested in highly tilted Dirac cones in the energy-momentum space. Evoked by the discovery of type-II Weyl points (Soluyanov *et al.*, 2015), researchers have predicted a variety of type-II DSMs, such as the $VAl_3$ family (T.-R. Chang *et al.*, 2017), transition-metal dichalcogenides ($PtSe_2$, $PtTe_2$, $PdTe_2$, and $PtBi_2$) (Huang, Zhou, and Duan, 2016), the KMgBi family (Le *et al.*, 2017), $C_4Li$ (Cuamba *et al.*, 2017), the $YPd_2Sn$ class (Guo *et al.*, 2017), $La_{1.77}Sr_{0.23}CuO_4$ (Horio *et al.*, 2018), Heusler compounds $XInPd_2$ ($X = \mathrm{Ti, Zr, Hf}$) (Mondal *et al.*, 2019), and $NiTe_2$ (Ghosh *et al.*, 2019). In the following, we discuss the type-II DSM phase in the transition-metal dichalcogenides, which have been experimentally verified by multiple research groups (Noh *et al.*, 2017; M. Yan *et al.*, 2017; Zhang, Yan *et al.*, 2017; Bahramy *et al.*, 2018; Clark *et al.*, 2018; Fei *et al.*, 2018; Fu *et al.*, 2019a).

Taking $PtTe_2$ as a representative, as with $Na_3Bi$, it has $\mathcal{T}$, $\mathcal{P}$, and $C_3$ rotation symmetries, which are required for the stabilization of type-II Dirac points. Figure 18(a) shows the calculated bulk band structure of $PtTe_2$ with the inclusion of SOC. There is a clear band crossing feature at ~0.9 eV below $E_F$ along the $\Gamma$-$A$ line. As the two crossing bands belong to different irreducible representations under the $C_3$ rotational symmetry, the band crossing is protected against hybridization. Owing to the coexistence of $\mathcal{PT}$ symmetry, the two crossing bands are always doubly degenerate; thus, the unavoidable band crossing forms a fourfold-degenerate Dirac point at $D = (0, 0, 0.346c^*)$, $c^* = 2\pi/c$, as illustrated in Fig. 18(b). The Dirac cone is strongly tilted along the out-of-plane ($\Gamma$-$A$) direction but not tilted along the in-plane ($S$-$D$-$T$) direction, which is the characteristic feature of type-II Dirac fermions. This 3D type-II Dirac cone has been directly observed by ARPES measurements, as shown in Figs. 18(d) and 18(e). However, the observed type-II Dirac points in $PtTe_2$ reside far below $E_F$, which hinders the investigation of unique transport or optical properties of type-II Dirac fermions, as they make little contribution to the low-energy quasiparticle excitations at $E_F$. Recently Fei *et al.* (2018) and Fu *et al.* (2019a) reported that the energy position of the type-II Dirac points in $PtTe_2$ could be easily tuned by element substitution, such as that with Ir. As shown in Fig. 18(c), $1T-IrTe_2$, which is isostructural to $PtTe_2$, has an electronic structure similar to $PtTe_2$ and hosts a pair of type-II Dirac points at ~0.2 eV above $E_F$. The energy position of the Dirac points can be further adjusted by Pt doping, and the Dirac point can be tuned to $E_F$ in $Ir_{1-x}Pt_xTe_2$, with $x = 0.1$, as

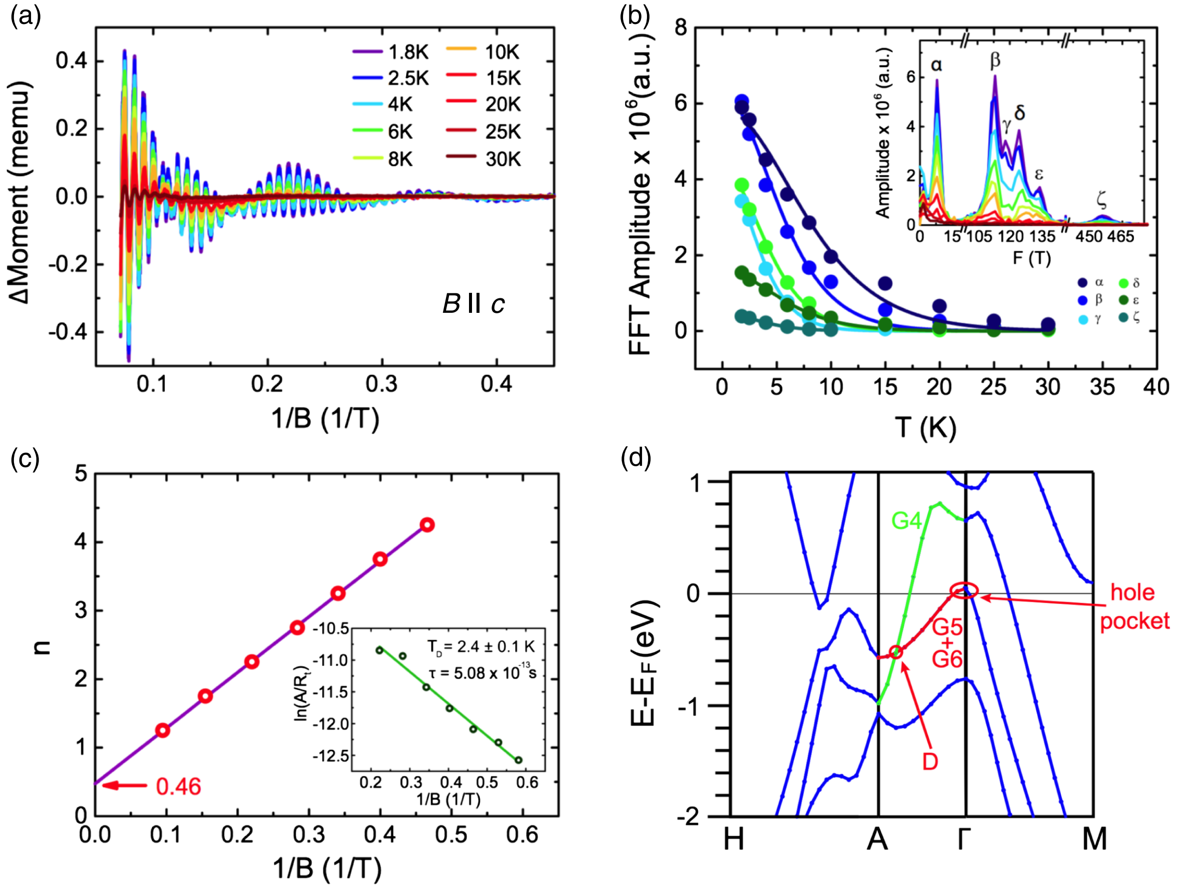

FIG. 19. dHvA oscillations for $PdTe_2$. (a) Oscillatory components of the out-of-plane magnetization vs $1/B$ at various temperatures. (b) Temperature dependence of the fast Fourier transformation (FFT) amplitude for six oscillation modes ($\alpha$ to $\zeta$). The solid lines represent the LK fits for the effective mass. Inset: FFT spectra of $\Delta M$ oscillations. (c) Landau-level fan diagram of the $\alpha$ mode. Inset: fit of the Dingle temperature. (d) The calculated electronic structures of $PdTe_2$ along high-symmetry lines. The Dirac point and the hole pocket with the $\alpha$ mode are indicated by red arrows. Adapted from Fei *et al.*, 2017.

demonstrated in Fig. 18(f). Thus, $Ir_{1-x}Pt_xTe_2$ offers a practical platform for further study of the transport properties of type-II Dirac fermions. The substitution of Pt in $IrTe_2$ not only raises the chemical potential, making the type-II Dirac points approach $E_F$, but also introduces bulk superconductivity into the system, making $Ir_{1-x}Pt_xTe_2$ a promising material for studying the TSC of both bulk and surface states in DSMs.

### *b. Quantum transport*

In addition to ARPES, the geometry of 3D Fermi surfaces in $PdTe_2$ (Y. Wang *et al.*, 2016b; Fei *et al.*, 2017; Zheng *et al.*, 2018), $PtTe_2$ (Fu *et al.*, 2018; Pavlosiuk and Kaczorowski, 2018), and $PtSe_2$ (Yang, Schmidt *et al.*, 2018) have also been investigated using SdH and de Haas–van Alphen (dHvA) measurements. Take $PdTe_2$ as a representative. Figure 19(a) shows the measured oscillatory components of the out-of-plane ($\boldsymbol{B}\|\boldsymbol{c}$) magnetization at various temperatures. By employing the fast Fourier transform method, Fei *et al.* (2017) identified multiple sets of oscillations [$\alpha$ to $\zeta$ in Fig. 19(b)], which is in agreement with the multiband feature of the $PdTe_2$ compound. As with Eq. (14), the dHvA oscillation of a 3D Dirac system can be described using the LK formula (Lifshitz and Kosevich, 1956):

$$\Delta M \propto R_T R_D R_S \sin\left\{2\pi\left[\frac{F}{B}-\left(\frac{1}{2}-\phi\right)\right]\right\}, \qquad (17)$$

where $R_T = \chi T/\sin h(\chi T)$ is the temperature damping factor, $R_D = \exp(-\chi T_D)$ is the Dingle damping factor, and $R_S = \cos(\pi g m^*/2m_e)$ is the spin damping factor. $\chi = 2\pi^2 k_B m^*/eB\hbar$, and $m^*$ and $m_e$ are the effective cyclotron mass and free electron mass, respectively. $T_D = \hbar/2\pi k_B \tau_q$ is the Dingle temperature, where $\tau_q$ is the cyclotron relaxation time. The phase factor $\phi = \beta - \delta$, where $2\pi\beta$ is the Berry phase and $2\pi\delta$ is a second phase shift that takes values of 0 and $\pm 1/8$ for 2D and 3D Fermi surfaces, respectively. Several physical parameters can be extracted based on the LK formula. For example, at a fixed magnetic field, the amplitude of the quantum oscillation is proportional to $R_T$. Therefore, $m^*$ can be obtained by fitting the oscillation amplitude at different temperatures, as shown in Fig. 19(b). Similarly, at a fixed temperature $T_D$ or $\tau_q$ can be extracted by the fit of the Dingle damping factor $R_D$.

Specifically, the Berry phase can be determined by plotting the Landau index versus $1/B$ and tracking the intercept. As summarized in Fig. 19(c), Fei *et al.* (2017) got an intercept of 0.46 by assigning integer Landau indices to the valleys of $\alpha$

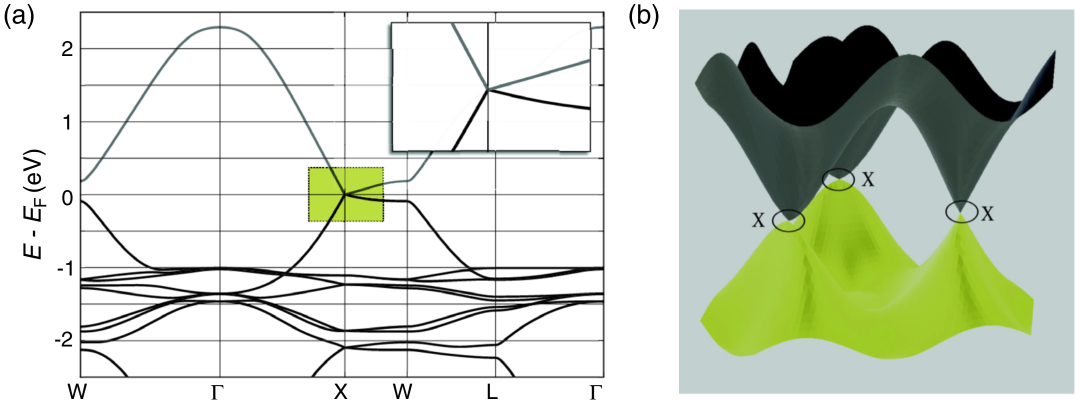

FIG. 20. Symmetry-enforced Dirac semimetal beta-cristobalite $BiO_2$. (a) Calculated bulk band structures along high-symmetry lines. (b) Summary of 3D bulk Dirac cones at the center of the three zone faces of the BZ. Adapted from Young *et al.*, 2012.

oscillation (8 T).This implies that the Berry phase is close to $\pi$, a signature of nontrivial Dirac transport. By making a further comparison to first-principles calculations, Fei *et al.* identified that the $\alpha$ mode originates in the hole pocket of the tilted type-II Dirac cone; therefore, they ascribed the observed Berry phase of $\alpha$ mode to the type-II Dirac fermions. Last, we mention that the PHE has been observed in the $PdTe_2$ family (Vashist *et al.*, 2018; Xu, Wang *et al.*, 2018; Li *et al.*, 2020; Meng *et al.*, 2020). However, detailed analysis (Li *et al.*, 2020; Meng *et al.*, 2020) revealed that the observed PHE results from anisotropic orbital magnetoresistance rather than the chiral anomaly.

### 3. Symmetry-enforced Dirac semimetals

The mechanism underpinning the Dirac points in the aforementioned type-I and type-II DSMs combines band inversion with crystal rotational symmetry. Young *et al.* (2012) proposed that certain nonsymmorphic space groups that admit four-dimensional irreducible representations can also enforce fourfold Dirac points at high-symmetry momenta on the BZ boundary. Though many nonsymmorphic space groups can host such fourfold irreducible representations, to realize an ideal nonsymmorphic Dirac semimetal phase the material should also satisfy the following criteria: (i) the Dirac point should be located at or close to $E_F$ and no other trivial Fermi surfaces should cross $E_F$, so that the low-energy excitations come only from the Dirac nodes; (ii) the Dirac band should remain doubly degenerate and disperse linearly in all $k$ directions in the vicinity of the Dirac point; and (iii) the two Dirac bands should carry zero total monopole charge. Several promising material candidates have been predicted to host such Dirac points, such as beta-cristobalite $BiO_2$ (Young *et al.*, 2012), Bi-containing distorted spinels (Steinberg *et al.*, 2014), a family of cluster compounds $A(\mathrm{Mo}X)_3$, with $A = (\mathrm{Na, K, Rb, In, Tl})$ and $X = (\mathrm{Se, Te})$, and $HfI_3$ (Gibson *et al.*, 2015). Take $BiO_2$ as an example; the calculated band structure in Fig. 20 reveals band crossings with linear dispersion at the $X$ points. As the material has both the inversion and $\mathcal{T}$ symmetries, each crossing band is doubly degenerate, and thus these band crossings form fourfold-degenerate Dirac points at $E_F$. Therefore, $BiO_2$ is a promising nonsymmorphic DSM with three essential Dirac cones located at the center of the three zone faces of the first BZ. As for experimental efforts, despite many predictions experimental evidence of nonsymmorphic DSMs has remained elusive.

### 4. Quadratic and cubic Dirac semimetals

In addition to linear dispersion, Dirac cones can also have quadratic or cubic band dispersions along certain $k$ directions. Quadratic Dirac points were found to exist in several compounds with a cubic lattice structure, such as $\alpha$-Sn (Groves and Paul, 1963; Zhang, Wang *et al.*, 2018), $Cu_2Se$ (Zhu, Liu *et al.*, 2018), and $Pr_2Ir_2O_7$ (Kondo *et al.*, 2015). Take $\alpha$-Sn as a representative. As with $BiO_2$, $\alpha$-Sn crystallizes in the nonsymmorphic face-centered-cubic crystal structure (SG227) with both the inversion and $\mathcal{T}$ symmetries. Thus, each band is double degenerate. The quadratic conduction and valence bands touch each other at the Γ point, form a quadratic Dirac point, as shown in Fig. 21(a). Materials with such a quadratic band touching at $E_F$ are known as Luttinger semimetals (Moon *et al.*, 2013). The Luttinger semimetal phase is usually adjacent to a variety of topological phases, including topological insulator, massless Dirac semimetal, type-I, type-II, and double Weyl semimetal phases, which can be induced and engineered in $\alpha$-Sn by external strain, magnetic field, and circularly polarized light (Zhang, Wang *et al.*, 2018). Indeed, several ARPES groups reported realizations of the topological insulator phase or linear Dirac semimetal phase in $\alpha$-Sn/InSb films by inducing compressive or epitaxial strains (Barfuss *et al.*, 2013; Ohtsubo *et al.*, 2013; C.-Z. Xu *et al.*, 2017). Regarding the pristine quadratic Dirac point, we note the observation of the quadratic bulk valence band at the Γ point in $\alpha$-Sn/InSb films made by Barfuss *et al.* (2013), as shown in Fig. 21(b), though the quadratic Dirac point and the conduction band were not observed by conventional ARPES, as it lies above $E_F$.

The cubic Dirac point, a fourfold-degenerate nodal point with cubic dispersion in a plane and a linear dispersion in the third direction, has rarely been reported in real materials. One reason for this is that the stabilization of a cubic Dirac point requires at least the following four symmetries, $\mathcal{P}$, $\mathcal{T}$, $C_3$, and $C_6$ rotation, and nonsymmorphic symmetries, and these requirements exclude most of the space groups. Still, the density functional theory has identified two groups of

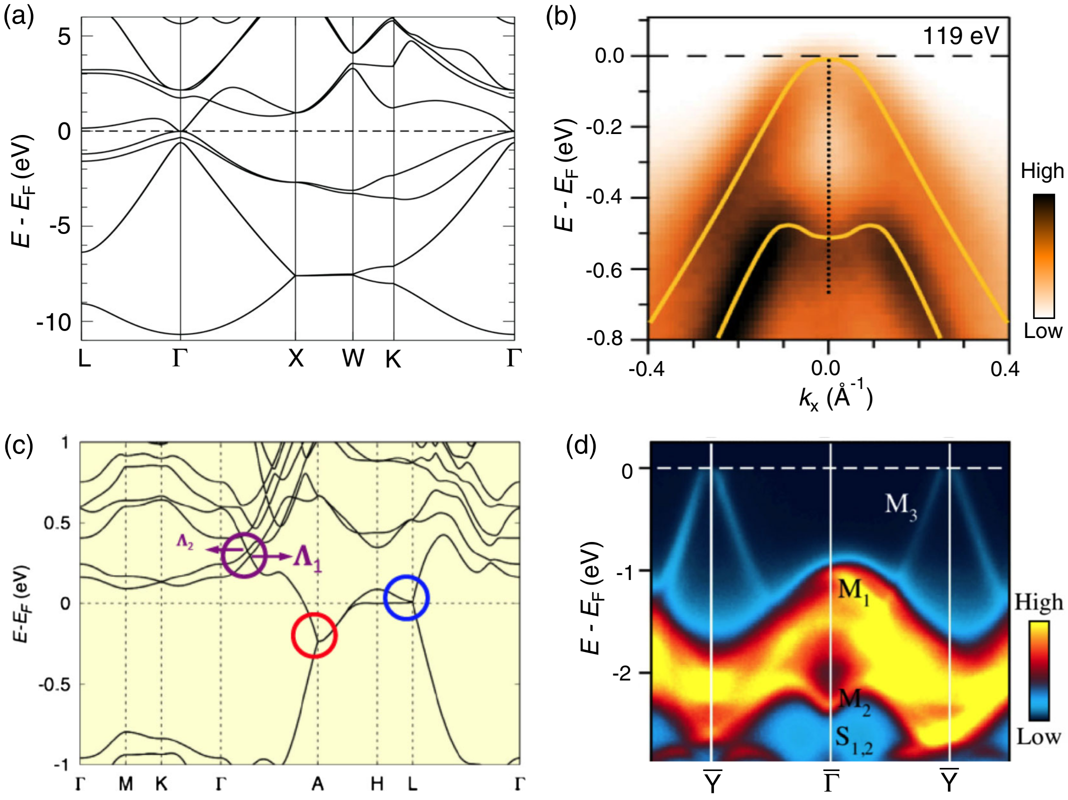

FIG. 21. (a) Calculated bulk band structures of $\alpha$-Sn along high-symmetry lines. (b) ARPES spectra on $\alpha$-Sn/InSb film, measured along the $k_x$ direction with 119 eV photon energy, which corresponds to the $\Gamma$ point of the BZ. (c) Calculated bulk band structures of $\mathrm{Tl(MoTe)_3}$ as a representative of stable $A(\mathrm{Mo}X)_3$ compounds. The cubic and symmetry-enforced Dirac point at $A$, the linear and symmetry-enforced Dirac point at $L$, and the band-inversion-induced Dirac points along $\Gamma$-$A$ are marked with red, blue, and purple circles, respectively. (d) ARPES spectra on $\mathrm{Tl(MoSe)_3}$ measured along the $k_z$ direction with 50 eV photon energy. Adapted from Barfuss *et al.*, 2013, Liu and Zunger, 2017, Nakayama *et al.*, 2018, and Zhang, Wang *et al.*, 2018.

promising material candidates, i.e., $A(\mathrm{Mo}X)_3$, with space group $P6_3/m$ (no. 176) (Liu and Zunger, 2017), and the nonferroelectric phase of $\mathrm{LiOsO_3}$ compound with space group $R\bar{3}c$ (no. 167) (Yu *et al.*, 2018). Figure 21(c) shows the calculated bulk band dispersion of $\mathrm{Tl(MoTe)_3}$, a representative of quasi-1D $A(\mathrm{Mo}X)_3$ compounds that is immune to Peierls distortion. Four types of Dirac points can be identified. (i) One cubic Dirac point at $A$, which shows a cubic dispersion along the $A$-$H$ direction. (ii) Three linear Dirac points stabilized by the nonsymmorphic symmetry at the $L$ points, which are identical to those in beta-cristobalite $\mathrm{BiO_2}$. (iii) and (iv) Band-inversion-induced quadratic ($\Lambda_1$) and linear Dirac points ($\Lambda_2$) along the $\Gamma$-$A$ direction in the conduction bands. Recently ARPES measurements were performed on the $(1100)$ surface of the $\mathrm{Tl(MoSe)_3}$ compound (Nakayama *et al.*, 2018) and revealed the linearly dispersed Dirac bands along the chain direction ($k_z$), as shown in Fig. 21(d). However, the cubic or linear Dirac points at the $A$ or $L$ points were not resolved, as they shift above $E_F$ as a result of the imperfection of the crystal, i.e., the Tl deficiency.

### 5. Magnetic Dirac semimetals

The previously discussed DSMs are all nonmagnetic ones preserving both $\mathcal{T}$ and $\mathcal{P}$ symmetries, which are necessary to protect the double degeneracy of the Dirac bands. It is thus natural to ask whether Dirac fermions can exist in $\mathcal{T}$-breaking magnetic materials. Tang *et al.* (2016) answered this question in the affirmative when considering a specific three-dimensional system with an antiferromagnetic (AFM) order that breaks both $\mathcal{T}$ and $\mathcal{P}$ symmetries but respects their combination ($\mathcal{PT}$ symmetry). With the combined $\mathcal{PT}$ symmetry satisfying $(PT)^2 = -1$, the double degeneracy is reserved for the generic momentum $k$. Therefore, a crossing of two bands protected by certain crystal symmetry can give rise to a fourfold-degenerate Dirac point. Specifically, Tang *et al.* predicted that AFM CuMnAs and CuMnP could host the Dirac fermions around $E_F$. As shown in Fig. 22(a), *ab initio* calculations show a band inversion at the $X$ point of the BZ. Without considering SOC (red curves), this band inversion leads to unavoidable band crossings, e.g., along the $X$-$\Gamma$, $X$-$U$, and $X$-$Z$ directions. These band crossings together form a 1D nodal line on the $k_y = 0$ plane. When SOC is turned on, assuming that the orientation of magnetic moments is along the $z$ direction, most of the band crossings are fully gapped, except for the band crossing along the $X$-$U$ line, as the two doubly degenerate crossing bands carry opposite $S_{2z}$ $[S_{2z} = \{C_{2z}|((1/2), 0, (1/2))\}]$ eigenvalues along this direction. Therefore, CuMnAs holds one pair of fourfold Dirac points along the $X$-$U$ line, which is protected by the combined $\mathcal{PT}$ and twofold screw rotation ($S_{2z}$) symmetries. The topological feature of these Dirac points is further confirmed

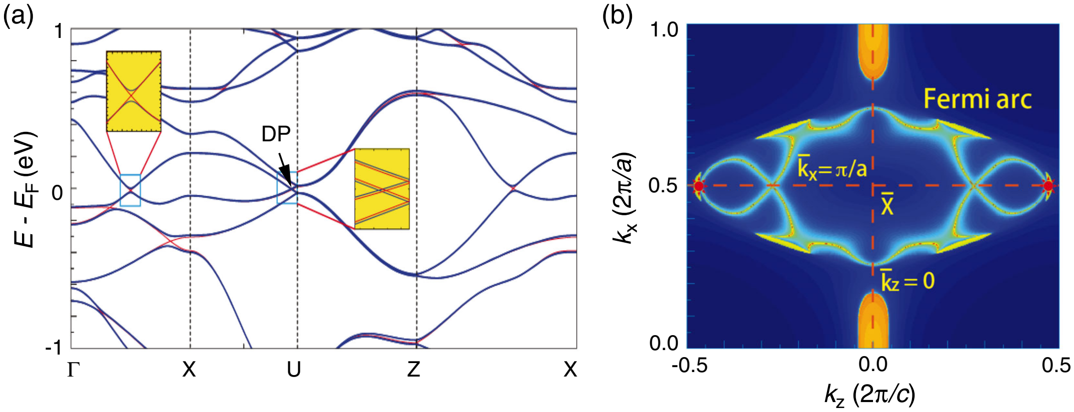

FIG. 22. AFM Dirac semimetal in CuMnAs. (a) Calculated bulk band structures of CuMnAs along the high-symmetric lines without (red lines) and with (blue lines) SOC. In the SOC case, the orientation of magnetic moments is along the $z$ direction. (b) Calculated Fermi surface contour on the (010) surface. The red stars indicate the projection of the gapless Dirac points. Adapted from Tang *et al.*, 2016.

by the appearance of nontrivial surface states. As shown in Fig. 22(b), one pair of Fermi arcs that connect the projection of two gapless Dirac points is identified on the (010) surface.

The Dirac points along the $X$-$U$ line in $\mathcal{T}$-breaking AFM CuMnAs are induced by band inversion. Recent progress has also been achieved in extending the symmetry-enforced Dirac semimetal states to magnetic systems in both two (Wang, 2017a; Young and Wieder, 2017) and three dimensions (Wang, 2017c; Watanabe, Po, and Vishwanath, 2018). In these systems, the Dirac points are mandated at high-symmetry momenta by the symmetries of the magnetic space group, i.e., the combination of crystal symmetries (either symmorphic or nonsymmorphic) and an essential antiunitary symmetry composed of $\mathcal{T}$ and a half translation, and cannot be gapped without lowering the previously mentioned symmetries. In particular, Watanabe, Po, and Vishwanath (2018) performed a systematic symmetry-based analysis of band topology in all 1651 magnetic space groups and identified an exhaustive list of magnetic space groups, which for specific electron filling constraints are capable of hosting symmetry-enforced gapless states. Watanabe, Po, and Vishwanath (2018) predicted that the magnetic compounds $YFe_4Ge_2$ and $LuFe_4Ge_2$ would be realistic magnetic Dirac semimetal candidates featuring essential Dirac points at high-symmetry momenta near $E_F$. In short, magnetic systems can host fourfold Dirac points either induced by band inversion or enforced by crystal symmetries. Material candidates include CuMnAs(P), Y(Lu)$Fe_4Ge_4$, $EuCd_2As_2$ (Hua *et al.*, 2018), CeSbTe (Schoop *et al.*, 2018), etc.

### 6. Dirac semimetals without Fermi arcs

A fingerprint of WSMs is the existence of surface Fermi arcs connecting the projection of Weyl points of opposite monopole charge. In view of DSMs, since a Dirac point can be viewed as two Weyl points of opposite chirality overlapping, it is natural to expect the surface states in a DSM to be two copies of the Fermi arc of a WSM, i.e., the double Fermi arcs shown schematically in Figs. 23(a) and 23(b). However, it has been pointed out that the double Fermi arcs are not topologically protected and that bulk perturbation preserving the Dirac nodes and all crystal symmetries can in principle deform the double Fermi arcs into a conventional Fermi contour (Kargarian, Randeria, and Lu, 2016; Kargarian, Lu, and Randeria, 2018), as shown in Fig. 23(c). Note that though the double Fermi arcs are not topologically protected, the previously discovered DSMs, including $Na_3Bi$ and $Cd_3As_2$, still exhibit seemingly robust double Fermi arcs (Shtanko and Levitov, 2018).

Le *et al.* (2018) provided a concrete material candidate $\beta$-CuI that manifests the lack of topological protection for double surface Fermi arcs in DSMs. Like $Na_3Bi$, $\beta$-CuI exhibits a pair of Dirac points along Γ-$Z$ protected by the $\mathcal{P}$, $\mathcal{T}$, and $C_3$ rotational symmetries, as shown in Fig. 23(d). Figure 23(e) shows the calculated surface states on the (100) surface in the conventional cell. As with $Na_3Bi$, the two surface states form a single Dirac point at the Γ point, which is protected by the nontrivial $Z_2$ invariant in the $k_z = 0$ plane. Conversely, the energy difference between the surface Dirac point at Γ and the projection of the bulk Dirac point is small, yielding two flat surface states along Γ-$Z$ that exhibit nonmonotonic dispersions and vanish at the projection of bulk Dirac points. The lower surface state first sinks below the energy level of the bulk Dirac point ($E_D$), then rises above, and finally bends down and sinks into the Dirac point, resulting in three crossing points for $k_y = 0$ at $E_D$ (denoted by white and red circles). The corresponding Fermi surface of the (100) surface at $E_D$ is shown in Fig. 23(f). There is one closed nontrivial Fermi pocket with spin helical texture (shown with green arrows) centered around $k_z = 0$ and two trivial pockets centered around $k_z = \pi$ that originate from the nontrivial $Z_2$ invariant in the $k_z = 0$ plane and the trivial $Z_2$ invariant in the $k_z = \pi$ plane, respectively. The nontrivial closed Fermi surface around $k_z = 0$ does not pass through the projections of the bulk Dirac points (red circles), indicating the absence of Fermi arcs. To summarize, the DSM $\beta$-CuI exhibits a closed Fermi surface instead of double Fermi arcs on its side surfaces, providing explicit proof that the Fermi arcs in DSMs are not topologically protected.

We previously discussed several distinctive types of DSMs. In addition to these materials, considerable groups of materials

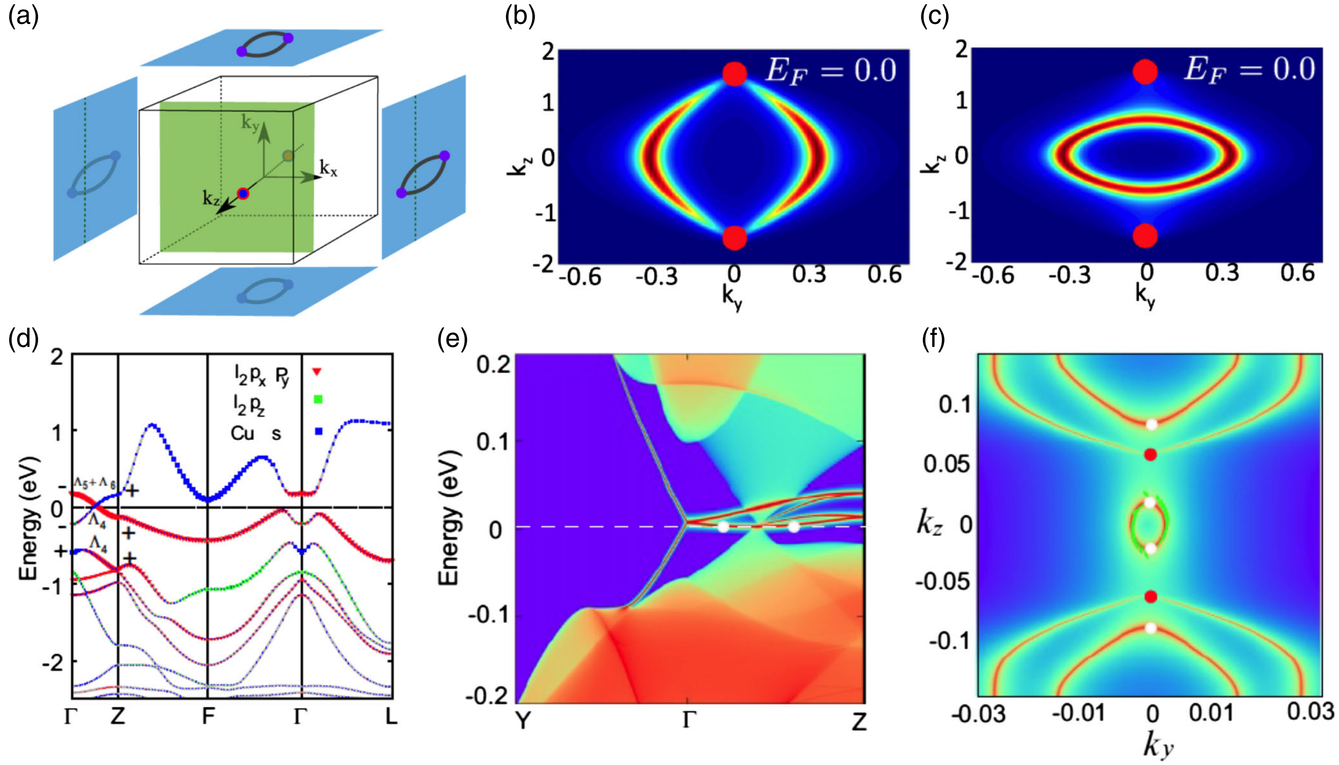

FIG. 23. (a) DSM showing a pair of Dirac points along the $k_z$ axis in the bulk BZ and double Fermi arcs on the side surfaces. Note that the surface perpendicular to the $z$ axis [(001) surface] has no arcs. (b) Surface spectral density showing the existence of double Fermi arcs connecting the projection of two Dirac points (solid red circles) on the (100) surface. (c) Deformation of double Fermi arcs into a closed Fermi contour by perturbations. (d) Calculated bulk band structures of $\beta$-CuI along high-symmetry lines with SOC. The orbital weights are represented by the areas of circles and triangles. (e) The projected surface density of states of $\beta$-CuI for the (100) surface. (f) Fermi surface at the energy of bulk Dirac points for the (100) surface. The green arrows indicate the spin textures of the closed nontrivial Fermi pocket centered at the $\Gamma$ point. From Kargarian, Randeria, and Lu, 2016, and Le *et al.*, 2018.

have also been proposed as DSMs; see Tang *et al.* (2019), Vergniory *et al.* (2019), and T. Zhang *et al.* (2019).

### B. Weyl semimetals

As discussed in Sec. II, Weyl fermions, which have not yet been discovered in high-energy physics, can be realized in WSMs as an emergent phenomenon by breaking either $\mathcal{T}$ or $\mathcal{P}$ symmetry in DSMs. This has inspired two broad categories of proposals for realizing WSMs in condensed-matter systems, i.e., $\mathcal{T}$-breaking magnetic and $\mathcal{P}$-breaking nonmagnetic noncentrosymmetric WSMs.

Historically, the first proposal to realize Weyl fermions in condensed-matter systems was suggested by Wan *et al.* (2011), for a class of magnetic pyrochlores $\mathrm{Rn_2Ir_2O_7}$ (Rn is Y or another rare-earth element) with all-in–all-out noncollinear magnetic order, where 24 pairs of Weyl points emerge as the system undergoes the magnetic phase transition. A relatively simple WSM system was then proposed by G. Xu *et al.* (2011), who considered the ferromagnetic half-metal $\mathrm{HgCr_2Se_4}$ and predicted that the ferromagnetic phase would give rise to a pair of Weyl points with quadratic band crossings, the so-called double Weyl points. Another route to the realization of $\mathcal{T}$-breaking WSMs involves a fine-tuned heterostructure of alternating layers of a magnetically doped topological insulator and a normal insulator (Burkov and Balents, 2011). All of these proposed WSM candidates are $\mathcal{T}$-breaking magnetic materials. However, experimental detection of magnetic WSM states using ARPES or other techniques faces several obstacles, including complex magnetic domains, strong correlations, and destruction of sample quality upon magnetic doping.

On the other hand, WSM can also be generated by breaking $\mathcal{P}$ symmetry. Compared to magnetic WSMs, $\mathcal{P}$-breaking nonmagnetic WSMs are more feasible for experimental verifications, as the alignment of magnetic domains is no longer required. Different routes were explored to realize the WSM phase in noncentrosymmetric systems. The first one is a superlattice system formed by alternately stacking trivial and topological insulators (Halász and Balents, 2012; Zyuzin, Wu, and Burkov, 2012; Das, 2013). The second takes advantage of the phase transition between the trivial and topological insulators in noncentrosymmetric materials (Singh *et al.*, 2012; Liu and Vanderbilt, 2014), as such a phase transition must happen via an intermediate Weyl semimetal phase (Shuichi, 2007). The third is a model based on the zinc blende lattice with fine-tuning of the relative strength between SOC and the $\mathcal{P}$-breaking term (Ojanen, 2013). The fourth involves tellurium or selenium crystals under certain values of pressure (Hirayama *et al.*, 2015). However, there has been no experimental realization of the previously mentioned proposals thus far, as they require a fabrication of heterostructure, a

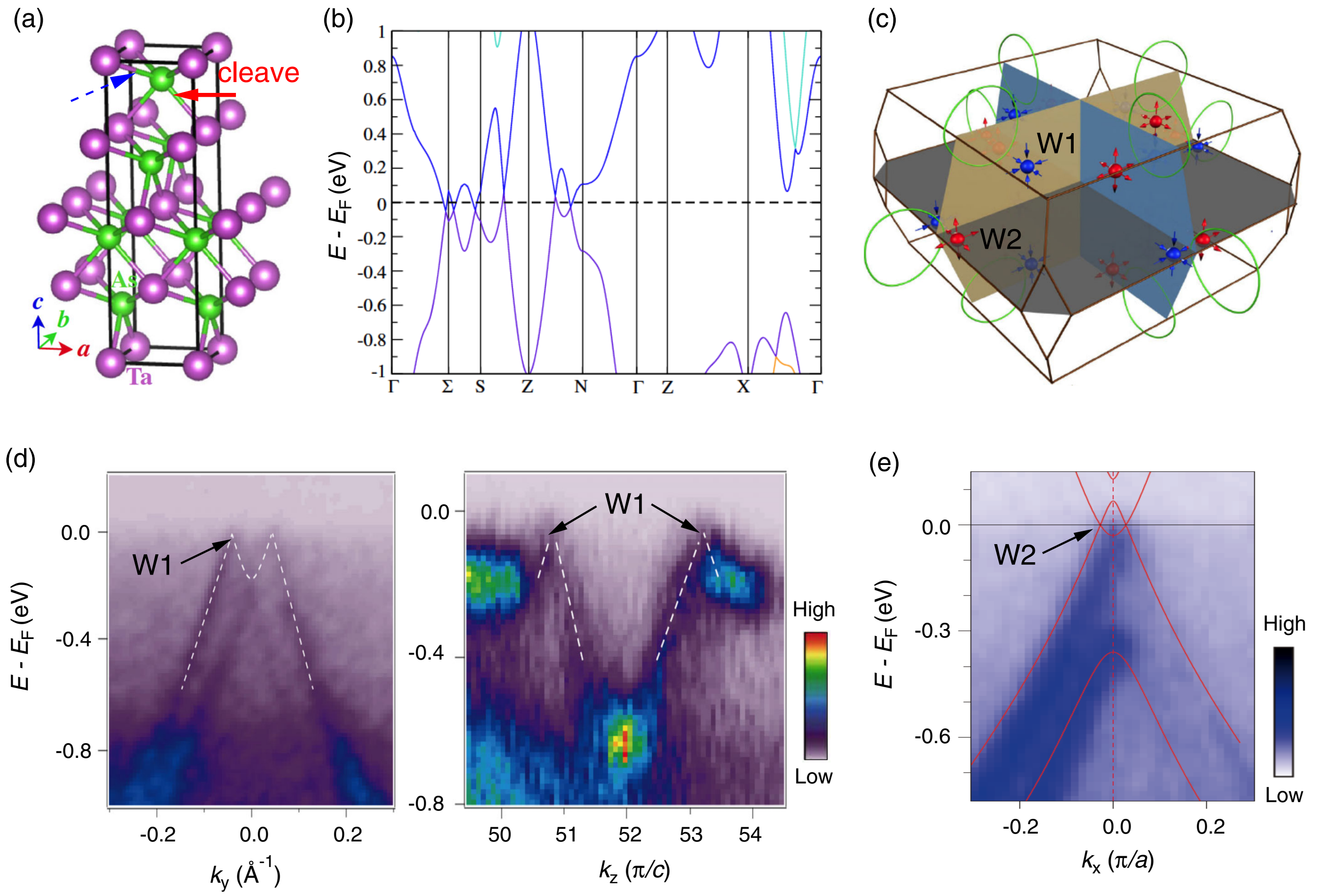

FIG. 24. (a) Crystal structure of TaAs. The arrow indicates that the cleavage occurs between the As and Ta atomic layers, producing two kinds of (001) surfaces with either As- or Ta-terminated atomic layers. (b) The calculated band structure of TaAs without SOC. (c) 3D view of the nodal rings (without SOC, green circles) and Weyl points (with SOC, blue and red dots) in the BZ. The red and blue areas represent opposite chiralities of the Weyl nodes. (d) ARPES intensity plots along the $k_y$ and $k_z$ directions through a pair of W1 Weyl nodes. The white dashed lines are guides for the eye. (e) ARPES intensity plots along the $k_x$ and $k_y$ directions near the Weyl nodes W2. For comparison, the calculated bands are plotted (red curves) on top of the experimental data. Adapted from Lv *et al.*, 2015c, Weng, Fang *et al.*, 2015, and S.-Y. Xu *et al.*, 2015b.

fine-tuning of the SOC, or an application of pressure. Looking for Weyl semimetal candidates in naturally $\mathcal{P}$-breaking noncentrosymmetric and stoichiometric compounds allows one to easily avoid the previously mentioned obstacles. Indeed, by following this route many distinctive experimentally feasible WSM candidates have been identified, including the TaAs family (S.-M. Huang *et al.*, 2015; Weng, Fang *et al.*, 2015), which was the first experimentally verified WSM.

### 1. $\mathcal{P}$-breaking Weyl semimetal TaAs family

#### a. Theoretical predictions and ARPES

*Bulk Weyl nodes.*—The TaAs family (TaAs, TaP, NbAs, NbP) crystallizes in the body-centered tetragonal structure with nonsymmorphic space group $I4_1md$ (no. 109). If we take TaAs as a representative, the crystal structure consists of alternating As and Ta layers [Fig. 24(a)]. The adjacent TaAs layers are rotated 90° and shifted by $a/2$, leading to a lack of inversion symmetry. Instead, the space group contains two mirror planes, namely, $M_x$ and $M_y$, which are necessary to protect the nodal rings, as discussed later. The calculated band structure of TaAs without SOC shows band inversion and multiple band crossing features near $E_F$, as shown in Fig. 24(b). Detailed symmetry analysis shows that the two crossing bands belong to different mirror irreducible representations, and hence the corresponding band crossings are protected by the mirror symmetry. Together these protected band crossing points form several nodal rings in the two mirror-invariant planes, as shown in Fig. 24(c). For each of the mirror-invariant planes, after turning on SOC the nodal rings are fully gapped within the plane. The valence and conduction bands accidentally touch at several discrete $k$ points slightly off the mirror plane, leading to the appearance of gapless Weyl nodes in TaAs. More precisely, there are 12 pairs of Weyl points with monopole charges of $\pm 1$ in the entire BZ, four pairs of Weyl points (labeled as W2) are located exactly in the $k_z = 0$ plane, and another eight pairs of Weyl points (labeled as W1) are located off the $k_z = 0$ plane with a larger $k$ distance, as illustrated in Fig. 24(c).

Taking advantage of the bulk-sensitive soft x-ray ARPES, both the W1 and W2 bulk Weyl cones in the TaAs family, which includes TaAs, TaP, NbAs, and NbP, have been confirmed (Lv *et al.*, 2015c; S.-Y. Xu *et al.*, 2015a, 2015b, 2015c; N. Xu *et al.*, 2016, 2017). We again take TaAs as our example. As shown in Figs. 24(d) and 24(e), both the W1 and W2 bulk Weyl cones are confirmed by the measured linearly dispersed band crossings along the in-plane ($k_x$, $k_y$) and out-of-plane ($k_z$) directions, which matches well with the calculations.

*Surface Fermi arcs.*—A striking topological consequence of the monopole feature of Weyl points is the existence of surface Fermi arcs on both the top and bottom surfaces connecting the projections of Weyl points of opposite chirality as illustrated in Fig. 3(d). In the case of TaAs, the crystals were cleaved in the (001) plane in the ARPES measurements. As illustrated in Fig. 24(a), the cleavage occurs easier by breaking two Ta—As bonds (red arrows) per unit cell instead of breaking four bonds (dashed blue arrows), giving rise to two kinds of (001) surfaces with either As-terminated (bottom surface) or Ta-terminated (top surface) atomic layers. As shown in Fig. 24(c), because W1 Weyl points at positive and negative $k_z$ have the same sign of chirality, their projection onto the (001) surface naturally carries a monopole charge of ±2, whereas the projection of W2 has a charge of ±1. Therefore, it is expected that two Fermi arcs terminate at W1, and one Fermi arc terminates at W2. These general aspects are independent of the surface terminations.

Several distinct criteria have been established to prove the existence of Fermi arcs. Among them, one of the most direct pieces of evidence is the disjoint Fermi surface, i.e., any surface-state constant-energy contour with an open curve is a Fermi arc. Besides, one can also count the number of Fermi surface crossings. As we know, a closed Fermi surface can cross an arbitrary $k$ loop in the surface BZ only an even number of times, and only an open Fermi arc can possibly cross this loop an odd number of times (Lv *et al.*, 2015b). Therefore, if one can find a specific loop containing a total odd number of Fermi surface crossings, Fermi arcs must exist. Another criterion is a nonzero Chern number, and one effective way is to add up the signs of the Fermi velocities of all surface states around a closed $k$ loop in the surface BZ where the bulk band structure is everywhere gapped. One can assign +1 for right movers and −1 for left movers, and the sum is the number of chiral edge states (Fermi arcs) enclosed in this loop, corresponding to a Chern number on a bulk (S.-Y. Xu *et al.*, 2015c). In principle, all of the previously mentioned signatures are experimentally accessible in ARPES measurements of surface states, and any surface band structure that satisfies any one of the previously mentioned criteria is sufficient to demonstrate the presence of topological Fermi arcs. In practice, these criteria may not always be met. Specifically, in the TaAs family with multiple pairs of Weyl nodes, the Fermi arcs near the W1 Weyl points always appear in pairs, which together may form a closed contour rather than disjoint arcs. Besides, some of the TaAs family (e.g., NbP) may not have a nonzero Fermi surface Chern number, as the energetic position of the nodes is far from $E_F$ (N. Xu *et al.*, 2017).

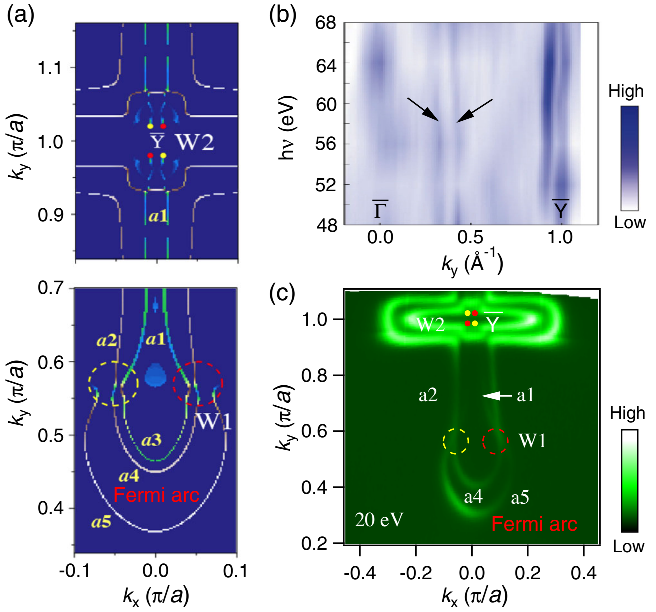

FIG. 25. (a) Fine $k$-point sampling calculations of surface states at $E_F$ near the WPs. W1 are indicated by dashed circles since the chemical potential is located slightly away from the nodes. Yellow and red areas represent opposite chiralities. (b) ARPES intensity plot at $E_F$ along $\bar{\Gamma}$-$\bar{Y}$ collected at different photon energies (48–68 eV), showing the observation $k_z$-nondispersive surface states. (c) ARPES intensity plot at $E_F$ recorded on the As-terminated (001) surface at $h\upsilon = 20$ eV. Adapted from Lv *et al.*, 2015b, and Yang *et al.*, 2015.

Though the topological nature of a WSM requires each Fermi arc to start and end at the surface projections of two Weyl nodes with opposite chirality, the surface connection pattern is not uniquely determined by the bulk band structure. It can be sensitive to other parameters, such as the lattice constants, the surface condition (surface relaxations, reconstructions, etc.), and the chemical potential. For the TaAs family with multiple pairs of Weyl nodes, such as on the (001) As-terminated surface of TaAs, there are topologically nontrivial surface states forming Fermi arcs as well as trivial surface states forming closed FS pockets. These trivial surface states, which usually mix with the Fermi arcs, will also complicate the identification of Fermi arcs. Nevertheless, the first-principles calculations [Fig. 25(a)] and surface-sensitive VUV ARPES measurements [Figs. 25(b) and 25(c)] have identified a5 as one of the surface Fermi arcs connecting the projections of W1 points on the (001) As-terminated surface, although there are some controversies on the complete Fermi-arc connection pattern.

Aside from TaAs, the Fermi arcs of the other three transition-metal monoarsenides have also been identified by VUV ARPES (D.-F. Xu *et al.*, 2015; Belopolski *et al.*, 2016b; Liu *et al.*, 2016; Souma *et al.*, 2016; Min *et al.*, 2019). In particular, Liu *et al.* (2016) carried out a systematic ARPES study on different compounds (NbP, TaP, and TaAs), revealing that the momentum separation of one pair of W1 Weyl points of opposite chirality and the length of corresponding Fermi arcs are proportional to the strength of the SOC, i.e., decreasing in the order TaAs, TaP, NbAs, and NbP. N. Xu *et al.* (2017) performed a comprehensive study on the relationship between the Fermi arcs and the intrinsic bulk Fermi surface topology in TaAs, TaP, and NbP and concluded

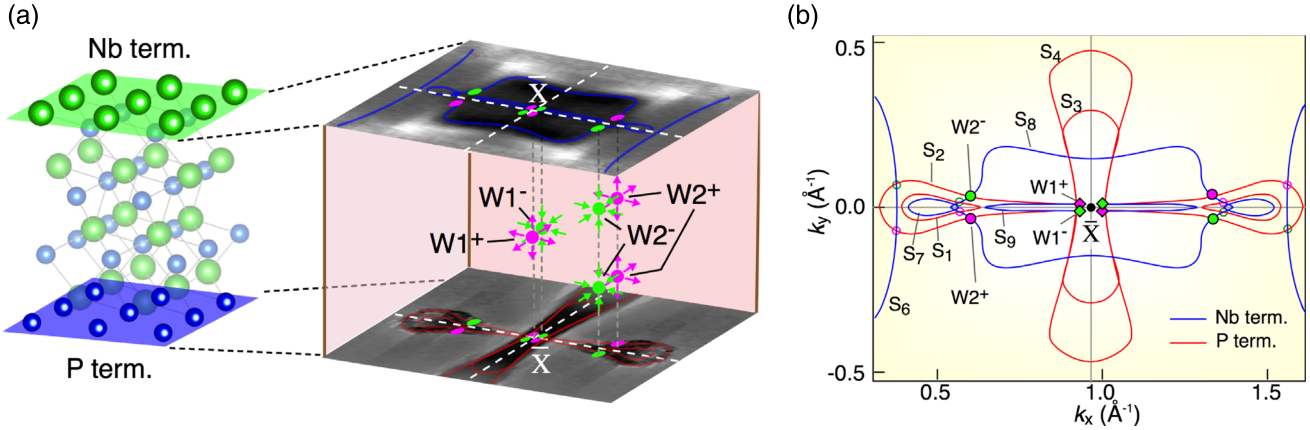

FIG. 26. (a) Left panel: crystal structure of NbP with two different (001) surface terminations. Right panel: schematics of the corresponding ARPES Fermi surface contours around $\bar{X}$ for the two surface terminations. (b) Summary of measured Fermi surfaces from the Nb-terminated (blue loops) and P-terminated (red loops) surfaces. The projections of the W2 Weyl points at the intersection of Fermi surfaces are overlaid by solid circles, whereas open circles show other intersections. Possible W1 Weyl nodes are also indicated with diamonds. From Souma *et al.*, 2016.

that, while the chiral Fermi surfaces exist only when the chemical potential is located in the energy window between two saddle points of the Weyl cone structure, the corresponding Fermi-arc states extend to a larger energy scale.

As discussed previously, there are two kinds of cleaved (001) surfaces in the TaAs family, i.e., the anion-terminated (As, P) and cation-terminated (Ta, Nb) surfaces. In principle, two such terminations must always appear on opposite cleaved surfaces as long as the crystal is composed of a single domain. In ARPES measurements, the samples were cleaved randomly with the [001] axis directed either upward or downward. Therefore, one expects to access both surface terminations after cleaving sufficient samples. In practice, the Fermi arcs on the anion-terminated surfaces have been observed in the entire transition-metal monopnictide family. In contrast, the Fermi arcs on the cation-terminated surfaces have been reported only in TaP and NbP thus far (Souma *et al.*, 2016; N. Xu *et al.*, 2016). Figure 26 shows the measured surface states in NbP for opposing (001) surfaces. At first glance, one can find that the Fermi surface topology is considerably different between these two terminations. Detailed analysis given by Souma *et al.* (2016) revealed that the Fermi surface $S_2$ is a nontrivial Fermi arc on the P-terminated surface, and the Fermi surfaces $S_8$ and $S_9$ are Fermi arcs on the Nb-terminated surface. The observed nonequivalent nature of the Fermi arcs between the Nb- and P-terminated surfaces suggests the possibility of controlling the shape of the Fermi arcs by tuning the surface conditions by the guest atom deposition (H. F. Yang *et al.*, 2019).

The long-sought-after bulk Weyl nodes and the nontrivial surface Fermi arcs have been directly observed in the TaAs family using soft x-ray and VUV ARPES. The Fermi arcs are the traces at $E_F$ of the chiral edge states. Since the chiral edge state is spin polarized, the Fermi arcs naturally possess a momentum distribution of spin, namely, spin texture, which can be directly detected by spin-resolved ARPES. In the case of the TaAs family, the spin texture of Fermi arcs on the (001) As-terminated surface of TaAs has been investigated by both calculations and spin-resolved ARPES (Lv *et al.*, 2015a; Sun, Wu, and Yan, 2015; S.-Y. Xu *et al.*, 2016), as summarized in Fig. 27. It has been shown that spin polarization signals in ARPES can also arise from the states that possess no net spin polarization due to final-state effects, and the nonintrinsic spin signal depends on the incident photon energy and polarization (Starke *et al.*, 1996; Jozwiak *et al.*, 2011; Heinzmann and Dil, 2012). Lv *et al.* (2015a) performed systematic photon-energy and polarization-dependent spin-resolved ARPES measurements to exclude the possible extrinsic effects, and the measured spin polarization does not change as a function of photon energies and polarizations, which supports the deduction that the observed spin polarizations reflect the intrinsic spin structure of the initial states in TaAs.

### b. STM and STS

In addition to ARPES, STM, a real-space surface measurement technique that measures the local density of states as well as the quasiparticle scattering and interference, has also been utilized to explore the surface states in the TaAs family (Batabyal *et al.*, 2016; G. Chang *et al.*, 2016b; Inoue *et al.*,

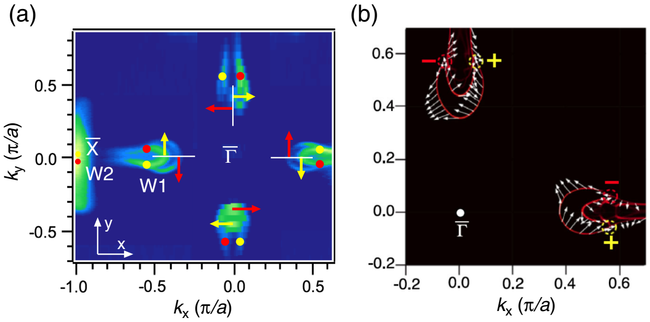

FIG. 27. (a) Photoemission intensity plot at $E_F$ of the (001) As-terminated surface of TaAs. The red and yellow arrows indicate the direction of spin polarization on the inner and outer Fermi surfaces at the high-symmetry lines, respectively. (b) Corresponding theoretical spin texture of surface states. Adapted from Lv *et al.*, 2015a.

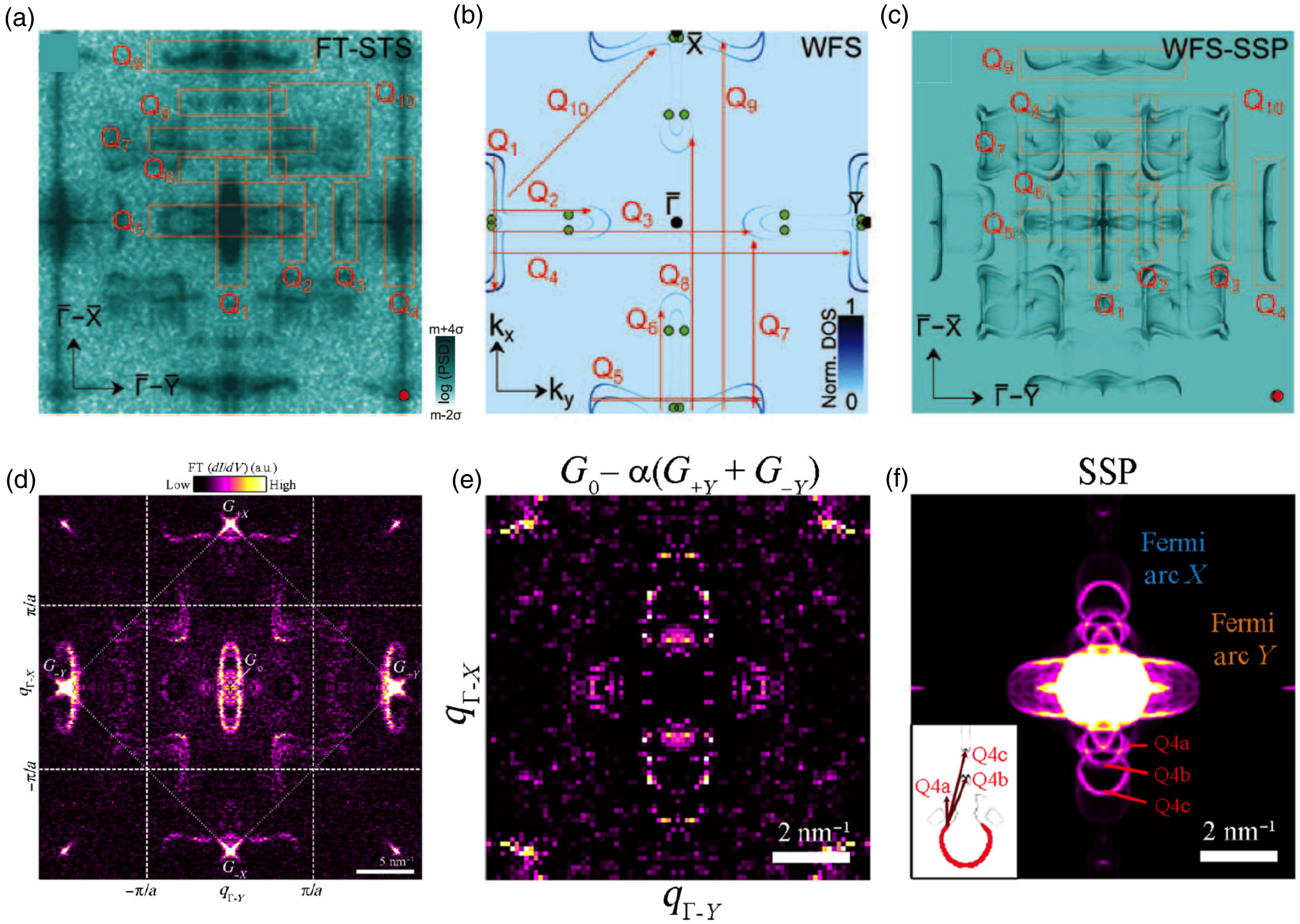

FIG. 28. (a) Fourier transform of the $dI/dV$ conductance map measured at $V_B = 40$ meV on the (001) As-terminated surface of TaAs. The red dot indicates the $(2\pi/a,\ 2\pi/a)$ point in the reciprocal space. (b) Weighted Fermi surface (WFS) calculated by projecting the electronic states only to the topmost As layer. The $Q$ vectors indicate the expected scattering wave vectors. (c) Calculated spin-dependent scattering probability (SSP) map based on the Fermi surface shown in (b). The orange rectangles in (a) and (c) indicate the corresponding quasiparticle interference vectors. (d) Similar to (a) but measured at $V_B = 0$ meV. (e) Subtraction of ellipselike QPI peaks at Bragg points [$G_{\pm y}$ in (d)] times $\alpha = 1.14$ from the central BZ. (f) Calculated SSP of Fermi arcs alone. Inset: contributing scattering processes (Q4a–Q4c) within the Fermi arc along Γ-$Y$. From Batabyal *et al.*, 2016, and Inoue *et al.*, 2016.

2016; Kourtis *et al.*, 2016; Zheng *et al.*, 2016b; Sessi *et al.*, 2017; H. Zheng *et al.*, 2017). Inoue *et al.* (2016) performed systematic STS measurements on the (001) As-terminated surface of TaAs and revealed ten different scattering wave vectors [Fig. 28(a)], which are well reproduced by the calculated spin-dependent scattering probability map [Fig. 28(c)] based on the weighted Fermi surfaces on the topmost As layer [Fig. 28(b)]. In particular, they identified the scattering between a Fermi arc and a trivial band (e.g., Q2 and Q3). They found that the observed QPI pattern can be understood with a theory that takes into account the shape, spin texture, and momentum-dependent propagation of the Fermi-arc surface states into the bulk. Therefore, these observations not only provide evidence for the specific scattering (e.g., Q2 and Q3) indicative of surface Fermi arcs in TaAs but also serve as an important signature of the unique topological sink effect of surface Fermi arcs. Batabyal *et al.* (2016) also performed STS measurements on the TaAs (001) As-terminated surface and obtained similar QPI patterns, as shown in Fig. 28(d). They performed an unusual analysis on the measured QPI pattern, i.e., subtracting the ellipselike pattern that appears around the $G_{\pm y}$ point from the QPI pattern that appears at the zone center ($q = 0$). In this way, the ellipselike pattern at the central region was eliminated [Fig. 28(e)], indicating a replication of this ellipselike pattern at $G_{\pm y}$. On the contrary, the leaflike QPI patterns in which surface Fermi arcs were involved were unaffected after the subtraction, signifying that this QPI pattern was not replicated at Bragg points. Batabyal *et al.* found that the residual QPI pattern fit well with the calculated scatterings between the Fermi arc along Γ-$Y$ and the nearby bulk states, as shown in Fig. 28(f). These results demonstrate that the QPI patterns involving the Fermi arcs are not replicated at Bragg peaks; therefore, Batabyal *et al.* believe that the Fermi arcs are unsusceptible to the underlying crystal structure.

Finally, we note that the transmission electron microscopy measurements have also been performed on the TaAs family and revealed that the single crystals contain a high density of defects, such as stacking faults and vacancies, which leads to a shift of the position of the bulk Weyl points relative to $E_F$

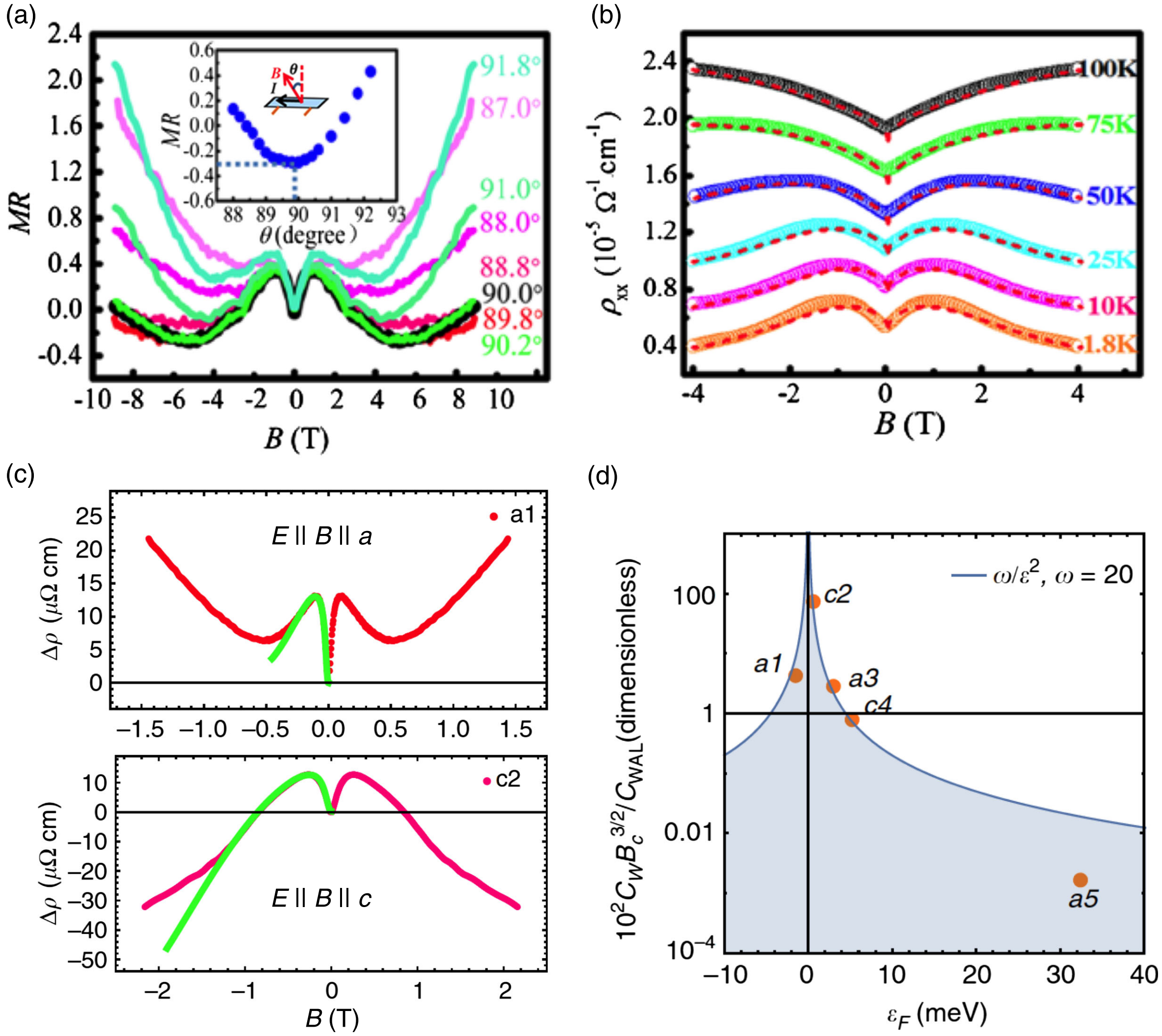

FIG. 29. (a) Angle-dependent magnetoresistance (MR) of a TaAs single crystal measured at $T = 1.8$ K, with $I$ along the $a$ axis. Here $\theta$ is defined as the angle between $B$ and $z$. Inset: the extracted minima of MR at different angles in a magnetic field from 1 to 6 T. (b) The measured longitudinal resistance (open circles) and the corresponding fitting curves (red dashed lines) at various temperatures. (c) Longitudinal magnetoresistance of TaAs measured at $T = 2$ K, with $B \| I$ along the $a$ and $c$ axes. The green curves are the fits to the longitudinal MR data in the semiclassical regime. (d) Chemical potential dependence of the chiral coefficient $C_W$. The chiral coefficient is defined as $C_W = e^4\tau_a/4\pi^4\hbar^4 g(E_F)$, where $g(E_F)$ is the density of states at $E_F$ and $\tau_a$ is the axial charge relaxation time. $B_C$ is a critical field that characterizes the crossover between the weak antilocalization (WAL) regime and the negative magnetoresistance regime, and $C_{\mathrm{WAL}}$ is the coefficient describing the magnitude of the 3D WAL effect. Adapted from X. Huang *et al.*, 2015, and Zhang *et al.*, 2016.

(Besara *et al.*, 2016). In addition, Liu, Richard *et al.* (2016) performed a comparative polarized Raman study of TaAs, NbAs, TaP, and NbP and confirmed the existence of various types of phonons modes that involve different atom vibrations.

### *c. Quantum transport*

The identification of Weyl fermions in the TaAs family paves the way for the exploration of exotic transport phenomena. One of the most intriguing transport phenomena is the chiral-anomaly-induced NLMR, which has been reported in TaAs (X. Huang *et al.*, 2015; Zhang *et al.*, 2016), TaP (Arnold *et al.*, 2016), and NbP (Z. Wang *et al.*, 2016; Niemann *et al.*, 2017). X. Huang *et al.* (2015) reported the observation of NLMR in TaAs. They found that the observed NLMR is sensitive to the angle between the electric and magnetic fields and that the NLMR at various temperatures can be well fitted by the chiral anomaly formula in the semiclassical regime, signifying that the observed NLMR originates from the chiral anomaly, as shown in Figs. 29(a) and 29(b). Zhang *et al.* (2016) summarized several pieces of supporting evidence to show that the observed NLMR in TaAs is induced by the chiral anomaly. These include the following: (i) There is a sharp dependence of the NLMR on the angle between $B$ and $E$, as described by X. Huang *et al.* (2015). (ii) In contrast, the observed NLMR does not depend on the direction of the $E$ field with respect to the crystalline axis, as shown in Fig. 29(c). (iii) The NLMR is closely related to the energy position of the Weyl points. Specifically, the measured chiral coefficient, which characterizes the magnitude of the chiral anomaly, diverges as the chemical potential approaches

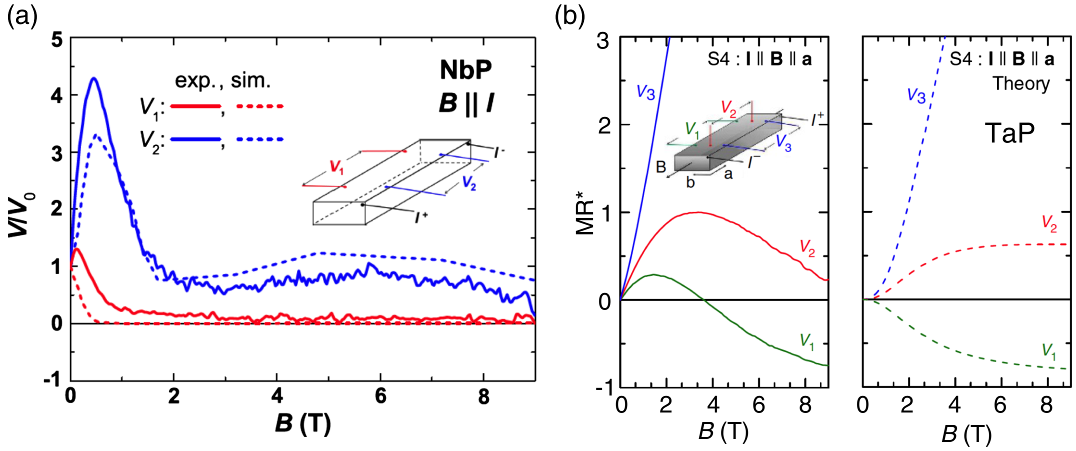

FIG. 30. (a) Magnetic field dependence of the voltage for two different contact configurations (inset) in NbP, measured at 2 K with $B\|I$. The dotted lines are the corresponding simulations of the voltage distribution taking into account the contact configurations and the field-induced inhomogeneous current distribution. (b) Experimental (left panel) and simulated (right panel) magnetic field dependence of the longitudinal MR ($\mathrm{MR}^* = [V(B) - V_0]/V_0$) for three different geometries in TaP, measured at 1.85 K with $B\|I\|a$ axis. Adapted from Arnold *et al.*, 2016, and dos Reis, Ajeesh *et al.*, 2016.

the energy of the Weyl points [Fig. 29(d)], which is consistent with the changes of the Berry curvature field.

As discussed in Sec. III.A.1.c, the chiral anomaly is not the only possible origin of NLMR. Other mechanisms, such as current jetting (Yoshida, 1976; Hu, Rosenbaum, and Betts, 2005), weak localization (Kim *et al.*, 2013; Lu and Shen, 2015), neutral and ionic impurity-induced scattering (Goswami, Pixley, and Das Sarma, 2015), helicity relaxation (Andreev and Spivak, 2018), and conductivity fluctuations (Schumann *et al.*, 2017), can also lead to NLMR. In particular, considerable concern has been raised about the validity of NLMR in high-mobility materials such as the $\mathrm{TaAs}_2$ family (Luo *et al.*, 2016; Yuan *et al.*, 2016) and the TaAs family (Arnold *et al.*, 2016; dos Reis, Ajeesh *et al.*, 2016; Li, Wang *et al.*, 2017; J. Yang *et al.*, 2019) due to the strongly enhanced current jetting effect. Figure 30 shows the measured apparent longitudinal magnetoresistance of NbP and TaP under different voltage contact configurations; one can see a strong dependence of the magnetoresistance on the geometry and even the NLMR can be realized under a specific geometry. The observed geometry-dependent magnetoresistance, which can be reproduced by a current conservation model taking into account the field-induced inhomogeneous current distribution, suggests that the current jetting effect is the predominant cause of the observed NLMR in NbP and TaP. Thus, we conclude that extrinsic effects like the current jetting effect must be seriously considered, and other complementary techniques are needed before we interpret measurements of the NLMR as evidence for the chiral anomaly in DSMs or WSMs.

The previously introduced NLMR at low fields has been controversial due to possible artifacts. Using intense magnetic fields to drive WSMs into the quantum limit provides a path for studying the pure Weyl phenomena. Indeed, many distinct features of Weyl fermions have been revealed by high-field measurements. Moll, Potter *et al.* (2016) uncovered a pronounced magnetic torque anomaly in NbAs manifests as a sudden reversal of the slope of the magnetic torque at the quantum limit, as shown in Fig. 31(a). This torque reversal was understood as a direct consequence of the nonzero Berry phase of Weyl points. In the high-field measurements on TaP (C.-L. Zhang *et al.*, 2017), a sharp sign reversal of Hall resistivity was observed for a magnetic field corresponding to the momentum separation of the W1 Weyl nodes [Fig. 31(b)], i.e., $\sqrt{eB/\hbar} \sim \Delta k_{w1}$. This finding points to the magnetic-tunneling-induced Weyl node annihilation, another topological phenomenon associated with Weyl fermions. Ramshaw *et al.* (2018) pushed the magnetic field to the extreme up to 95 T to drive the Weyl semimetal TaAs far into its quantum limit regime, where two interesting phenomena were unveiled. (i) The gap opening of the lowest Landau level due to the Weyl node annihilation is evidenced by the rapid increase of the $\rho_{zz}$ above 50 T [Fig. 31(c)]. (ii) The abrupt increase of ultrasonic attenuation [Fig. 31(d)] at $T < 2.5$ K and $B > 80$ T is possibly indicative of a field-induced phase transition. Other distinct features such as the additional oscillatory modes arising from the instability of Weyl electrons in TaAs (Zhang, Tong *et al.*, 2016), which is characteristic of Weyl nodes, the Berry paramagnetic response in NbP (Modic *et al.*, 2019), the topological phase transition associated with the suppression of the Weyl dispersion in TaAs (Q. R. Zhang *et al.*, 2019), and the nonsaturating quantum magnetization in TaAs (C.-L. Zhang *et al.*, 2019) have also been revealed when the systems enter the quantum limit.

Magnetotransport measurements have also revealed other properties of the WSM TaAs family, such as ultrahigh carrier mobility (Shekhar *et al.*, 2015), large positive transverse MR embedding with strong SdH oscillations (Luo *et al.*, 2015; Zhang, Guo *et al.*, 2015), and the nontrivial Berry phase related to Weyl fermions (Hu *et al.*, 2016a). Specifically, we note that the angle-dependent SdH oscillations play an important role in reconstructing the 3D bulk Fermi surface and precisely locating the energy position of Weyl points in the TaAs family, even under high pressure (Arnold, Naumann *et al.*, 2016; dos Reis, Wu *et al.*, 2016; Klotz *et al.*, 2016).

As discussed in Sec. III.A.1.c, Fermi-arc surface states can lead to unique transport phenomena, such as Weyl-orbit-based

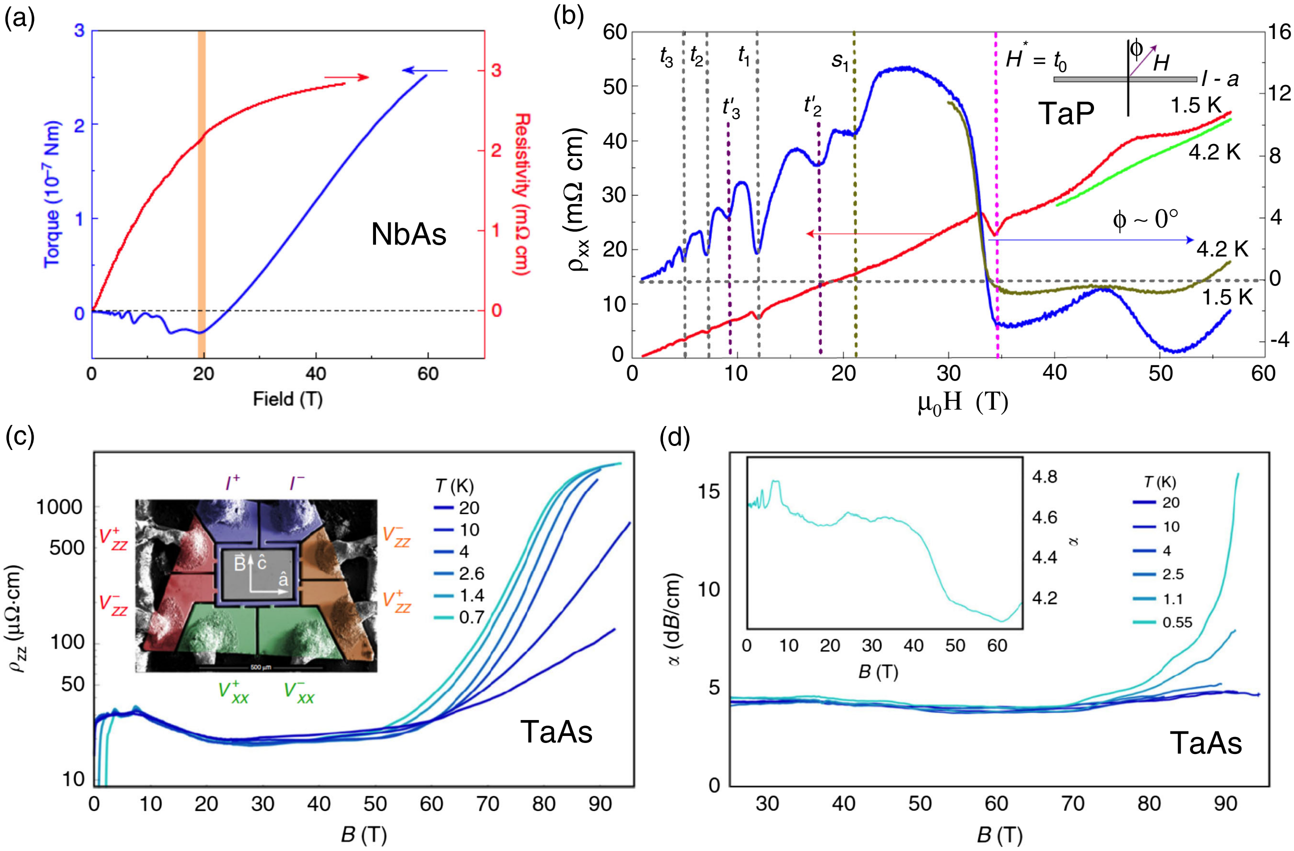

FIG. 31. (a) Magnetic torque and resistivity of NbAs measured at 4 K and an angle of 25° off the $c$ axis toward the $a$ axis. The orange line indicates the quantum limit determined as the position of the last quantum oscillations. (b) $\rho_{xx}$ and $\rho_{yx}$ of TaP as a function of the magnetic field at 1.5 and 4.2 K. $t$ and $s$ correspond to the Landau levels from the electronlike and holelike Weyl pockets, respectively, with the subscripts denoting the Landau indices. (c) Longitudinal magnetoresistance of TaAs for $I \| B \| c$ measured at different temperatures. Inset: microstructured TaAs device. (d) Ultrasonic attenuation of TaAs measured at 315 MHz for $k \| B \| c$, where $k$ is the propagation wave vector of the longitudinal sound. Inset: enlargement of the data from 0 to 65 T. Adapted from Moll, Potter *et al.*, 2016, C.-L. Zhang *et al.*, 2017, and Ramshaw *et al.*, 2018.

quantum oscillations and 3D QHE, which have been extensively studied in $Cd_3As_2$ films or nanostructures. In addition to Weyl orbits, Gorbar *et al.* (2016) pointed out that Fermi-arc transport is dissipative as a result of the surface-to-bulk scattering. Resta *et al.* (2018) found that the Fermi-arc curvature in the momentum space has a strong influence on surface transport. They predicted that a straight Fermi arc is disorder tolerant and can lead to a high surface conductivity that is up to 1 to 2 orders of magnitude larger than a comparable TI. Such Fermi-arc-enhanced surface conductivity was recently confirmed in WSM NbAs nanobelts with thicknesses of 100–300 nm (C. Zhang *et al.*, 2019a), where sheet conductance of up to 5–100 S per □ (per surface) is realized, beyond other 2D and quasi-2D systems, such as 2D electron gases and TI surface states, as summarized in Fig. 32.

### *d. Optical spectroscopy*

Triggered by the peculiar optical properties of Dirac and Weyl fermions, which include linear optical conductivity, optical spectroscopy has been utilized to examine several WSM candidates, such as pyrochlore iridates $R_2Ir_2O_7$ ($R$, rare-earth and Y ions) (Sushkov *et al.*, 2015; Ueda, Fujioka, and Tokura, 2016; Cheng *et al.*, 2017), $YbMnBi_2$ (Chinotti *et al.*, 2016; Chaudhuri *et al.*, 2017), TaAs (B. Xu *et al.*, 2016, 2017; Kimura *et al.*, 2017; Yuan *et al.*, 2018, 2020), $Mn_3Sn$ (Cheng, Wang *et al.*, 2019), and $Co_3Sn_2S_2$ (Yang,

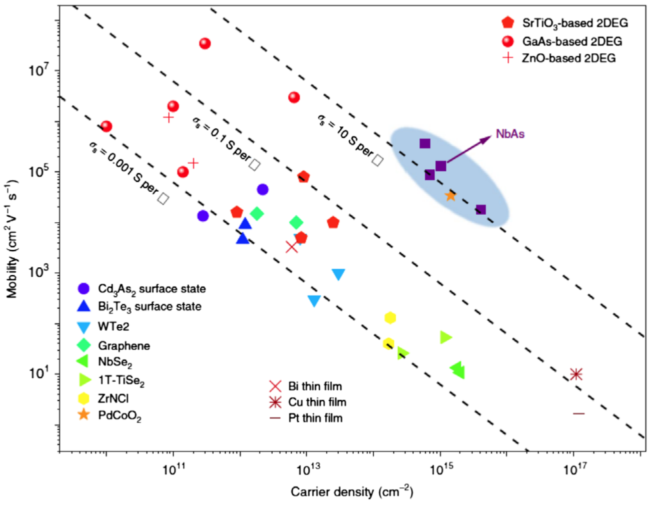

FIG. 32. The mobility–carrier density scaling plot of various 2D and quasi-2D systems. From C. Zhang *et al.*, 2019a.

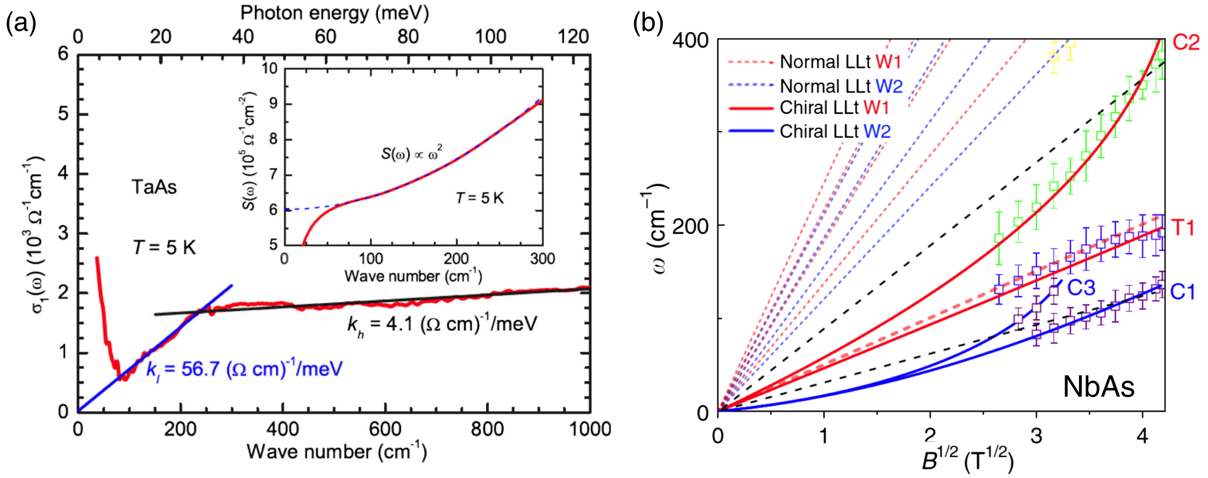

FIG. 33. (a) Real part of the optical conductivity of TaAs measured at 5 K. The blue and black lines are guides for the eye. Inset: corresponding spectra weight $S(\omega)$, which is proportional to $\omega^2$. (b) Landau-level resonance energy vs $B$ measured at 5 K for NbAs. C1 and C3 (W2) and C2 (W1) denote the interband transitions that involve the zeroth chiral Landau-level of Weyl bands (W1 has a higher Fermi velocity), respectively; the blue and red lines are the corresponding fitting curves. T1 represents the nonzero Landau-level transition, which follows a $\sqrt{B}$ dependence. Adapted from B. Xu *et al.*, 2016, and Yuan *et al.*, 2018.

Zhang *et al.*, 2020). Specifically, Fig. 33(a) shows the measured $\sigma_1(\omega)$ of TaAs at 5 K (B. Xu *et al.*, 2016), from which two $\omega$-linear components with different slopes can be identified. The low-energy component persists down to $\sim 70\ \mathrm{cm}^{-1}$ (8.7 meV), which implies that $2E_F < 8.7$ meV based on Eq. (16). Therefore, this low-energy linear conductivity was reasonably attributed to the interband transitions in the vicinity of the four pairs of Weyl points (W2 in Fig. 24), which lie on the $k_z = 0$ plane and are predicted to be only $\sim 2$ meV above $E_F$. On the other hand, the high-energy linear conductivity ($\sim 230\ \mathrm{cm}^{-1}$) was concluded to arise from the interband transitions that involve both the 12 pairs of Weyl points and the trivial bands in TaAs.

As discussed in Sec. III.A.1.d, the chiral zeroth Landau level of Weyl fermions can be checked by pushing the system into the quantum limits, i.e., under a high magnetic field. Indeed, Yuan *et al.* (2018) provided evidence for the characteristic zeroth Landau level in NbAs through a high-field magneto-optical study. As summarized in Fig. 33(b), Yuan *et al.* identified three specific cyclotron resonance absorptions in the quantum limits, denoted as C1–C3. These three modes, following neither linear-in-$B$ or linear-in-$\sqrt{B}$ dependence, can be fitted by the optical transitions involving the zeroth Landau levels of the two types of Weyl nodes, suggesting the existence of two inequivalent chiral Weyl nodes in NbAs.

Apart from the linear optical measurements, the nonlinear optical and thermal measurements likewise revealed many interesting features of Weyl fermions in the TaAs family, such as the CPGE, which is attributed to the asymmetric optical excitation of the Weyl cone and can be utilized to detect the Weyl fermion chirality (de Juan *et al.*, 2017; Q. Ma *et al.*, 2017; Sun, Sun *et al.*, 2017; Osterhoudt *et al.*, 2019; Sirica *et al.*, 2019), the mixed axial–gravitational anomaly–induced positive magnetothermoelectric conductance (Gooth *et al.*, 2017). Beyond those features, the TaAs family exhibits other interesting properties or applications such as the resonance-enhanced SHG efficiency in TaAs (Wu, Patankar *et al.*, 2017; Patankar *et al.*, 2018), the tip- or ion-induced superconductivity (Aggarwal *et al.*, 2017; Bachmann *et al.*, 2017; Li *et al.*, 2017; H. Wang *et al.*, 2017), the wide-range photodetection (Chi *et al.*, 2018), and the hydrogen evolution reaction catalysts (Rajamathi *et al.*, 2017).

### 2. Type-II Weyl semimetals

#### *a. Theoretical prediction and ARPES*

Type-II WSMs, manifested as a strongly tilted and Lorentz-violating Weyl cone in the bulk band structure, were first proposed by Soluyanov *et al.* (2015) in orthorhombic $\mathrm{WTe_2}$. Following this proposal, more material candidates were identified, such as the $\mathrm{Mo}_{1-x}\mathrm{W}_x\mathrm{Te}_2$ family (Sun *et al.*, 2015; T.-R. Chang *et al.*, 2016; Wang, Gresch *et al.*, 2016), the LaAlGe family (S.-Y. Xu *et al.*, 2017), and $\mathrm{Ta_3S_2}$ (G. Chang *et al.*, 2016a). Among them the most intensively studied materials are the $\mathrm{Mo}_{1-x}\mathrm{W}_x\mathrm{Te}_2$ family (Belopolski *et al.*, 2016a; Deng *et al.*, 2016; L. Huang *et al.*, 2016; Tamai *et al.*, 2016; C. Wang *et al.*, 2016). Figure 34(b) shows the calculated electronic band structure of $\mathrm{MoTe_2}$ in the presence of SOC along a specific $K$-$K'$ direction in the $k_z = 0$ plane. The electron and hole pockets touch each other at 6 meV (labeled as W1) and 59 meV (labeled as W2) above $E_F$, forming four pairs of type-II Weyl points with monopole charges of ±1, as illustrated in Fig. 34(a). Consequently, topological Fermi arcs are expected to emerge on the (001) surface, connecting the projections of the W1 and W2 Weyl points with opposite chirality, as shown in Fig. 34(c). Experimentally, it is difficult to distinguish the surface Fermi arcs from the trivial surface states or projected bulk states, as both of them are squeezed into the narrow surface gap between the projected bulk electron and hole pockets [Fig. 34(d)]. Nevertheless, the type-II WSM states in the $\mathrm{Mo}_{1-x}\mathrm{W}_x\mathrm{Te}_2$ family were confirmed by various spectroscopic measurements. Deng *et al.* (2016) confirmed the existence of surface Fermi arcs on the (001) surface of $\mathrm{MoTe_2}$ [Fig. 34(e)]

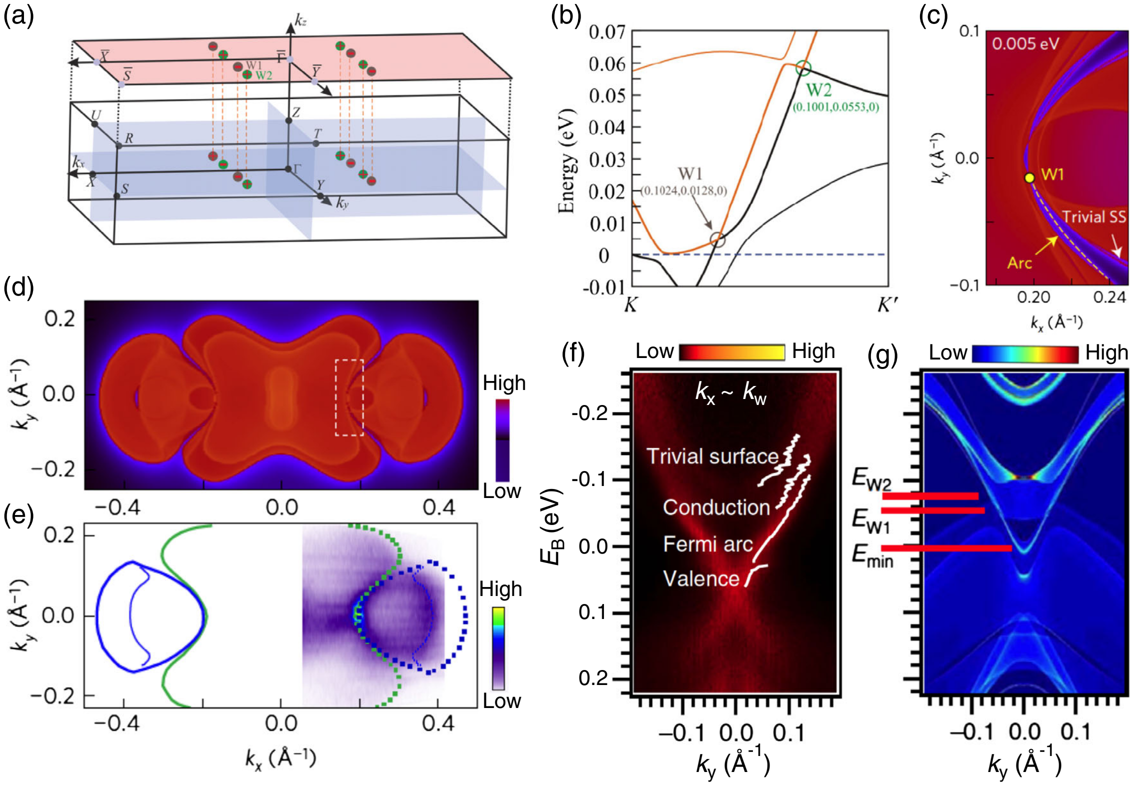

FIG. 34. (a) 3D bulk BZ and the projected (001) surface BZ of $MoTe_2$. Weyl points with positive and negative monopole charges are displayed as green and gray dots. (b) Calculated fine band structure of $MoTe_2$ along the $K$-$K'$ direction crossing two types of Weyl points. (c) Calculated spectral intensity maps of $MoTe_2$ at $E_F + 5$ meV. (d) Calculated spectral intensity maps of $MoTe_2$ at $E_F$ (shifted by −0.02 eV to account for the slight hole doping). The white dashed boxes indicate the regions of interest shown in (c). (e) ARPES intensity maps of $MoTe_2$ measured at $E_F$ with a 6.3 eV laser. (f),(g) ARPES intensity plot and the calculated electronic structure of $Mo_{0.25}W_{0.75}Te_2$ at $k_x \sim k_w$ along the $k_y$ direction. The red lines indicate the energy positions of the surface band bottom, the W1 point, and the W2 point, respectively. Adapted from Sun *et al.*, 2015, Belopolski *et al.*, 2016a, and Deng *et al.*, 2016.

by performing systematic ARPES. Taking advantage of pump-probe ARPES, Belopolski *et al.* (2016a) demonstrated the type-II Weyl fermion state in $Mo_{0.25}W_{0.75}Te_2$ by observing a topological Fermi arc above $E_F$ [Figs. 34(f) and 34(g)].

### *b. STM and STS*

In addition to ARPES, STM and STS have been employed to visualize the topological surface states of the $Mo_{1-x}W_xTe_2$ family (Zheng *et al.*, 2016a; Deng *et al.*, 2017; Zhang, Wu *et al.*, 2017; Rüßmann *et al.*, 2018). Take $Mo_{0.66}W_{0.34}Te_2$ as an example. First-principle calculations revealed four pairs of Weyl points in the BZ: two pairs are located at 15 meV above $E_F$ (W1), while the other two pairs sit at 62 meV (W2). Figure 35(a) shows the calculated surface states and projected bulk states on the (001) surface; the middle segments of the large semicircular contours are the surface Fermi arcs that connect the projection of Weyl nodes. Several scattering vectors can be identified from Fig. 35(a). Two dominant scattering vectors involving the projected Weyl pockets are $Q_1$, which connects the two electron Weyl pockets, and $Q_2$, which links the electron Weyl pocket and the topological trivial surface pocket; two dominant scattering processes involving the surface Fermi arcs are $Q_3$, which connects two Fermi-arc-derived surface contours, and $Q_4$, which links the Fermi arcs to the trivial surface state, as illustrated in Fig. 35(b). These scatterings form QPI patterns in the Fourier transform of conductance maps. By comparing the experimental QPI pattern [Fig. 35(d)] with the calculations

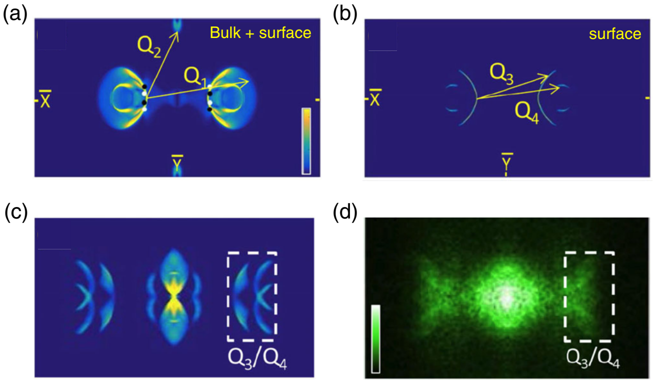

FIG. 35. (a) The calculated surface and projected bulk states of $Mo_{0.66}W_{0.34}Te_2$ (001) surface at $E = 50$ meV. The black and white dots represent the projected Weyl nodes with opposing chiralities. (b) Same as (a), but with only the surface states considered. (c) Calculated QPI patterns based on (b). (d) Experimental QPI patterns at $E = 50$ meV. The white dotted rectangles in (c) and (d) highlight the Fermi-arc-derived QPI patterns. Adapted from Zheng *et al.*, 2016a.

[Fig. 35(c)], Zheng *et al.* (2016a) unveiled the Fermi-arc-derived quantum interference patterns ($Q_3/Q_4$), signifying the existence of surface Fermi arcs. Furthermore, they also found that the contribution of bulk states to the QPI pattern (e.g., $Q_1/Q_2$) is negligible and interpreted as the signature of a pronounced topological sink effect; i.e., a surface electron from Fermi arcs can sink into the bulk Weyl cones due to a topological bulk-surface connection and thereby does not contribute to the surface standing waves.

### *c. Quantum transport*

Quantum transport measurements have intensively studied the $Mo_{1-x}W_xTe_2$ family. To begin, SdH oscillation measurements revealed multiple Fermi pockets, and large nonsaturating magnetoresistance manifested as the perfect compensation for electron and hole carriers (Ali *et al.*, 2014; Cai *et al.*, 2015; Zhao *et al.*, 2015a; Zhu *et al.*, 2015). The anisotropic chiral anomaly effect, a distinctive feature of type-II WSMs, was recently confirmed in gate-tunable $WTe_2$ thin flakes (Y. Wang *et al.*, 2016a), Fermi-level, delicately adjusted $WTe_{1.98}$ single crystals (Y.-Y. Lv *et al.*, 2017), CVD-grown $WTe_2$ nanosheets (E. Zhang *et al.*, 2017), and $WTe_2$ nanoribbons (Li, Wen *et al.*, 2017) through anisotropic NLMR observation.

As we know, in type-I WSMs the chiral-anomaly-induced NLMR always appears, regardless of the direction of the parallel magnetic field. In contrast, in type-II WSMs the chiral anomaly occurs only if the external magnetic field is applied along the direction where the kinetic energy of electrons is larger than their potential energy, e.g., the tilt direction of the Weyl cones. Indeed, the chiral-anomaly-induced NLMR is observed along the tilt direction of the Weyl cones (i.e., the $b$ axis) in $WTe_2$, whereas only positive longitudinal magnetoresistance is observed under the $B\|I\|a$-axis condition, as shown in Figs. 36(a) and 36(b). Note that the strength of the chiral anomaly contribution or the anomaly coefficient is determined by the energy location of the Weyl points, which can be tuned via gate voltage; therefore, the observation of gate-tunable NLMR in Figs. 36(a) and 36(c) further supports its chiral anomaly origin. Along with the anisotropic NLMR, an extraquantum oscillation (78 T), which is absent in the $WTe_2$ bulk form, was observed in $WTe_2$ nanoribbons in the presence of a perpendicular magnetic field ($B\|c$), as shown in Fig. 36(d). This oscillation was attributed to the Weyl orbit formed by the connection between the (001) surface Fermi arcs and the bulk Weyl points. Last, we point out that the PHE has been observed in both $WTe_2$ and $MoTe_2$ (Chen *et al.*, 2018; Wang, Gong *et al.*, 2018; Liang *et al.*, 2019); however, it is still under debate whether the observed PHE arises from the chiral anomaly.

## 3. Magnetic Weyl semimetals

The proposals of magnetic WSMs are not rare, and many materials have been predicted to be magnetic WSMs, such as $HgCr_2Se_4$ (G. Xu *et al.*, 2011), magnetic pyrochlores $A_2Ir_2O_7$ ($A$ = rare-earth element) (Wan *et al.*, 2011), $YbMnBi_2$ (Borisenko *et al.*, 2019), magnetic Heusler and half-Heusler compounds (Wang, Vergniory *et al.*, 2016; Chadov *et al.*, 2017), the antiferromagnetic $Mn_3Sn$ family (Yang, Sun *et al.*, 2017), the layered half-metal $Co_3Sn_2S_2$ (Xu, Liu *et al.*, 2018), and GdSI (Nie *et al.*, 2017). Despite so many proposals, experimental evidence has been scant. Recently the large intrinsic anomalous Hall conductivity, one of the distinct signatures of magnetic Weyl fermions, was observed in half-Heusler GdPtBi (Suzuki *et al.*, 2016; Shekhar *et al.*, 2018), $Mn_3Ge$ (Nakatsuji, Kiyohara, and Higo, 2015; Nayak *et al.*, 2016), and $Co_3Sn_2S_2$ (E. Liu *et al.*, 2018; Wang, Xu *et al.*, 2018), indicating the existence of Weyl fermions in these systems. In particular, recent ARPES and STS measurements have provided direct evidence for the existence of the magnetic Weyl semimetal phase in $YbMnBi_2$ (Borisenko *et al.*, 2019) and $Co_3Sn_2S_2$ (D. F. Liu *et al.*, 2019; Morali *et al.*, 2019) by identifying the characteristic surface Fermi arcs or linearly dispersed bulk Weyl cones.

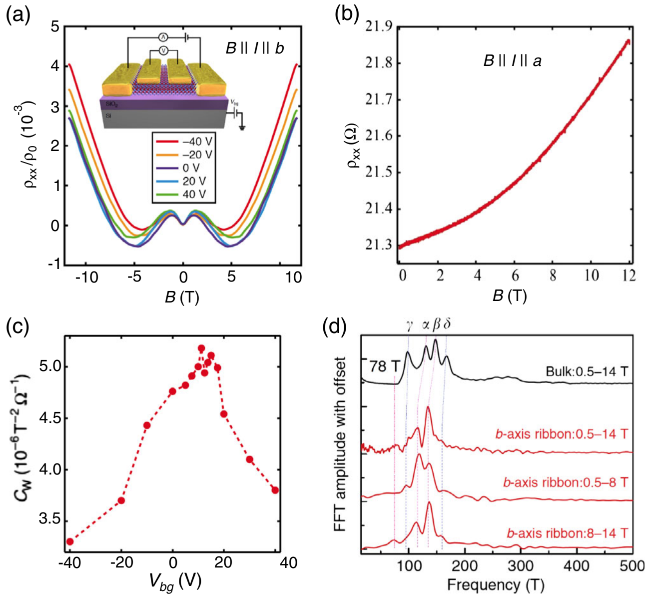

FIG. 36. (a) NLMR of a $WTe_2$ thin flake measured at various gate voltages under the $B\|I\|b$-axis condition. Inset: schematic structure of the gated four-probe devices. (b) Positive longitudinal magnetoresistance with current along the $a$ axis. (c) Chiral coefficient ($C_W$) extracted from (a), where the maximum value of $C_W$ indicates the crossing of the type-II Weyl points. (d) FFT spectra of the $b$-axis $WTe_2$ ribbon. An extra frequency of 78 T shows at $B > 8.0$ T relative to the bulk $WTe_2$. Adapted from Y. Wang *et al.*, 2016a, and Li, Wen *et al.*, 2017.

Take $Co_3Sn_2S_2$ as a representative. It crystallizes in a rhombohedral structure with the magnetic moments of cobalt atoms aligned along the $c$ direction. In the absence of SOC, there are several band inversions centered at the $L$ points, and these band inversions result in several nodal rings located at the three mirror planes in the BZ, as shown in Figs. 37(a) and 37(b). When SOC is taken into account, these nodal rings are gapped out and pairs of Weyl points appear off the high-symmetry line at ~60 meV above $E_F$. These Weyl points give rise to pairs of nontrivial surface Fermi arcs on the (001) surface, as shown in Fig. 37(c), which can be directly detected by ARPES. Indeed, ARPES measurements performed by D. F. Liu *et al.* (2019) visualized the surface Fermi arcs on the (001) Sn-terminated surface, as shown in Fig. 37(d). Furthermore, by *in situ* electron doping, the Fermi level was raised in $Co_3Sn_2S_2$, enabling direct observation of the bulk Weyl

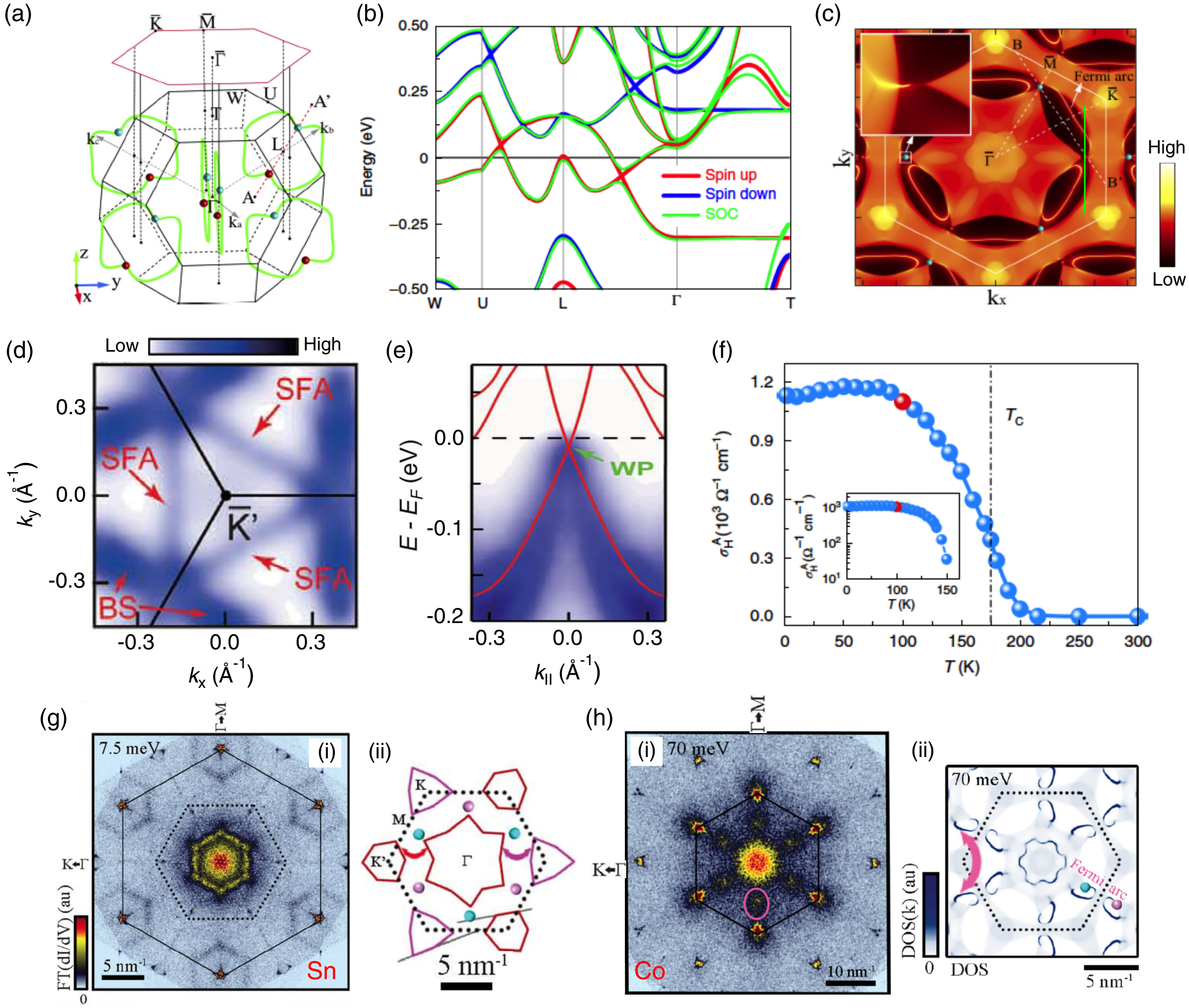

FIG. 37. (a) 3D bulk BZ (black) and the projected (001) surface BZ (red) of $Co_3Sn_2S_2$. The green lines and red and blue dots indicate the locations of the nodal lines and the Weyl points in the BZ. (b) Calculated band structures of $Co_3Sn_2S_2$ along high-symmetry lines with and without SOC. (c) Calculated spectral intensity maps for the (001) Sn-terminated surface of $Co_3Sn_2S_2$ at $E_F + 60$ meV. (d) ARPES intensity plots recorded with 124 eV photons. Red arrows indicate surface Fermi arcs (SFA). (e) ARPES intensity plot along the direction parallel to $k_y$ [green line in (c)], showing the linear band dispersion across the Weyl point. (f) Temperature-dependent anomalous Hall conductivity measured at zero magnetic field. Inset: logarithmic temperature dependence of $\sigma_H^A$. (g) Fourier transform of a $dI/dV$ map taken at $V_{\mathrm{bias}} = 7.5$ meV on the (001) Sn-terminated surface, showing hexagonal-shaped QPI patterns originating from the scattering processes involving Fermi arcs [pink arrows in (ii)] and surface-projected bands [red arrows in (ii)]. (h) Fourier transform of a $dI/dV$ map taken at $V_{\mathrm{bias}} = 70$ meV on the (001) Co-terminated surface showing QPI broad peaks along $\Gamma$-$M$ [marked with pink ellipses in (i)] that originate from the scattering processes involving the Fermi-arc bands [pink arrows in (ii)]. Adapted from E. Liu *et al.*, 2018, Xu, Liu *et al.*, 2018, D. F. Liu *et al.*, 2019, and Morali *et al.*, 2019.

points, as shown in Fig. 37(e). In addition to ARPES measurements, transport and STS measurements have also been performed and revealed the Weyl nodes induced by large anomalous Hall conductivity [Fig. 37(f)] (E. Liu *et al.*, 2018; Wang, Xu *et al.*, 2018) and the surface Fermi arcs on different surface terminations [Figs. 37(g) and 37(h)] (Morali *et al.*, 2019), respectively. Last, we mention that Yin *et al.* (2019) performed a systematic STS measurement and further observed a unique spin-orbit coupled flatband at $E_F$, which is associated with the Berry curvature field in $Co_3Sn_2S_2$.

### 4. Double and triple Weyl semimetals

Apart from traditional WSMs with a linear-dispersed Weyl cone and $C = \pm 1$, there are multiple WSMs in which the monopole charges of Weyl points are larger than unity. Two known examples are double and triple WSMs, with monopole charges of $\pm 2$ and $\pm 3$, respectively. Accordingly, the double (triple) Weyl nodes have quadratic (cubic) dispersions in two momentum directions and linear dispersion in the third direction. The double Weyl nodes, usually protected by $C_4$ or $C_6$ rotation symmetry, are predicted to be realized in

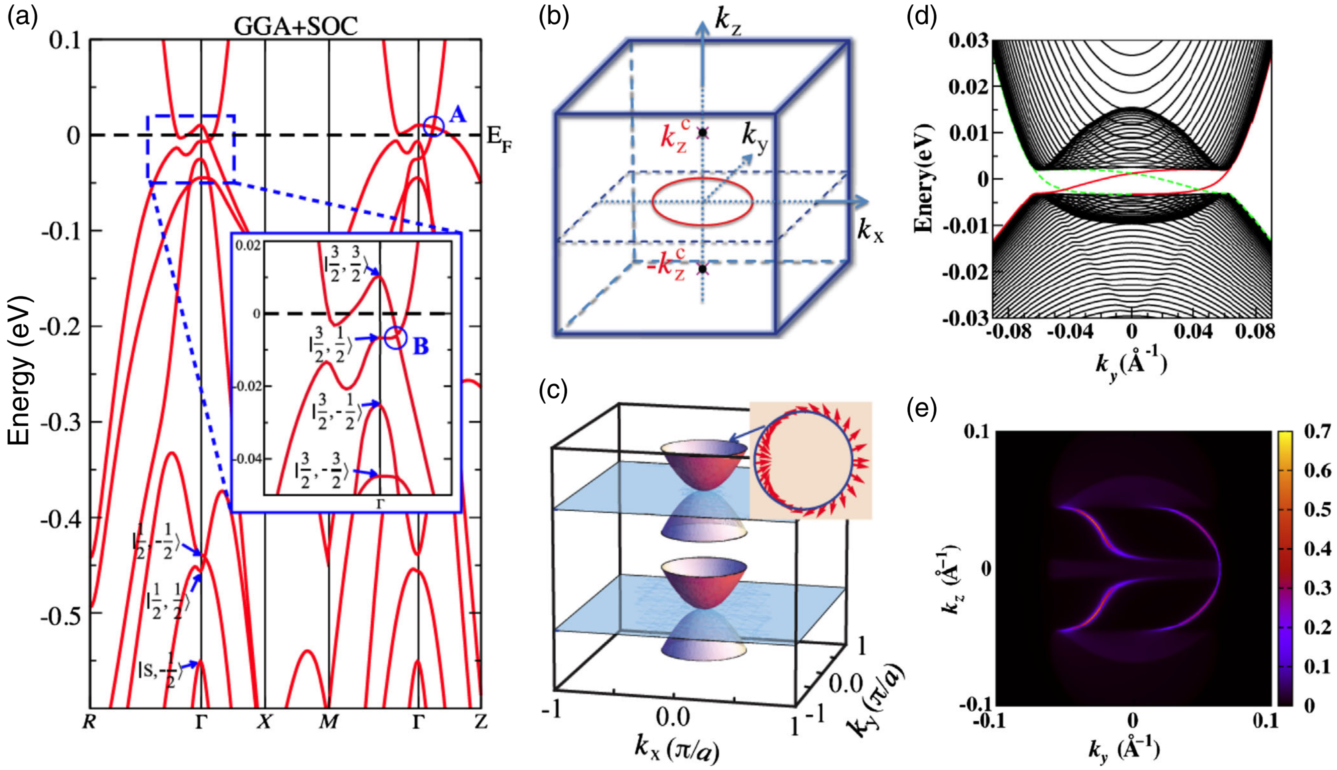

FIG. 38. (a) Calculated band structure of $HgCr_2Se_4$ after including SOC [with majority spin aligning to the $(001)$ direction]. Two kinds of band crossings (labeled A and B) are observed near $E_F$. (b) Band crossings in $k$ space. Crossing A gives rise to two isolated Weyl points along the $\Gamma$-$Z$ line, and the trajectory of crossing B is a closed loop surrounding the $\Gamma$ point along the $k_z = 0$ plane. (c) Schematic of the in-plane quadratic band dispersion around the Weyl nodes. Inset: chiral spin texture. (d) Calculated edge states for the plane with $k_z = 0.06\pi$. The red and green lines indicate the states located at different edges. (e) Calculated surface Fermi arcs for the $(k_y, k_z)$ side surface. From G. Xu *et al.*, 2011.

$HgCr_2Se_4$ in the ferromagnetic phase, with a pair of double Weyl nodes along the $\Gamma$-$Z$ direction (Fig. 38), as well as in $SrSi_2$ (Singh *et al.*, 2018). Conversely, the triple Weyl node can be protected only by the largest rotation symmetry, the $C_6$ symmetry, and it has not yet been realized in any material candidates. Multiple WSMs are expected to exhibit many distinct features. One direct consequence of multiple Weyl fermions is the existence of the same number of surface Fermi arcs on certain surfaces connecting the projection of two bulk Weyl nodes of opposite charges. Indeed, $HgCr_2Se_4$ exhibits double Fermi arcs on the side surface BZ, as shown in Figs. 38(d) and 38(e). Besides, since the multiple Weyl nodes are protected by $C_n$ invariance, an applied strain or magnetic field that breaks such symmetry can split a multiple Weyl node into several single Weyl nodes. Thus, multiple WSMs also offer a promising platform to examine quantum phase transitions.

### 5. Ideal Weyl semimetals

The first Weyl semimetal phase was discovered in the TaAs family, in which up to 12 pairs of Weyl nodes, as well as many trivial hole and electron Fermi pockets, coexist near the $E_F$. Such complicated electronic structures have led to many debates on the spectroscopic and transport properties, especially the origin of the NLMR. Therefore, to avoid such controversies and ensure the robustness of the Weyl fermion-induced features, it is desirable to find ideal and robust WSMs with simpler electronic structures. Generally, an ideal and robust Weyl semimetal should meet the following criteria: (i) It is a material with fewer pairs of Weyl nodes residing at $E_F$. (ii) Weyl points of opposite chirality are well separated in the momentum space. This large separation naturally guarantees large surface Fermi arcs. (iii) No other trivial band structures overlap with Weyl points near $E_F$. Several promising material candidates that fully or partly satisfy these criteria have been proposed. Jin *et al.* (2017) predicted that magnetic, with magnetization along the [110] direction, $\beta$-$V_2OPO_4$ is a promising ideal WSM, with a minimum number of two well-separated Weyl points, as well as long surface Fermi arcs for a $(001)$ surface. In addition to $\beta$-$V_2OPO_4$, magnetic GdSI is also predicted to be an ideal $\mathcal{T}$-breaking Weyl semimetal with two pairs of Weyl nodes residing at $E_F$ (Nie *et al.*, 2017). As for ideal $\mathcal{P}$-breaking WSMs, type-II WSM $TaIrTe_4$ (Koepernik *et al.*, 2016) has a minimum number of four Weyl points located close to $E_F$; however, many trivial states coexist with the Weyl points near $E_F$. Besides, the $CuTlTe_2$ family of materials provides promising type-I WSMs with four pairs of Weyl points sitting at $E_F$ (Ruan *et al.*, 2016). Furthermore, $Ta_3S_2$ (G. Chang *et al.*, 2016a) and the InSTl family of materials (Wang, Zhao *et al.*, 2017) are predicted to be robust WSM candidates with well-separated Weyl points and long surface Fermi arcs near $E_F$. Despite the previously mentioned proposals, ideal WSMs still await experimental evidence.

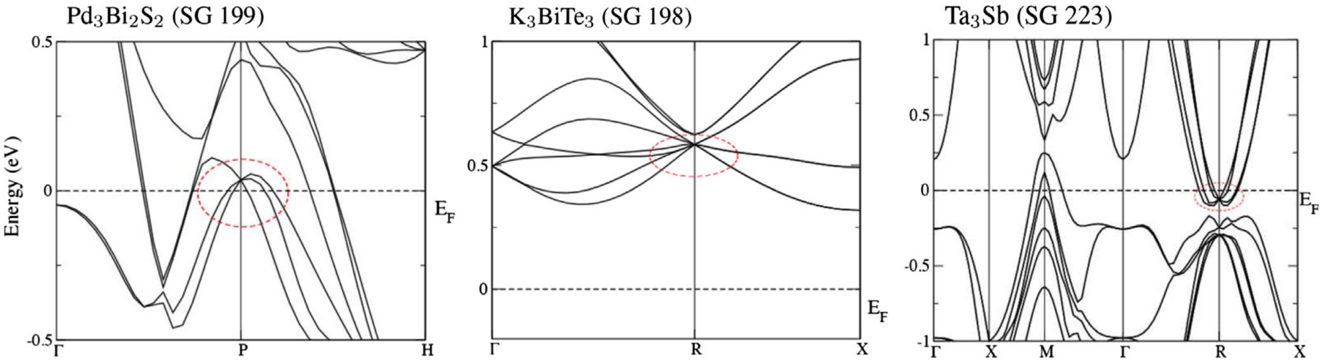

FIG. 39. The calculated band structures of the representative compounds $Pd_3Bi_2S_2$ (SG 199), $K_3BiTe_3$ (SG198), and $Ta_3Sb$ (SG 223) showing the existence of threefold, sixfold, and eightfold band degeneracies, respectively. From Bradlyn *et al.*, 2016.

We have discussed several distinctive types of WSMs, including type-I and type-II WSMs, magnetic WSMs, multiple WSMs, and ideal and robust WSMs. In addition, considerable groups of materials have also been proposed as WSMs, such as Kramer symmetry-enforced WSMs in chiral space groups (Chang *et al.*, 2018), Weyl-Kondo semimetals (Xu, Yue *et al.*, 2017), and Weyl ferroelectric semimetals (Di Sante *et al.*, 2016; He *et al.*, 2018).

### C. Unconventional fermions

#### 1. Nonsymmorphic symmetry-enforced unconventional fermions

As discussed in Sec. II.C.1, nonsymmorphic crystal symmetries can enforce threefold, fourfold, sixfold, and eightfold degeneracies at high-symmetry points. The low-energy excitations near the threefold band degeneracy, namely, three-component fermions, could also be regarded as spin-1 Weyl fermions, as they can be described by a higher spin generalization of the Weyl Hamiltonian $H = \boldsymbol{k} \cdot \mathbf{S}$, where instead of the spin-$1/2$ $2 \times 2$ Pauli matrices, $\mathbf{S}$ takes $3 \times 3$ spin-1 matrices. The spin-1 Weyl point carries a topological charge of $\pm 2$ (a derivation can be found in Appendix B.3) and can be viewed as a generalization of conventional spin-$1/2$ Weyl fermions. Similarly, $\mathbf{S}$ can also take $4 \times 4$ spin-$3/2$ matrices, and the quasiparticle excitations are called spin-$3/2$ Rarita-Schwinger-Weyl fermions, which correspond to fourfold band degeneracy and a monopole charge of $\pm 4$. The sixfold and eightfold fermions, on the other hand, can be viewed as doublings of spin-1 Weyl fermions and Dirac fermions, respectively.

First-principles calculations (Bradlyn *et al.*, 2016) have predicted the presence of these unconventional fermions in numerous materials with specific nonsymmorphic group symmetry. For example, $Pd_3Bi_2S_2$ in SG 199 has threefold band degeneracy at the $P$ point, $K_3BiTe_3$ in SG 198 exhibits sixfold band degeneracy at the $R$ point, and $Ta_3Sb$ in SG 223 can stabilize eightfold degeneracy at the $R$ point, as shown in Fig. 39. However, in many proposed material candidates, the multifold band degeneracies either are located far from $E_F$ or overlap in energy with the other trivial Fermi surfaces. Obtaining ideal material candidates with well-isolated band degeneracy at $E_F$ is still difficult.

Until 2018, transition-metal silicides in the CoSi family of materials (space group $P2_13$) were proposed to host various types of unconventional fermions owing to the chiral lattice (Tang, Zhou, and Zhang, 2017; Chang *et al.*, 2018; Zhang, Song *et al.*, 2018). As shown in Fig. 40(a), first-principles calculations without SOC suggest that CoSi exhibits two types of symmetry-protected unconventional crossings near $E_F$, one at the $\Gamma$ point with threefold degeneracy and the other at the $R$ point with fourfold degeneracy. The nodes at the $\Gamma$ and $R$ points carry nonzero Chern numbers of $\pm 2$, where the quasiparticle excitations are described as spin-1 Weyl fermions and charge-2 fourfold fermions, respectively. These two near-$E_F$ band crossings are well separated in the momentum space as they are pinned to the $\Gamma$ and $R$ points. They also do not overlap in energy with the other Fermi surfaces, suggesting that CoSi could provide a favorable platform for accessing the physical phenomena associated with these unconventional fermions using a variety of experimental techniques. Several ARPES groups (Rao *et al.*, 2019; Sanchez *et al.*, 2019; Takane *et al.*, 2019) first systematically studied the electronic structure of CoSi and directly observed the threefold-degenerate point and fourfold-degenerate point near $E_F$, as shown in Figs. 40(b) and 40(c). Because the threefold and fourfold nodes in CoSi carry Chern numbers of $\pm 2$, it is expected that two surface Fermi arcs emanate from their projections on certain surfaces. Specifically, on the $(001)$ surface, the $\Gamma$ and $R$ points are projected onto the center and corner of the surface BZ, respectively; therefore, there should be two Fermi arcs connecting the $\bar{\Gamma}$ and $\bar{M}$ points. These two surface Fermi arcs were directly observed using surface-sensitive VUV ARPES. As shown in Figs. 40(d) and 40(e), the measured Fermi surfaces at $h\upsilon = 75$ and 110 eV shows two surface Fermi arcs stretching diagonally across the entire $(001)$ surface BZ to connect the bulk FS pockets at the $\bar{\Gamma}$ and $\bar{M}$ points, which is consistent with expectations. The double Fermi arcs were further evidenced by their chiral band dispersions on the loop that encircles the projection of the charge-2 Weyl node, as shown in Fig. 40(f).

STM and STS measurements were performed on various surfaces of CoSi to characterize the Fermi arcs (Yuan *et al.*, 2019). Figure 40(g) summarizes the QPI pattern on the $(001)$ surface. By comparing it to simulations [Fig. 40(h)], Yuan *et al.* concluded that the eye-shaped features (yellow arrows) and the crescent-moon-shaped features (black arrows) resulted from the scattering between surface Fermi arcs, indicated by $q_1$ and $q_2$ in Fig. 40(i).

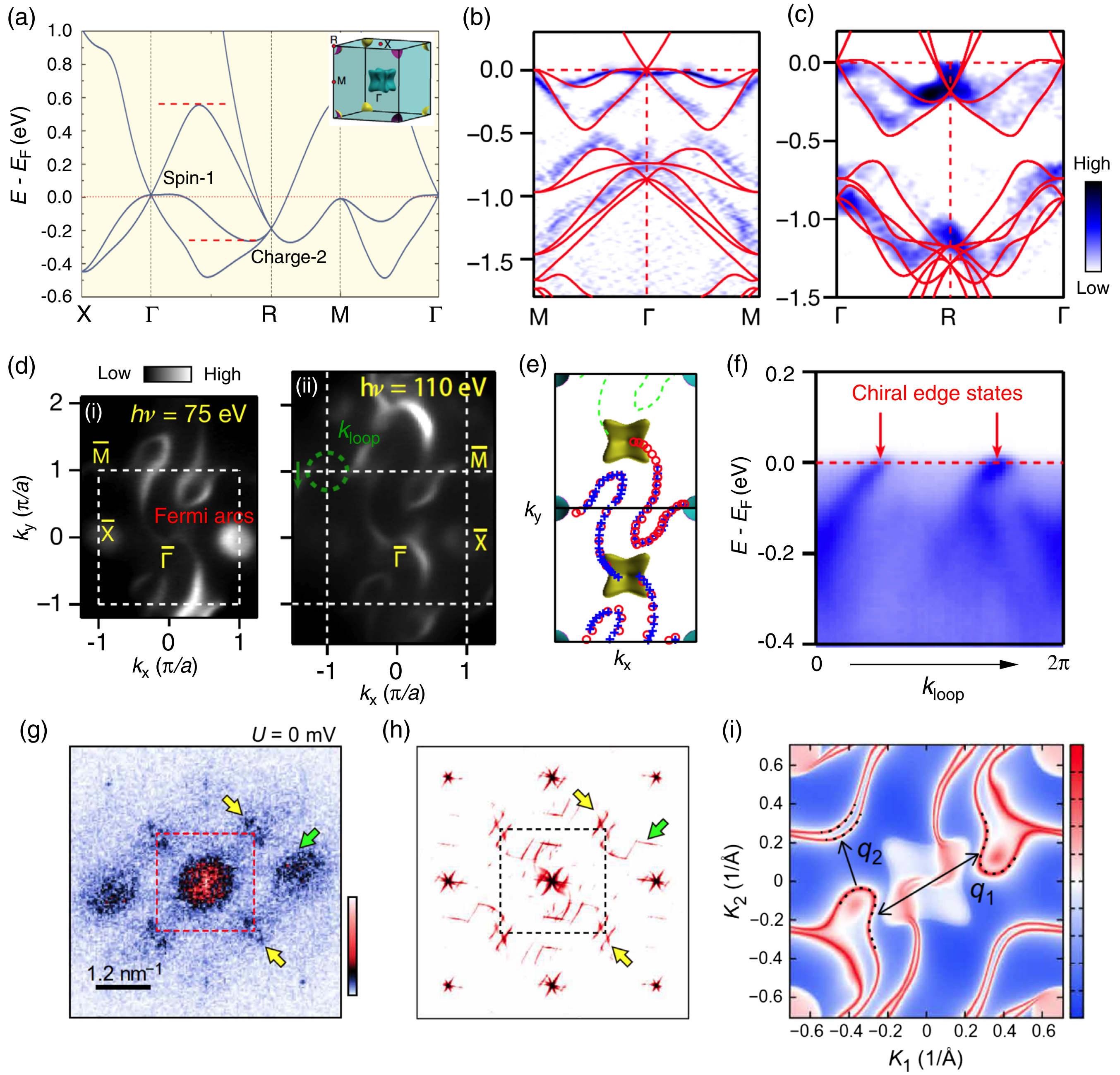

FIG. 40. (a) Calculated band structures of CoSi along high-symmetry lines without spin-orbit coupling. Inset: calculated 3D bulk Fermi surfaces. (b),(c) Curvature intensity plot of the ARPES data together with the calculated band structure (red curves) showing the band dispersions along the $R$-Γ-$R$ and $M$-Γ-$M$ directions, respectively. (d) ARPES intensity maps at $E_F$, measured with (i) $h\upsilon = 75$ eV and (ii) $h\upsilon = 110$ eV. (e) Surface Fermi arcs extracted from the ARPES intensity maps with 75 (blue dots) and 110 eV (red dots) photon energy showing the connection between the (001) surface projections of the bulk Fermi surfaces at $\bar{\Gamma}$ and $\bar{M}$. (f) ARPES intensity plot showing the chiral band dispersions on the closed loop indicated in (d). (g) Experimental QPI patterns taken on the (001) surface of CoSi at $U = 0$ mV. (h) Corresponding QPI simulations including SOC. The dotted rectangles in (g) and (h) mark the surface's first BZ, and the yellow and green arrows highlight the Fermi-arc-derived QPI patterns. (i) The calculated surface states of the CoSi (001) surface at $E_F$ with SOC included. Adapted from Tang, Zhou, and Zhang, 2017, Rao *et al.*, 2019, and Yuan *et al.*, 2019.

Several groups recently investigated the transport and optical responses of chiral fermions. Concretely, transport measurements revealed energy-dependent interband and intraband electron scatterings (Pshenay-Severin, Ivanov, and Burkov, 2018), and a large phonon-drag-induced Nernst effect in CoSi at intermediate temperatures (Xu *et al.*, 2019). As for the optical responses, the $\omega$-linear optical conductivity, a signature of linearly dispersed band crossings, was predicted and observed in RhSi, as shown in Fig. 41(a) (Li, Iitaka *et al.*, 2019; Sánchez-Martínez, de Juan, and Grushin, 2019; Maulana *et al.*, 2020). Besides, the fact that the two bulk nodes at the Γ and $R$ points have large energy separation in Co(Rh)Si makes it possible to realize a specific nonlinear optical phenomenon, the quantized CPGE. Specifically, under

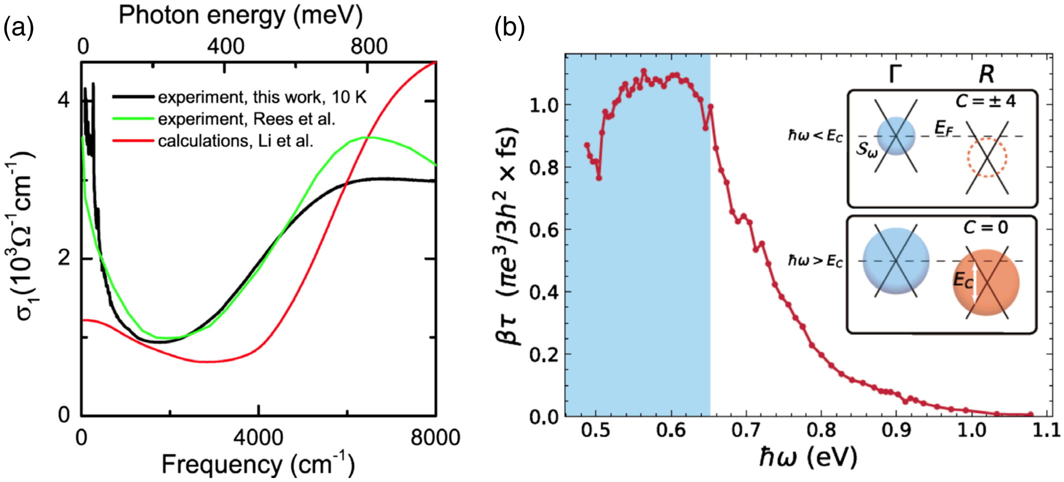

FIG. 41. (a) Experimental and calculated real part of the optical conductivity of RhSi. The linear-in-frequency region (below ~600 meV) was assigned to transitions between the linear crossing bands near the Γ and $R$ points. (b) Measured circular photogalvanic effect (CPGE) amplitude of RhSi as a function of photon energy. Inset: schematic photon-energy dependence of the CPGE, which is proportional to the total flux ($C$) of the Berry curvature passing through the surface $S_W$. For $\hbar w < E_c$ (blue shaded region), $S_W$ corresponds to a single surface enclosing the Γ point, and $C$ is thereby identical to the Chern number at the Γ point, i.e., 4. Above $E_c$, $S_W$ encloses two nodes of opposite chirality at the Γ and $R$ points, resulting in a zero $C$ and a vanishing CPGE. From Maulana *et al.*, 2020, and Rees *et al.*, 2020.

circularly polarized light the rate of photocurrent generation associated with optical transitions near a monopole is proportional to its charge (de Juan *et al.*, 2017; Flicker *et al.*, 2018). Recently the CPGE effect was reported in RhSi, as shown in Fig. 41(b) (Rees *et al.*, 2020). However, Rees *et al.* realized that the measured photocurrent rate is not precisely quantized to the monopole charge due to some specific factors, such as hot carries. The data reveal a current cutoff at 0.65 eV, which is in quantitative agreement with the prediction from the electronic structure.

We note that SOC was not considered in the previous discussion. When considering SOC, the bands split at arbitrary non-TRIM due to the lack of inversion symmetry, except for those at the BZ boundaries whose double degeneracy is protected by $\mathcal{T}$ and nonsymmorphic screw symmetries. Consequently, at the Γ point, the sixfold node is split by SOC into two crossing points with twofold and fourfold degeneracy, corresponding to a Weyl fermion and a spin-3/2 Rarita-Schwinger-Weyl fermion with $C = +4$. Similarly, at the $R$ point, the eightfold degeneracy point splits into sixfold and twofold degeneracy points, which give rise to double spin-1 fermions with $C = -4$ and Weyl fermions, respectively. However, this band splitting is of the order of meV, and thus the SOC effects can be ignored in the experimental work. Materials with heavy elements are desired to resolve the band splitting and charge-4 fermions. Indeed, recent soft x-ray ARPES measurements resolved the band splitting and the fourfold and sixfold band degeneracy in AlPt and PdBiSe (Lv *et al.*, 2019; Schröter *et al.*, 2019), providing evidence for the existence of spin-3/2 fermions and double spin-1 fermions in solids.

### 2. Symmorphic symmetry-protected unconventional fermions

Nonsymmorphic symmetries can enforce threefold, sixfold, and eightfold degenerate points at the TRIM. In addition to nonsymmorphic symmetries, the combination of band inversion and proper symmorphic crystal symmetries such as mirror and rotational symmetries can also protect the triply degenerate points on the high-symmetry lines. These triply degenerate points are accidental degeneracy points between the bands of one- and two-dimensional irreducible representations. They can be viewed as an intermediate species between twofold Weyl points and fourfold Dirac points. Three-component fermions exhibit many unique properties, such as Fermi surface Lifshitz transitions. As shown in Fig. 42(a), when the cut of the Fermi surfaces is placed above, between, and below the two triple points, one can observe two electron pockets, one hole pocket and one electron pocket, and two hole pockets, respectively. In other words, at each triple point a topological Lifshitz transition takes place. Another notable feature is that the Fermi surfaces touch near the triple points for arbitrary $E_F$ because the triple points are tied to one doubly degenerate nodal line. The Fermi surface touching may cause a "magnetic breakdown" in quantum oscillations whereby the semiclassical orbits become undefined as a result of tunneling between the touching Fermi surfaces (Weng *et al.*, 2016b). Moreover, these bulk electron or hole pockets near the triple points also have a topologically robust spin texture with a winding number of 2 (Weng *et al.*, 2016b).

Many material candidates have been predicted to host three-component fermions, such as materials in space group 187 with tungsten carbide-type structure (such as WC, MoP, TaN, and ZrTe) (Weng *et al.*, 2016a, 2016b; Zhu *et al.*, 2016; G. Chang *et al.*, 2017a), $InAs_{0.5}Sb_{0.5}$ (Winkler *et al.*, 2016), half-Heusler materials (Yang, Yu *et al.*, 2017), and the $NaCu_3Te_2$ family (Wang, Sui *et al.*, 2017). In particular, triple points have been observed in MoP and WC (B. Q. Lv *et al.*, 2017; Ma *et al.*, 2018). If we take WC as a representative, the calculated band structure shows two crossings between

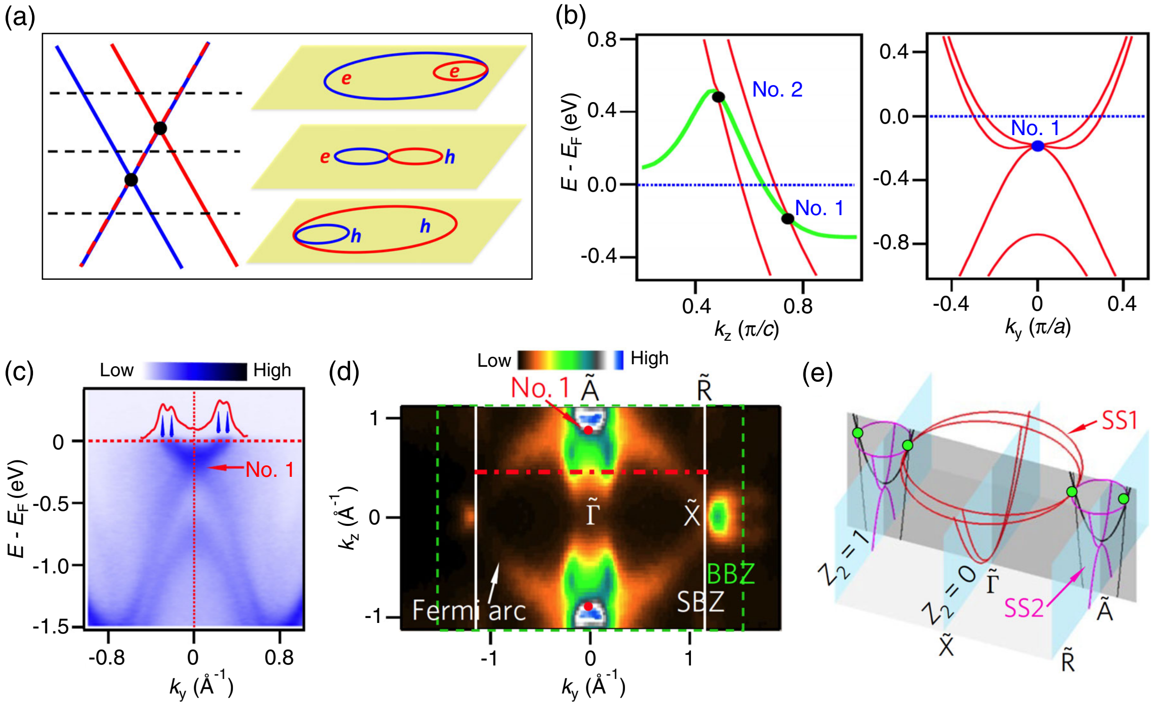

FIG. 42. (a) Schematics of the band structures of three-component fermions (left) and the equal-energy contours at three different energy cuts: below, between, and above the two triple points. (b) Calculated band structures of WC near the triple point with SOC. The black dots indicate the triple points. The green and red curves represent doubly degenerate and nondegenerate bands, respectively. (c) ARPES intensity plot of WC along the $k_y$ direction with $h\upsilon = 555$ eV (corresponds to the no. 1 triple point in WC). (d) ARPES intensity plot at $-200$ meV recorded with $h\upsilon = 555$ eV. The white and green rectangles indicate the $(100)$ surface BZ (SBZ) and the bulk BZ (BBZ) on the $k_x = 0$ plane, respectively. (e) Schematic of surface Fermi arcs (red and pink curves) connecting the surface projections of bulk TPs (green dots) on the $(100)$ surface as well as the surface-state (SS) bands along the $\tilde{\Gamma}$-$\tilde{X}$ and $\tilde{A}$-$\tilde{R}$ directions. Adapted from Ma *et al.*, 2018.

doubly degenerated bands and nondegenerated bands along the $\Gamma$-$A$ direction, as shown in Fig. 42(b). These two band crossings, namely, the triple points, are protected by a combination of mirror symmetry and $C_3$ rotational symmetries. Specifically, the no. 1 triple point, located close to $E_F$, has been directly visualized by soft x-ray ARPES, as shown in Fig. 42(c).

As discussed, the topological nature of the bulk nodes is usually characterized by Chern numbers. However, near the triple point the Chern numbers are undefined, as the triple point arises from the crossing between a nondegenerate band and a doubly degenerate band, and it is impossible to enclose it with a sphere on which the band structure is fully gapped. While the topological invariant for the triple point is an open question, the band topology within the $k_z = 0$ and $\pi$ planes can be identified by $Z_2$ topological invariants. The calculated $Z_2$ numbers for the $k_z = 0$ and $\pi$ planes are 0 and 1, respectively, which implies that the $k_z = \pi$ plane is a quantum spin Hall insulator plane and that topologically protected Dirac cone surface states should appear along the $\tilde{A}$-$\tilde{R}$ line of the $(100)$ surface BZ. Indeed, ARPES measurements show a surface Dirac cone (SS2) located at the $\tilde{A}$ point, with its upper and lower branches connected to the conduction and valence bands, respectively (Ma *et al.*, 2018). As summarized in Figs. 42(d) and 42(e), the surface states forming the topological Dirac cone emerges from a pair of Fermi arcs connecting the projection of the triple points, which is similar to the Fermi arcs in DSMs $Na_3Bi$ and $Cd_3As_2$. In addition to SS2, the ARPES data [Fig. 42(d)] show two other pairs of surface Fermi arcs (SS1) emerging from the triple point. However, they are not topologically protected, as $Z_2$ is zero for the $k_z = 0$ plane. Apart from pairs of Fermi arcs on the $(100)$ surface, other distinguished quantum phenomena have also been reported. Kumar *et al.* (2019) reported extremely low resistivity and high mobility of carriers in MoP, as shown in Fig. 43(a). He *et al.* (2017) observed an anisotropic magnetoresistivity in WC that shows NLMR only under the $B \| I \| x$ configuration [Fig. 43(b)], in contrast to the isotropic one in type-I Dirac points and WSMs.

We have summarized the unconventional fermions in $\mathcal{T}$-invariant nonmagnetic symmorphic and nonsymmorphic space groups. Recently Cano, Bradlyn, and Vergniory (2019) enumerated the unconventional band degeneracies that can occur in 1651 magnetic space groups and revealed that only threefold, sixfold, and eightfold degeneracies are possible (in addition to the conventional twofold and fourfold degeneracies), as in nonmagnetic space groups. They provided a list of space groups as well as several material candidates where these unconventional fermions can be realized, including three-component fermions in $Mn_3IrSi$, sixfold fermions in $Cu_3O_6Te$, and eightfold fermions in $Zr_2V_6Sb_9$. These results can serve as a foundation for finding multifold nodal fermions in realistic magnetic systems and exploring their topological phenomena, such as Fermi arcs,

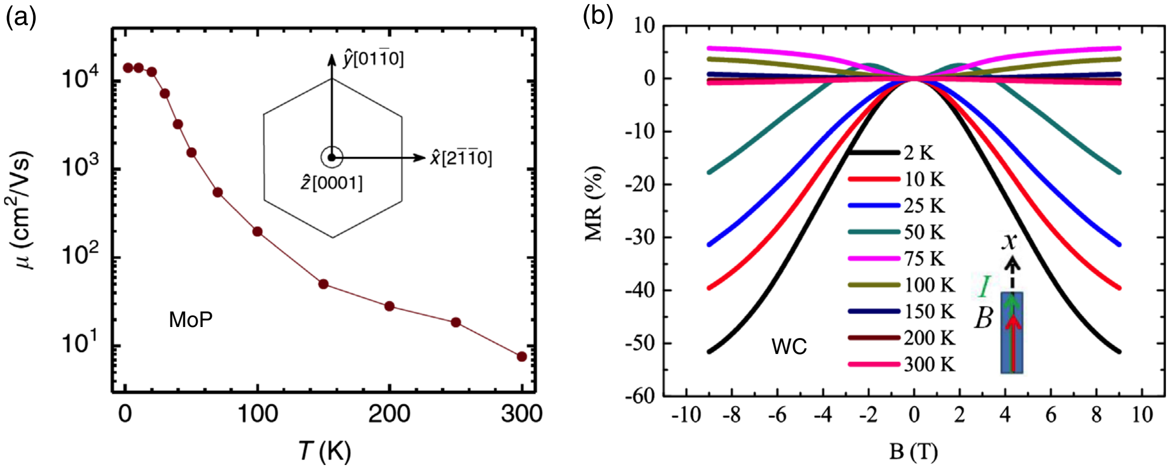

FIG. 43. (a) Temperature-dependent charge-carrier mobility of MoP. Inset: crystallographic directions in the hexagonal representation. (b) Longitudinal magnetoresistance of WC measured at various temperatures for $B\|I\|x$ (inset). Adapted from He *et al.*, 2017 and Kumar *et al.*, 2019.

large anomalous Hall conductances, and nonlinear optical responses.

## IV. TOPOLOGICAL NODAL-LINE AND NODAL-SURFACE SEMIMETALS

### A. Distinct features

In Sec. III, we discussed TSMs with 0D band crossings, i.e., discrete nodes. As we know, in addition to discrete points, the band crossing points can form 1D loops in 3D momentum space. Materials with such 1D band crossings at or close to $E_F$ are called topological nodal-line semimetals. Compared to Dirac and WSMs, TNLSMs manifest several distinct features:

(i) TNLSMs with 1D band crossings naturally have the 1D bulk Fermi surface, in contrast to the 0D Fermi surfaces of DSMs and WSMs.

(ii) In contrast to massless Weyl and Dirac cones, which have linear band dispersion in all $k$ directions, 1D nodal lines exhibit linear band dispersion only along directions perpendicular to the nodal line. As a result, the low-energy excitations of nodal-line semimetals are massless along the two transverse directions but massive along the direction tangent to the nodal lines. Therefore, nodal-line fermions have no counterpart of particles in high-energy physics. This unique electronic structure of nodal-line semimetals also gives rise to a higher density of states of low-energy excitations that is proportional to $|E-E_F|$, in contrast to the $(E-E_F)^2$-like density of states seen in WSMs. Consequently, stronger electron correlation effects are expected in nodal-line semimetals. It is predicted that the Coulomb interaction will be only partially screened, and long-range Coulomb interactions are expected due to the vanishing density of states at $E_F$ (Huh, Moon, and Kim, 2016).

(iii) Generally, topological materials can be associated with nontrivial topological invariants. For example, topological nodal point semimetals can be characterized by monopole charges. For TNLSMs, one can also associate each nodal line with a topological invariant whose form depends on the symmetry group that protects the nodal-line structure. Given the variety of symmetry groups that protect the nodal lines, different types of topological invariants can be found (Burkov, Hook, and Balents, 2011; Chiu and Schnyder, 2014; Fang *et al.*, 2015; Kim, Wieder *et al.*, 2015; Yu *et al.*, 2015; Fang, Weng *et al.*, 2016; Hyart, Ojajärvi, and Heikkilä, 2018), such as the $Z_2$ Berry phase or monopole charge or topological charge characterized nodal lines protected by $\mathcal{PT}$ symmetries, a mirror-reflection symmetry-protected nodal line with a $Z$ invariant and a nonsymmorphic symmetry-enforced nodal line with a $Z$ invariant.

To further elucidate the variety of topological invariants of nodal lines, we consider two of the simplest examples in spinless systems (neglecting the SOC). In the first example, consider a single nodal line on the mirror plane, as illustrated in Fig. 44(a). Since the nodal line is protected by the mirror symmetry, one can use the mirror eigenvalues as the topological invariant. One can pick two points $P_1$ and $P_2$ at the two sides of the nodal line and count the number of bands below $E_F$ that have mirror eigenvalues of $+1$, denoted as $N_1$ and $N_2$. The corresponding topological invariant is then given by $Z=|N_1-N_2|$. $Z=1$ indicates that the two crossing bands have opposing mirror eigenvalues, and the nodal line is topologically protected by the mirror symmetry. The other widely encountered topological invariant comes from the Berry phase. Specifically, in spinless systems with both $\mathcal{P}$ and $\mathcal{T}$ symmetries, it has been proven that the Berry phase along any closed loop must be quantized as an integer multiple of $\pi$. As a result, any loop encircling the nodal line has a nontrivial $\pi$ Berry phase,

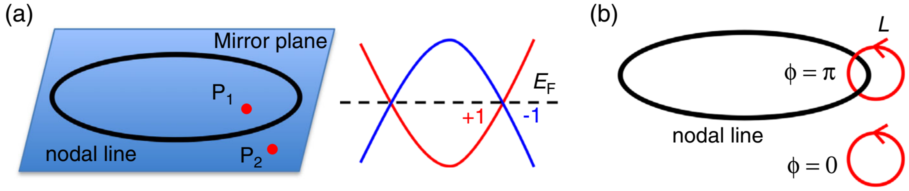

FIG. 44. (a),(b) Schematic illustration of the topological invariants of mirror-symmetry-protected and $\mathcal{PT}$-symmetry-protected nodal lines in spinless systems, respectively. The blue and red curves in (a) indicate the crossing valence and conduction bands of opposing mirror eigenvalues. The red circles and $\phi$ in (b) indicate the closed loop ($L$) and the corresponding Berry phases. Adapted from Fang, Weng *et al.*, 2016.

whereas the other loops have zero Berry phase, as these loops can smoothly shrink to an infinitesimal loop, which necessarily has zero Berry phase [Fig. 44(b)]. Therefore, one can take the $\pi$ Berry phase as a topological invariant to characterize the $\mathcal{PT}$-symmetric nodal lines in the absence of SOC. We point out that in addition to the $\pi$ Berry phase, the $\mathcal{PT}$-symmetric nodal lines can further carry a nonzero $Z_2$ monopole charge. Unlike the $\pi$ Berry-phase-protected nodal-line systems, in which a single nodal line can exist, the nodal lines with nonzero monopole charges can be created or annihilated only in pairs, in analogy to Weyl points (Fang, Weng *et al.*, 2016).

(iv) Crystallographic symmetries are necessary for stabilizing nodal lines. However, none of the symmetries that protected the nodal lines, including mirror reflection, inversion, and nonsymmorphic symmetries, are preserved on the surfaces. Therefore, the bulk-edge correspondence may not be applied to TNLSMs, and the surface states in TNLSMs are not topologically protected by bulk nodal lines. Nevertheless, TNLSMs are still accompanied by distinct surface states, which are embedded inside the gap between the conduction and valence bands in the surface projection of the bulk nodal lines. The distinguishing feature of these surface states is that they are flat in dispersion and are therefore referred to as "drumhead" surface states (Weng, Liang *et al.*, 2015). These drumhead surface states give rise to a large density of states at $E_F$; consequently, they could potentially realize high-temperature superconductivity, surface magnetism, or other interesting correlated effects on the surface (Heikkilä, Kopnin, and Volovik, 2011; Kopnin, Heikkilä, and Volovik, 2011). These drumhead surface states are not topologically protected, and a small perturbation to the surface will destroy the "flatness" of the surface bands and can even push the surface states into the bulk continuum spectrum.

(v) Finally, the unique bulk and surface electronic structures of TNLSMs have also been predicted to lead to interesting transport and optical phenomena, such as the nondispersive Landau-level spectrum (Rhim and Kim, 2015), distinct collective modes (Yan, Huang, and Wang, 2016), and a quasitopological electromagnetic response (Ramamurthy and Hughes, 2017).

One-dimensional nodal lines are not rare in condensed-matter systems. In recent years, various TNLSMs that can be distinguished based on the characteristics of nodal lines have been identified, such as crystal symmetry or generation mechanisms; the degeneracy of the band crossing, slope, and order of band dispersion; and the linking structure of multiple nodal lines. In the following, we review these characteristic features and some representative material candidates.

## B. Nodal lines in the absence of SOC

### 1. $\mathcal{PT}$-symmetry-protected nodal lines

Crystallographic symmetries play an important role in realizing 1D nodal lines. Without SOC, the combination of $\mathcal{T}$ symmetry and inversion or mirror symmetries can stabilize the 1D band crossings arising from band inversion. For $\mathcal{PT}$-symmetry-protected nodal lines, various materials have been theoretically proposed, including $Cu_3PdN$ (Kim, Wieder *et al.*,

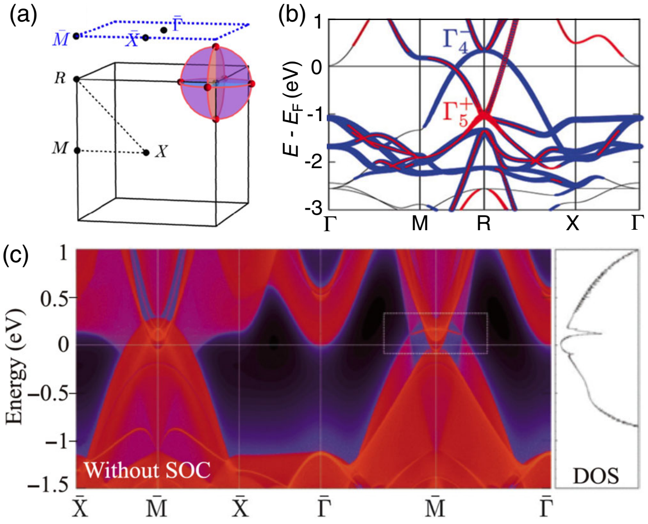

FIG. 45. (a) 3D bulk BZ and the projected (001) surface BZ of $Cu_3PdN$. The orange curves and red points indicate the locations of nodal rings and nodal points without and with SOC included, respectively. (b) Calculated band structures of $Cu_3PdN$ along high-symmetry lines without SOC. (c) Calculated surface band structures and density of states for (001) surface without SOC. Adapted from Yu *et al.*, 2015.

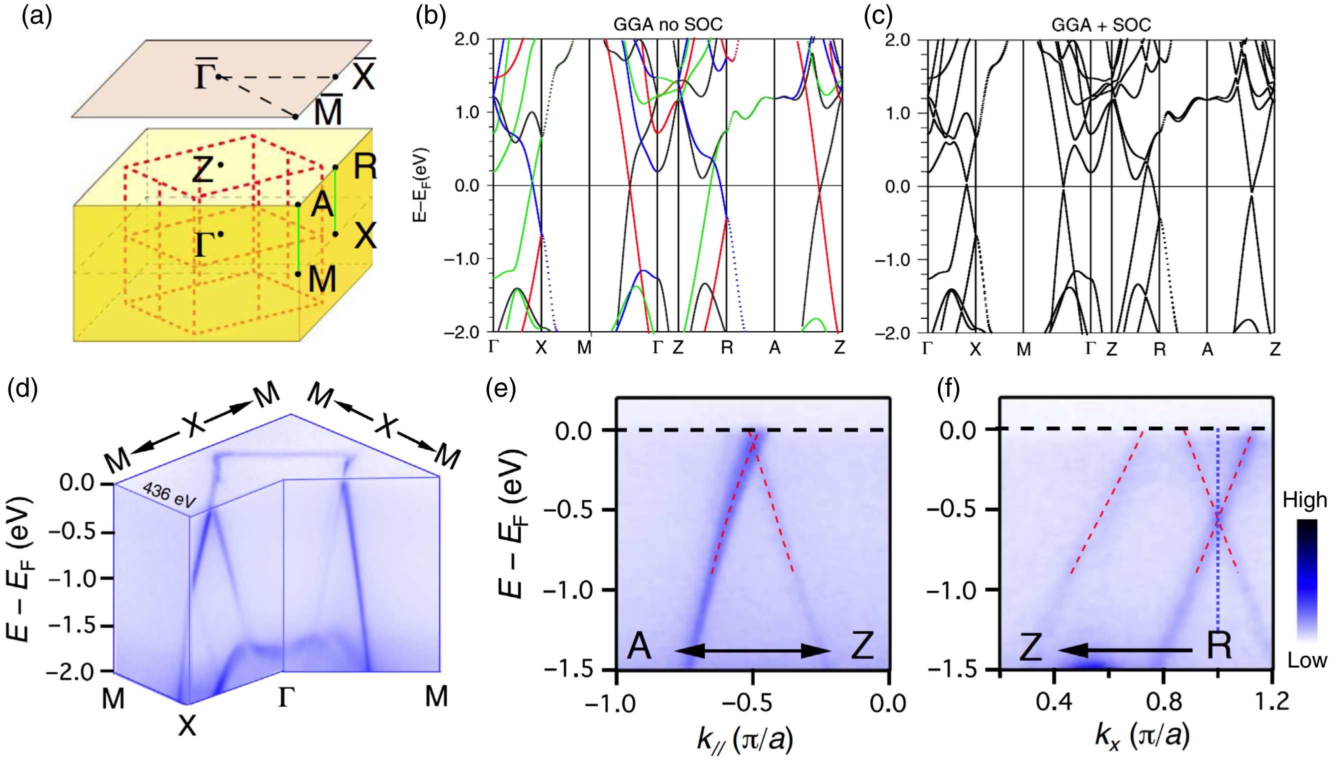

FIG. 46. (a) 3D bulk BZ and the projected (001) surface BZ of ZrSiS. The red dashed lines and yellow planes indicate the momentum locations of nodal lines and nodal surfaces without SOC. The green lines represent the Dirac nodal lines in the presence of SOC. (b),(c) Calculated band structures of ZrSiS along high-symmetry lines without and with SOC, respectively. Differently colored lines in (b) represent different irreducible representations. (d) 3D intensity plot of the ARPES spectra measured with $h\upsilon = 436$ eV showing the nodal-line structure in the $k_z = 0$ plane. (e),(f) ARPES intensity plots showing the band dispersion along the $A$-$Z$ and $Z$-$R$ directions, respectively. Adapted from Schoop *et al.*, 2016, and Fu *et al.*, 2019b.

2015; Yu *et al.*, 2015), graphene networks (Weng, Liang *et al.*, 2015), CaTe (Du, Tang *et al.*, 2017), compressed black phosphorus (Zhao *et al.*, 2016), the $CaP_3$ family (Quan, Yin, and Pickett, 2017; Xu, Yu *et al.*, 2017), La$X$ ($X = $ N, P, As, Sb, Bi) (Zeng *et al.*, 2015), $WHM$ ($W = $ Zr, Hf, or La; $H = $ Si, Ge, Sn, or Sb; $M = $ O, S, Se, and Te) (Schoop *et al.*, 2016) (nodal lines near $E_F$ are discussed later), and $Mg_3Bi_2$ (Zhang, Jin *et al.*, 2017). Take $Cu_3PdN$ as an example, without SOC included. Band inversion happens at the $R$ point, forming three nodal rings perpendicular to each other, as shown in Fig. 45. On the (001) surface, the nearly flat surface bands, namely, the drumhead surface states, which are nestled inside the projected node rings, can be seen around the $\bar{M}$ point.

### 2. Mirror-symmetry-protected nodal lines

#### a. Theoretical prediction and ARPES

As mentioned, mirror symmetry, including mirror reflection and mirror glide, can stabilize nodal lines on the mirror plane. Examples of mirror-reflection symmetry-protected nodal lines include TaAs (Weng, Fang *et al.*, 2015), $Ca_3P_2$ (Xie *et al.*, 2015; Chan, Chiu *et al.*, 2016), CaAgAs (Yamakage *et al.*, 2016), and HfC (Yu, Wu *et al.*, 2017). In TaAs, the band inversion leads to 12 nodal rings in the two mirror planes, which allows the two crossing bands to have two different irreducible representations, as shown in Fig. 24(c).

Similarly, many materials with mirror-glide symmetry-protected nodal lines have also been predicted, such as $SrIrO_3$ (Chen, Lu, and Kee, 2015), $WHM$ ($W = $ Zr, Hf, or La; $H = $ Si, Ge, Sn, or Sb; $M = $ O, S, Se, and Te) (Schoop *et al.*, 2016), and $IrO_2$ (Sun, Zhang *et al.*, 2017). Among these, the most well-studied materials are $WHM$. Take ZrSiS as a representative. It is a tetragonal PbFCl-type compound with nonsymmorphic space group $P4/nmm$ (no. 129). The crystal structure includes the $\mathcal{PT}$, $C_{2v}$, $\{C_{2x}|(1/2,0,0)\}$ and $\{C_{2y}|(0,1/2,0)\}$ screw, and mirror-glide $\{M_Z|(1/2,1/2,0)\}$ symmetries, which are required for protecting the nodal-line structures in ZrSiS. Figures 46(b) and 46(c) display the calculated bulk electronic structure of ZrSiS without and with SOC. Without SOC, several Dirac-like band crossings can be identified near $E_F$, e.g., along the $\Gamma$-$X$, $\Gamma$-$M$, $Z$-$R$, and $Z$-$A$ high-symmetry lines. These near-$E_F$ band crossings, protected by the mirror-glide and $C_{2v}$ symmetries, together form multiple interconnected nodal lines in the BZ, as displayed in Fig. 46(a) (red dashed lines). In addition, the screw and mirror-glide symmetries enforce band degeneracies in the $k_x = \pi$ and $k_y = \pi$ planes [the yellow planes in Fig. 46(a)]. However, these band degeneracies are located relatively far from $E_F$. Note that the band degeneracies in the yellow planes are different from those near-$E_F$ 1D nodal lines in the sense that they have Dirac-like band dispersions along only one $k$ direction that is transverse to the plane, such as the $\Gamma$-$X$ or $Z$-$R$ direction. Such band degeneracies, located at the 2D BZ boundaries, give rise to Dirac nodal surfaces, as discussed later.

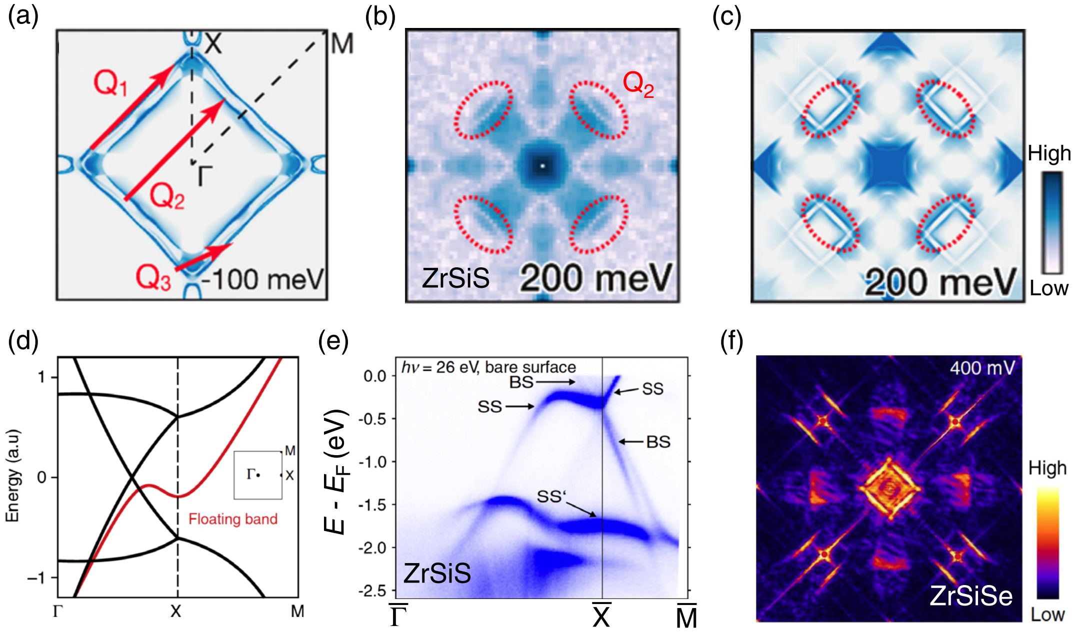

FIG. 47. (a) Calculated surface spectral weight of ZrSiS at $E_F - 100$ meV illustrating the possible scattering vectors. (b), (c) Experimental and $T$-matrix-calculated QPI patterns of ZrSiS at $E_F + 200$ meV, respectively. (d) Schematic illustration of the bulk nodal lines (black curves) and surface floating band (red curves) of ZrSiS without SOC. (e) ARPES intensity plot of a bare ZrSiS surface showing the high-intensity surface states (SS and SS′) and the bulk bands (BS). (f) Experimental single-defect-induced QPI patterns of ZrSiSe measured at $E_F + 400$ meV. Adapted from Lodge *et al.*, 2017, Topp *et al.*, 2017, and Zhu *et al.*, 2018.

Experimentally, the electronic structures of *WHM* have been explored extensively by ARPES measurements (Lou *et al.*, 2016; Neupane *et al.*, 2016; Schoop *et al.*, 2016; Chen *et al.*, 2017; Topp *et al.*, 2017; Hosen *et al.*, 2018). In particular, we note that the bulk nodal lines and nodal surfaces of ZrSiS were recently verified by bulk-sensitive soft x-ray ARPES (Fu *et al.*, 2019b). Figures 46(d)–46(f) summarize the measured electronic structure in the $k_z = 0$ and $\pi$ planes. The band crossings along the $\Gamma$-$X$, $\Gamma$-$M$, and $Z$-$A$ directions can be resolved, providing direct evidence of the mirror-glide symmetry-protected Dirac nodal lines in the $k_z = 0$ and $\pi$ planes. Moreover, the observation of Dirac points at the $X$ and $R$ points indicate the existence of nodal surfaces in ZrSiS.

Note that when SOC is turned on, all the near-$E_F$ Dirac nodal lines are gapped out. Similarly, most of the band degeneracies in the two nodal surfaces also split after the inclusion of SOC. However, the nonsymmorphic-protected crossings along the $A$-$M$ and $R$-$X$ directions [Fig. 46(a)] are robust against SOC, giving rise to two nodal lines, although the nodal line is buried below $E_F$. In practice, the SOC-induced band gaps (~20 meV) and band splitting are small and can be ignored in experiments.

### *b. STM and STS*

The electronic topology and band-selective scattering of *WHM* have been visualized using STM and STS measurements (Butler *et al.*, 2017; Lodge *et al.*, 2017; Bu *et al.*, 2018; Jiao *et al.*, 2018; Su *et al.*, 2018; Zhu *et al.*, 2018). Lodge *et al.* (2017) performed STS measurements on ZrSiS at 4.5 K and resolved the QPI arising from scattering and interactions with single-atom defects, as shown in Figs. 47(a)–47(c). In particular, they observed a split feature of the $Q_2$ vector [red ellipses in Fig. 47(b)] at energy close to the line node (~200 meV above $E_F$). This splitting, consisting with the $T$-matrix calculation [Fig. 47(c)], provides evidence of pseudospin conservation near the line nodes. As discussed, in *WHM* the nonsymmorphic symmetries enforce bulk band degeneracies along the $k_x = \pi$ and $k_y = \pi$ planes, such as the $X$-$M$ line shown in Fig. 47(d). However, the nonsymmorphic symmetries break at the surface and give rise to a unique floating surface state [the red curves in Fig. 47(d)], which has been directly visualized by ARPES measurements, as shown in Fig. 47(e). In addition to the ARPES measurements, a recent STS study (Zhu *et al.*, 2018) of ZrSiSe also identified the characteristic properties of the floating band surface state, i.e., rotational symmetry breaking interference near $E_F$ and the healing effect at a higher bias (~400 meV), and half-missing Umklapp scattering manifests as a double-parallel arc QPI pattern near the Bragg point [Fig. 47(f)].

### *c. Quantum transport*

The previously mentioned calculated electronic structure and ARPES results show that the nodal lines are the only feature near $E_F$, making ZrSiS a promising platform for studying the physical properties governed by Dirac nodal-line fermions. Indeed, several interesting transport phenomena have been found in this material system. One popular feature is the so-called butterfly-shaped angular magnetoresistance (Ali *et al.*, 2016; X. Wang *et al.*, 2016; H. Pan *et al.*, 2018; Chiu *et al.*, 2019), which shows a maximum when the applied current and magnetic field form an angle of 45°, as shown in Fig. 48(a). A recent quantum oscillation study revealed some high-frequency oscillations induced by magnetic breakdown across gaps along the nodal loop, as shown in

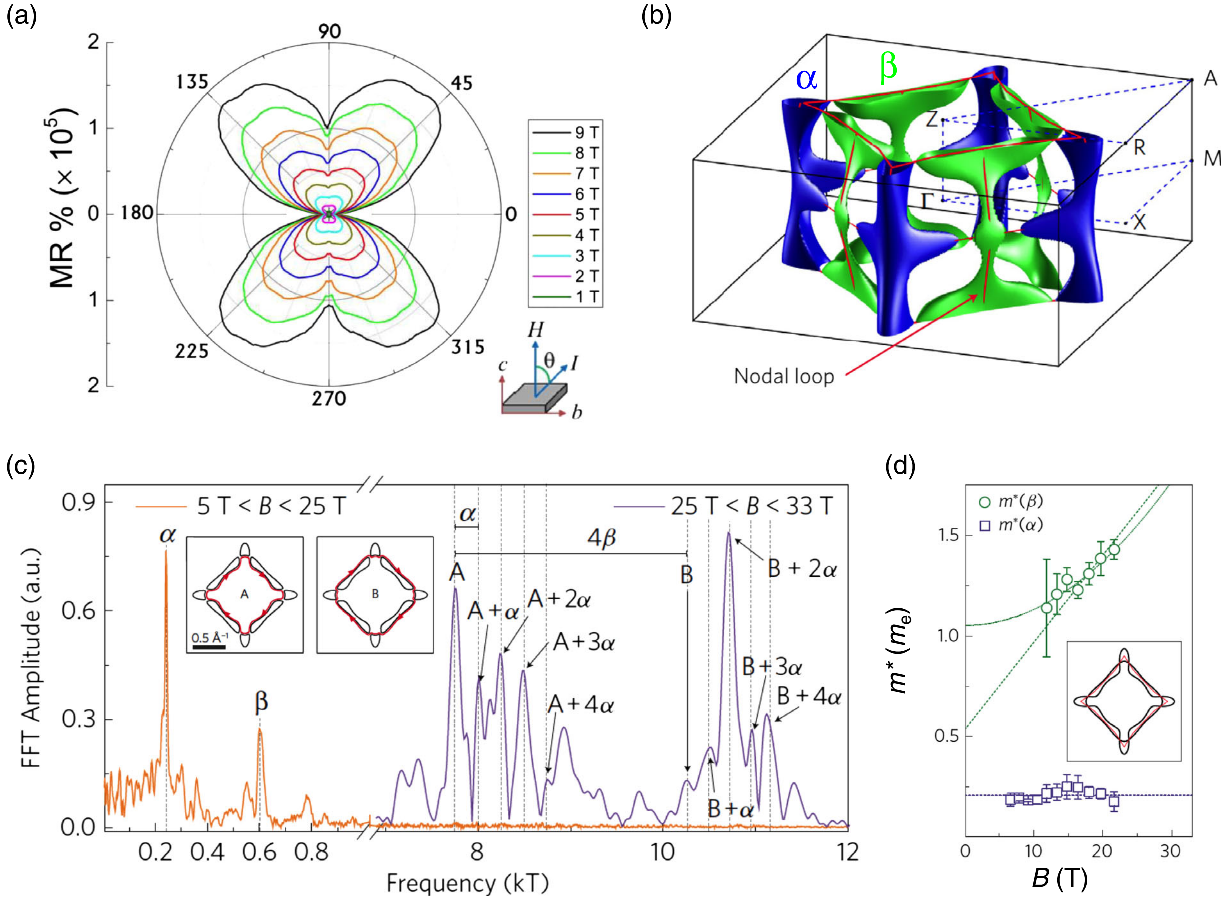

FIG. 48. (a) Polar plot of the angular magnetoresistance of ZrSiS measured at different magnetic fields. (b) Calculated FSs of ZrSiS in the 3D bulk BZ. (c) Fast Fourier transform of the magnetoresistance sweep at $T = 1.5$ K. $\alpha$ and $\beta$ represent the frequencies of the hole and electron pockets [indicated in (b)], respectively. Labels A and B correspond to the “inner” and “outer” breakdown orbits, respectively, as illustrated in the inset. (d) Field-dependent effective masses for the $\alpha$ and $\beta$ pockets. The dashed and dotted lines are guides for the eye under the assumption that the zero-field mass is unrenormalized or renormalized, respectively. Adapted from Ali *et al.*, 2016, and Pezzini *et al.*, 2018.

Figs. 48(b) and 48(c). Pezzini *et al.* (2018) also observed an unconventional mass enhancement around the nodal loop [Fig. 48(d)], demonstrating strong correlation effects associated with the Dirac-like quasiparticles in ZrSiS. Other interesting phenomena such as large nonsaturating magnetoresistance (Sankar *et al.*, 2017; Singha *et al.*, 2017), the nontrivial $\pi$ Berry phase as a consequence of Dirac-type band dispersions (Hu *et al.*, 2016b; Kumar *et al.*, 2017), and strong Zeeman splitting (Hu *et al.*, 2017) have also been revealed.

### d. Optical spectroscopy

Dirac and Weyl fermions in solids are known to manifest themselves in unique transport and optical responses. For example, the interband optical response of linearly dispersed $d$-dimensional Dirac and Weyl bands is expected to follow a power-law frequency dependence, i.e., $\sigma_1(\omega) \propto \omega^{d-2}$ (Hosur, Parameswaran, and Vishwanath, 2012; Ashby and Carbotte, 2013; Bácsi and Virosztek, 2013; Timusk *et al.*, 2013). Specifically, 2D and 3D Dirac fermions give rise to an $\omega$-independent and an $\omega$-linear $\sigma_1$, respectively. Equivalently, nodal lines exhibit distinct optical phenomena. In the simplest case, consider an energy-flat, gapless, and electron-hole-symmetric nodal line, the corresponding $\sigma_1(\omega)$ under a perpendicular electric-field component of the probing light ($E \perp k_{\text{line}}$) is predicted to be (Kotov and Lozovik, 2016; Ahn, Mele, and Min, 2017; Barati and Abedinpour, 2017; Carbotte, 2017; Mukherjee and Carbotte, 2017)

$$\sigma_1(\omega) = \frac{e^2 k_0 N}{16h} \Theta\{\hbar\omega - 2E_F\}, \tag{18}$$

where $k_0$ is the length of the nodal-line, $N$ is the degeneracy of the nodal-line, $e$ is the electron charge, $h$ is Planck’s constant, and $\Theta\{x\}$ is the Heaviside step function. From Eq. (18), one can conclude that $\sigma_1(\omega)$ is frequency independent for a flat nodal line, as shown in Fig. 49(a). Note that Eq. (18) assumes $E \perp k_{\text{line}}$; conversely, if $E \| k_{\text{line}}$, $\sigma_1(\omega)$ vanishes. More generally, when we consider an energy-dispersive and gapped nodal line, Eq. (18) is replaced by (Shao *et al.*, 2019)

$$\sigma_1{}^i(\omega) = \frac{e^2 N}{16h} k_0(\omega) \frac{v_i^2}{v_1 v_2} \left(1 + \frac{4\Delta^2}{\omega^2}\right) \Theta\{\hbar\omega - 2\Delta_{\text{op}}\}, \tag{19}$$

where $v_i$ is the asymptotic velocity along the $E$ direction, $k_0(\omega)$ is the effective length of the nodal line where the

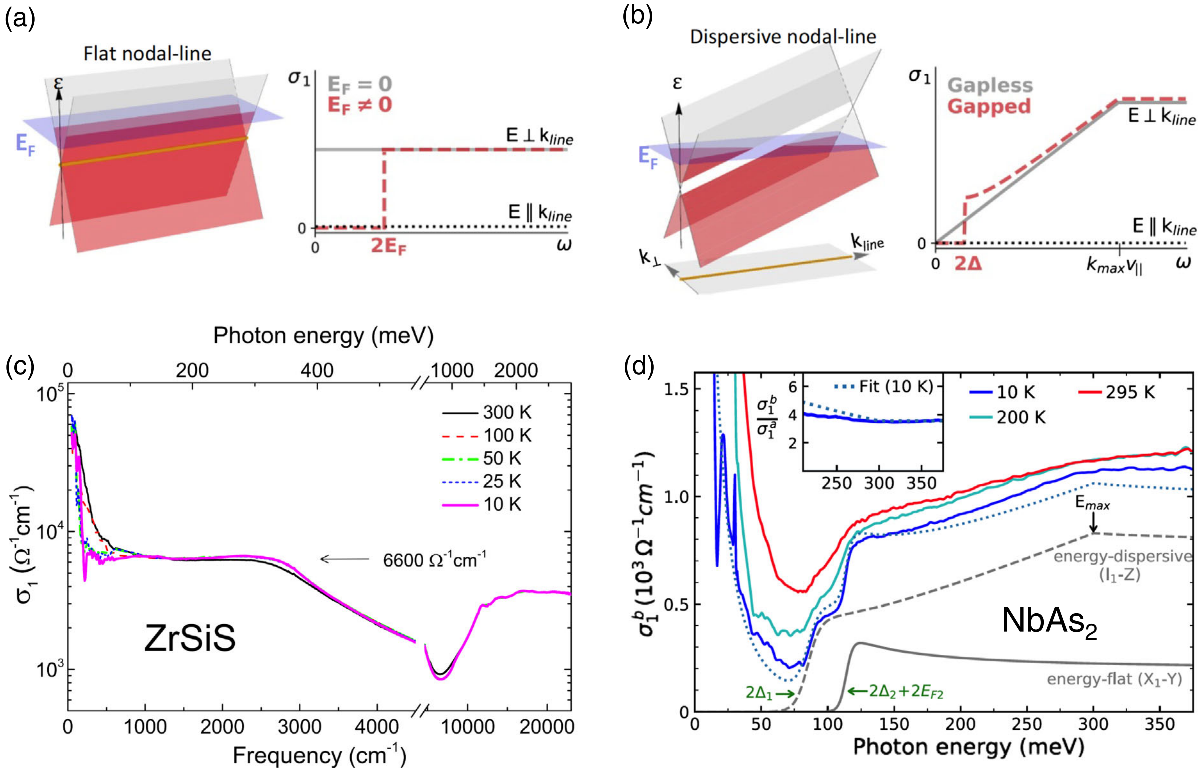

FIG. 49. (a) Schematic illustrations of the electronic structure and the corresponding $\sigma_1(\omega)$ for (a) energy-flat and (b) energy-dispersive nodal lines. $E$ and $k_{\rm line}$ denote the direction of the electric field and the nodal line, respectively. 2Δ in (b) denotes the gap induced by SOC, and $k_m axv_\parallel$ indicates the threshold of the $\omega$-linear region. (c) $\sigma_1(\omega)$ of ZrSiS measured at various temperatures. (d) Real part of the optical conductivity of NbAs$_2$ for $E \| b$. The blue dotted line is the fit to ${\sigma_1}^b(\omega)$ at 10 K. Gray dashed and solid lines represent the contributions from the energy-dispersive and energy-flat nodal lines, respectively. Inset: ratio ${\sigma_1}^b(\omega)/{\sigma_1}^a(\omega)$ above the gap region. Adapted from Schilling *et al.*, 2017, and Shao *et al.*, 2019.

interband transition takes place, 2Δ is the SOC-induced energy gap, and $2\Delta_{\rm op} = 2(\Delta + E_F)$ is the optical gap. Again, along the nodal-line direction $v_3 = 0$ ${\sigma_1}^3(\omega)$ thereby vanishes. Put simply, if the nodal line is linearly energy dispersed, $k_0(\omega)$ is found to be $k_0(\omega) = \omega/v_\parallel$, where $v_\parallel$ corresponds to the slope of the energy shift along the nodal line. The corresponding ${\sigma_1}^i(\omega)$ is thereby given by ${\sigma_1}^i(\omega) \sim (v_i^2/v_1 v_2)\omega$. Note that this $\omega$-linear behavior is valid only in a certain frequency range. In other words, when the entire dispersive nodal line is photon activated above a certain photon energy ($E > k_{\rm max} v_\parallel$), $\sigma_1^i(\omega)$ becomes $\omega$ independent, as shown in Fig. 49(b).

Experimentally, the flat or $\omega$-linear $\sigma_1(\omega)$ has been confirmed in several nodal-line materials, including ZrSiS (Schilling *et al.*, 2017; Ebad-Allah *et al.*, 2019), YbMnSb$_2$ (Qiu *et al.*, 2019), and NbAs$_2$ (Shao *et al.*, 2019). Figure 49(c) shows the measured $\sigma_1(\omega)$ for ZrSiS. One can see that $\sigma_1(\omega)$ is nearly $\omega$ independent in a broad range of 250 to 2500 cm$^1$. Such flat optical conductivity was fairly assigned to the transitions between the quasi-2D nodal-line Dirac bands near $E_F$ (Schilling *et al.*, 2017). On the other hand, in another compound NbAs$_2$, which hosts both energy-flat and energy-dispersive gapped nodal lines, a more complex $\sigma_1(\omega)$ with steps was observed, as shown in Fig. 49(d). Shao *et al.* (2019) found that the low-temperature (10 K) $\sigma_1(\omega)$ can be well fitted by Eq. (19) by considering interband transitions from both the dispersive and flat nodal lines. This observation thus demonstrates the existence of nodal lines in NbAs$_2$.

### C. Nodal lines in the presence of SOC

#### 1. Mirror-symmetry-protected Weyl nodal lines

As clarified in Sec. II.C.1, in the presence of SOC the nodal-line state can transform into a trivial insulator, TI, DSM, WSM, or triple point semimetal state, depending on the crystal symmetries and the strength of SOC. Specifically, two types of nodal lines can be stabilized in the presence of SOC, i.e., the mirror-symmetry-protected Weyl nodal lines and nonsymmorphic symmetry-enforced Dirac nodal lines. Mirror-symmetry-protected Weyl nodal lines can be stabilized in the systems with breaking of either $\mathcal{P}$ or $\mathcal{T}$ symmetry, and material candidates include HgCr$_2$Se$_4$ (G. Xu *et al.*, 2011), Pb(Tl)TaSe$_2$ (Bian *et al.*, 2016), KCu$_2$EuTe$_4$ (Yang, Yang *et al.*, 2018), and InNbS$_2$ (Du, Bo *et al.*, 2017). When the magnetization is along the [001] axis, the $\mathcal{T}$-breaking HgCr$_2$Se$_4$ hosts a Weyl nodal line inside the $k_z = 0$ mirror plane, as shown in Fig. 38(b). On the other hand, in noncentrosymmetric PbTaSe$_2$ without inversion symmetry, two Weyl nodal rings appear within the $k_z = \pi$ mirror plane around the $H$ point when SOC is included, as shown in Fig. 50. SOC also gives rise to another accidental nodal ring centered at the $K$ point on the $k_z = 0$ plane. The ARPES

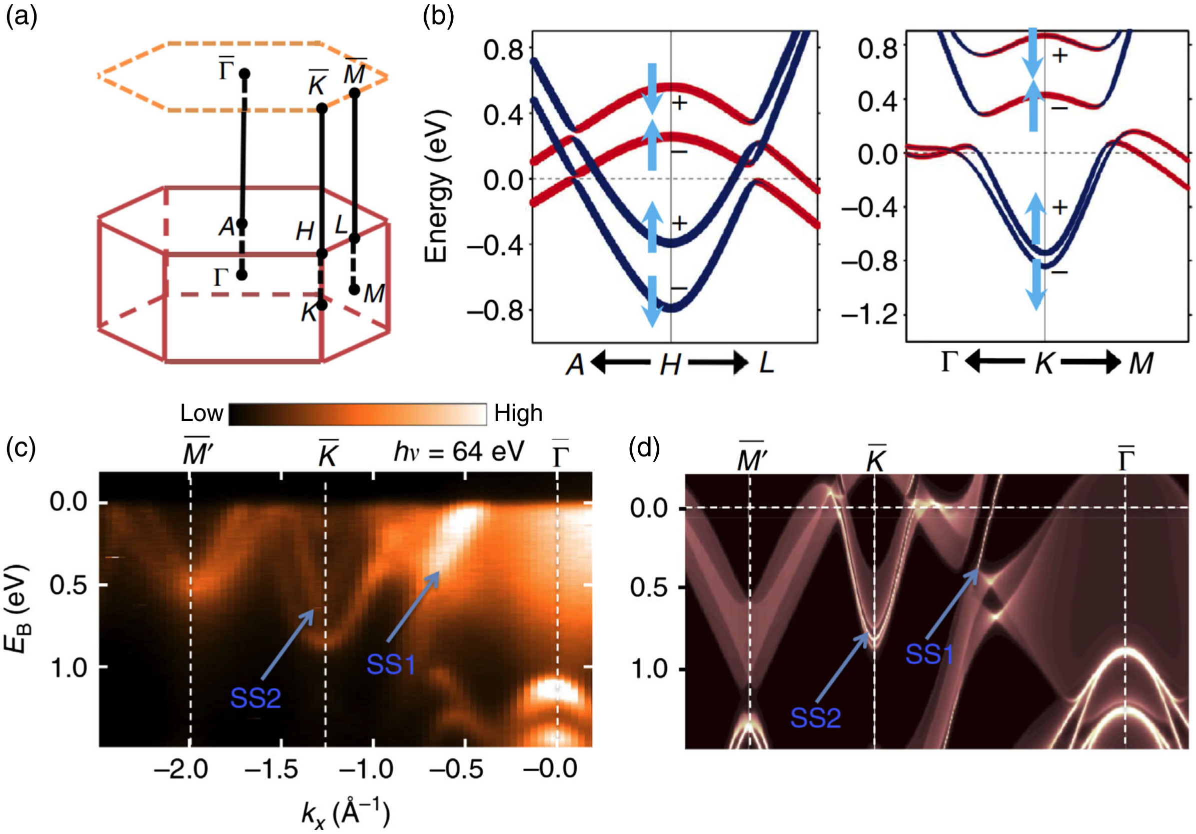

FIG. 50. (a) 3D bulk BZ and the projected (001) surface BZ of $PbTaSe_2$. (b) Calculated band structures of $PbTaSe_2$ along the $A$-$H$-$L$ and $\Gamma$-$K$-$M$ lines with SOC. (c) ARPES intensity plot showing band dispersion along the high-symmetry path $\bar{M}$-$\bar{K}$-$\bar{\Gamma}$. (d) Calculated surface bands of the (001) surface with Pb termination along the same high-symmetry path. Adapted from Bian *et al.*, 2016.

measurements along $\bar{M}$-$\bar{K}$-$\bar{\Gamma}$ show the dispersion of both the bulk and surface states, which is consistent with the calculated surface bands for a (001) Pb-terminated surface, thus supporting the existence of a Weyl nodal line protected by the mirror-reflection symmetry in $PbTaSe_2$.

### 2. Nonsymmorphic symmetry-enforced Dirac nodal lines

The combination of $\mathcal{PT}$ and nonsymmorphic crystalline symmetries can enforce the Dirac nodal lines at the boundary of the BZ. Multiple material candidates in nonsymmorphic space groups are predicted to host Dirac nodal lines, including $SrIrO_3$ (Chen, Lu, and Kee, 2015), $WHM$ (Schoop *et al.*, 2016), $BaMX_3$ ($M = $ V, Nb, or Ta; $X = $ S or Se) (Liang *et al.*, 2016), $IrF_4$ (Bzdušek *et al.*, 2016), and InBi (Ekahana *et al.*, 2017). As discussed in Sec. IV.B.2.a, ZrSiS has been proven to host mirror-glide symmetry-enforced nodal lines at the BZ boundary (Fig. 46); however, the nodal lines are located far from $E_F$. On the other hand, $IrF_4$ was predicted to exhibit near-$E_F$ nodal lines. $IrF_4$ belongs to space group 43, which contains two mutually orthogonal glide planes, formed by a reflection with respect to the (100) and (010) planes, respectively. The density functional theory revealed several band crossings near the $E_F$, such as those along the Γ-$X$ and Γ-$Y$ high-symmetry lines, as shown in Fig. 51(a). These near-$E_F$ band crossings, protected by mirror-glide symmetry, form two nodal loops in the (100) and (010) planes, as plotted in Fig. 51(b). The two nodal loops touch at a specific $k$ point in the $X$-$Y$ direction, thereby forming a nodal-chain structure.

## D. Type-I and type-II nodal lines

By analogy to the type-I and type-II Weyl and DSMs, nodal-line semimetals could also be classified as type I or

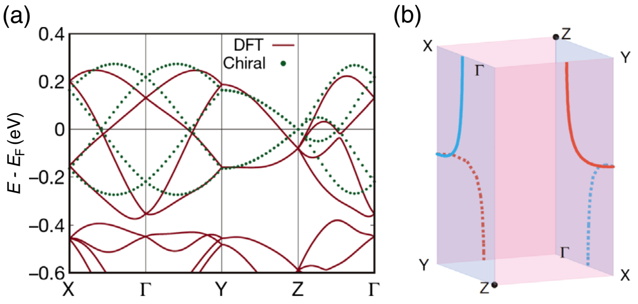

FIG. 51. (a) Calculated band structures of paramagnetic $IrF_4$ along high-symmetry lines with SOC. The solid red lines and dotted green lines correspond to bands determined from density functional theory and a tight-binding model with chiral symmetry, respectively. (b) Nodal-chain structure in $IrF_4$. The solid and dotted lines indicate nodal lines in the visible and hidden faces of the box, respectively. Different colors represent different orientations of the nodal loops. Adapted from Bzdušek *et al.*, 2016.

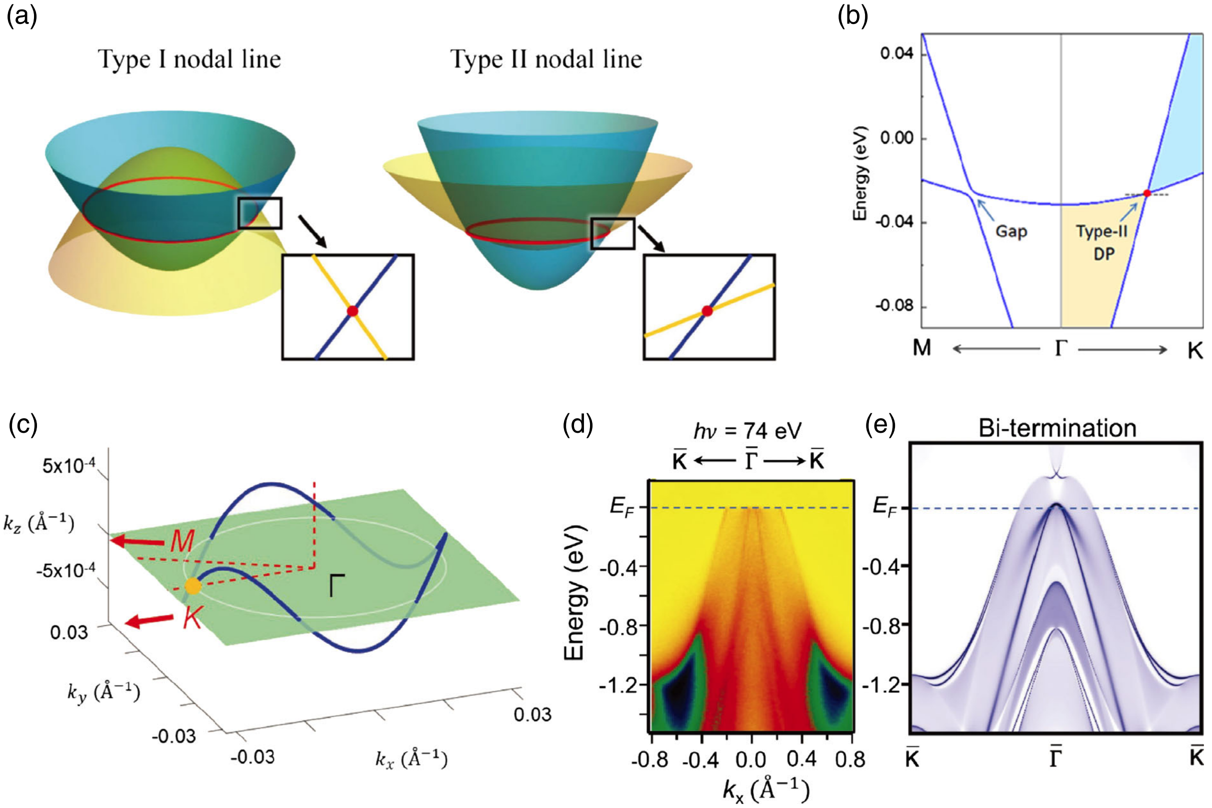

FIG. 52. (a) Schematic plots of the characteristic electronic structures of type-I and type-II nodal lines. (b) Calculated electronic band structure of $Mg_3Bi_2$ along the $M$-$\Gamma$-$K$ direction without SOC. (c) 3D plot of the type-II nodal line in the bulk BZ of $Mg_3Bi_2$. (d) ARPES intensity plot measured with $h\upsilon = 74$ eV, showing band dispersion in the $\bar{\Gamma}$-$\bar{K}$ direction. (e) Corresponding calculated band structure with SOC for a Bi-terminated (001) surface. Adapted from Zhang, Jin *et al.*, 2017, and Chang *et al.*, 2019.

type II, depending on the band dispersion. As illustrated in Fig. 52(a), type-I nodal lines are typically formed by the crossing between an electronlike band and a holelike band, and the two crossing bands have opposing signs of Fermi velocities along the transverse directions of nodal lines. While type-II nodal lines emerge from the crossing between two electronlike or two holelike bands, consequently, the two crossing bands have the same sign for their slopes along one transverse direction of the nodal lines. Under such a classification, the previously mentioned material candidates, including $Cu_3PdN$, $PbTaSe_2$, and ZrSiS, all belong to type-I nodal-line semimetals. As for type-II nodal lines, several compounds have been proposed recently, including $K_4P_3$ (Li, Yu *et al.*, 2017), $Mg_3Bi_2$ (Zhang, Jin *et al.*, 2017), and $Na_3N$ (D. Kim *et al.*, 2018).

Take $Mg_3Bi_2$ as a representative. Without SOC, a band inversion centered at the $\Gamma$ point gives rise to a nodal line surrounding the $\Gamma$ point, as shown in Fig. 52(c). The nodal line, wiggling slightly with respect to the $k_z = 0$ plane, is simply protected by a combination of $\mathcal{PT}$ symmetries. As shown in Fig. 52(b), in the vicinity of the nodal point on the $k_z = 0$ plane the two bands have the same sign for their slope in one transverse direction, i.e., the $\Gamma$-$K$ direction, and form a highly tilted type-II cone structure. Detailed band calculations revealed that this type-II feature holds on every point of the nodal line, demonstrating that $Mg_3Bi_2$ is a type-II nodal-line semimetal. ARPES measurements were performed to verify the type-II nodal-line phase. As shown in Fig. 52(d), the measured electronic structure along the $\bar{\Gamma}$-$\bar{K}$ direction is consistent with the calculated surface bands with SOC for the Bi-terminated (001) surface, confirming the surface electronic structure of $Mg_3Bi_2$ and supporting the existence of type-II bulk nodal lines. Last, we note that, in addition to type-I and type-II nodal lines, there is a third type of nodal lines, termed hybrid nodal lines, composed of both type-I and type-II crossing points (Zhang, Yu *et al.*, 2018).

### E. Magnetic nodal lines

Another important identity of nodal lines, magnetism, is based on which nodal lines can be divided into nonmagnetic and magnetic nodal lines (Wang, 2017b). Several magnetic nodal-line materials have been uncovered, including $Fe_3GeTe_2$ (K. Kim *et al.*, 2018), $CrO_2$ (Wang, Zhao *et al.*, 2018), $Cs_2ZrCu_3F_12$ (Roychowdhury, Rocklin, and Lawler, 2018), Ln$X$ (Ln = La, Gd; $X$ = Cl, Br) (Nie, Weng, and Prinz, 2019), and $Eu_5Bi_3$ (Wu *et al.*, 2019). In particular, the ferromagnetic Weyl nodal lines and the corresponding drumhead surface states were recently observed in a full Heusler compound $Co_2MnGa$ (Belopolski *et al.*, 2019).

$Co_2MnGa$ is known to be ferromagnetic, with a Curie temperature of up to 690 K (Ido and Yasuda, 1988). The calculated bulk majority spin states [Fig. 53(a)] exhibit several band crossings near $E_F$. These twofold band crossings, which

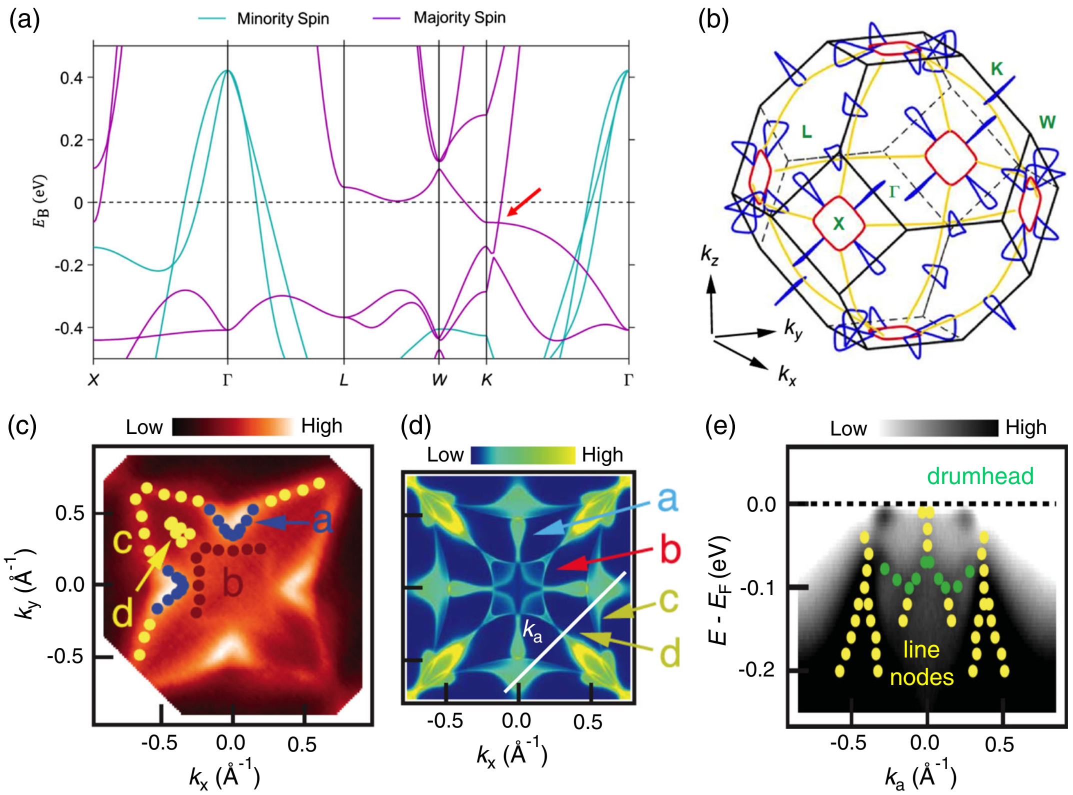

FIG. 53. (a) Calculated electronic structures of $Co_2MnGa$ in the ferromagnetic state without SOC. The red arrow indicates the Weyl band crossing near the $K$ point. (b) 3D plot of the three types of Weyl nodal lines in the bulk BZ of $Co_2MnGa$. The yellow and red nodal lines lie on the $M_x$, $M_y$, and $M_z$ mirror planes. The blue nodal lines are located on the $M_{xy}$, $M_{x\bar{y}}$, $M_{yz}$, $M_{y\bar{z}}$,$M_{xz}$, and $M_{x\bar{z}}$ mirror planes. (c) ARPES constant-energy contour of $Co_2MnGa$ at $E_B = 0.01$ eV measured at $\hbar\upsilon = 50$ eV and $T = 20$ K. (d) Calculated constant-energy surface at $E_B = 0.08$ eV for the (001) MnGa-terminated surface, showing consistent multiple nodal-line features, as marked by letters a–d. (e) ARPES intensity plot in the $k_a$ direction [the white line in (d)] highlighting the bulk line nodes (yellow ovals) and the drumhead surface states (green ovals). Adapted from Belopolski *et al.*, 2019.

are protected by the crystal mirror symmetries, form three types of Weyl nodal lines near the BZ boundaries, as depicted in red, yellow, and blue in Fig. 53(b). Among them, the two yellow nodal lines are interlinked, forming a Hopf link. In addition, nodal lines of each type are pinned to one other, forming a nodal chain. Recently Belopolski *et al.* (2019) identified these bulk Weyl nodal lines by systematic ARPES measurements, as marked by letters a–d in Figs. 53(c) and 53(d). They directly observed a drumhead surface state stretching across the bulk Weyl lines [Fig. 53(e)], thus demonstrating the nontrivial bulk-boundary topological correspondence in $Co_2MnGa$.

### F. Nodal chain, nodal link, and nodal knots

Topological nodal-line semimetals manifest as 1D band crossings in the BZ. Compared to the 0D nodal points, the 1D nodal lines allow richer topological configurations in the momentum space. They can (i) be isolated, (ii) touch at certain points, (iii) link with each other, and (iv) entangle with themselves, enabling the formation of a single nodal line, nodal chains, nodal links, and nodal knots, respectively. Nodal chains were initially proposed in several nonsymmorphic space groups, such as $IrF_4$ in space group 43 (Bzdušek *et al.*, 2016), which is displayed in Fig. 51. Since the initial proposal, more and more material candidates have been discovered, including HfC (Yu, Wu *et al.*, 2017), $Co_2MnGa$ (G. Chang *et al.*, 2017c) [illustrated in Fig. 53(b)], and $MB_2$ ($M =$ Sc, Ti, V, Zr, Hf, Nb, and Ta) (Zhang, Yu *et al.*, 2017; Feng *et al.*, 2018), which exhibit nodal chains in their electronic structure, and AsRhTi, which possesses a nodal link structure (Lian *et al.*, 2019). As for experimental evidence, nodal-chain states have recently been confirmed in a metallic-mesh photonic crystal (Yan *et al.*, 2018), $TiB_2$ (Z. Liu *et al.*, 2018; Yi *et al.*, 2018), and the previously discussed $Co_2MnGa$ (Belopolski *et al.*, 2019).

As discussed, topological nodal lines can be categorized based on the crystal symmetry or generation mechanism, the degeneracy of band crossing, the slope of band dispersion, the linking structure of multiple nodal lines, and the magnetism of nodal lines. Beyond these, topological nodal lines can also be distinguished by the order of band dispersion into three categories: linear, quadratic, and cubic nodal lines, which have linear, quadratic, and cubic band dispersions along one transverse direction, respectively (Yu *et al.*, 2019).

### G. Nodal surfaces

TSMs can be classified based on the dimensionality of band crossings. Materials with 0D nodal points, such as DSMs and

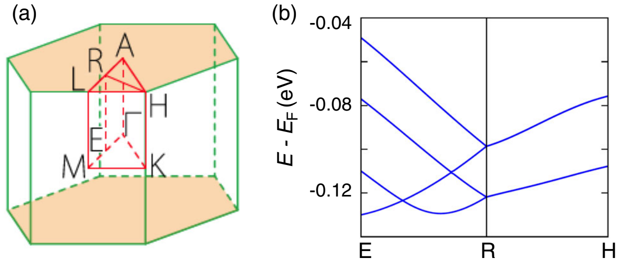

FIG. 54. (a) 3D bulk BZ with high-symmetry points indicated. $R$ and $E$ are the midpoints of the paths $A$-$L$ and $\Gamma$-$M$, respectively. (b) Calculated electronic structure of $Ta_3TeI_7$ along the $E$-$R$-$H$ path in the presence of SOC. Adapted from Wu, Liu *et al.*, 2018.

WSMs, and with 1D nodal lines have been intensively studied in the past few years. For a 3D system, the band crossings may also form a 2D nodal surface. Specifically, any point on the nodal surface is a band degeneracy point of two bands, and the two crossing bands have linear dispersion only along one specific direction, i.e., the surface normal direction. Materials with such band degeneracies are thus called topological nodal-surface semimetals. Topological nodal-surface semimetals are also expected to exhibit distinct features in their electronic, transport, and optical properties, such as the constant density of states near the nodal surface, a stronger quantum oscillation, and peculiar plasmon excitations (Wu, Liu *et al.*, 2018).

In the absence of SOC, the nodal surfaces can either be protected by the combination of $\mathcal{PT}$ symmetry and sublattice symmetry, e.g., graphene networks (Zhong *et al.*, 2016), or dictated by nonsymmorphic symmetry, e.g., $BaVS_3$ (Liang *et al.*, 2016), ZrSiS (Chen *et al.*, 2017; Topp *et al.*, 2017), $K_6YO_4$ (Wu, Liu *et al.*, 2018). In particular, the nodal-surface states in the BZ boundaries of ZrSiS have recently been confirmed by soft x-ray ARPES measurements (Fu *et al.*, 2019b). In the presence of SOC, the previously mentioned node surfaces are usually destroyed or reduced into 1D node lines. The nodal surfaces in ZrSiS are reduced into two nodal lines along the $A$-$M$ and $R$-$X$ paths after the inclusion of SOC (Chen *et al.*, 2017; Topp *et al.*, 2017). Especially in 3D systems with either breaking inversion or breaking time-reversal symmetry, the nonsymmorphic symmetry can guarantee the Weyl nodal surfaces at the BZ boundaries, which are robust against SOC. $Ta_3TeI_7$ (Wu, Liu *et al.*, 2018) was predicted to host such Weyl nodal surfaces. $Ta_3TeI_7$ crystallizes a hexagonal crystal structure with space group $P6_3mc$ (no. 186), which does not have inversion symmetry; instead, the crystal structure contains the $S_{2z}$ screw and $\mathcal{T}$ symmetries, which guarantee a nodal surface on the $k_z = \pi$ plane. The bands are doubly degenerate in the $R$-$H$ direction and nondegenerate with linear dispersion in the $E$-$R$ direction, which is perpendicular to the $k_z = \pi$ plane, demonstrating the existence of nodal surfaces in the $k_z = \pi$ plane, as shown in Fig. 54 (Wang, Liu *et al.*, 2018).

## V. CONCLUSIONS AND OUTLOOK

We have reviewed recent progress in the understanding and classification of various TSMs. We note that what has been presented in this review is not a complete account of TSMs; some theoretical insights and experimental observations were not highlighted. For example, recent theoretical progress in systematically searching for and classifying topological phases of matter was not discussed (Bradlyn *et al.*, 2017; Po, Vishwanath, and Watanabe, 2017; Tang *et al.*, 2019; Vergniory *et al.*, 2019; T. Zhang *et al.*, 2019). Looking forward, many interesting issues deserve future attention and effort.

(i) One crucial issue is to find new types of topological semimetal phases. As noted, recent theoretical breakthroughs in topological phase screening have pointed to the fact that more than 27% of all materials in nature are topological (Vergniory *et al.*, 2019). Given the variety of materials in nature, we believe that the current classification of gapless TSMs is far from complete, and that many new types of gapless topological states will be discovered in the near future. Indeed, recently Xu *et al.* (2020) predicted the existence of new types of antiferromagnetic topological materials, such as higher-order magnetic Dirac semimetals with hinge arcs. T. Zhang *et al.* (2020) proposed twofold quadruple Weyl nodes in chiral cubic crystals.

(ii) In addition to new types of topological semimetal phases, many predicted topological phases are still waiting for stronger experimental evidence, including eightfold fermions (Wieder *et al.*, 2016), magnetic multifold fermions (Cano, Bradlyn, and Vergniory, 2019), quadratic and cubic fermions (Liu and Zunger, 2017), and symmetry-enforced nodal surfaces (Wu, Liu *et al.*, 2018).

(iii) The search for ideal TSMs is also a critical issue in this field. In the past few years, many different types of TSMs have been realized; however, most of the existing materials are not ideal. For example, the DSM $Cd_3As_2$ has a complicated superstructure of As vacancies, which tune the Dirac points away from $E_F$. The other well-studied DSM $Na_3Bi$ hosts a pair of Dirac points sitting close to $E_F$; however, it is not stable in air. As for WSMs, the TaAs family contains 12 pairs of WPs that are not well separated in the momentum space. In contrast, type-II WSMs of the $WTe_2$ family have fewer Weyl points, but trivial bands coexist with the Weyl nodes near $E_F$. Finally, regarding nodal-line materials, $PbTaSe_2$ hosts many trivial bands overlapping with the Weyl nodal line near $E_F$, and the near-$E_F$ Dirac nodal lines in ZrSiS are complicated and not robust against SOC. Taken together, these considerations suggest that a search for ideal TSMs is necessary. An ideal TSM should exhibit the following features: (i) it should be air stable; (ii) the nodal points or nodal lines should be located sufficiently close to $E_F$, with no other states at $E_F$; (iii) it should contain the fewest nodal points or nodal lines possible; and (iv) pairs of nodal points or nodal lines should be well separated in the momentum space. To realize ideal TSMs, one direct way is to continue searching for new material candidates.

Specifically, recent achievements in high-throughput topological phase screening and database development (Tang *et al.*, 2019; Vergniory *et al.*, 2019; T. Zhang *et al.*, 2019) will hasten the discovery of new materials that fully or partly meet the previous criteria. The second way is to tailor the known TSMs by a method such as chemical doping or electrostatic gating, both of which have been widely used in tuning the Fermi level of TSM films. Last, we mention that an alternative way to realize ideal topological phases is by artificial periodic structures, including photonic crystals (Ozawa *et al.*, 2019), optical lattices (Jiang, 2012; Sun *et al.*, 2012), and phononic crystals (Xiao *et al.*, 2015; Li, Huang *et al.*, 2018). The ideal type-I and charge-2 Weyl phases were realized in photonic crystals (B. Yang *et al.*, 2018; Yang, Gao *et al.*, 2020), and the ideal type-II Weyl points were observed in phononic crystals (Huang *et al.*, 2020).

(iv) It is also of significant interest, from both fundamental and practical points of view, to explore the interplay between the nontrivial topology of TSMs and other effects, including *e-e* interactions, superconductivity, magnetism, charge order, etc. In particular, WSMs offer novel and diverse platforms for realizing topological superconductivity due to the naturally nontrivial topology. Topological superconductivity can give rise to Majorana quasiparticles, which are believed to obey non-Abelian statistics in two dimensions and can potentially be used for topological quantum computing (Nayak *et al.*, 2008). Actually, superconducting TSMs have been realized in multiple systems: $\mathrm{Ir}_{1-x}\mathrm{Pt}_x\mathrm{Te}_2$ (Fei *et al.*, 2018; Fu *et al.*, 2019a), $\mathrm{MgB}_2$ (Jin *et al.*, 2019; Zhou *et al.*, 2019), $\mathrm{PbTaSe}_2$ (Bian *et al.*, 2016; Guan *et al.*, 2016), etc. On the other hand, some external tunings, such as point contact (Wang, Wang *et al.*, 2016), pressure (Kang *et al.*, 2015; Pan *et al.*, 2015), and the proximity effect (Bachmann *et al.*, 2017), have also been reported to introduce superconducting pairs in a TSM. Despite these diverse superconducting TSMs, the possible Majorana boundary states remain to be explored. Looking forward, we highlight three possible pathways for creating Majorana quasiparticles in TSMs. First, a time-reversal-invariant TSC could be realized in electron-hole nesting WSMs with a nontrivial total of Fermi surface Chern number (Qi *et al.*, 2009; Zhang, Kane, and Mele, 2013), and the Majorana Kramer modes could be found on their boundary or topological defects. Second, pair density waves in a spin-orbit coupled 2D DSM could support a single Majorana zero mode and effective TSC in their fractional quantized superconducting vortex (Chan, Zhang *et al.*, 2017). Last, it has been predicted that Majorana zero modes could emerge from 3D DSMs with rotational symmetry breaking (König and Coleman, 2019; Qin *et al.*, 2019). In this case, the quasiparticles of a superconducting vortex perform similarly to that of a superconducting TI. Recently evidence has been reported in an impurity-assisted vortex of a LiFeAs superconductor (Kong *et al.*, 2020), which signifies the incorporation of a DSM state into a Majorana playground. In addition to topological superconductivity, the *e-e* interactions could also lead to new topological states of matter, such as a fractionalized analog of the WSMs, the fractional chiral metal (Meng *et al.*, 2016), and the Weyl Mott insulator (Morimoto and Nagaosa, 2016). Beyond the *e-e* interaction, many other correlation effects, including the interplay of the chiral anomaly and collective modes (spin or charge) in WSMs (Liu, Ye, and Qi, 2013; Panfilov, Burkov, and Pesin, 2014), also deserve further exploration. Specifically, we note a recent study reporting the observation of an axionic charge-density wave in the WSM $(\mathrm{TaSe}_4)_2\mathrm{I}$ (Gooth *et al.*, 2019).

(v) Light, a time-periodic wave, can interact with solids through the Floquet effect, which offers a platform to create Floquet states of matter on ultrafast timescales. On the theoretical front, there have been extensive studies on Floquet engineered TSM phases. For example, a Floquet-WSM state can be induced from a DSM (Chan, Oh *et al.*, 2016; Hübener *et al.*, 2017) or TNLSM (Narayan, 2016; Taguchi *et al.*, 2016; Yan and Wang, 2016; Ezawa, 2017a) under the irradiation of circularly polarized light, which breaks time-reversal symmetry. Other systems, such as TIs (Wang *et al.*, 2014), band insulators (Zhang, Ong, and Nagaosa, 2016), and 3D stacked graphene systems (Zou and Liu, 2016), have also been predicted to exhibit Floquet-WSM states. In addition to Floquet WSMs, there have also been proposals of Floquet DSMs and NLSMs in various systems (Narayan, 2015; Li, Lee, and Gong, 2018; Liu, Sun *et al.*, 2018; Kim, Kwon, and Park, 2019). In terms of detection, the most direct way would be time-resolved ARPES. However, ARPES evidence of Floquet-TSM states and phase transitions is lacking, which could be due to a lack of promising materials or limitations in energy resolution, pump fluence, or photon energy of time-resolved ARPES. On the other hand, light-electron interactions in TSMs can also result in interesting phenomena: the anomalous Hall effect (Chan, Lee *et al.*, 2016), the circular photogalvanic effect (Chan, Lindner *et al.*, 2017; de Juan *et al.*, 2017), the macroscopic surface chiral current (González and Molina, 2016), and the nonlinear Hall effect (Zhang, Sun, and Yan, 2018) in DSMs and WSMs, the chiral pumping effect (Ebihara, Fukushima, and Oka, 2016), and the Weyl half-metal phase and spin-filter effect (Li, Wang *et al.*, 2019) in DSMs, etc. Specifically, the circular photogalvanic effect has been observed in the WSM TaAs (Q. Ma *et al.*, 2017; Sun, Sun *et al.*, 2017; Osterhoudt *et al.*, 2019) and the chiral semimetal RhSi (Rees *et al.*, 2020). In short, the current experimental investigations of light-electron interactions in TSMs are at a preliminary stage; more efforts are desired.

(vi) Most of the discovered TSMs are in macroscopic single-crystal or polycrystalline forms, which usually contain defects and impurities. High-quality thin films, nanoparticles, and heterostructures are more desirable, from both a fundamental and an applied standpoint.

(vii) TSMs have been investigated intensively in the last decade, not only because of fundamental interest but also due to their potential for applications in future devices and technologies. The following is an incomplete list of applications of TSMs. First, TSMs exhibit many unique properties that may provide platforms for device applications, such as exploiting the chiral anomaly effect and the bulk Weyl nodes by employing WSMs in so-called chiral electronic devices, including chiral batteries and high-sensitivity magnetic field sensors (Kharzeev and Yee, 2013), axial-current-based valleytronic devices (Parameswaran *et al.*, 2014; Jiang *et al.*, 2015), and even the quantum computing chiral qubit (Kharzeev and Li, 2019). By reducing the dimension of 3D TSMs to two dimensions, both the quantum spin and anomalous Hall phases can be achieved; the robust spin-polarized edge states can give rise to possible Hall-effect devices such as a spin-filter transistor (Shi, Wang, and Wu, 2015). It was also predicted that the interplay of Dirac or Weyl fermions and Néel spin-orbit torques in antiferromagnetic DSMs and WSMs could open up possibilities for antiferromagnetic spintronics (Šmejkal *et al.*, 2017). Second, TSMs with nonzero monopole charges such as WSMs are characterized by robust Fermi-arc surface states, which, like TIs, could provide a good platform for surface-related chemical processes, including catalysis (Chen *et al.*, 2011; Kong and Cui, 2011). Indeed, it has been reported that the WSM TaAs family can be used as a high-activity hydrogen evolution reaction catalyst thanks to its topological surface states (Rajamathi *et al.*, 2017). The low-dissipation Fermi-arc transport gives rise to ultrahigh surface conductivity, which was recently confirmed in NbAs nanobelts (C. Zhang *et al.*, 2019a), facilitating electronic applications such as thermoelectric conversion and supercapacitors. Third, the 2D analog of Dirac or Weyl semimetals, graphene, is an attractive photosensitive material due to the linear-dispersed crossing bands, which can potentially absorb photons with an arbitrarily long wavelength (F. Xia *et al.*, 2009; Mueller, Xia, and Avouris, 2010). Three-dimensional DSMs and WSMs such as $Cd_3As_2$ and TaAs not only possess the same advantages of graphene as a high-performance photodetector but also show good potential in realizing ultrafast broadband photodetectors owing to their fast photorelaxation time and enhanced absorption efficiency (Q. Wang *et al.*, 2017; Yavarishad *et al.*, 2017; Zhu *et al.*, 2017; Chi *et al.*, 2018). Last, as discussed previously, TSMs exhibit not only unique electrical transport and optical behaviors but also interesting thermal phenomena. In particular, it has been found that the linearly dispersed Dirac or Weyl cones can give rise to the axial gravitational anomaly (Landsteiner, Megías, and Pena-Benitez, 2011; Gooth *et al.*, 2017), a large Nernst effect, and quantized thermoelectric Hall conductivity (Han *et al.*, 2020; W. Zhang *et al.*, 2020), providing an interesting platform for high-performance thermoelectric applications such as heat reservoirs and highly efficient thermoelectric energy converters. In summary, TSMs are a promising frontier in condensed-matter physics, but the explorations are far from complete. With the continuous and integrated efforts of theoretical modeling and predictions, material synthesis, characterization, and device demonstrations, more and more breakthroughs are expected in this rapidly developing field.

## ACKNOWLEDGMENTS

The authors thank B. Fichera, N. Gedik, L. Kong, H. Po, Y. Su, F. Yang, R. Yang, L. Ye, T. Zhang, Y. Zhang, J. Zhao, and A. Zong for useful discussions and feedback in the preparation of this review. This work is supported by the Ministry of Science and Technology of China (Grants No. 2016YFA0401000 and No. 2016YFA0300600), the National Natural Science Foundation of China (Grants No. 11888101 and No. U1832202), and the Chinese Academy of Sciences (Grants No. XDB28000000, No. XDB33020100, and No. QYZDB-SSW-SLH043). B. Q. L. acknowledges support from the National Science Foundation under Grant No. NSF DMR-1809815 (manuscript writing).

## APPENDIX A: TABLE LIST OF EXPERIMENTALLY CONFIRMED TSMS

We summarize, to the best of our knowledge, the experimentally confirmed topological semimetals in Table I.

## APPENDIX B: MONOPOLE CHARGES

### 1. Monopole charges of linear, quadratic, and cubic-Weyl fermions

Consider a Weyl semimetal with certain rotational symmetry along the $z$ axis. The crossing bands can have linear, quadratic, or cubic dispersions in two in-plane momentum directions, i.e., the $k_x$ and $k_y$ directions, and linear dispersion in the rotation axis, i.e., the $k_z$ direction. Accordingly, the Weyl Hamiltonian in the vicinity of the Weyl point can be written as

$$H_{\pm} = \pm\begin{pmatrix} \nu_z k_z & \nu_{\parallel}(k_x - ik_y)^N \\ \nu_{\parallel}(k_x + ik_y)^N & -\nu_z k_z \end{pmatrix}, \quad \text{(B1)}$$

where $\nu_z$ and $\nu_{\parallel}$ are constants and $N = 1, 2, 3$ correspond to a Weyl point with linear, linear, quadratic, or cubic dispersion. Correspondingly, the eigenvalues or energy-momentum

TABLE I. An incomplete survey of experimentally confirmed TSMs. DSM, Dirac semimetal; WSM, Weyl semimetal; UTSM, unconventional topological semimetal; TNLSM, topological nodal-line semimetal; WNL, Weyl nodal line; DNL, Dirac nodal line.

| TSM | Classification | Material | References |
|---|---|---|---|
| DSM | Type I | Na$_3$Bi | (Liu *et al.*, 2014b; S.-Y. Xu *et al.*, 2015d) |
| | Type I | Cd$_3$As$_2$ | (Borisenko *et al.*, 2014; Liu *et al.*, 2014a; Neupane *et al.*, 2014) |
| | Type I | Black phosphorus | (Kim, Baik *et al.*, 2015) |
| | Type II | PtTe$_2$ family | (Noh *et al.*, 2017; M. Yan *et al.*, 2017; Zhang, Yan *et al.*, 2017) |
| | Type II | NiTe$_2$ | (Ghosh *et al.*, 2019) |
| | Type II | La$_{1.77}$Sr$_{0.23}$CuO$_4$ | (Horio *et al.*, 2018) |
| | Quadratic | $\alpha$-Sn | (Barfuss *et al.*, 2013; Ohtsubo *et al.*, 2013; C.-Z. Xu *et al.*, 2017) |
| | Cubic | Tl(MoSe)$_3$ | (Nakayama *et al.*, 2018) |
| | $\mathcal{T}$ breaking | CeSbTe | (Schoop *et al.*, 2018) |
| WSM | $\mathcal{P}$ breaking | TaAs family | (Lv *et al.*, 2015b; S.-Y. Xu *et al.*, 2015b; Yang *et al.*, 2015) |
| | $\mathcal{P}$ breaking | (TaSe$_4$)$_2$I | (Gooth *et al.*, 2019; Li, Deng *et al.*, 2019) |
| | Type II | Mo$_{1-x}$W$_x$Te$_2$ | (Belopolski *et al.*, 2016a; Deng *et al.*, 2016; L. Huang *et al.*, 2016) |
| | Type II | LaAlGe | (S.-Y. Xu *et al.*, 2017) |
| | Type II | TaIrTe$_4$ | (Belopolski *et al.*, 2017; Haubold *et al.*, 2017; Zhou *et al.*, 2018) |
| | Type II | MoP$_2$ | (Razzoli *et al.*, 2018; Yao *et al.*, 2019) |
| | $\mathcal{T}$ breaking | YbMnBi$_2$ | (Borisenko *et al.*, 2019) |
| | $\mathcal{T}$ breaking | Mn$_3$Ge | (Nakatsuji, Kiyohara, and Higo, 2015; Nayak *et al.*, 2016) |
| | $\mathcal{T}$ breaking | GdPtBi | (Suzuki *et al.*, 2016; Shekhar *et al.*, 2018) |
| | $\mathcal{T}$ breaking | Co$_3$Sn$_2S_2$ | (E. Liu *et al.*, 2018; Wang, Xu *et al.*, 2018; D. F. Liu *et al.*, 2019; Morali *et al.*, 2019) |
| | $\mathcal{T}$ breaking | EuCd$_2$As$_2$ | (Ma *et al.*, 2019) |
| | $\mathcal{T}$ breaking | Sr$_{1-y}$Mn$_{1-z}$Sb$_2$ | (Liu *et al.*, 2017) |
| UTSM | Class I threefold | MoP, WC | (B. Q. Lv *et al.*, 2017; Ma *et al.*, 2018) |
| | Charge 2 | CoSi, RhSi | (Rao *et al.*, 2019; Sanchez *et al.*, 2019; Takane *et al.*, 2019) |
| | Charge 4 | AlPt, PdGa | (Schröter *et al.*, 2019, 2020) |
| | Charge 4 | PdBiSe | (Lv *et al.*, 2019) |
| TNLSM | Without SOC | CaAgAs family | (X.-B. Wang *et al.*, 2017; Nayak *et al.*, 2018; Takane *et al.*, 2018; N. Xu *et al.*, 2018) |
| | Without SOC | MgB$_2$ | (Zhou *et al.*, 2019) |
| | Without SOC | PtSn$_4$ | (Wu *et al.*, 2016) |
| | Without SOC | SrAs$_3$ | (Song *et al.*, 2020) |
| | Mirror WNL | PbTaSe$_2$ | (Bian *et al.*, 2016) |
| | Nonsymmorphic DNL | ZrSiS family | (Lou *et al.*, 2016; Neupane *et al.*, 2016; Schoop *et al.*, 2016) |
| | Nonsymmorphic DNL | InBi | (Ekahana *et al.*, 2017) |
| | Nonsymmorphic DNL | IrO$_2$ | (Nelson *et al.*, 2019) |
| | Nonsymmorphic DNL | RuO$_2$ | (Jovic *et al.*, 2019) |
| | Nodal chain | TiB$_2$ family | (Z. Liu *et al.*, 2018; Yi *et al.*, 2018) |
| | Type II | Mg$_3$Bi$_2$ | (Chang *et al.*, 2019) |
| | $\mathcal{T}$ breaking | Co$_2$MnGa | (Belopolski *et al.*, 2019) |
| | Hourglass | Ta$_3$SiTe$_6$ | (Sato *et al.*, 2018) |

relations are given by $\varepsilon_\pm(k) = \pm\sqrt{\nu_z^2 k_z^2 + \nu_\parallel^2 (k_x^2 + k_y^2)^N}$, with the positive and negative values corresponding to the conduction and valence bands, respectively. Without losing generality, we assume that the Weyl point is slightly above the chemical potential and consider the valence band. In polar coordinates, the corresponding eigenstates of $H_\pm$ are given by

$$|u_+(k,\theta,f)\rangle = \begin{pmatrix} \sin(\theta/2) \\ -\cos(\theta/2)e^{iNf} \end{pmatrix},$$
$$|u_-(k,\theta,f)\rangle = \begin{pmatrix} \cos(\theta/2) \\ \sin(\theta/2)e^{iNf} \end{pmatrix}, \tag{B2}$$

where $\cos\theta = \nu_z k_z / E_k$, $\tan f = k_y/k_x$, and $E_k = \sqrt{\nu_z^2 k_z^2 + \nu_\parallel^2 (k_x^2 + k_y^2)^N}$. The Berry connections are given as

$$\boldsymbol{A}_+ = (A_k, A_\theta, A_f) = \left(0, 0, -N\frac{\cos^2(\theta/2)}{k\sin\theta}\right),$$
$$\boldsymbol{A}_- = \left(0, 0, -N\frac{\sin^2(\theta/2)}{k\sin\theta}\right). \tag{B3}$$

The Berry curvature then can be expressed as

$$\begin{aligned}\boldsymbol{\Omega}_{\pm}(\boldsymbol{k}) &= \boldsymbol{\nabla}_{\boldsymbol{k}} \times \boldsymbol{A}_{\pm}(\boldsymbol{k}) \\ &= \frac{1}{k\sin\theta}\left[\frac{\partial(A_f \sin\theta)}{\partial\theta}\right]\hat{e}_k = \pm N\frac{\hat{e}_k}{2k^2}.\end{aligned} \tag{B4}$$

Finally, the monopole charge can be calculated by integrating the Berry curvature over an arbitrary Fermi surface that encloses the Weyl node

$$C_{\mathrm{FS}}^{\pm} = \frac{1}{2\pi}\oiint_{\mathrm{FS}} \boldsymbol{\Omega}_{\pm}(k)\cdot d\boldsymbol{S} = \pm N. \tag{B5}$$

This indicates that the monopole charge of the Weyl node is closely related to the dispersion power at the crossing point. Specifically, Weyl points with linear, quadratic, and cubic dispersions along certain momentum directions would have monopole charges of ±1, ±2, and ±3, respectively.

### 2. Monopole charges of class-II threefold fermions

The effective $\boldsymbol{k}\cdot\boldsymbol{p}$ model of a class-II threefold fermion is given by (Bradlyn *et al.*, 2016)

$$H_{3\times3} = v_F\boldsymbol{k}\cdot\boldsymbol{S}_1 = v_F\begin{pmatrix} 0 & ik_x & -ik_y \\ -ik_x & 0 & ik_z \\ ik_y & -ik_z & 0 \end{pmatrix}, \tag{B6}$$

where $\boldsymbol{k} = (k_x, k_y, k_z)$ represents the momentum and $\boldsymbol{S}_1 = (S_x, S_y, S_z)$ stands for the spin-1 generators. $\nu_F$ is the Fermi velocity. As expected, the three eigenvalues of Eq. (B6) are $E_{\pm} = \pm\nu_F|k|$ and $E_0 = 0$. This means that their spectrum consists of two linearly dispersed bands and one flatband, that these three bands cross each other at $k = 0$, and that they form a threefold degenerate point. In polar coordinates, the corresponding eigenfunctions can be expressed as

$$\begin{aligned}\psi_{\pm} &= \frac{1}{\sqrt{2}}\begin{pmatrix} \pm\sin\theta \\ -i\cos f \mp \cos\theta\sin f \\ i\sin f \mp \cos\theta\cos f \end{pmatrix}, \\ \psi_0 &= \begin{pmatrix} i\cos\theta \\ i\sin\theta\sin f \\ i\sin\theta\cos f \end{pmatrix},\end{aligned} \tag{B7}$$

where $\cos\theta = k_z/k$, $\tan f = k_y/k_x$, and $k = \sqrt{k_x^2 + k_y^2 + k_z^2}$. The associate Berry connections are given by

$$\begin{aligned}\boldsymbol{A}_{\pm} &= i\langle\psi_{\pm}|\boldsymbol{\nabla}_{\boldsymbol{k}}|\psi_{\pm}\rangle = (A_k^{\pm}, A_{\theta}^{\pm}, A_f^{\pm}) = \left(0, 0, \pm\frac{\cos\theta}{k\sin\theta}\right), \\ \boldsymbol{A}_0 &= i\langle\psi_0|\boldsymbol{\nabla}_k|\psi_0\rangle = (0, 0, 0).\end{aligned} \tag{B8}$$

The Berry curvature then is given as

$$\begin{aligned}\boldsymbol{\Omega}_{\pm}(\boldsymbol{k}) &= \boldsymbol{\nabla}_{\boldsymbol{k}} \times \boldsymbol{A}_{\pm}(\boldsymbol{k}) = \frac{1}{k\sin\theta}\left[\frac{\partial(A_f\sin\theta)}{\partial\theta}\right]\hat{e}_k = \mp\frac{\hat{e}_k}{k^2}, \\ \boldsymbol{\Omega}_0(\boldsymbol{k}) &= 0.\end{aligned} \tag{B9}$$

Finally, the Chern numbers of $\boldsymbol{\Omega}_{\pm}$ are calculated as

$$C_{\mathrm{FS}}^{\pm} = \frac{1}{2\pi}\oiint_{\mathrm{FS}} \boldsymbol{\Omega}_{\pm}(\boldsymbol{k})\cdot d\boldsymbol{S} = \mp 2. \tag{B10}$$

Equations (B6)–(B10) demonstrate that the threefold spin-1 fermions hold a Chern number of ±2.

### 3. Monopole charges of fourfold fermions

For fourfold degeneracy, three species exist. The famous example is Dirac fermions, which can be described by Eq. (2). Since a Dirac point can be viewed as two overlapping Weyl points of opposite chirality, it naturally has a monopole charge of zero.

On the other hand, two Weyl points of the same chirality can also overlap and form a fourfold degenerate point. As with Eq. (2), the corresponding low-energy excitations of such a fourfold point can be written as

$$H_{4\times4}^2 \sim \begin{pmatrix} \boldsymbol{\sigma}\cdot\boldsymbol{k} & 0 \\ 0 & \boldsymbol{\sigma}\cdot\boldsymbol{k} \end{pmatrix}. \tag{B11}$$

The corresponding Chern number is the direct sum of two identical Weyl points, i.e., ±2. The low-energy excitations are thus called charge-2 fourfold fermions (Zhang, Song *et al.*, 2018).

The third example is so-called spin-3/2 Weyl fermions (Mañes, 2012; Bradlyn *et al.*, 2016; Ezawa, 2016; Isobe and Fu, 2016; Liang and Yu, 2016). As with Eq. (B6), the effective Hamiltonian can be expressed as

$$H_{4\times4}^4 \sim \boldsymbol{k}\cdot\boldsymbol{S}_{3/2} = \tfrac{1}{2}\begin{pmatrix} 3k_z & \sqrt{3}(k_x - ik_y) & 0 & 0 \\ \sqrt{3}(k_x + ik_y) & k_z & 2(k_x - ik_y) & 0 \\ 0 & 2(k_x + ik_y) & -k_z & \sqrt{3}(k_x - ik_y) \\ 0 & 0 & \sqrt{3}(k_x + ik_y) & -3k_z \end{pmatrix}, \tag{B12}$$

where $\boldsymbol{k} = (k_x, k_y, k_z)$ represents the momentum and $\boldsymbol{S}_{3/2} = (S_x, S_y, S_z)$ stands for the spin-3/2 generators. The eigenvalues of Eq. (B12) are given by

$$E_j = j|k|, \quad j = \pm\tfrac{1}{2}, \quad \pm\tfrac{3}{2}. \tag{B13}$$

As a result, the energy spectrum is formed by two types of linearly dispersed bands that differ by the Fermi velocity. These four bands degenerate at $k = 0$. In polar coordinates, i.e., $(k_x, k_y, k_Z) = k(\sin\theta\cos f, \sin\theta\sin f, \cos\theta)$, the corresponding Berry curvature then can be given as

$$\boldsymbol{\Omega}_j(\boldsymbol{k}) = \nabla_{\boldsymbol{k}} \times \boldsymbol{A}_{\pm}(\boldsymbol{k}) = j\frac{\hat{e}_k}{k^2}. \tag{B14}$$

The Chern numbers of $\boldsymbol{\Omega}_j$ are given by

$$C_j = \frac{1}{2\pi}\int\int\oiint_{\mathrm{FS}} \boldsymbol{\Omega}_j(\boldsymbol{k}) \cdot d\boldsymbol{S} = 2j = -1, -3, 1, 3. \tag{B15}$$

Therefore, the total Chern number of spin-3/2 fermions is $C_{\mathrm{FS}}^{\pm} = \pm(1+3) = \pm 4$.

## REFERENCES

Adler, S. L., 1969, Phys. Rev. **177**, 2426.

Aggarwal, L., S. Gayen, S. Das, R. Kumar, V. Süß, C. Felser, C. Shekhar, and G. Sheet, 2017, Nat. Commun. **8**, 13974.

Ahn, S., E. H. Hwang, and H. Min, 2016, Sci. Rep. **6**, 34023.

Ahn, S., E. J. Mele, and H. Min, 2017, Phys. Rev. Lett. **119**, 147402.

Akrap, A., *et al.*, 2016, Phys. Rev. Lett. **117**, 136401.

Ali, M. N., Q. Gibson, S. Jeon, B. B. Zhou, A. Yazdani, and R. J. Cava, 2014, Inorg. Chem. **53**, 4062.

Ali, M. N., L. M. Schoop, C. Garg, J. M. Lippmann, E. Lara, B. Lotsch, and S. S. P. Parkin, 2016, Sci. Adv. **2**, e1601742.

Ali, M. N., *et al.*, 2014, Nature (London) **514**, 205.

Ando, Y., and L. Fu, 2015, Annu. Rev. Condens. Matter Phys. **6**, 361.

Andreev, A. V., and B. Z. Spivak, 2018, Phys. Rev. Lett. **120**, 026601.

Araki, Y., and K. Nomura, 2016, Phys. Rev. B **93**, 094438.

Armitage, N. P., E. J. Mele, and A. Vishwanath, 2018, Rev. Mod. Phys. **90**, 015001.

Arnold, F., M. Naumann, S.-C. Wu, Y. Sun, M. Schmidt, H. Borrmann, C. Felser, B. Yan, and E. Hassinger, 2016, Phys. Rev. Lett. **117**, 146401.

Arnold, F., *et al.*, 2016, Nat. Commun. **7**, 11615.

Ashby, P. E. C., and J. P. Carbotte, 2013, Phys. Rev. B **87**, 245131.

Ashby, P. E. C., and J. P. Carbotte, 2014, Phys. Rev. B **89**, 245121.

Bachmann, M. D., N. Nair, F. Flicker, R. Ilan, T. Meng, N. J. Ghimire, E. D. Bauer, F. Ronning, J. G. Analytis, and P. J. W. Moll, 2017, Sci. Adv. **3**, e1602983.

Bácsi, A., and A. Virosztek, 2013, Phys. Rev. B **87**, 125425.

Bahramy, M. S., *et al.*, 2018, Nat. Mater. **17**, 21.

Balents, L., 2011, Physics **4**, 36.

Bansil, A., H. Lin, and T. Das, 2016, Rev. Mod. Phys. **88**, 021004.

Barati, S., and S. H. Abedinpour, 2017, Phys. Rev. B **96**, 155150.

Bardarson, J. H., P. W. Brouwer, and J. E. Moore, 2010, Phys. Rev. Lett. **105**, 156803.

Barfuss, A., *et al.*, 2013, Phys. Rev. Lett. **111**, 157205.

Batabyal, R., N. Morali, N. Avraham, Y. Sun, M. Schmidt, C. Felser, A. Stern, B. Yan, and H. Beidenkopf, 2016, Sci. Adv. **2**, e1600709.

Bednik, G., A. A. Zyuzin, and A. A. Burkov, 2015, Phys. Rev. B **92**, 035153.

Bednorz, J. G., and K. A. Müller, 1986, Z. Phys. B **64**, 189.

Bell, J. S., and R. Jackiw, 1969, Nuovo Cimento A **60**, 47.

Belopolski, I., *et al.*, 2016a, Nat. Commun. **7**, 13643.

Belopolski, I., *et al.*, 2016b, Phys. Rev. Lett. **116**, 066802.

Belopolski, I., *et al.*, 2017, Nat. Commun. **8**, 942.

Belopolski, I., *et al.*, 2019, Science **365**, 1278.

Benalcazar, W. A., B. A. Bernevig, and T. L. Hughes, 2017, Science **357**, 61.

Bernevig, A., H. Weng, Z. Fang, and X. Dai, 2018, J. Phys. Soc. Jpn. **87**, 041001.

Bernevig, B. A., T. L. Hughes, and S.-C. Zhang, 2006, Science **314**, 1757.

Besara, T., *et al.*, 2016, Phys. Rev. B **93**, 245152.

Bi, R., Z. Yan, L. Lu, and Z. Wang, 2017, Phys. Rev. B **96**, 201305.

Bian, G., *et al.*, 2016, Nat. Commun. **7**, 10556.

Bodnar, J., 1977, in *Proceedings of the 3rd International Conference on the Physics of Narrow Gap Semiconductors, Warsaw, 1977*, edited by J. Rauluszkiewicz, M. Gorska, and E. Kaczmarek (Polish Scientific Publishers PWN, Warsaw), pp. 311–316.

Borisenko, S., Q. Gibson, D. Evtushinsky, V. Zabolotnyy, B. Büchner, and R. J. Cava, 2014, Phys. Rev. Lett. **113**, 027603.

Borisenko, S., *et al.*, 2019, Nat. Commun. **10**, 3424.

Bradlyn, B., J. Cano, Z. Wang, M. G. Vergniory, C. Felser, R. J. Cava, and B. A. Bernevig, 2016, Science **353**, aaf5037.

Bradlyn, B., L. Elcoro, J. Cano, M. G. Vergniory, Z. Wang, C. Felser, M. I. Aroyo, and B. A. Bernevig, 2017, Nature (London) **547**, 298.

Bu, K., *et al.*, 2018, Phys. Rev. B **98**, 115127.

Burkov, A. A., 2014, Phys. Rev. Lett. **113**, 247203.

Burkov, A. A., 2015a, J. Phys. Condens. Matter **27**, 113201.

Burkov, A. A., 2015b, Phys. Rev. B **91**, 245157.

Burkov, A. A., 2016, Nat. Mater. **15**, 1145.

Burkov, A. A., 2017, Phys. Rev. B **96**, 041110.

Burkov, A. A., 2018, Annu. Rev. Condens. Matter Phys. **9**, 359.

Burkov, A. A., and L. Balents, 2011, Phys. Rev. Lett. **107**, 127205.

Burkov, A. A., M. D. Hook, and L. Balents, 2011, Phys. Rev. B **84**, 235126.

Butler, C. J., Y.-M. Wu, C.-R. Hsing, Y. Tseng, R. Sankar, C.-M. Wei, F.-C. Chou, and M.-T. Lin, 2017, Phys. Rev. B **96**, 195125.

Bzdušek, T., Q. Wu, A. Rüegg, M. Sigrist, and A. A. Soluyanov, 2016, Nature (London) **538**, 75.

Cai, P. L., J. Hu, L. P. He, J. Pan, X. C. Hong, Z. Zhang, J. Zhang, J. Wei, Z. Q. Mao, and S. Y. Li, 2015, Phys. Rev. Lett. **115**, 057202.

Cano, J., B. Bradlyn, and M. G. Vergniory, 2019, APL Mater. **7**, 101125.

Cao, J., *et al.*, 2015, Nat. Commun. **6**, 7779.

Carbotte, J. P., 2017, J. Phys. Condens. Matter **29**, 045301.

Castro Neto, A. H., F. Guinea, N. M. R. Peres, K. S. Novoselov, and A. K. Geim, 2009, Rev. Mod. Phys. **81**, 109.

Cayssol, J., 2013, C.R. Phys. **14**, 760.

Chadov, S., S.-C. Wu, C. Felser, and I. Galanakis, 2017, Phys. Rev. B **96**, 024435.

Chan, C., L. Zhang, T. F. J. Poon, Y.-P. He, Y.-Q. Wang, and X.-J. Liu, 2017, Phys. Rev. Lett. **119**, 047001.

Chan, C. K., N. H. Lindner, G. Refael, and P. A. Lee, 2017, Phys. Rev. B **95**, 041104.

Chan, C.-K., P. A. Lee, K. S. Burch, J. H. Han, and Y. Ran, 2016, Phys. Rev. Lett. **116**, 026805.

Chan, C.-K., Y.-T. Oh, J. H. Han, and P. A. Lee, 2016, Phys. Rev. B **94**, 121106.

Chan, Y.-H., C.-K. Chiu, M. Y. Chou, and A. P. Schnyder, 2016, Phys. Rev. B **93**, 205132.

Chang, C.-Z., *et al.*, 2013, Science **340**, 167.

Chang, G., *et al.*, 2016a, Sci. Adv. **2**, e1600295.

Chang, G., *et al.*, 2016b, Phys. Rev. Lett. **116**, 066601.

Chang, G., *et al.*, 2017a, Sci. Rep. **7**, 1688.

Chang, G., *et al.*, 2017b, Phys. Rev. Lett. **119**, 206401.

Chang, G., *et al.*, 2017c, Phys. Rev. Lett. **119**, 156401.

Chang, G., *et al.*, 2018, Nat. Mater. **17**, 978.

Chang, P.-Y., and C.-H. Yee, 2017, Phys. Rev. B **96**, 081114.

Chang, T.-R., *et al.*, 2016, Nat. Commun. **7**, 10639.

Chang, T.-R., *et al.*, 2017, Phys. Rev. Lett. **119**, 026404.

Chang, T.-R., *et al.*, 2019, Adv. Sci. **6**, 1800897.

Chaudhuri, D., B. Cheng, A. Yaresko, Q. D. Gibson, R. J. Cava, and N. P. Armitage, 2017, Phys. Rev. B **96**, 075151.

Chen, C., *et al.*, 2017, Phys. Rev. B **95**, 125126.

Chen, F. C., *et al.*, 2018, Phys. Rev. B **98**, 041114.

Chen, H., W. Zhu, D. Xiao, and Z. Zhang, 2011, Phys. Rev. Lett. **107**, 056804.

Chen, Q., and G. A. Fiete, 2016, Phys. Rev. B **93**, 155125.

Chen, R. Y., S. J. Zhang, J. A. Schneeloch, C. Zhang, Q. Li, G. D. Gu, and N. L. Wang, 2015, Phys. Rev. B **92**, 075107.

Chen, W., H.-Z. Lu, and J.-M. Hou, 2017, Phys. Rev. B **96**, 041102.

Chen, Y., Y.-M. Lu, and H.-Y. Kee, 2015, Nat. Commun. **6**, 6593.

Chen, Y., Y. Xie, S. A. Yang, H. Pan, F. Zhang, M. L. Cohen, and S. Zhang, 2015, Nano Lett. **15**, 6974.

Chen, Y. L., *et al.*, 2009, Science **325**, 178.

Cheng, B., N. Kanda, T. N. Ikeda, T. Matsuda, P. Xia, T. Schumann, S. Stemmer, J. Itatani, N. P. Armitage, and R. Matsunaga, 2020, Phys. Rev. Lett. **124**, 117402.

Cheng, B., T. Ohtsuki, D. Chaudhuri, S. Nakatsuji, M. Lippmaa, and N. P. Armitage, 2017, Nat. Commun. **8**, 2097.

Cheng, B., T. Schumann, S. Stemmer, and N. P. Armitage, 2019, arXiv:1910.13655.

Cheng, B., T. Schumann, Y. Wang, X. Zhang, D. Barbalas, S. Stemmer, and N. P. Armitage, 2020, Nano Lett. **20**, 5991.

Cheng, B., Y. Wang, D. Barbalas, T. Higo, S. Nakatsuji, and N. P. Armitage, 2019, Appl. Phys. Lett. **115**, 012405.

Cheng, P., C. Zhang, Y. Liu, X. Yuan, F. Song, Q. Sun, P. Zhou, D. W. Zhang, and F. Xiu, 2016, New J. Phys. **18**, 083003.

Chi, S., *et al.*, 2018, Adv. Mater. **30**, 1801372.

Chinotti, M., A. Pal, W. J. Ren, C. Petrovic, and L. Degiorgi, 2016, Phys. Rev. B **94**, 245101.

Chiu, C.-K., and A. P. Schnyder, 2014, Phys. Rev. B **90**, 205136.

Chiu, Y.-C., *et al.*, 2019, Phys. Rev. B **100**, 125112.

Clark, O. J., *et al.*, 2018, Phys. Rev. Lett. **120**, 156401.

Collins, J. L., *et al.*, 2018, Nature (London) **564**, 390.

Crassee, I., R. Sankar, W.-L. Lee, A. Akrap, and M. Orlita, 2018, Phys. Rev. Mater. **2**, 120302.

Crassee, I., *et al.*, 2018, Phys. Rev. B **97**, 125204.

Cuamba, A. S., P. Hosur, H.-Y. Lu, L. Hao, and C. S. Ting, 2017, Phys. Rev. B **96**, 195159.

Dai, X., H.-Z. Lu, S.-Q. Shen, and H. Yao, 2016, Phys. Rev. B **93**, 161110.

Damascelli, A., Z. Hussain, and Z.-X. Shen, 2003, Rev. Mod. Phys. **75**, 473.

Das, T., 2013, Phys. Rev. B **88**, 035444.

de Juan, F., A. G. Grushin, T. Morimoto, and J. E. Moore, 2017, Nat. Commun. **8**, 15995.

Deng, K., *et al.*, 2016, Nat. Phys. **12**, 1105.

Deng, P., Z. Xu, K. Deng, K. Zhang, Y. Wu, H. Zhang, S. Zhou, and X. Chen, 2017, Phys. Rev. B **95**, 245110.

Di Sante, D., P. Barone, A. Stroppa, K. F. Garrity, D. Vanderbilt, and S. Picozzi, 2016, Phys. Rev. Lett. **117**, 076401.

dos Reis, R. D., M. O. Ajeesh, N. Kumar, F. Arnold, C. Shekhar, M. Naumann, M. Schmidt, M. Nicklas, and E. Hassinger, 2016, New J. Phys. **18**, 085006.

dos Reis, R. D., S. C. Wu, Y. Sun, M. O. Ajeesh, C. Shekhar, M. Schmidt, C. Felser, B. Yan, and M. Nicklas, 2016, Phys. Rev. B **93**, 205102.

Du, Y., X. Bo, D. Wang, E.-j. Kan, C.-G. Duan, S. Y. Savrasov, and X. Wan, 2017, Phys. Rev. B **96**, 235152.

Du, Y., F. Tang, D. Wang, L. Sheng, E.-j. Kan, C.-G. Duan, S. Y. Savrasov, and X. Wan, 2017, npj Quantum Mater. **2**, 3.

Dzero, M., K. Sun, V. Galitski, and P. Coleman, 2010, Phys. Rev. Lett. **104**, 106408.

Dziawa, P., *et al.*, 2012, Nat. Mater. **11**, 1023.

Ebad-Allah, J., M. Krottenmüller, J. Hu, Y. L. Zhu, Z. Q. Mao, and C. A. Kuntscher, 2019, Phys. Rev. B **99**, 245133.

Ebihara, S., K. Fukushima, and T. Oka, 2016, Phys. Rev. B **93**, 155107.

Ekahana, S. A., *et al.*, 2017, New J. Phys. **19**, 065007.

Ezawa, M., 2016, Phys. Rev. B **94**, 195205.

Ezawa, M., 2017a, Phys. Rev. B **96**, 041205.

Ezawa, M., 2017b, Phys. Rev. B **96**, 041202.

Fang, C., Y. Chen, H.-Y. Kee, and L. Fu, 2015, Phys. Rev. B **92**, 081201.

Fang, C., M. J. Gilbert, X. Dai, and B. A. Bernevig, 2012, Phys. Rev. Lett. **108**, 266802.

Fang, C., L. Lu, J. Liu, and L. Fu, 2016a, Nat. Phys. **12**, 936.

Fang, C., H. Weng, X. Dai, and Z. Fang, 2016, Chin. Phys. B **25**, 117106.

Fang, Z., 2003, Science **302**, 92.

Fei, F., *et al.*, 2017, Phys. Rev. B **96**, 041201.

Fei, F., *et al.*, 2018, Adv. Mater. **30**, 1801556.

Feng, J., Y. Pang, D. Wu, Z. Wang, H. Weng, J. Li, X. Dai, Z. Fang, Y. Shi, and L. Lu, 2015, Phys. Rev. B **92**, 081306.

Feng, X., C. Yue, Z. Song, Q. Wu, and B. Wen, 2018, Phys. Rev. Mater. **2**, 014202.

Flicker, F., F. de Juan, B. Bradlyn, T. Morimoto, M. G. Vergniory, and A. G. Grushin, 2018, Phys. Rev. B **98**, 155145.

Fu, B.-B., *et al.*, 2019a, Chin. Phys. B **28**, 037103.

Fu, B.-B., *et al.*, 2019b, Sci. Adv. **5**, eaau6459.

Fu, D., *et al.*, 2018, Phys. Rev. B **97**, 245109.

Fu, L., 2011, Phys. Rev. Lett. **106**, 106802.

Fu, L., and C. L. Kane, 2006, Phys. Rev. B **74**, 195312.

Fu, L., and C. L. Kane, 2007, Phys. Rev. B **76**, 045302.

Fu, L., C. L. Kane, and E. J. Mele, 2007, Phys. Rev. Lett. **98**, 106803.

Ghosh, B., D. Mondal, C.-N. Kuo, C. S. Lue, J. Nayak, J. Fujii, I. Vobornik, A. Politano, and A. Agarwal, 2019, Phys. Rev. B **100**, 195134.

Gibson, Q. D., L. M. Schoop, L. Muechler, L. S. Xie, M. Hirschberger, N. P. Ong, R. Car, and R. J. Cava, 2015, Phys. Rev. B **91**, 205128.

González, J., and R. A. Molina, 2016, Phys. Rev. Lett. **116**, 156803.

Gooth, J., G. Schierning, C. Felser, and K. Nielsch, 2018, MRS Bull. **43**, 187.

Gooth, J., *et al.*, 2017, Nature (London) **547**, 324.

Gooth, J., *et al.*, 2019, Nature (London) **575**, 315.

Gorbar, E. V., V. A. Miransky, and I. A. Shovkovy, 2013, Phys. Rev. B **88**, 165105.

Gorbar, E. V., V. A. Miransky, I. A. Shovkovy, and P. O. Sukhachov, 2016, Phys. Rev. B **93**, 235127.

Goswami, P., J. H. Pixley, and S. Das Sarma, 2015, Phys. Rev. B **92**, 075205.

Groves, S., and W. Paul, 1963, Phys. Rev. Lett. **11**, 194.

Guan, S.-Y., P.-J. Chen, M.-W. Chu, R. Sankar, F. Chou, H.-T. Jeng, C.-S. Chang, and T.-M. Chuang, 2016, Sci. Adv. **2**, e1600894.

Guo, P.-J., H.-C. Yang, K. Liu, and Z.-Y. Lu, 2017, Phys. Rev. B **95**, 155112.

Guo, S.-T., R. Sankar, Y.-Y. Chien, T.-R. Chang, H.-T. Jeng, G.-Y. Guo, F. C. Chou, and W.-L. Lee, 2016, Sci. Rep. **6**, 27487.

Hakl, M., *et al.*, 2018, Phys. Rev. B **97**, 115206.

Halász, G. B., and L. Balents, 2012, Phys. Rev. B **85**, 035103.

Haldane, F. D. M., 1988, Phys. Rev. Lett. **61**, 2015.

Han, F., *et al.*, 2020, Nat. Commun. **11**, 6167.

Hasan, M. Z., and C. L. Kane, 2010, Rev. Mod. Phys. **82**, 3045.

Hasan, M. Z., S.-Y. Xu, I. Belopolski, and S.-M. Huang, 2017, Annu. Rev. Condens. Matter Phys. **8**, 289.

Hasan, M. Z., S.-Y. Xu, and G. Bian, 2015, Phys. Scr. **T164**, 014001.

Haubold, E., *et al.*, 2017, Phys. Rev. B **95**, 241108.

He, J., D. Di Sante, R. Li, X.-Q. Chen, J. M. Rondinelli, and C. Franchini, 2018, Nat. Commun. **9**, 492.

He, J. B., D. Chen, W. L. Zhu, S. Zhang, L. X. Zhao, Z. A. Ren, and G. F. Chen, 2017, Phys. Rev. B **95**, 195165.

He, L. P., X. C. Hong, J. K. Dong, J. Pan, Z. Zhang, J. Zhang, and S. Y. Li, 2014, Phys. Rev. Lett. **113**, 246402.

He, L.-P., and S.-Y. Li, 2016, Chin. Phys. B **25**, 117105.

Heikkilä, T. T., N. B. Kopnin, and G. E. Volovik, 2011, JETP Lett. **94**, 233.

Heikkilä, T. T., and G. E. Volovik, 2011, JETP Lett. **93**, 59.

Heikkilä, T. T., and G. E. Volovik, 2015, New J. Phys. **17**, 093019.

Heinzmann, U., and J. H. Dil, 2012, J. Phys. Condens. Matter **24**, 173001.

Herring, C., 1937, Phys. Rev. **52**, 365.

Hirayama, M., R. Okugawa, S. Ishibashi, S. Murakami, and T. Miyake, 2015, Phys. Rev. Lett. **114**, 206401.

Hirayama, M., R. Okugawa, and S. Murakami, 2018, J. Phys. Soc. Jpn. **87**, 041002.

Hirschberger, M., S. Kushwaha, Z. Wang, Q. Gibson, S. Liang, C. Belvin, B. Bernevig, R. Cava, and N. Ong, 2016, Nat. Mater. **15**, 1161.

Horio, M., *et al.*, 2018, Nat. Commun. **9**, 3252.

Hosen, M. M., *et al.*, 2018, Phys. Rev. B **97**, 121103.

Hosur, P., X. Dai, Z. Fang, and X.-L. Qi, 2014, Phys. Rev. B **90**, 045130.

Hosur, P., S. A. Parameswaran, and A. Vishwanath, 2012, Phys. Rev. Lett. **108**, 046602.

Hosur, P., and X. Qi, 2013, C.R. Phys. **14**, 857.

Hsieh, D., D. Qian, L. Wray, Y. Xia, Y. S. Hor, R. J. Cava, and M. Z. Hasan, 2008, Nature (London) **452**, 970.

Hsieh, D., *et al.*, 2009, Nature (London) **460**, 1101.

Hsieh, T. H., H. Lin, J. Liu, W. Duan, A. Bansil, and L. Fu, 2012, Nat. Commun. **3**, 982.

Hu, J., T. F. Rosenbaum, and J. B. Betts, 2005, Phys. Rev. Lett. **95**, 186603.

Hu, J., Z. Tang, J. Liu, Y. Zhu, J. Wei, and Z. Mao, 2017, Phys. Rev. B **96**, 045127.

Hu, J., *et al.*, 2016a, Sci. Rep. **6**, 18674.

Hu, J., *et al.*, 2016b, Phys. Rev. Lett. **117**, 016602.

Hua, G., S. Nie, Z. Song, R. Yu, G. Xu, and K. Yao, 2018, Phys. Rev. B **98**, 201116.

Huang, H., K.-H. Jin, and F. Liu, 2018, Phys. Rev. B **98**, 121110.

Huang, H., S. Zhou, and W. Duan, 2016, Phys. Rev. B **94**, 121117.

Huang, L., *et al.*, 2016, Nat. Mater. **15**, 1155.

Huang, S.-M., *et al.*, 2015, Nat. Commun. **6**, 7373.

Huang, S.-M., *et al.*, 2016, Proc. Natl. Acad. Sci. U.S.A. **113**, 1180.

Huang, X., W. Deng, F. Li, J. Lu, and Z. Liu, 2020, Phys. Rev. Lett. **124**, 206802.

Huang, X., *et al.*, 2015, Phys. Rev. X **5**, 031023.

Huang, Z.-M., J. Zhou, and S.-Q. Shen, 2017, Phys. Rev. B **96**, 085201.

Hübener, H., M. A. Sentef, U. De Giovannini, A. F. Kemper, and A. Rubio, 2017, Nat. Commun. **8**, 13940.

Huh, Y., E.-G. Moon, and Y. B. Kim, 2016, Phys. Rev. B **93**, 035138.

Hyart, T., and T. T. Heikkilä, 2016, Phys. Rev. B **93**, 235147.

Hyart, T., R. Ojajärvi, and T. T. Heikkilä, 2018, J. Low Temp. Phys. **191**, 35.

Ido, H., and S. Yasuda, 1988, J. Phys. (Paris), Colloq. **49**, C8-167.

Imhof, S., *et al.*, 2018, Nat. Phys. **14**, 925.

Inoue, H., A. Gyenis, Z. Wang, J. Li, S. W. Oh, S. Jiang, N. Ni, B. A. Bernevig, and A. Yazdani, 2016, Science **351**, 1184.

Isobe, H., and L. Fu, 2016, Phys. Rev. B **93**, 241113.

Jenkins, G. S., *et al.*, 2016, Phys. Rev. B **94**, 085121.

Jeon, S., B. B. Zhou, A. Gyenis, B. E. Feldman, I. Kimchi, A. C. Potter, Q. D. Gibson, R. J. Cava, A. Vishwanath, and A. Yazdani, 2014, Nat. Mater. **13**, 851.

Jia, S., S.-Y. Xu, and M. Z. Hasan, 2016, Nat. Mater. **15**, 1140.

Jia, Z., C. Li, X. Li, J. Shi, Z. Liao, D. Yu, and X. Wu, 2016, Nat. Commun. **7**, 13013.

Jian, S.-K., and H. Yao, 2015, Phys. Rev. B **92**, 045121.

Jiang, J., *et al.*, 2013, Nat. Commun. **4**, 3010.

Jiang, J.-H., 2012, Phys. Rev. A **85**, 033640.

Jiang, Q.-D., H. Jiang, H. Liu, Q.-F. Sun, and X. C. Xie, 2015, Phys. Rev. Lett. **115**, 156602.

Jiao, L., Q. N. Xu, Y. P. Qi, S.-C. Wu, Y. Sun, C. Felser, and S. Wirth, 2018, Phys. Rev. B **97**, 195137.

Jin, K.-H., H. Huang, J.-W. Mei, Z. Liu, L.-K. Lim, and F. Liu, 2019, npj Comput. Mater. **5**, 57.

Jin, Y. J., R. Wang, Z. J. Chen, J. Z. Zhao, Y. J. Zhao, and H. Xu, 2017, Phys. Rev. B **96**, 201102.

Jovic, V., *et al.*, 2019, arXiv:1908.02621.

Jozwiak, C., *et al.*, 2011, Phys. Rev. B **84**, 165113.

Kane, C. L., and E. J. Mele, 2005a, Phys. Rev. Lett. **95**, 226801.

Kane, C. L., and E. J. Mele, 2005b, Phys. Rev. Lett. **95**, 146802.

Kane, E. O., 1957, J. Phys. Chem. Solids **1**, 249.

Kang, D., *et al.*, 2015, Nat. Commun. **6**, 7804.

Kargarian, M., Y.-M. Lu, and M. Randeria, 2018, Phys. Rev. B **97**, 165129.

Kargarian, M., M. Randeria, and Y.-M. Lu, 2016, Proc. Natl. Acad. Sci. U.S.A. **113**, 8648.

Kharzeev, D. E., and Q. Li, 2019, arXiv:1903.07133.

Kharzeev, D. E., and H.-U. Yee, 2013, Phys. Rev. B **88**, 115119.

Kim, D., S. Ahn, J. H. Jung, H. Min, J. Ihm, J. H. Han, and Y. Kim, 2018, Phys. Rev. Mater. **2**, 104203.

Kim, H.-J., K.-S. Kim, J.-F. Wang, M. Sasaki, N. Satoh, A. Ohnishi, M. Kitaura, M. Yang, and L. Li, 2013, Phys. Rev. Lett. **111**, 246603.

Kim, H.-S., Y. Chen, and H.-Y. Kee, 2015, Phys. Rev. B **91**, 235103.

Kim, J., S. S. Baik, S. H. Ryu, Y. Sohn, S. Park, B.-G. Park, J. Denlinger, Y. Yi, H. J. Choi, and K. S. Kim, 2015, Science **349**, 723.

Kim, K., *et al.*, 2018, Nat. Mater. **17**, 794.

Kim, K. W., H. Kwon, and K. Park, 2019, Phys. Rev. B **99**, 115136.

Kim, Y., B. J. Wieder, C. L. Kane, and A. M. Rappe, 2015, Phys. Rev. Lett. **115**, 036806.

Kimura, S.-i., H. Yokoyama, H. Watanabe, J. Sichelschmidt, V. Süß, M. Schmidt, and C. Felser, 2017, Phys. Rev. B **96**, 075119.

Klitzing, K. V., G. Dorda, and M. Pepper, 1980, Phys. Rev. Lett. **45**, 494.

Klotz, J., *et al.*, 2016, Phys. Rev. B **93**, 121105.

Kobayashi, S., and M. Sato, 2015, Phys. Rev. Lett. **115**, 187001.

Koepernik, K., D. Kasinathan, D. V. Efremov, S. Khim, S. Borisenko, B. Büchner, and J. van den Brink, 2016, Phys. Rev. B **93**, 201101.

Kondo, T., *et al.*, 2015, Nat. Commun. **6**, 10042.

Kong, D., and Y. Cui, 2011, Nat. Chem. **3**, 845.

Kong, L., *et al.*, 2020, arXiv:2010.04735.

König, E. J., and P. Coleman, 2019, Phys. Rev. Lett. **122**, 207001.

König, M., S. Wiedmann, C. Brüne, A. Roth, H. Buhmann, L. W. Molenkamp, X.-L. Qi, and S.-C. Zhang, 2007, Science **318**, 766.

Kopnin, N. B., T. T. Heikkilä, and G. E. Volovik, 2011, Phys. Rev. B **83**, 220503.

Koshino, M., 2016, Phys. Rev. B **94**, 035202.

Kotov, O. V., and Y. E. Lozovik, 2016, Phys. Rev. B **93**, 235417.

Kourtis, S., J. Li, Z. Wang, A. Yazdani, and B. A. Bernevig, 2016, Phys. Rev. B **93**, 041109.

Kumar, N., S. N. Guin, C. Felser, and C. Shekhar, 2018, Phys. Rev. B **98**, 041103.

Kumar, N., K. Manna, Y. Qi, S.-C. Wu, L. Wang, B. Yan, C. Felser, and C. Shekhar, 2017, Phys. Rev. B **95**, 121109.

Kumar, N., *et al.*, 2019, Nat. Commun. **10**, 2475.

Kushwaha, S. K., *et al.*, 2015, APL Mater. **3**, 041504.

Lai, H.-H., 2015, Phys. Rev. B **91**, 235131.

Landau, L. D., and E. M. Lifshitz, 1980, *Statistical Physics* (Pergamon, Oxford).

Landsteiner, K., E. Megías, and F. Pena-Benitez, 2011, Phys. Rev. Lett. **107**, 021601.

Langbehn, J., Y. Peng, L. Trifunovic, F. von Oppen, and P. W. Brouwer, 2017, Phys. Rev. Lett. **119**, 246401.

Laughlin, R. B., 1981, Phys. Rev. B **23**, 5632.

Laughlin, R. B., 1983, Phys. Rev. Lett. **50**, 1395.

Le, C., S. Qin, X. Wu, X. Dai, P. Fu, C. Fang, and J. Hu, 2017, Phys. Rev. B **96**, 115121.

Le, C., X. Wu, S. Qin, Y. Li, R. Thomale, F.-C. Zhang, and J. Hu, 2018, *Proc. Natl. Acad. Sci. U.S.A.* 115, 8311.

Li, C.-Z., L.-X. Wang, H. Liu, J. Wang, Z.-M. Liao, and D.-P. Yu, 2015, Nat. Commun. **6**, 10137.

Li, F., X. Huang, J. Lu, J. Ma, and Z. Liu, 2018, Nat. Phys. **14**, 30.

Li, F.-Y., X. Luo, X. Dai, Y. Yu, F. Zhang, and G. Chen, 2016, Phys. Rev. B **94**, 121105.

Li, H., H. He, H.-Z. Lu, H. Zhang, H. Liu, R. Ma, Z. Fan, S.-Q. Shen, and J. Wang, 2016, Nat. Commun. **7**, 10301.

Li, H., H.-W. Wang, H. He, J. Wang, and S.-Q. Shen, 2018, Phys. Rev. B **97**, 201110.

Li, L., C. H. Lee, and J. Gong, 2018, Phys. Rev. Lett. **121**, 036401.

Li, P., Y. Wen, X. He, Q. Zhang, C. Xia, Z.-M. Yu, S. A. Yang, Z. Zhu, H. N. Alshareef, and X.-X. Zhang, 2017, Nat. Commun. **8**, 2150.

Li, P., C. H. Zhang, J. W. Zhang, Y. Wen, and X. X. Zhang, 2018, Phys. Rev. B **98**, 121108.

Li, Q., D. E. Kharzeev, C. Zhang, Y. Huang, I. Pletikosić, A. Fedorov, R. Zhong, J. Schneeloch, G. Gu, and T. Valla, 2016, Nat. Phys. **12**, 550.

Li, S., Z.-M. Yu, Y. Liu, S. Guan, S.-S. Wang, X. Zhang, Y. Yao, and S. A. Yang, 2017, Phys. Rev. B **96**, 081106.

Li, X., B. Roy, and S. Das Sarma, 2016, Phys. Rev. B **94**, 195144.

Li, X.-p., K. Deng, B. Fu, Y. Li, J. Han, J. Zhou, S. Zhou, and Y. Yao, 2019, arXiv:1909.12178.

Li, X.-S., C. Wang, M.-X. Deng, H.-J. Duan, P.-H. Fu, R.-Q. Wang, L. Sheng, and D. Y. Xing, 2019, Phys. Rev. Lett. **123**, 206601.

Li, Y., Z. Wang, P. Li, X. Yang, Z. Shen, F. Sheng, X. Li, Y. Lu, Y. Zheng, and Z.-A. Xu, 2017, Front. Phys. **12**, 127205.

Li, Y., *et al.*, 2017d, npj Quantum Mater. **2**, 66.

Li, Z., T. Iitaka, H. Zeng, and H. Su, 2019, Phys. Rev. B **100**, 155201.

Li, Z., T. Xiao, R. Zou, J. Li, Y. Zhang, Y. Zeng, M. Zhou, J. Zhang, and W. Wu, 2020, J. Appl. Phys. **127**, 054306.

Lian, J., L. Yu, Q.-F. Liang, J. Zhou, R. Yu, and H. Weng, 2019, npj Comput. Mater. **5**, 10.

Liang, D. D., *et al.*, 2019, AIP Adv. **9**, 055015.

Liang, L., and Y. Yu, 2016, Phys. Rev. B **93**, 045113.

Liang, Q.-F., J. Zhou, R. Yu, Z. Wang, and H. Weng, 2016, Phys. Rev. B **93**, 085427.

Liang, S., J. Lin, S. Kushwaha, J. Xing, N. Ni, R. J. Cava, and N. P. Ong, 2018, Phys. Rev. X **8**, 031002.

Liang, T., Q. Gibson, M. N. Ali, M. Liu, R. J. Cava, and N. P. Ong, 2015, Nat. Mater. **14**, 280.

Liang, T., J. Lin, Q. Gibson, T. Gao, M. Hirschberger, M. Liu, R. J. Cava, and N. P. Ong, 2017, Phys. Rev. Lett. **118**, 136601.

Liang, T., *et al.*, 2018, Nat. Phys. **14**, 451.

Lifshitz, I. M., and A. M. Kosevich, 1956, Sov. Phys. JETP **2**, 636, http://www.jetp.ac.ru/cgi-bin/dn/e_002_04_0636.pdf.

Lin, B.-C., S. Wang, S. Wiedmann, J.-M. Lu, W.-Z. Zheng, D. Yu, and Z.-M. Liao, 2019, Phys. Rev. Lett. **122**, 036602.

Liu, C.-X., P. Ye, and X.-L. Qi, 2013, Phys. Rev. B **87**, 235306.

Liu, D. F., *et al.*, 2019, Science **365**, 1282.

Liu, E., *et al.*, 2018, Nat. Phys. **14**, 1125.

Liu, G., L. Jin, X. Dai, G. Chen, and X. Zhang, 2018, Phys. Rev. B **98**, 075157.

Liu, H., J.-T. Sun, C. Cheng, F. Liu, and S. Meng, 2018, Phys. Rev. Lett. **120**, 237403.

Liu, H. W., P. Richard, L. X. Zhao, G.-F. Chen, and H. Ding, 2016, J. Phys. Condens. Matter **28**, 295401.

Liu, J., and D. Vanderbilt, 2014, Phys. Rev. B **90**, 155316.

Liu, J. Y., *et al.*, 2017, Nat. Mater. **16**, 905.

Liu, Q., and A. Zunger, 2017, Phys. Rev. X **7**, 021019.

Liu, Q., *et al.*, 2019, Phys. Rev. B **99**, 155119.

Liu, Z., *et al.*, 2018, Phys. Rev. X **8**, 031044.

Liu, Z. K., *et al.*, 2014a, Nat. Mater. **13**, 677.

Liu, Z. K., *et al.*, 2014b, Science **343**, 864.

Liu, Z. K., *et al.*, 2016, Nat. Mater. **15**, 27.

Lodge, M. S., *et al.*, 2017, Nano Lett. **17**, 7213.

Lou, R., *et al.*, 2016, Phys. Rev. B **93**, 241104.

Lu, F., J. Zhao, H. Weng, Z. Fang, and X. Dai, 2013, Phys. Rev. Lett. **110**, 096401.

Lu, H.-Z., and S.-Q. Shen, 2015, Phys. Rev. B **92**, 035203.

Lu, H.-Z., and S.-Q. Shen, 2017, Front. Phys. **12**, 127201.

Lucas, A., R. A. Davison, and S. Sachdev, 2016, Proc. Natl. Acad. Sci. U.S.A. **113**, 9463.

Lundgren, R., P. Laurell, and G. A. Fiete, 2014, Phys. Rev. B **90**, 165115.

Luo, Y., N. J. Ghimire, M. Wartenbe, H. Choi, M. Neupane, R. D. McDonald, E. D. Bauer, J. Zhu, J. D. Thompson, and F. Ronning, 2015, Phys. Rev. B **92**, 205134.

Luo, Y., R. D. McDonald, P. F. S. Rosa, B. Scott, N. Wakeham, N. J. Ghimire, E. D. Bauer, J. D. Thompson, and F. Ronning, 2016, Sci. Rep. **6**, 27294.

Lv, B., T. Qian, and H. Ding, 2019, Nat. Rev. Phys. **1**, 609.

Lv, B. Q., *et al.*, 2015a, Phys. Rev. Lett. **115**, 217601.

Lv, B. Q., *et al.*, 2015b, Phys. Rev. X **5**, 031013.

Lv, B. Q., *et al.*, 2015c, Nat. Phys. **11**, 724.

Lv, B. Q., *et al.*, 2017, Nature (London) **546**, 627.

Lv, B. Q., *et al.*, 2019, Phys. Rev. B **99**, 241104.

Lv, Y.-Y., *et al.*, 2017, Phys. Rev. Lett. **118**, 096603.

Ma, J., *et al.*, 2017, Sci. Adv. **3**, e1602415.

Ma, J.-Z., *et al.*, 2018, Nat. Phys. **14**, 349.

Ma, J.-Z., *et al.*, 2019, Sci. Adv. **5**, eaaw4718.

Ma, Q., *et al.*, 2017, Nat. Phys. **13**, 842.

Mañes, J. L., 2012, Phys. Rev. B **85**, 155118.

Manna, K., Y. Sun, L. Muechler, J. Kübler, and C. Felser, 2018, Nat. Rev. Mater. **3**, 244.

Maulana, L. Z., K. Manna, E. Uykur, C. Felser, M. Dressel, and A. V. Pronin, 2020, Phys. Rev. Research **2**, 023018.

Meng, J., H. Xue, M. Liu, W. Jiang, Z. Zhang, J. Ling, L. He, R. Dou, C. Xiong, and J. Nie, 2020, J. Phys. Condens. Matter **32**, 015702.

Meng, T., and L. Balents, 2012, Phys. Rev. B **86**, 054504.

Meng, T., A. G. Grushin, K. Shtengel, and J. H. Bardarson, 2016, Phys. Rev. B **94**, 155136.

Min, C.-H., *et al.*, 2019, Phys. Rev. Lett. **122**, 116402.

Modic, K. A., T. Meng, F. Ronning, E. D. Bauer, P. J. W. Moll, and B. J. Ramshaw, 2019, Sci. Rep. **9**, 2095.

Moll, P. J. W., N. L. Nair, T. Helm, A. C. Potter, I. Kimchi, A. Vishwanath, and J. G. Analytis, 2016, Nature (London) **535**, 266.

Moll, P. J. W., *et al.*, 2016, Nat. Commun. **7**, 12492.

Mondal, C., C. K. Barman, B. Pathak, and A. Alam, 2019, Phys. Rev. B **100**, 245151.

Moon, E.-G., C. Xu, Y. B. Kim, and L. Balents, 2013, Phys. Rev. Lett. **111**, 206401.

Moore, J. E., and L. Balents, 2007, Phys. Rev. B **75**, 121306.

Morali, N., R. Batabyal, P. K. Nag, E. Liu, Q. Xu, Y. Sun, B. Yan, C. Felser, N. Avraham, and H. Beidenkopf, 2019, Science **365**, 1286.

Morimoto, T., and N. Nagaosa, 2016, Sci. Rep. **6**, 19853.

Mueller, T., F. Xia, and P. Avouris, 2010, Nat. Photonics **4**, 297.

Mukherjee, S. P., and J. P. Carbotte, 2017, Phys. Rev. B **95**, 214203.

Murakawa, H., M. S. Bahramy, M. Tokunaga, Y. Kohama, C. Bell, Y. Kaneko, N. Nagaosa, H. Y. Hwang, and Y. Tokura, 2013, Science **342**, 1490.

Nakatsuji, S., N. Kiyohara, and T. Higo, 2015, Nature (London) **527**, 212.

Nakayama, K., Z. Wang, C. X. Trang, S. Souma, E. D. L. Rienks, T. Takahashi, Y. Ando, and T. Sato, 2018, Phys. Rev. B **98**, 140502.

Nandy, S., G. Sharma, A. Taraphder, and S. Tewari, 2017, Phys. Rev. Lett. **119**, 176804.

Narayan, A., 2015, Phys. Rev. B **91**, 205445.

Narayan, A., 2016, Phys. Rev. B **94**, 041409.

Narayanan, A., *et al.*, 2015, Phys. Rev. Lett. **114**, 117201.

Nayak, A. K., *et al.*, 2016, Sci. Adv. **2**, e1501870.

Nayak, C., S. H. Simon, A. Stern, M. Freedman, and S. Das Sarma, 2008, Rev. Mod. Phys. **80**, 1083.

Nayak, J., N. Kumar, S.-C. Wu, C. Shekhar, J. Fink, E. D. L. Rienks, G. H. Fecher, Y. Sun, and C. Felser, 2018, J. Phys. Condens. Matter **30**, 045501.

Nazmul, A. M., H. T. Lin, S. N. Tran, S. Ohya, and M. Tanaka, 2008, Phys. Rev. B **77**, 155203.

Nelson, J. N., *et al.*, 2019, Phys. Rev. Mater. **3**, 064205.

Neubauer, D., J. P. Carbotte, A. A. Nateprov, A. Löhle, M. Dressel, and A. V. Pronin, 2016, Phys. Rev. B **93**, 121202.

Neupane, M., *et al.*, 2013, Nat. Commun. **4**, 2991.

Neupane, M., *et al.*, 2014, Nat. Commun. **5**, 3786.

Neupane, M., *et al.*, 2016, Phys. Rev. B **93**, 201104.

Nie, S., H. Weng, and F. B. Prinz, 2019, Phys. Rev. B **99**, 035125.

Nie, S., G. Xu, F. B. Prinz, and S.-c. Zhang, 2017, Proc. Natl. Acad. Sci. U.S.A. **114**, 10596.

Nielsen, H., and M. Ninomiya, 1981a, Nucl. Phys. **B185**, 20.

Nielsen, H., and M. Ninomiya, 1981b, Nucl. Phys. **B193**, 173.

Nielsen, H., and M. Ninomiya, 1983, Phys. Lett. **130B**, 389.

Niemann, A. C., *et al.*, 2017, Sci. Rep. **7**, 43394.

Nishihaya, S., M. Uchida, Y. Nakazawa, M. Kriener, Y. Kozuka, Y. Taguchi, and M. Kawasaki, 2018, Sci. Adv. **4**, eaar5668.

Noh, H.-J., J. Jeong, E.-J. Cho, K. Kim, B. I. Min, and B.-G. Park, 2017, Phys. Rev. Lett. **119**, 016401.

Novoselov, K. S., D. Jiang, F. Schedin, T. J. Booth, V. V. Khotkevich, S. V. Morozov, and A. K. Geim, 2005, Proc. Natl. Acad. Sci. U.S.A. **102**, 10451.

O'Brien, T. E., M. Diez, and C. W. J. Beenakker, 2016, Phys. Rev. Lett. **116**, 236401.

Ohtsubo, Y., P. Le Fèvre, F. m. c. Bertran, and A. Taleb-Ibrahimi, 2013, Phys. Rev. Lett. **111**, 216401.

Ojanen, T., 2013, Phys. Rev. B **87**, 245112.

Osterhoudt, G. B., *et al.*, 2019, Nat. Mater. **18**, 471.

Ozawa, T., *et al.*, 2019, Rev. Mod. Phys. **91**, 015006.

Pan, H., *et al.*, 2016, Appl. Phys. Lett. **108**, 183103.

Pan, H., *et al.*, 2018, Sci. Rep. **8**, 9340.

Pan, X.-C., X. Wang, F. Song, and B. Wang, 2018, Adv. Phys. X **3**, 1468279.

Pan, X.-C., *et al.*, 2015, Nat. Commun. **6**, 7805.

Panfilov, I., A. A. Burkov, and D. A. Pesin, 2014, Phys. Rev. B **89**, 245103.

Parameswaran, S. A., T. Grover, D. A. Abanin, D. A. Pesin, and A. Vishwanath, 2014, Phys. Rev. X **4**, 031035.

Pariari, A., P. Dutta, and P. Mandal, 2015, Phys. Rev. B **91**, 155139.

Park, S., S. Woo, E. J. Mele, and H. Min, 2017, Phys. Rev. B **95**, 161113.

Patankar, S., *et al.*, 2018, Phys. Rev. B **98**, 165113.

Pavlosiuk, O., and D. Kaczorowski, 2018, Sci. Rep. **8**, 11297.

Peng, H., K. Lai, D. Kong, S. Meister, Y. Chen, X.-L. Qi, S.-C. Zhang, Z.-X. Shen, and Y. Cui, 2010, Nat. Mater. **9**, 225.

Peterson, C. W., W. A. Benalcazar, T. L. Hughes, and G. Bahl, 2018, Nature (London) **555**, 346.

Pezzini, S., M. R. van Delft, L. M. Schoop, B. V. Lotsch, A. Carrington, M. I. Katsnelson, N. E. Hussey, and S. Wiedmann, 2018, Nat. Phys. **14**, 178.

Pietraszko, A., and K. Åukaszewicz, 1973, Phys. Status Solidi (a) **18**, 723.

Po, H. C., A. Vishwanath, and H. Watanabe, 2017, Nat. Commun. **8**, 1.

Potter, A. C., I. Kimchi, and A. Vishwanath, 2014, Nat. Commun. **5**, 5161.

Pronin, A. V., and M. Dressel, 2021, Phys. Status Solidi (b) **258**, 2000027.

Pshenay-Severin, D. A., Y. V. Ivanov, and A. T. Burkov, 2018, J. Phys. Condens. Matter **30**, 475501.

Qi, X.-L., T. L. Hughes, S. Raghu, and S.-C. Zhang, 2009, Phys. Rev. Lett. **102**, 187001.

Qi, X.-L., T. L. Hughes, and S.-C. Zhang, 2008, Phys. Rev. B **78**, 195424.

Qi, X.-L., and S. C. Zhang, 2011, Rev. Mod. Phys. **83**, 1057.

Qin, S., L. Hu, C. Le, J. Zeng, F.-c. Zhang, C. Fang, and J. Hu, 2019, Phys. Rev. Lett. **123**, 027003.

Qiu, Z., C. Le, Z. Liao, B. Xu, R. Yang, J. Hu, Y. Dai, and X. Qiu, 2019, Phys. Rev. B **100**, 125136.

Quan, Y., Z. P. Yin, and W. E. Pickett, 2017, Phys. Rev. Lett. **118**, 176402.

Rajamathi, C. R., *et al.*, 2017, Adv. Mater. **29**, 1606202.

Ramamurthy, S. T., and T. L. Hughes, 2017, Phys. Rev. B **95**, 075138.

Ramshaw, B. J., *et al.*, 2018, Nat. Commun. **9**, 2217.

Rao, Z., *et al.*, 2019, Nature (London) **567**, 496.

Razzoli, E., B. Zwartsenberg, M. Michiardi, F. Boschini, R. P. Day, I. S. Elfimov, J. D. Denlinger, V. Süss, C. Felser, and A. Damascelli, 2018, Phys. Rev. B **97**, 201103.

Rees, D., K. Manna, B. Lu, T. Morimoto, H. Borrmann, C. Felser, J. E. Moore, D. H. Torchinsky, and J. Orenstein, 2020, Sci. Adv. **6**, eaba0509.

Resta, G., S.-T. Pi, X. Wan, and S. Y. Savrasov, 2018, Phys. Rev. B **97**, 085142.

Rhim, J.-W., and Y. B. Kim, 2015, Phys. Rev. B **92**, 045126.

Roth, S., *et al.*, 2018, Phys. Rev. B **97**, 165439.

Roy, B., P. Goswami, and V. Juričić, 2017, Phys. Rev. B **95**, 201102.

Roy, R., 2009, Phys. Rev. B **79**, 195322.

Roychowdhury, K., D. Z. Rocklin, and M. J. Lawler, 2018, Phys. Rev. Lett. **121**, 177201.

Ruan, J., S.-K. Jian, D. Zhang, H. Yao, H. Zhang, S.-C. Zhang, and D. Xing, 2016, Phys. Rev. Lett. **116**, 226801.

Rüßmann, P., *et al.*, 2018, Phys. Rev. B **97**, 075106.

Sanchez, D. S., *et al.*, 2019, Nature (London) **567**, 500.

Sánchez-Martínez, M.-A., F. de Juan, and A. G. Grushin, 2019, Phys. Rev. B **99**, 155145.

Sankar, R., G. Peramaiyan, I. P. Muthuselvam, C. J. Butler, K. Dimitri, M. Neupane, G. N. Rao, M.-T. Lin, and F. C. Chou, 2017, Sci. Rep. **7**, 40603.

Sato, M., and Y. Ando, 2017, Rep. Prog. Phys. **80**, 076501.

Sato, T., K. Segawa, K. Kosaka, S. Souma, K. Nakayama, K. Eto, T. Minami, Y. Ando, and T. Takahashi, 2011, Nat. Phys. **7**, 840.

Sato, T., *et al.*, 2018, Phys. Rev. B **98**, 121111.

Schilling, M. B., L. M. Schoop, B. V. Lotsch, M. Dressel, and A. V. Pronin, 2017, Phys. Rev. Lett. **119**, 187401.

Schindler, F., A. M. Cook, M. G. Vergniory, Z. Wang, S. S. P. Parkin, B. A. Bernevig, and T. Neupert, 2018, Sci. Adv. **4**, eaat0346.

Schindler, F., *et al.*, 2018, Nat. Phys. **14**, 918.

Schnyder, A. P., and P. M. R. Brydon, 2015, J. Phys. Condens. Matter **27**, 243201.

Schoop, L. M., M. N. Ali, C. Straßer, A. Topp, A. Varykhalov, D. Marchenko, V. Duppel, S. S. P. Parkin, B. V. Lotsch, and C. R. Ast, 2016, Nat. Commun. **7**, 11696.

Schoop, L. M., F. Pielnhofer, and B. V. Lotsch, 2018, Chem. Mater. **30**, 3155.

Schoop, L. M., *et al.*, 2018, Sci. Adv. **4**, eaar2317.

Schröter, N. B. M., *et al.*, 2019, Nat. Phys. **15**, 759.

Schröter, N. B. M., *et al.*, 2020, Science **369**, 179.

Schumann, T., L. Galletti, D. A. Kealhofer, H. Kim, M. Goyal, and S. Stemmer, 2018, Phys. Rev. Lett. **120**, 016801.

Schumann, T., M. Goyal, D. A. Kealhofer, and S. Stemmer, 2017, Phys. Rev. B **95**, 241113.

Serra-Garcia, M., V. Peri, R. Süsstrunk, O. R. Bilal, T. Larsen, L. G. Villanueva, and S. D. Huber, 2018, Nature (London) **555**, 342.

Sessi, P., *et al.*, 2017, Phys. Rev. B **95**, 035114.

Shama, R. Gopal, and Y. Singh, 2020, J. Magn. Magn. Mater. **502**, 166547.

Shao, Y., *et al.*, 2019, Proc. Natl. Acad. Sci. U.S.A. **116**, 1168.

Shekhar, C., *et al.*, 2015, Nat. Phys. **11**, 645.

Shekhar, C., *et al.*, 2018, Proc. Natl. Acad. Sci. U.S.A. **115**, 9140.

Shi, Z., M. Wang, and J. Wu, 2015, Appl. Phys. Lett. **107**, 102403.

Shtanko, O., and L. Levitov, 2018, Proc. Natl. Acad. Sci. U.S.A. **115**, 5908.

Shuichi, Murakami, 2007, New J. Phys. **9**, 356.

Simon, B., 1983, Phys. Rev. Lett. **51**, 2167.

Singh, B., A. Sharma, H. Lin, M. Z. Hasan, R. Prasad, and A. Bansil, 2012, Phys. Rev. B **86**, 115208.

Singh, S., *et al.*, 2018, Nat. Phys. **14**, 355.

Singha, R., A. K. Pariari, B. Satpati, and P. Mandal, 2017, Proc. Natl. Acad. Sci. U.S.A. **114**, 2468.

Singha, R., S. Roy, A. Pariari, B. Satpati, and P. Mandal, 2018, Phys. Rev. B **98**, 081103.

Sirica, N., *et al.*, 2019, Phys. Rev. Lett. **122**, 197401.

Šmejkal, L., J. Železný, J. Sinova, and T. Jungwirth 2017, Phys. Rev. Lett. **118**, 106402.

Soluyanov, A. A., D. Gresch, Z. Wang, Q. Wu, M. Troyer, X. Dai, and B. A. Bernevig, 2015, Nature (London) **527**, 495.

Son, D. T., and B. Z. Spivak, 2013, Phys. Rev. B **88**, 104412.

Song, H.-D., D. Sheng, A.-Q. Wang, J.-G. Li, D.-P. Yu, and Z.-M. Liao, 2017, Chin. Phys. B **26**, 037301.

Song, Y. K., *et al.*, 2020, Phys. Rev. Lett. **124**, 056402.

Song, Z., Z. Fang, and C. Fang, 2017b, Phys. Rev. Lett. **119**, 246402.

Souma, S., *et al.*, 2016, Phys. Rev. B **93**, 161112.

Starke, K., A. P. Kaduwela, Y. Liu, P. D. Johnson, M. A. Van Hove, C. S. Fadley, V. Chakarian, E. E. Chaban, G. Meigs, and C. T. Chen, 1996, Phys. Rev. B **53**, R10544.

Steigmann, G. A., and J. Goodyear, 1968, Acta Crystallogr. Sect. B **24**, 1062.

Steinberg, J. A., S. M. Young, S. Zaheer, C. L. Kane, E. J. Mele, and A. M. Rappe, 2014, Phys. Rev. Lett. **112**, 036403.

Su, C.-C., C.-S. Li, T.-C. Wang, S.-Y. Guan, R. Sankar, F. Chou, C.-S. Chang, W.-L. Lee, G.-Y. Guo, and T.-M. Chuang, 2018, New J. Phys. **20**, 103025.

Sun, K., W. V. Liu, A. Hemmerich, and S. Das Sarma, 2012, Nat. Phys. **8**, 67.

Sun, K., S.-S. Sun, L.-L. Wei, C. Guo, H.-F. Tian, G.-F. Chen, H.-X. Yang, and J.-Q. Li, 2017, Chin. Phys. Lett. **34**, 117203.

Sun, Y., S.-C. Wu, M. N. Ali, C. Felser, and B. Yan, 2015, Phys. Rev. B **92**, 161107.

Sun, Y., S.-C. Wu, and B. Yan, 2015, Phys. Rev. B **92**, 115428.

Sun, Y., Y. Zhang, C. Felser, and B. Yan, 2016, Phys. Rev. Lett. **117**, 146403.

Sun, Y., Y. Zhang, C.-X. Liu, C. Felser, and B. Yan, 2017, Phys. Rev. B **95**, 235104.

Sushkov, A. B., J. B. Hofmann, G. S. Jenkins, J. Ishikawa, S. Nakatsuji, S. Das Sarma, and H. D. Drew, 2015, Phys. Rev. B **92**, 241108.

Suzuki, T., R. Chisnell, A. Devarakonda, Y.-T. Liu, W. Feng, D. Xiao, J. Lynn, and J. Checkelsky, 2016, Nat. Phys. **12**, 1119.

Tabert, C. J., and J. P. Carbotte, 2016, Phys. Rev. B **93**, 085442.

Tabert, C. J., J. P. Carbotte, and E. J. Nicol, 2016, Phys. Rev. B **93**, 085426.

Taguchi, K., D.-H. Xu, A. Yamakage, and K. T. Law, 2016, Phys. Rev. B **94**, 155206.

Takane, D., *et al.*, 2018, npj Quantum Mater. **3**, 1.

Takane, D., *et al.*, 2019, Phys. Rev. Lett. **122**, 076402.

Tamai, A., *et al.*, 2016, Phys. Rev. X **6**, 031021.

Tanaka, Y., Z. Ren, T. Sato, K. Nakayama, S. Souma, T. Takahashi, K. Segawa, and Y. Ando, 2012, Nat. Phys. **8**, 800.

Tang, F., H. C. Po, A. Vishwanath, and X. Wan, 2019, Nature (London) **566**, 486.

Tang, H. X., R. K. Kawakami, D. D. Awschalom, and M. L. Roukes, 2003, Phys. Rev. Lett. **90**, 107201.

Tang, P., Q. Zhou, G. Xu, and S.-C. Zhang, 2016, Nat. Phys. **12**, 1100.

Tang, P., Q. Zhou, and S.-C. Zhang, 2017, Phys. Rev. Lett. **119**, 206402.

Taskin, A. A., H. F. Legg, F. Yang, S. Sasaki, Y. Kanai, K. Matsumoto, A. Rosch, and Y. Ando, 2017, Nat. Commun. **8**, 1340.

Tchoumakov, S., M. Civelli, and M. O. Goerbig, 2016, Phys. Rev. Lett. **117**, 086402.

Thouless, D. J., M. Kohmoto, M. P. Nightingale, and M. den Nijs, 1982, Phys. Rev. Lett. **49**, 405.

Timusk, T., J. P. Carbotte, C. C. Homes, D. N. Basov, and S. G. Sharapov, 2013, Phys. Rev. B **87**, 235121.

Topp, A., *et al.*, 2017, Phys. Rev. X **7**, 041073.

Tsui, D. C., H. L. Stormer, and A. C. Gossard, 1982, Phys. Rev. Lett. **48**, 1559.

Uchida, M., *et al.*, 2017, Nat. Commun. **8**, 2274.

Udagawa, M., and E. J. Bergholtz, 2016, Phys. Rev. Lett. **117**, 086401.

Ueda, K., J. Fujioka, and Y. Tokura, 2016, Phys. Rev. B **93**, 245120.

Uykur, E., R. Sankar, D. Schmitz, and C. A. Kuntscher, 2018, Phys. Rev. B **97**, 195134.

Vafek, O., and A. Vishwanath, 2014, Annu. Rev. Condens. Matter Phys. **5**, 83.

Vashist, A., R. K. Singh, N. Wadehra, S. Chakraverty, and Y. Singh, 2018, arXiv:1812.06485.

Vergniory, M. G., L. Elcoro, C. Felser, N. Regnault, B. A. Bernevig, and Z. Wang, 2019, Nature (London) **566**, 480.
Volovik, G. E., 2016, JETP Lett. **104**, 645.
Volovik, G. E., 2018, Phys. Usp. **61**, 89.
Volovik, G. E., and K. Zhang, 2017, J. Low Temp. Phys. **189**, 276.
Wan, X., A. M. Turner, A. Vishwanath, and S. Y. Savrasov, 2011, Phys. Rev. B **83**, 205101.
Wang, C., *et al.*, 2016, Phys. Rev. B **94**, 241119.
Wang, C. M., H.-P. Sun, H.-Z. Lu, and X. C. Xie, 2017, Phys. Rev. Lett. **119**, 136806.
Wang, H., H. Wang, H. Liu, H. Lu, W. Yang, S. Jia, X.-J. Liu, X. C. Xie, J. Wei, and J. Wang, 2016, Nat. Mater. **15**, 38.
Wang, H., and J. Wang, 2018, Chin. Phys. B **27**, 107402.
Wang, H., *et al.*, 2017, Sci. Bull. **62**, 425.
Wang, J., 2017a, Phys. Rev. B **95**, 115138.
Wang, J., 2017b, Phys. Rev. B **96**, 081107.
Wang, J., 2017c, arXiv:1701.00896.
Wang, J., Y. Liu, K.-H. Jin, X. Sui, L. Zhang, W. Duan, F. Liu, and B. Huang, 2018, Phys. Rev. B **98**, 201112.
Wang, J., X. Sui, W. Shi, J. Pan, S. Zhang, F. Liu, S.-H. Wei, Q. Yan, and B. Huang, 2017, Phys. Rev. Lett. **119**, 256402.
Wang, L., S.-K. Jian, and H. Yao, 2017, Phys. Rev. B **96**, 075110.
Wang, L.-X., C.-Z. Li, D.-P. Yu, and Z.-M. Liao, 2016, Nat. Commun. **7**, 10769.
Wang, Q., Y. Xu, R. Lou, Z. Liu, M. Li, Y. Huang, D. Shen, H. Weng, S. Wang, and H. Lei, 2018, Nat. Commun. **9**, 3681.
Wang, Q., *et al.*, 2017, Nano Lett. **17**, 834.
Wang, R., B. Wang, R. Shen, L. Sheng, and D. Y. Xing, 2014, Europhys. Lett. **105**, 17004.
Wang, R., J. Z. Zhao, Y. J. Jin, Y. P. Du, Y. X. Zhao, H. Xu, and S. Y. Tong, 2018, Phys. Rev. B **97**, 241111.
Wang, R., J. Z. Zhao, Y. J. Jin, W. P. Xu, L.-Y. Gan, X. Z. Wu, H. Xu, and S. Y. Tong, 2017, Phys. Rev. B **96**, 121104.
Wang, S., B.-C. Lin, A.-Q. Wang, D.-P. Yu, and Z.-M. Liao, 2017, Adv. Phys. X **2**, 518.
Wang, X., *et al.*, 2016, Adv. Electron. Mater. **2**, 1600228.
Wang, X.-B., *et al.*, 2017, Phys. Rev. B **96**, 161112.
Wang, Y., *et al.*, 2016a, Nat. Commun. **7**, 13142.
Wang, Y., *et al.*, 2016b, Sci. Rep. **6**, 31554.
Wang, Y. J., J. X. Gong, D. D. Liang, M. Ge, J. R. Wang, W. K. Zhu, and C. J. Zhang, 2018, arXiv:1801.05929.
Wang, Z., A. Alexandradinata, R. J. Cava, and B. A. Bernevig, 2016, Nature (London) **532**, 189.
Wang, Z., D. Gresch, A. A. Soluyanov, W. Xie, S. Kushwaha, X. Dai, M. Troyer, R. J. Cava, and B. A. Bernevig, 2016g, Phys. Rev. Lett. **117**, 056805.
Wang, Z., Y. Sun, X. Q. Chen, C. Franchini, G. Xu, H. Weng, X. Dai, and Z. Fang, 2012, Phys. Rev. B **85**, 195320.
Wang, Z., M. G. Vergniory, S. Kushwaha, M. Hirschberger, E. V. Chulkov, A. Ernst, N. P. Ong, R. J. Cava, and B. A. Bernevig, 2016, Phys. Rev. Lett. **117**, 236401.
Wang, Z., H. Weng, Q. Wu, X. Dai, and Z. Fang, 2013, Phys. Rev. B **88**, 125427.
Wang, Z., *et al.*, 2016, Phys. Rev. B **93**, 121112.
Watanabe, H., H. C. Po, and A. Vishwanath, 2018, Sci. Adv. **4**, eaat8685.
Wehling, T., A. Black-Schaffer, and A. Balatsky, 2014, Adv. Phys. **63**, 1.
Wei, B. Y., H. J. Bu, S. Zhang, and F. Q. Song, 2019, Acta Phys. Sin. **68**, 227203.
Weng, H., X. Dai, and Z. Fang, 2014, MRS Bull. **39**, 849.
Weng, H., X. Dai, and Z. Fang, 2016, J. Phys. Condens. Matter **28**, 303001.
Weng, H., C. Fang, Z. Fang, B. Andrei Bernevig, and X. Dai, 2015, Phys. Rev. X **5**, 011029.
Weng, H., C. Fang, Z. Fang, and X. Dai, 2016a, Phys. Rev. B **94**, 165201.
Weng, H., C. Fang, Z. Fang, and X. Dai, 2016b, Phys. Rev. B **93**, 241202.
Weng, H., Y. Liang, Q. Xu, R. Yu, Z. Fang, X. Dai, and Y. Kawazoe, 2015, Phys. Rev. B **92**, 045108.
Wieder, B. J., Y. Kim, A. M. Rappe, and C. L. Kane, 2016, Phys. Rev. Lett. **116**, 186402.
Winkler, G. W., Q. Wu, M. Troyer, P. Krogstrup, and A. A. Soluyanov, 2016, Phys. Rev. Lett. **117**, 076403.
Wu, H., M. Brahlek, R. Valdés Aguilar, A. V. Stier, C. M. Morris, Y. Lubashevsky, L. S. Bilbro, N. Bansal, S. Oh, and N. P. Armitage, 2013, Nat. Phys. **9**, 410.
Wu, H., D.-S. Ma, B. Fu, W. Guo, and Y. Yao, 2019, J. Phys. Chem. Lett. **10**, 2508.
Wu, L., S. Patankar, T. Morimoto, N. L. Nair, E. Thewalt, A. Little, J. G. Analytis, J. E. Moore, and J. Orenstein, 2017, Nat. Phys. **13**, 350.
Wu, M., *et al.*, 2018, Phys. Rev. B **98**, 161110.
Wu, S.-C., Y. Sun, C. Felser, and B. Yan, 2017, Phys. Rev. B **96**, 165113.
Wu, W., Y. Liu, S. Li, C. Zhong, Z.-M. Yu, X.-L. Sheng, Y. X. Zhao, and S. A. Yang, 2018, Phys. Rev. B **97**, 115125.
Wu, Y., L. L. Wang, E. Mun, D. D. Johnson, D. Mou, L. Huang, Y. Lee, S. L. Bud'ko, P. C. Canfield, and A. Kaminski, 2016, Nat. Phys. **12**, 667.
Xia, F., T. Mueller, Y.-m. Lin, A. Valdes-Garcia, and P. Avouris, 2009, Nat. Nanotechnol. **4**, 839.
Xia, Y., *et al.*, 2009, Nat. Phys. **5**, 398.
Xiang, Z. J., D. Zhao, Z. Jin, C. Shang, L. K. Ma, G. J. Ye, B. Lei, T. Wu, Z. C. Xia, and X. H. Chen, 2015, Phys. Rev. Lett. **115**, 226401.
Xiao, M., W.-J. Chen, W.-Y. He, and C. T. Chan, 2015, Nat. Phys. **11**, 920.
Xie, L. S., L. M. Schoop, E. M. Seibel, Q. D. Gibson, W. Xie, and R. J. Cava, 2015, APL Mater. **3**, 083602.
Xiong, J., S. K. Kushwaha, T. Liang, J. W. Krizan, M. Hirschberger, W. Wang, R. J. Cava, and N. P. Ong, 2015, Science **350**, 413.
Xu, B., L. X. Zhao, P. Marsik, E. Sheveleva, F. Lyzwa, Y. M. Dai, G. F. Chen, X. G. Qiu, and C. Bernhard, 2018, Phys. Rev. Lett. **121**, 187401.
Xu, B., *et al.*, 2016, Phys. Rev. B **93**, 121110.
Xu, B., *et al.*, 2017, Nat. Commun. **8**, 14933.
Xu, C.-Z., *et al.*, 2017, Phys. Rev. Lett. **118**, 146402.
Xu, D.-F., Y.-P. Du, Z. Wang, Y.-P. Li, X.-H. Niu, Q. Yao, D. Pavel, Z.-A. Xu, X.-G. Wan, and D.-L. Feng, 2015, Chin. Phys. Lett. **32**, 107101.
Xu, G., H. Weng, Z. Wang, X. Dai, and Z. Fang, 2011, Phys. Rev. Lett. **107**, 186806.
Xu, N., *et al.*, 2013, Phys. Rev. B **88**, 121102.
Xu, N., *et al.*, 2016, Nat. Commun. **7**, 11006.
Xu, N., *et al.*, 2017, Phys. Rev. Lett. **118**, 106406.
Xu, N., *et al.*, 2018, Phys. Rev. B **97**, 161111.
Xu, Q., E. Liu, W. Shi, L. Muechler, J. Gayles, C. Felser, and Y. Sun, 2018, Phys. Rev. B **97**, 235416.
Xu, Q., R. Yu, Z. Fang, X. Dai, and H. Weng, 2017, Phys. Rev. B **95**, 045136.
Xu, S., H. Wang, X.-Y. Wang, Y. Su, P. Cheng, and T.-L. Xia, 2018, arXiv:1811.06767.
Xu, S.-Y., *et al.*, 2011, Science **332**, 560.
Xu, S.-Y., *et al.*, 2012, Nat. Commun. **3**, 1192.
Xu, S.-Y., *et al.*, 2015a, Nat. Phys. **11**, 748.

Xu, S.-Y., *et al.*, 2015b, Science **349**, 613.

Xu, S.-Y., *et al.*, 2015c, Sci. Adv. **1**, e1501092.

Xu, S.-Y., *et al.*, 2015d, Science **347**, 294.

Xu, S.-Y., *et al.*, 2016, Phys. Rev. Lett. **116**, 096801.

Xu, S.-Y., *et al.*, 2017, Sci. Adv. **3**, e1603266.

Xu, X., *et al.*, 2019, Phys. Rev. B **100**, 045104.

Xu, X.-T., and S. Jia, 2016, Chin. Phys. B **25**, 117204.

Xu, Y., L. Elcoro, Z.-D. Song, B. J. Wieder, M. G. Vergniory, N. Regnault, Y. Chen, C. Felser, and B. A. Bernevig, 2020, Nature (London) **586**, 702.

Xu, Y., C. Yue, H. Weng, and X. Dai, 2017, Phys. Rev. X **7**, 011027.

Yamakage, A., Y. Yamakawa, Y. Tanaka, and Y. Okamoto, 2016, J. Phys. Soc. Jpn. **85**, 013708.

Yan, B., and C. Felser, 2017, Annu. Rev. Condens. Matter Phys. **8**, 337.

Yan, M., *et al.*, 2017, Nat. Commun. **8**, 257.

Yan, Q., R. Liu, Z. Yan, B. Liu, H. Chen, Z. Wang, and L. Lu, 2018, Nat. Phys. **14**, 461.

Yan, Z., R. Bi, H. Shen, L. Lu, S.-C. Zhang, and Z. Wang, 2017, Phys. Rev. B **96**, 041103.

Yan, Z., P.-W. Huang, and Z. Wang, 2016, Phys. Rev. B **93**, 085138.

Yan, Z., and Z. Wang, 2016, Phys. Rev. Lett. **117**, 087402.

Yang, B., *et al.*, 2018, Science **359**, 1013.

Yang, B.-J., and N. Nagaosa, 2014, Nat. Commun. **5**, 4898.

Yang, H., A. Liang, C. Chen, C. Zhang, N. B. M. Schroeter, and Y. Chen, 2018, Nat. Rev. Mater. **3**, 341.

Yang, H., M. Schmidt, V. Süss, M. Chan, F. F. Balakirev, R. D. McDonald, S. S. P. Parkin, C. Felser, B. Yan, and P. J. W. Moll, 2018, New J. Phys. **20**, 043008.

Yang, H., Y. Sun, Y. Zhang, W.-J. Shi, S. S. P. Parkin, and B. Yan, 2017, New J. Phys. **19**, 015008.

Yang, H., J. Yu, S. S. P. Parkin, C. Felser, C.-X. Liu, and B. Yan, 2017, Phys. Rev. Lett. **119**, 136401.

Yang, H. F., *et al.*, 2019, Nat. Commun. **10**, 3478.

Yang, J., *et al.*, 2019, Phys. Rev. Mater. **3**, 014201.

Yang, K.-Y., Y.-M. Lu, and Y. Ran, 2011, Phys. Rev. B **84**, 075129.

Yang, L. X., *et al.*, 2015, Nat. Phys. **11**, 728.

Yang, R., T. Zhang, L. Zhou, Y. Dai, Z. Liao, H. Weng, and X. Qiu, 2020, Phys. Rev. Lett. **124**, 077403.

Yang, S.-Y., H. Yang, E. Derunova, S. S. P. Parkin, B. Yan, and M. N. Ali, 2018, Adv. Phys. X **3**, 1414631.

Yang, Y., Z. Gao, X. Feng, Y.-X. Huang, P. Zhou, S. A. Yang, Y. Chong, and B. Zhang, 2020, Phys. Rev. Lett. **125**, 143001.

Yao, M.-Y., *et al.*, 2019, Phys. Rev. Lett. **122**, 176402.

Yavarishad, N., T. Hosseini, E. Kheirandish, C. P. Weber, and N. Kouklin, 2017, Appl. Phys. Express **10**, 052201.

Yi, C.-J., *et al.*, 2018, Phys. Rev. B **97**, 201107.

Yin, J.-X., *et al.*, 2019, Nat. Phys. **15**, 443.

Yoshida, K., 1976, J. Phys. Soc. Jpn. **41**, 574.

Young, S. M., S. Chowdhury, E. J. Walter, E. J. Mele, C. L. Kane, and A. M. Rappe, 2011, Phys. Rev. B **84**, 085106.

Young, S. M., and B. J. Wieder, 2017, Phys. Rev. Lett. **118**, 186401.

Young, S. M., S. Zaheer, J. C. Y. Teo, C. L. Kane, E. J. Mele, and A. M. Rappe, 2012, Phys. Rev. Lett. **108**, 140405.

Yu, R., Z. Fang, X. Dai, and H. Weng, 2017, Front. Phys. **12**, 127202.

Yu, R., H. Weng, Z. Fang, X. Dai, and X. Hu, 2015, Phys. Rev. Lett. **115**, 036807.

Yu, R., Q. Wu, Z. Fang, and H. Weng, 2017, Phys. Rev. Lett. **119**, 036401.

Yu, R., W. Zhang, H.-J. Zhang, S.-C. Zhang, X. Dai, and Z. Fang, 2010, Science **329**, 61.

Yu, W. C., X. Zhou, F.-C. Chuang, S. A. Yang, H. Lin, and A. Bansil, 2018, Phys. Rev. Mater. **2**, 051201.

Yu, Z.-M., W. Wu, X.-L. Sheng, Y. X. Zhao, and S. A. Yang, 2019, Phys. Rev. B **99**, 121106.

Yu, Z.-M., Y. Yao, and S. A. Yang, 2016, Phys. Rev. Lett. **117**, 077202.

Yuan, Q.-Q., *et al.*, 2019, Sci. Adv. **5**, eaaw9485.

Yuan, X., *et al.*, 2017, Nano Lett. **17**, 2211.

Yuan, X., *et al.*, 2018, Nat. Commun. **9**, 1854.

Yuan, X., *et al.*, 2020, Nat. Commun. **11**, 1259.

Yuan, Z., H. Lu, Y. Liu, J. Wang, and S. Jia, 2016, Phys. Rev. B **93**, 184405.

Zeng, M., C. Fang, G. Chang, Y.-A. Chen, T. Hsieh, A. Bansil, H. Lin, and L. Fu, 2015, arXiv:1504.03492.

Zhang, C., C. Guo, H. Lu, X. Zhang, Z. Yuan, Z. Lin, J. Wang, and S. Jia, 2015, Phys. Rev. B **92**, 041203.

Zhang, C., *et al.*, 2017a, Nat. Commun. **8**, 1272.

Zhang, C., *et al.*, 2017b, Nat. Commun. **8**, 13741.

Zhang, C., *et al.*, 2019a, Nat. Mater. **18**, 482.

Zhang, C., *et al.*, 2019b, Nature (London) **565**, 331.

Zhang, C.-L., B. Tong, Z. Yuan, Z. Lin, J. Wang, J. Zhang, C.-Y. Xi, Z. Wang, S. Jia, and C. Zhang, 2016, Phys. Rev. B **94**, 205120.

Zhang, C.-L., *et al.*, 2016, Nat. Commun. **7**, 10735.

Zhang, C.-L., *et al.*, 2017, Nat. Phys. **13**, 979.

Zhang, C.-L., *et al.*, 2019, Nat. Commun. **10**, 1028.

Zhang, D., H. Wang, J. Ruan, G. Yao, and H. Zhang, 2018, Phys. Rev. B **97**, 195139.

Zhang, E., Y. Liu, W. Wang, C. Zhang, P. Zhou, Z.-G. Chen, J. Zou, and F. Xiu, 2015, ACS Nano **9**, 8843.

Zhang, E., *et al.*, 2017, Nano Lett. **17**, 878.

Zhang, F., C. L. Kane, and E. J. Mele, 2013, Phys. Rev. Lett. **111**, 056402.

Zhang, H., C. X. Liu, X. L. Qi, X. Dai, Z. Fang, and S. C. Zhang, 2009, Nat. Phys. **5**, 438.

Zhang, K., M. Yan, H. Zhang, H. Huang, M. Arita, Z. Sun, W. Duan, Y. Wu, and S. Zhou, 2017, Phys. Rev. B **96**, 125102.

Zhang, Q. R., *et al.*, 2019, Phys. Rev. B **100**, 115138.

Zhang, T., Y. Jiang, Z. Song, H. Huang, Y. He, Z. Fang, H. Weng, and C. Fang, 2019, Nature (London) **566**, 475.

Zhang, T., Z. Song, A. Alexandradinata, H. Weng, C. Fang, L. Lu, and Z. Fang, 2018, Phys. Rev. Lett. **120**, 016401.

Zhang, T., R. Takahashi, C. Fang, and S. Murakami, 2020, Phys. Rev. B **102**, 125148.

Zhang, W., Q. Wu, L. Zhang, S.-W. Cheong, A. A. Soluyanov, and W. Wu, 2017, Phys. Rev. B **96**, 165125.

Zhang, W., *et al.*, 2020, Nat. Commun. **11**, 1046.

Zhang, X., L. Jin, X. Dai, and G. Liu, 2017, J. Phys. Chem. Lett. **8**, 4814.

Zhang, X., Z.-M. Yu, Y. Lu, X.-L. Sheng, H. Y. Yang, and S. A. Yang, 2018, Phys. Rev. B **97**, 125143.

Zhang, X., Z.-M. Yu, X.-L. Sheng, H. Y. Yang, and S. A. Yang, 2017, Phys. Rev. B **95**, 235116.

Zhang, X.-X., T. T. Ong, and N. Nagaosa, 2016, Phys. Rev. B **94**, 235137.

Zhang, Y., Y. Sun, and B. Yan, 2018, Phys. Rev. B **97**, 041101.

Zhang, Y., and A. Vishwanath, 2010, Phys. Rev. Lett. **105**, 206601.

Zhao, J., R. Yu, H. Weng, and Z. Fang, 2016, Phys. Rev. B **94**, 195104.

Zhao, Y., *et al.*, 2015a, Phys. Rev. B **92**, 041104.

Zhao, Y., *et al.*, 2015b, Phys. Rev. X **5**, 031037.

Zheng, G., *et al.*, 2017, Phys. Rev. B **96**, 121407.

Zheng, H., and M. Zahid Hasan, 2018, Adv. Phys. X **3**, 1466661.

Zheng, H., *et al.*, 2016a, Phys. Rev. Lett. **117**, 266804.

Zheng, H., *et al.*, 2016b, ACS Nano **10**, 1378.

Zheng, H., *et al.*, 2017, Phys. Rev. Lett. **119**, 196403.

Zheng, W., *et al.*, 2018, Phys. Rev. B **97**, 235154.

Zhong, C., Y. Chen, Y. Xie, S. A. Yang, M. L. Cohen, and S. B. Zhang, 2016, Nanoscale **8**, 7232.

Zhou, J., H.-R. Chang, and D. Xiao, 2015, Phys. Rev. B **91**, 035114.

Zhou, X., *et al.*, 2018, Phys. Rev. B **97**, 241102.

Zhou, X., *et al.*, 2019, Phys. Rev. B **100**, 184511.

Zhu, C., *et al.*, 2017, Nat. Commun. **8**, 14111.

Zhu, Z., X. Lin, J. Liu, B. Fauqué, Q. Tao, C. Yang, Y. Shi, and K. Behnia, 2015, Phys. Rev. Lett. **114**, 176601.

Zhu, Z., Y. Liu, Z.-M. Yu, S.-S. Wang, Y. X. Zhao, Y. Feng, X.-L. Sheng, and S. A. Yang, 2018, Phys. Rev. B **98**, 125104.

Zhu, Z., G. W. Winkler, Q. Wu, J. Li, and A. A. Soluyanov, 2016, Phys. Rev. X **6**, 031003.

Zhu, Z., *et al.*, 2018, Nat. Commun. **9**, 4153.

Zou, J. Y., and B. G. Liu, 2016, Phys. Rev. B **93**, 205435.

Zyuzin, A. A., and R. P. Tiwari, 2016, JETP Lett. **103**, 717.

Zyuzin, A. A., S. Wu, and A. A. Burkov, 2012, Phys. Rev. B **85**, 165110.